Université de Montréal

Modèle du pseudo-atome neutre pour l'étude de métaux simples dans le régime de la matière dense et chaude à deux températures

par

Louis Harbour

Département de physique
Faculté des arts et des sciences

Thèse présentée à la Faculté des études supérieures
en vue de l'obtention du grade de
Philosophiæ Doctor (Ph.D.)
en Physique de la matière condensée et des plasmas

8 juin 2018

SOMMAIRE

L'étude de la matière dense et chaude (MDC), ce régime particulier à la frontière entre la phase solide et la phase plasma, est en pleine effervescence due à ses nombreuses applications en astrophysique et dans le domaine de la fusion nucléaire. Son étude théorique pose plusieurs défis majeurs et le développement d'outils mathématiques appropriés pour ce régime constitue le cœur de cette thèse. En particulier, on s'intéresse à deux états distincts de MDC obtenue par différentes méthodes expérimentales appliquées sur les métaux simples. Le premier cas est la matière ultra-rapide (MUR), cet état où la température du système électronique est très élevée tandis que celle des ions reste à la température ambiante. La MUR ne subit aucune compression et reste à la densité initiale du matériel étudié. La stabilité de ce système est étudiée par le biais du spectre de phonons ainsi que par le calcul de la pression interne qui subit une énorme augmentation. Le deuxième cas est la matière compressée par choc (MCC), où la densité du système peut atteindre deux à trois fois la densité initiale. La température des deux sous-systèmes est considérablement augmentée, mais s'avère ne pas toujours être en équilibre malgré tout. Dans cette thèse, l'étude de la MUR et de la MCC est réalisée à l'aide du modèle du pseudo-atome neutre (PAN) dont la simplicité et l'efficacité s'avèrent idéales pour la MDC. La diffusion Thomson des rayons X, la technique expérimentale la plus utilisée pour obtenir les propriétés de la MDC, nécessite un lissage à un spectre théorique qui est aisément calculable avec le modèle PAN. La conductivité électrique, une propriété fondamentale pour les applications technologiques de la MDC, est aussi étudiée en détail en comparant les diverses méthodes pour ce type de calculs. Finalement, puisque la création de MDC résulte généralement en des systèmes où la température électronique diffère de la température ionique, l'obtention des propriétés de la MDC dans cet état de quasi-équilibre à deux températures est constamment mis de l'avant tout au long de ce travail et constitue l'un des éléments innovateurs de cette thèse.

Mots-clé : Matière dense et chaude, Métaux simples, Matière ultra-rapide, Matière compressée par choc, Phonon, Équation d'état, Potentiel de paires, Quasi-équilibre

SUMMARY

The study of the warm dense matter (WDM), this particular state at the frontier of the solid phase and plasma phase, is in huge effervescence since it has many applications in astrophysics and in nuclear fusion technologies. Its theoretical description is filled with challenges and the development of mathematical tools adequate for this state is at the heart of this dissertation. In particular, we are interested at two distinct states of WDM obtained from different experimental techniques applied to simple metals. The first case is the ultra-fast matter (UFM) state where the temperature of the electronic system is super high while the ionic system one is kept at the room temperature. The UFM is not compressed of any kind and the density of the system is kept at the initial density of the material studied. The stability of this system is studied by computing the phonon spectrum and the internal pressure which is highly increased. The second case is the shock compressed matter (SCM) where the density of the system can reach up to two or three time the initial density. The temperature of both subsystems is considerably increased but the system can still be out of equilibrium. In this dissertation, the study of the UFM and the SCM is done by using the neutral pseudo-atom (NPA) model which efficiently and simplicity is perfect for the WDM. The x-ray Thomson scattering, the most used experimental technique to obtain WDM properties, requires a fitting to a theoretical spectrum which is easily obtainable from the NPA model. The electrical conductivity, a fundamental property for technological applications of the WDM, is studied in detail by comparing different approaches for this kind of calculations. Finally, since the creation of WDM usually leads to systems with the electron temperature different from the ion temperature, the calculation of WDM properties in this quasi-equilibrium state with two temperatures is one of the principal topics of this work and is one of the innovative elements of this dissertation.

Keywords : Warm dense matter, Simple metals, Ultra-fast matter, Shock compressed matter, Phonon, Equation of state, Pair potential, Quasi-equilibrium

Table des matières

Liste des tableaux

Table des figures

LISTE DES ACRONYMES

SECTION EN FRANÇAIS :

ADL	Approximation de la Densité Locale
CHNC	Classical Hyper-Netted-Chain
DM	Dynamique Moléculaire
FCI	Fusion par Confinement Inertiel
FDP	Fonction de Distribution de Paires
FDR	Fonction de Distribution Radiale
FEC	Fonctionnelle d'Échange et Corrélation
FID	Fonction Intermédiaire de Diffusion
FSD	Facteur de Structure Dynamique
FSS	Facteur de Structure Statique
HNC	Hyper-Netted-Chain
MCC	Matière Compressée sous Choc
MDC	Matière Dense et Chaude
MHNC	Modified Hyper-Netted-Chain
MUR	Matière Ultra-Rapide
OZ	Orstein-Zernike
PAN	Pseudo-Atome Neutre
TFD	Théorie de la Fonctionnelle de la Densité
TPFD	Théorie Perturbative de la Fonctionnelle de la Densité

SECTION EN ANGLAIS :

AA	Average Atom
BCC	Body Centered Cubic
CS	Correlation Sphere
DFPT	Density Fonctional Perturbation Theory
DFT	Density Fonctional Theory
DOS	Density Of States
DSF	Dynamic Structure Factor

EAM	Embedded-Atom Method
EOS	Equation Of State
FCC	Face Centered Cubic
FGR	Fermi Golden Rule
GGA	Generalized Gradient Approximation
HEG	Homogenous Electron Gas
HK	Hohenberg-Kohn
HNC	Hyper-Netted-Chain
HSE	Heyd, Seuseria and Ernzerhof
IS	Ion Sphere
KG	Kubo-Greenwood
KS	Kohn-Sham
LCLS	Linac Coherent Light Source
LDA	Local Density Approximation
LFA	Lado, Foiles and Ashcroft
LFC	Local Field Correction
MD	Molecular Dynamic
MHNC	Modified Hyper-Netted-Chain
NPA	Neutral Pseudo Atom
OF	Orbital Free
OZ	Orstein-Zernike
PAW	Projected Augmented Wave
PBE	Perdew, Burke and Ernzerhof
PDF	Pair Distribution Funcion
PP	Pair Potentials
RPA	Random Phase Approximation
SSF	Static Structure Factor
TTM	Two-Temperature Model
TTP	Two-Temperature Pairpotential
UFM	Ultra-Fast Matter
WDM	Warm Dense Matter
WS	Wigner-Seitz
XCF	Exchange-Correlation Functional
XRTS	X-Ray Thomson Scattering
YSRR	Yukawa + Short Range Repulsion

REMERCIEMENTS

L'accomplissement de cette thèse de doctorat en physique fut un défi d'une très grande amplitude que je suis extrêmement fier d'avoir surmonté. Ma passion pour la physique m'a permis de persévérer lors des moments les plus durs incluant des problèmes de santé qui ont bouleversé ma vie. La ligne d'arrivée de ce marathon est finalement dans mon champ de vue et je ressens un étrange mélange de peur et d'excitation. J'aimerais donc souligner plusieurs personnes merveilleuses qui ont su me soutenir lors de ce périple de plusieurs années.

La concrétisation de cette thèse n'aurait jamais pu avoir lieu sans l'encadrement professionnel et personnel que mes directeurs, Laurent J. Lewis et M. W. Chandre Dharmawardana, m'ont apporté. Ils ont su me transmettre leur passion pour la science au travers de multiples conversations remplies de conseils et d'encouragements. Je me sens privilégié d'avoir pu être supervisé par ces hommes dont la rigueur scientifique est sans pareille et j'espère poursuivre ma carrière en gardant leurs leçons en mémoire pour toujours.

Ce travail n'aurait pas été possible sans le soutien de l'Université de Montréal, en particulier le département de physique, qui m'a permis de m'épanouir au sein d'une communauté dynamique. Les conférences organisées par le groupe de matière condensée ainsi que par le département m'ont permis de garder les yeux ouverts sur divers domaines de la physique et d'épanouir ma curiosité scientifique. Il m'est impossible d'oublier les nombreuses conversations enflammées avec mes merveilleux collègues, notamment, Mickaël Trochet, Vincent Gosselin, Maxime Gill-Comeau et Daniel Förster. Je me dois d'aussi remercier les professeurs Michel Côté, François Schiettekatte et Sjoerd Roorda qui m'ont enseigné avec passion durant mes cours gradués.

Jamais je n'aurais pu espérer accomplir ce travail sans l'appui des parents, Simon Harbour et Nathalie Routhier, ainsi que de ma soeur, Audrey Harbour, qui m'ont toujours encouragé à poursuivre mes études. Leur soutien moral et émotionnel au cours de toutes mes études universitaires fut d'une importance inimaginable et je ne saurai jamais les remercier suffisamment. Mes études en physique sont à l'origine de la personne que je suis aujourd'hui et c'est grâce à ma famille que j'ai pu profiter de cette expérience extraordinaire.

En effet,dès mon premier jour d'université, ma vie fut complètement chamboulée puisque j'y ai rencontré une femme merveilleuse, Caroline Fortin, que j'ai eu l'énorme privilège

d'épouser très récemment. Ensemble, nous avons forgé une relation indestructible sur laquelle j'ai toujours pu m'appuyer pour franchir tous les obstacles. Durant cette dernière épreuve académique, elle a su me guider et me motiver afin d'accomplir le plus grand travail de ma vie. J'appréhende infiniment la suite de notre histoire au terme de notre cheminement académique. Je ne pourrai oublier mes beaux-parents, André Fortin et Nicole Cléroux, qui ont toujours cru en moi en m'encourageant sans cesse.

C'est ainsi, avec le cœur plein d'émotion, que je vous remercie tous pour ces années extraordinaires qui seront à jamais gravées dans ma mémoire.

Chapitre 1

INTRODUCTION

1.1. Contexte

Tout autour de nous, la matière se manifeste sous des formes si différentes qu'il est facile d'oublier que tout est constitué de ces blocs fondamentaux que sont les atomes. Uniquement sur terre, pour ces conditions particulières de pression et de température, les atomes se présentent sous une multitude de phases différentes. À basse température et haute densité, l'interaction potentielle entre les atomes est si forte qu'ils sont pratiquement incapables de bouger et forment des structures cristallines. L'étude de la physique des solides permet une compréhension profonde des propriétés quantiques de la matière et créa une révolution de l'électronique. À l'opposé, à haute température et basse densité, l'énergie cinétique des atomes est si grande que les électrons se libèrent de leur noyau formant un plasma. Dans cette phase, les particules possèdent tellement d'énergie thermique qu'elles ne se perçoivent pratiquement pas les unes les autres et voyagent presque librement. La compréhension théorique des plasmas permit de les contrôler et de les exploiter industriellement. Tandis que les physiciens ont développé de puissants outils pour décrire ses différentes phases, ces méthodes deviennent généralement inutilisables lorsque le système atomique est soumis à des conditions extrêmes. La matière dense et chaude (MDC), un régime caractérisé par des pressions et des températures à la frontière entre la phase solide et la phase plasma, a récemment piqué l'intérêt des physiciens.

D'une part, ces types de systèmes sont très répandus en astrophysique et constituent, par exemple, l'intérieur de naines blanches, l'atmosphère d'une étoile à neutrons ou l'intérieur de planètes géantes telles que Saturne et Jupiter. En effet, l'intérieur de Jupiter est principalement constitué d'un gaz d'hydrogène où la densité d'ion $n \approx 6 \times 10^{24}$ cm^{-3} et la température $T \approx 10^4$ K sont très supérieures aux conditions ambiantes $n \approx 0.04 \times 10^{24}$ cm^{-3} et $T = 298$ K [3]. Puisqu'il est impossible d'effectuer directement des mesures au cœur de ces planètes, les propriétés de celles-ci sont généralement obtenues indirectement en reliant les mesures de champs magnétiques et d'équations d'état à des modèles théoriques. Il est donc primordial

d'avoir une description adéquate de la conductivité et de l'équation d'état de la MDC pour l'étude de planètes géantes.

D'autre part, la MDC joue un rôle fondamental dans la quête pour l'énergie à fusion nucléaire par son application dans la fusion par confinement inertiel (FCI)(connue en anglais sous *Inertial Confinement Fusion*). La FCI est l'une des deux méthodes, l'autre étant la fusion par confinement magnétique, qui cherche à chauffer et compresser suffisamment une mixture d'isotopes d'hydrogène pour atteindre la fusion nucléaire. Dans la méthode FCI, le gaz est confiné à l'intérieur de petites capsules sphériques sur lesquelles de puissants lasers sont appliqués de façon homogène afin d'obtenir la pression nécessaire à la fusion. La compréhension de la MDC joue alors un rôle important dans la description du gaz d'hydrogène précédant la fusion, mais aussi pour la description des capsules soumises à l'intense énergie des lasers. Puisque ces capsules sont généralement constituées de métaux simples, tel que le béryllium, il est très important de comprendre comment ces derniers se comportent dans le régime de la MDC. On retrouve aussi des métaux dans ce régime lorsqu'ils passent rapidement de la phase solide à la phase plasma, par exemple, lors d'entrée dans l'atmosphère de navettes ainsi que durant l'ablation de surface par lasers. Que ce soit pour améliorer notre compréhension fondamentale des systèmes atomiques ou pour ses multiples applications technologiques, l'étude de la MDC s'avère extrêmement importante.

1.2. Matière dense et chaude

1.2.1. Définition du régime

Formellement, la MDC n'est pas une phase physique, mais une région de densité et de température à l'interface entre les phases solide, liquide, gazeuse et plasma telle qu'illustrée à la Fig.1.2. Dans ce régime, le système est trop dense pour être décrit par la physique des plasmas et trop chaud pour être décrit par la physique de la matière condensée. Il est fréquent de caractériser ce type de système grâce à deux paramètres sans dimension. D'une part, le paramètre de couplage ion-ion défini comme le rapport entre l'énergie de Coulomb et l'énergie thermique moyenne

$$\Gamma_{ii} = \frac{E_C}{E_T} = \frac{\bar{Z}^2 e^2}{4\pi\epsilon_0 r_{ws} k_B T_i}, \tag{1.1}$$

où $\bar{Z}$ est l'ionisation moyenne du système, e est la charge élémentaire, ϵ_0 est la permittivité du vide, k_B est la constante de Boltzmann, T_i est la température du système ionique et $r_{ws} = (3/4\pi\rho)^{1/3}$ est le rayon de Wigner-Seitz qui représente la rayon moyen atomique pour une densité ionique ρ. D'autre part, le paramètre de dégénérescence électronique, définit

comme le rapport entre la température du système électronique et la température de Fermi de ce dernier

$$\tau = \frac{T_e}{T_F} = \frac{2m_e T_e}{\hbar^2 (3\pi^2 n)^{2/3}}, \tag{1.2}$$

où m_e est la masse d'un électron, T_e et n la température et la densité du système électronique respectivement.

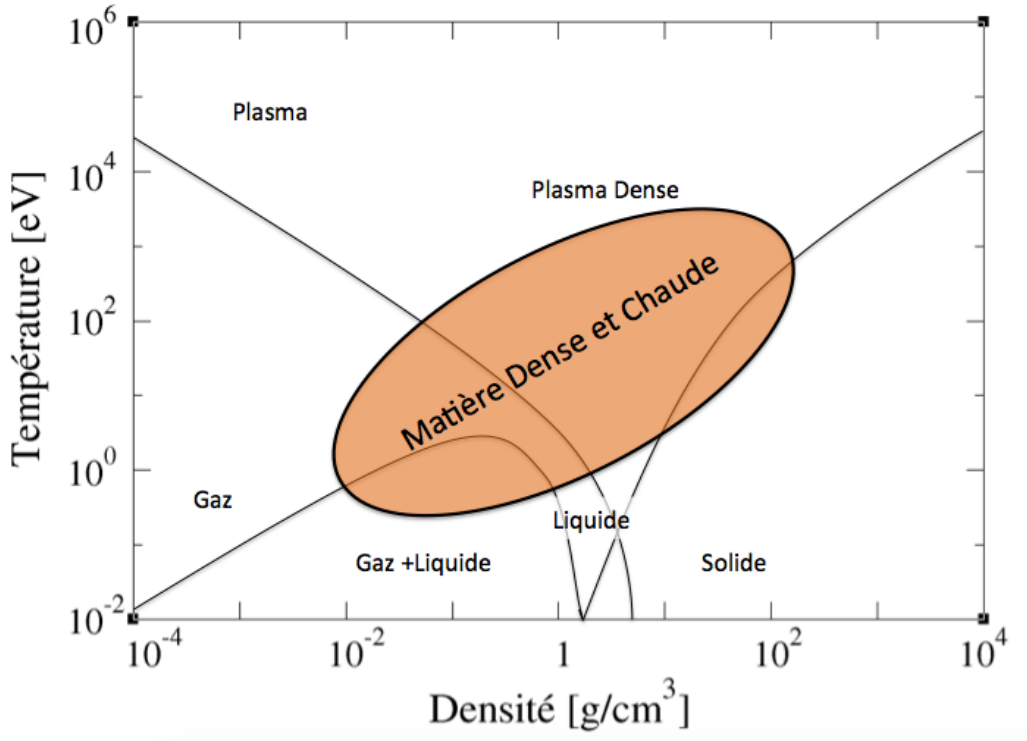

Figure 1.1. Diagramme de phase idéalisé, basé sur les Ref.[1, 2] illustrant la région de densité et de température définissant la matière dense et chaude à l'interface entre les différentes phases physiques.

Dans la phase solide, les paramètres prennent les valeurs $\Gamma_{ii} \to \infty$ et $\tau \to 0$ puisque les températures des deux systèmes sont très faibles et la densité très élevée. Les ions sont ainsi piégés autour de leur position d'équilibre cristalline et il est généralement possible de décrire leurs mouvements en termes de modes propres d'oscillations d'un cristal harmonique, c'est-à-dire en termes de phonons. Les ions possèdent ainsi des corrélations à longue portée responsable de la structure cristalline. Dans cette phase, les électrons se retrouvent plongés dans un potentiel extérieur périodique donnant lieu à une description, dans l'espace réciproque, de leurs niveaux d'énergie en termes de bandes d'énergie. Ils sont fortement dégénérés et ils sont ainsi confinés à l'intérieur de la sphère de Fermi. Lorsque l'interaction

électron-ion peut être considérée très faible, il existe une solution de l'équation de Schrödinger donnant naissance au phénomène de gap dans la structure de bande électronique. Pour les métaux et semi-métaux, l'énergie de Fermi E_F se situe à l'intérieur d'une bande tandis que pour les semi-conducteurs et isolant, E_F se situe à l'intérieur d'un gap. De façon générale, des méthodes plus élaborées, telles que le modèle de liaisons fortes [4] (connu en anglais sous *tight-binding model*) ou la méthode des ondes planes augmentées [5] (connue en anglais sous *augmented plane-wave method*), permettent d'obtenir la structure de bande d'éléments plus complexes.

Dans la phase plasma, les paramètres prennent les valeurs $\Gamma_{ii} \to 0$ et $\tau \to \infty$ puisque, à l'opposé de la phase solide, les températures des deux systèmes sont très élevées et la densité très faible. Dans ces conditions, le système ionique ainsi que le système électronique sont faiblement corrélés et peuvent être traités de façon classique. Une description fondamentale du plasma se base sur la fonction de distribution $f(\mathbf{x},\mathbf{p},t)$ qui décrit la densité de particules ayant une quantité de mouvement (p_x, p_y, p_z) à une position (x, y, z) au temps t au lieu de traiter chaque particule individuellement. L'évolution de cette fonction, pour un système hors d'équilibre, est déterminée en résolvant l'équation de Boltzmann ou l'équation de Vlasov incluant le champ électromagnétique créé par la fonction de distribution [6]. De façon générale, ces équations divisent l'évolution temporelle de $f(\mathbf{x},\mathbf{p},t)$ en trois parties distinctes : un terme décrivant la force exercée sur les particules par un potentiel externe, un terme de diffusion décrivant le mouvement des particules suivant un gradient de pression ou température ainsi qu'un terme de collisions décrivant l'interaction entre particules. Lorsqu'il y a suffisamment de collisions dans le plasma, il est possible d'utiliser une approche beaucoup plus simple en traitant le plasma comme un fluide. Cela permet de décrire le système grâce aux équations de Navier-Stockes couplées aux équations de Maxwell simplifiant énormément le problème.

Dans le cas de la MDC, les deux paramètres prennent des valeurs intermédiaires et les méthodes applicables à la physique du solide et des plasmas ne sont généralement plus applicable. À titre d'exemples, on présente les valeurs de ces paramètres pour deux systèmes particuliers étudiés dans le chapitre 5. Pour l'aluminium, dans les conditions $\rho/\rho_0 = 2.32$, $T_e = T_i = 1.75$ eV et $\bar{Z} = 3$, on obtient $\Gamma \approx 62$ et $\tau \approx 0.086$, tandis que dans le cas du béryllium, dans les conditions $\rho/\rho_0 = 2.99$, $T_e = 2$ eV, $T_i = 1.75$ eV et $\bar{Z} = 2$, on obtient $\Gamma \approx 33$ et $\tau \approx 0.436$. En effet, pour ces valeurs de Γ, le système possède des corrélations ion-ion à moyenne portée semblables à celle d'un liquide simple et le système électronique doit être traité quantiquement puisque les effets quantiques sont toujours important jusqu'à une valeur approximative de$\tau \approx 2$. En effet, les électrons ne peuvent plus

être décrits comme des particules ponctuelles classiques lorsque leurs longueurs d'onde de de Broglie $\lambda_{db} = \hbar/\sqrt{2mk_BT_e}$ est comparable à la distance inter-électronique moyenne. Cette situation survient pour une densité électronique suffisamment élevée ou pour une température suffisamment faible telle que décrit par le paramètre τ. Dans le cas $\tau \to \infty$, la distribution statistique des électrons peut être décrit par la distribution de Boltzmann $n_B(\epsilon) = \exp[(\mu - \epsilon)/k_BT_e]$, tandis que pour $\tau \to 0$, il est nécessaire d'utiliser la distribution de Fermi-Dirac $n_{FD}(\epsilon) = 1/(1 + \exp[(\mu - \epsilon)/k_BT_e])$. La transition entre $n_B(\epsilon)$ et $n_{FD}(\epsilon)$ devient notable près de $\tau \approx 2$ ce qui explique cette limite approximative.

L'un des modèles le plus simples pour décrire la MDC est le modèle à un-composant [7] (connu en anglais sous *one-component plasma model*) qui consiste à traiter uniquement les ions chargés interagissant par la force de Coulomb (ou par un potentiel de Yukawa) plongé dans un arrière-plan uniforme de charge opposée (système électronique) pour maintenir la neutralité du système. Malgré que ces modèles permettent une compréhension générale des propriétés complexes de la MDC, plusieurs expériences et simulations *ab initio* démontrèrent qu'ils ne permettent pas une description réaliste de la physique de la MDC (plus de détails dans le chapitre 5). C'est pourquoi l'un des objectifs de cette thèse est d'investiguer de nouvelles approches pour prédire adéquatement les propriétés de la MDC.

1.2.2. Système en quasi-équilibre

La création en laboratoire d'échantillons dans le régime de la MDC sera décrit en détail dans la section (1.3.1), mais il est important de noter que la majorité de ces méthodes créent un état hors d'équilibre où la température du système électronique T_e diffère de celle du système ionique T_i. Le retour vers l'équilibre peut être décrit grâce à un modèle à deux températures [8, 9, 10] décrivant l'échange énergétique entre le système ionique et le système électronique. Suite à une perturbation de la température $S_\mu(\mathbf{r},t)$ d'un des sous-systèmes, il est possible de décrire le transfert d'énergie entre ceux-ci par les équations différentielles couplées

$$C_e\frac{\partial T_e(\mathbf{r},\mathbf{t})}{\partial t} = g\left[T_i(\mathbf{r},\mathbf{t}) - T_e(\mathbf{r},\mathbf{t})\right] - \nabla[K_e(T_e)\nabla T_e]_e + S_e(\mathbf{r},\mathbf{t}), \tag{1.3}$$

$$C_i\frac{\partial T_i(\mathbf{r},\mathbf{t})}{\partial t} = g\left[T_e(\mathbf{r},\mathbf{t}) - T_i(\mathbf{r},\mathbf{t})\right] - \nabla[K_i(T_i)\nabla T_i]_i \ + S_i(\mathbf{r},\mathbf{t}), \tag{1.4}$$

où C est la capacité calorifique, g est le coefficient de couplage électron-ion et K est la conductivité thermique.

Grâce à ces équations, il est possible de déterminer que le temps caractéristique de thermalisation électron-ion τ_{ei} est de l'ordre des picosecondes tandis que les temps de thermalisation électron-électron ainsi que ion-ion sont de plusieurs ordres de grandeur inférieurs. En effet, quoique le temps entre une collision électron-électron, électron-ion et ion-ion soit essentiellement le même, l'énorme différence entre la masse des ions et celle des électrons $m_i \gg m_e$ influence grandement l'échange d'impulsion $p = mv$ entre les deux systèmes. Au sein d'un même système, les masses sont identiques ce qui résulte en une thermalisation rapide des systèmes électron-électron et ion-ion. D'un côté, lorsque $T_e > T_i$, les électrons entre fréquemment en collision avec les ions, mais ils échangent très peu d'impulsion ce qui entraine une thermalisation très lente. Cela permet de définir un système en quasi-équilibre pour un temps caractéristique τ_{qe}. D'un autre côté, lorsque $T_e < T_i$, le transfert d'impulsion des ions chauds vers les électrons froids est très important ce qui favorise une thermalisation plus rapide que dans l'autre situation. C'est pour cela qu'il est généralement préférable d'utiliser un paramètre de couplage électron-ion g qui dépend des deux températures $g(T_e,T_i)$ au lieu d'utiliser uniquement la différence de celles-ci $g(|T_e - T_i|)$. Déterminer et comprendre les différences entre les propriétés physiques de la MDC à l'équilibre de celle en quasi-équilibre est l'un des principaux buts de cet ouvrage.

1.3. Motivations expérimentales

1.3.1. Création de la matière dense et chaude en laboratoire

L'effervescence de l'intérêt pour la MDC dans la communauté scientifique provient principalement du fait qu'il est dorénavant possible de créer et d'effectuer des mesures sur ces systèmes en laboratoire. Tandis qu'il est possible de créer les conditions de la MDC en bombardant des cibles avec des ions lourds [11], la méthode la plus répandue reste l'irradiation de cibles métalliques avec un laser. En effet, l'utilisation de lasers à haute intensité de photons, avec des photons de haute énergie et avec des impulsions ultra-courtes, permet de déposer rapidement suffisamment d'énergie pour chauffer la cible tout en gardant une densité de l'ordre de celle du solide. On considère deux régimes particuliers de MDC qui dépendent du type de laser utilisé.

D'une part, lorsque l'énergie des photons est très inférieure à l'énergie de liaison des électrons de cœur de l'échantillon, l'énergie du laser est essentiellement toute absorbée par les électrons libres du système (voir Fig.1.2.(b)). Cela aboutit en un système fortement hors d'équilibre avec la température des électrons T_e largement supérieure à la température des électrons de cœur et des ions T_i qui reste fixée à la température ambiante $T_r = T_i$. Puisque

le laser ne se couple pas directement avec les ions, le système ne subit aucune compression et reste sensiblement à sa densité initiale [12, 13]. L'irradiation avec des lasers dans les longueurs d'onde ultraviolet, visible ou infrarouge sur des cibles métalliques est la méthode la plus répandue pour créer ce genre de système que l'on classifie comme étant de la matière ultra-rapide (MUR) (connue en anglais sous *Ultra-Fast Matter*).

D'autre part, si l'énergie du laser est suffisamment élevée, ce dernier peut transmettre directement une partie de son énergie aux électrons de cœur et aux ions, tandis que le reste sera absorbé par le système d'électrons libres (voir Fig.1.2.(c)). La température des deux sous-systèmes augmentera considérablement, mais ne sera pas nécessairement égale au moment d'une mesure. Le transfert d'impulsion du laser vers le système ionique est généralement si élevé qu'une onde de choc est générée dans l'échantillon, compressant le système à des densités deux à trois fois la densité initiale. Cela nécessite l'utilisation de puissants lasers à rayons X tels que le OMEGA-60 au *Laboratory for Laser Energetics* [14] ou le *Matter in Extreme Condition Instrument* au *Linac Coherent Light Source Laboratory* [15]. On classifie ce type de système comme étant de la matière compressée sous choc (MCC).

1.3.2. Quantités mesurables

Une fois l'échantillon irradié et soumis aux conditions de la MDC, plusieurs techniques de mesure ont été développés pour déterminer ses propriétés physiques. Dans cette section, on présente les quantités les plus fréquemment mesurées expérimentalement ainsi que la façon de calculer celles-ci théoriquement.

1.3.2.1. *Spectre de diffusion Thomson des rayons X*

La diffusion de Thomson est l'une des méthodes expérimentales les plus répandues [2] pour déterminer les propriétés de l'échantillon de MDC créé en laboratoire puisqu'elle permet d'obtenir la température, la densité ainsi que l'ionisation moyenne du système irradié. Dans le cas de la MDC, le système est généralement si dense qu'il est nécessaire d'utiliser un rayonnement dans les longueurs d'onde des rayons X afin qu'il puisse se propager au travers de l'échantillon. La source de rayons X peut être obtenue en irradiant une cible solide, par exemple une feuille de parylene-D ($C_6H_4Cl_2$) [16] ou de manganèse [17], par de puissants lasers ou en utilisant directement un laser à électrons libres [18, 19]. Généralement, l'énergie du rayonnement $\hbar\omega_0$ est largement inférieure à l'énergie d'ionisation E_I de tous les électrons de cœur, $\hbar\omega_0 \ll E_I$, ce qui permet d'ignorer les résonances dans la diffusion. Lors de la diffusion, le photon incident échange avec l'électron une quantité de mouvement $\hbar\mathbf{k}$ et une énergie $\hbar\omega = \hbar^2|\mathbf{k}|^2/2m_e = \hbar\omega_0 - \hbar\omega_d$ avec $\hbar\omega_d$ l'énergie du photon diffusé. Dans la limite

non-relativiste ($\hbar\omega \ll \hbar\omega_0$) et pour un petit transfer d'impulsion, l'angle de diffusion θ, c'est-à-dire la position du détecteur, est lié à la quantité de mouvement k par la relation $k = |\mathbf{k}| = 4\pi \sin(\theta/2)/\lambda_0$ avec λ_0 la longueur d'onde du rayon incident [2]. La puissance diffusée P_d par un ensemble de N électrons dans un intervalle de fréquences $d\omega$ et pour un angle solide $d\Omega$ est donnée par [20]

$$P_d(\mathbf{k},\omega) = \frac{NP_0r_0^2}{2\pi A} S_{ee}(\mathbf{k},\omega)\ |\hat{\mathbf{k}}_d \times (\hat{\mathbf{k}}_d \times \mathbf{E}_0)|\ d\omega d\Omega \tag{1.5}$$

où P_0 est la puissance du faisceau incident, $r_0 \approx 2.8$ fm est le rayon classique d'un électron, A est l'aire d'irradiation et $S_{ee}(\mathbf{k},\omega)$ est le facteur de structure dynamique (FSD) électron-électron. Le dernier terme est une contribution dépendante de la polarisation du faisceau incident (plus de détail dans Ref.[2]).

La diffusion des rayons X permet ainsi d'obtenir expérimentalement le FSD du système électronique qui décrit les corrélations dans le système et est ainsi une quantité fondamentale à la compréhension de la MDC. Suivant les travaux de Chihara [21] et en supposant un système isotrope $\mathbf{k} = |\mathbf{k}| = k$, le FSD électron-électron peut être décomposé en une somme de trois termes

$$S_{ee}(k,\omega) = \bar{Z}S^0_{ee}(k,\omega) + |f(k) + q(k)|^2 S_{ii}(k,\omega) + Z_b \int d\omega'\ \tilde{S}_{ee}(k,\omega-\omega')S_S(k,\omega'). \tag{1.6}$$

Le premier terme représente les transitions d'états libres vers d'autres états libres avec $S^0_{ee}(k,\omega)$ le FSD des électrons libres du système avec $\bar{Z}$ l'ionisation moyenne de chaque nucléon. Ce terme peut être calculé à partir de la fonction de réponse χ_{ee} du système électronique interagissant à température finie par le théorème de fluctuation-dissipation [22]

$$S^0_{ee}(k,\omega) = -\frac{\hbar}{\pi n}\frac{1}{1-e^{-\beta\hbar\omega}}\mathrm{Im}[\chi_{ee}(k,\omega)] \tag{1.7}$$

avec n la densité moyenne d'électrons. Le calcul de ce terme ne sera pas abordé dans cette thèse, mais fût couvert pour le régime de la MDC dans les références [23, 24]. Le troisième terme représente les transitions d'états liés vers des états libres au sein d'un seul ion décrit par $\tilde{S}_{ee}(k,\omega-\omega')$ qui sont affectées par le mouvement intrinsèque de l'ion décrit par $S_S(k,\omega')$. La contribution de ce terme se situe aux extrémités du spectre et est généralement ignorée dût à sa faible intensité. Le deuxième terme représente la diffusion élastique des électrons suivant, de façon adiabatique, le mouvement des ions décrit par le FSD ion-ion $S_{ii}(k,\omega)$ avec $f(k)$ et $q(k)$ la transformée de Fourier de la densité d'électrons libres $n_f(r)$ et liés $n_b(r)$ autour d'un ion respectivement. Les modes de vibrations ioniques, de l'ordre du meV, sont actuellement trop finement résolus spectralement pour être mesurés expérimentalement et il est fréquent

d'utiliser l'approximation $S_{ii}(k,\omega) = S_{ii}(k)\delta(\omega)$ avec $S_{ii}(k)$ le facteur de structure statique (FSS).

Expérimentalement, la densité électronique n et ionique ρ ainsi que la température électronique T_e et ionique T_i sont extraites en effectuant un lissage du spectre expérimental avec le spectre théorique de l'Eq.(1.6). Puisque que le premier terme dépend uniquement des propriétés du système électronique, son lissage permet de déterminer rapidement n et T_e. La dépendance du spectre en fonction de T_i provient de $S_{ii}(k,\omega)$ (ou de $S_{ii}(k)$) ce qui permet de déterminer si le système est en équilibre avec $T_e = T_i$ ou en quasi-équilibre $T_e \neq T_i$. Le calcul de ce terme est l'un des objectifs principaux de cette thèse.

1.3.2.2. *Thermalisation électron-ion*

Tel que mentionné dans les sections 1.3.1 et 1.2.2, lors de la création de systèmes dans le régime de la MDC, ceux-ci sont généralement dans un état de hors d'équilibre avec $T_e \neq T_i$. Grâce au laser à impulsions avec un taux de répétition élevé, il est possible d'obtenir la température des deux systèmes en fonction du temps $T_e(t)$ et $T_i(t)$. En utilisant les Eq.(1.3) et Eq.(1.4), il est ainsi possible de déterminer le coefficient de couplage électron-ion g qui, techniquement, dépend de la température des deux systèmes $g \rightarrow g(T_e,T_i)$. Le calcul théorique de g peut être effectué en utilisant la règle d'or de Fermi [25] qui permet d'obtenir le taux de perte d'énergie du système électronique

$$\dot{E} = \int_0^\infty d\omega \, \frac{\omega}{2\pi} \int dk^3 \frac{|U_{ei}(k)|^2}{(2\pi)^3} [N_e(\omega) - N_i(\omega)] \left[\frac{2\pi S_{ee}(k,\omega)}{N_e(-\omega)}\right] \left[\frac{2\pi S_{ii}(k,\omega)}{N_i(-\omega)}\right], \tag{1.8}$$

où U_{ei} est un pseudo-potentiel électron-ion représentant l'interaction entre les électrons libres avec l'ion et $N_\mu(\omega) = [\exp(\omega/T_\mu) + 1]^{-1}$ décrit la population dans chaque mode. Dans le cas où les températures sont nettement supérieures à l'énergie de chaque mode $\hbar\omega$, le terme de population peut s'approximer tel que $N(\omega/T) \rightarrow \omega/T$. Cela permet de sortir un terme $(T_e - T_i)$ de l'intégrale de l'Eq.(1.8) et de définir le coefficient de couplage électron-ion

$$g(T_e,T_i) \equiv \frac{\dot{E}}{(T_e - T_i)} = \int_0^\infty \frac{d\omega}{2\pi} \int dk^3 \frac{|U_{ei}(k)|^2}{(2\pi)^3} \left[\frac{2\pi S_{ee}(k,\omega)}{N_e(-\omega)}\right] \left[\frac{2\pi S_{ii}(k,\omega)}{N_i(-\omega)}\right]. \tag{1.9}$$

On remarque que ce coefficient dépend du FSD électron-électron et ion-ion ce qui démontre l'importance de ces fonctions pour la compréhension de la MDC.

1.3.2.3. *Conductivité électrique*

La conductivité électrique σ de la MDC est l'une des propriétés les plus importantes pour comprendre le lien entre le champ magnétique des planètes géantes et leur composition ainsi

que pour comprendre le transfert d'énergie des capsules métalliques vers le gaz d'hydrogène pour la FCI. Les mesures expérimentales de la conductivité électrique, dans le régime de la MDC, effectuées pour l'aluminium [26] ainsi que pour le lithium [27] permettent de déterminer les différentes méthodes théoriques pour évaluer σ. L'une des façons les plus répandues pour évaluer la résistivité $R \equiv 1/\sigma$ des plasmas et des métaux liquides est la formule de Ziman [28] qui prend la forme

$$R = \frac{\rho}{3\pi n} \int_0^\infty \frac{df(\epsilon)}{d\epsilon}\, d\epsilon \int_0^{2\sqrt{\epsilon}} S_{ii}(k) \left| \frac{U_{ei}(k)}{\varepsilon(k)} \right|^2 k^3\, dk \tag{1.10}$$

où $f(\epsilon)$ est la fonction d'occupation de Fermi-Dirac, $U_{ei}(k)$ est le pseudo-potentiel électron-ion et $\varepsilon(k)$ est la fonction diélectrique du gaz d'électrons interagissant. Le facteur de structure statique $S_{ii}(k)$ intervient de nouveau dans le calcul d'une quantité mesurable expérimentalement, ce qui illustre encore son importance fondamentale dans la compréhension de la MDC.

1.3.2.4. *Spectre de phonons et vibrations dans les fluides*

Dans le cas particulier de la MUR, le système ionique est figé à température ambiante et la structure cristalline est conservée ; le FSS n'est pas modifié et reste celui du cristal initial. Cependant, il fut proposé [29, 30] que, lorsque la température électronique T_e est augmentée, les fréquences de vibrations des modes propres du cristal $\omega_s(k)$ sont grandement modifiées. En effet, lorsque T_e est augmentée, le système électronique écrante de moins en moins l'interaction interionique ce qui résulte en une interaction plus rigide modifiant ainsi le spectre de phonons. L'hypothèse du durcissement des phonons (connue en anglais sous *phonon hardening*) est l'un des principaux sujets de cette thèse et sera examinée en détail dans le cas des métaux simples. Le spectre de phonon peut être directement mesuré expérimentalement par la diffusion inélastique de neutrons [31, 32, 33] et s'avère donc être une quantité cruciale à la compréhension de la MUR.

Dans le cas de la matière compressée par choc, la température du système ionique est suffisante pour que celui-ci soit dans une phase fluide et le concept de phonons n'est plus applicable. Dans ce régime, les modes de vibrations transverses n'existent plus et uniquement les modes longitudinaux peuvent se propager dans le système. La relation de dispersion de ces modes $\omega_l(k)$ peut être calculée théoriquement en déterminant la position du pic de Brillouin dans le FSD $S_{ii}(k,\omega)$ et permet d'obtenir la vitesse du son $c_s = \omega_l(k \to 0)/k$ du système. Puisque ces quantités dépendent directement de l'interaction interionique, celles-ci seront

modifiées pour les systèmes à deux températures et seront aussi investiguées dans cette thèse.

1.4. Motivations théoriques

Dans la section précédente, on a déterminé que le FSD ion-ion $S_{ii}(k,\omega)$(ou le FSS $S_{ii}(k)$) est une fonction fondamentale permettant le calcul de plusieurs propriétés physiques de la MDC mesurable expérimentalement. De façon similaire, la relation de dispersion des modes de vibrations propres $\omega(k)$ contient aussi énormément d'information sur le système. Puisque ces deux quantités dépendent principalement de l'interaction interionique, cette section présente différentes approches théoriques permettant la modélisation de cette interaction dans le régime de la MDC.

1.4.1. Méthodes *ab initio*

Pour traiter le problème de façon *ab initio*, l'approche consiste à combiner la théorie de la fonctionnelle de la densité (TFD) (connue en anglais sous *Density Functional Theory*) [34, 35] pour traiter le système électronique avec la dynamique moléculaire (DM) (connue en anglais sous *Molecular Dynamics*)[36, 37] pour traiter le système ionique.

La TFD est l'une des techniques les plus répandues pour étudier le système électronique et de puissants codes, tels ABINIT [38, 39] et VASP [40], sont maintenant disponibles. Ces codes furent initialement développés pour étudier la structure électronique des solides, c'est-à-dire à température nulle, mais sont dorénavant en mesure de traiter les systèmes à température finie. La température électronique est introduite en utilisant la distribution de Fermi-Dirac pour définir l'occupation des différentes bandes électroniques. Puisque les systèmes sont à très haute température dans le régime de la MDC, il est généralement nécessaire de simuler un très grand nombre de bandes pour atteindre une occupation suffisamment faible de la dernière bande. Puisque le temps de calcul augmente comme le cube du nombre de bandes nécessaire, ces simulations deviennent rapidement couteuses numériquement. Un autre problème survenant avec l'utilisation des ces codes est l'absence de fonctionnelles d'échange et corrélation (FEC) à température finie, l'approximation la plus importante de la TFD, et l'utilisation d'une FEC à température nulle est généralement utilisée même pour l'étude de la MDC.

Au sein même de ces codes, des outils pour traiter le système ionique sont disponibles. Pour le cas de la MUR, la structure cristalline est conservée et le calcul de la structure électronique peut être fait uniquement pour une seule cellule unitaire en utilisant des conditions périodiques. Dans ces conditions, le mouvement des ions est complètement défini par les

modes propres de vibrations du cristal. Le spectre de phonons peut être calculé en utilisant la théorie perturbative de la fonctionnelle de la densité (connue en anglais sous *Density Functional Perturbation Theory*) qui permet d'obtenir la réponse du système à une perturbation, c'est-à-dire le faible déplacement hors site cristallin d'un ion. Dans le cas de la MCC, il est nécessaire d'utiliser la DM en effectuant une simulation avec le plus d'ions possible dans la cellule. Une fois que la densité électronique est déterminée par un calcul auto cohérent TFD, la force entre les ions est déterminée par le théorème généralisé de Hellman-Feynmann [41, 42, 43, 44] ce qui fournit une description fondamentale de l'interaction interionique. Cependant, en plus d'augmenter le nombre d'électrons dans le système, l'utilisation d'une plus grande cellule de simulation réduit la zone de Brillouin ce qui augmente considérablement le nombre de bandes nécessaire pour satisfaire l'occupation de Fermi-Dirac. Tandis que des simulations de DM classiques peuvent contenir des millions d'atomes, les simulations de TFD+DM contiennent généralement entre 60 et 256 atomes dut à leurs énormes coûts. L'une des approches pour éviter ce type de simulations coûteuses est de remplacer le calcul quantique de la structure électronique et en utilisant des potentiels interioniques classiques incluant directement l'écrantage du potentiel de Coulomb par le système d'électrons.

1.4.2. Potentiel interionique effectif

Pour être en mesure d'étudier la MDC adéquatement, il est préférable d'utiliser des potentiels interionique dépendant de la densité et/ou de la température du système. Le plus simple de ceux-ci est le potentiel de Yukawa (Y) qui provient de la théorie de Thomas-Fermi (voir chapitre 17 de Ref[45])

$$V_{ii}^{\mathrm{y}}(r) = \frac{e^{-k_0 r}}{r} \tag{1.11}$$

où $k_0^2 = 4\pi\partial n/\partial\mu$ est le vecteur d'onde d'écrantage avec n la densité électronique et μ le potentiel chimique du système (le système d'unités atomiques est utilisé pour le reste de la section). Dans le cas d'un plasma classique à haute température, il est nécessaire d'utiliser le vecteur d'onde de Debye, $k_{\mathrm{D}}^2 = T_e/n\bar{Z}^2$, tandis que, dans la limite où la température est très inférieure à la température de Fermi, $T_e \ll T_F$, il est nécessaire d'utiliser le vecteur d'onde de Thomas-Fermi, $k_{\mathrm{TF}}^2 = 4(3\pi/n)^{1/3}$. Étant donné sa simplicité, il fut démontré que ce potentiel n'est pas en mesure de reproduire le FSD [46] ni le FSS [47] obtenus par TFD+DM dans le cas de l'aluminium. Une extension de ce potentiel incluant un terme de répulsion à courte distance [47], servant à modéliser l'interaction entre les électrons de cœur de deux ions, fût aussi grandement utilisée dans la description de la diffusion[48, 49]. Le potentiel Yukawa + répulsion à courte distance (connu en anglais sous *Yukawa + Short Range Repulsion*) prend

la forme

$$V_{ii}^{\text{ysrr}}(r) = \frac{e^{-k_0 r}}{r} + T_i \left(\frac{\sigma}{r}\right)^4 \tag{1.12}$$

où le paramètre σ est lié à l'extension spatiale des électrons de cœur de l'ion et doit être fixé à l'aide d'un lissage avec une simulation TFD+DM. À condition que l'ionisation moyenne du système ne change pas, ce paramètre doit rester inchangé. On remarque que ce potentiel dépend directement de la température ionique. Dans le chapitre 5, on discute en détail de la validité de ce potentiel en illustrant qu'il n'est pas adéquat pour prédire d'autres propriétés physiques que le spectre de diffusion.

1.4.3. Modèles d'atomes moyens

Tandis que l'utilisation de potentiels interioniques effectifs permet d'effectuer des simulations de DM de grande envergure, le système électronique est essentiellement ignoré résultant en une mauvaise description de la MDC. Puisque le traitement *ab initio* du système électronique devient rapidement impraticable pour des systèmes de grandes tailles, l'utilisation de modèles d'atomes moyens (AM) [50, 51, 52, 53, 54] est devenue très populaire pour l'étude de la MDC [55, 56, 57, 58, 59]. Le modèle AM est essentiellement une version quantique du modèle de Thomas-Fermi à température finie développée par Feynman, Metropolis et Teller [60] à la fin des années 1940.

L'idée générale consiste à diviser le plasma en cellules sphériques neutres immergées dans un plasma uniforme et contenant chacune un nucléon de charge Z ainsi que Z électrons. Le rayon de la cellule est le rayon ionique moyen, c'est-à-dire le rayon de Wigner-Seitz $r_{ws} = (3/4\pi\rho)^{1/3}$ avec ρ la densité ionique. Il est alors possible de résoudre l'équation de Schrödinger uniquement pour une cellule afin d'obtenir la structure électronique du plasma. Contrairement à un nucléon isolé qui produirait uniquement des états liés n_b d'énergie discrète, la présence du plasma uniforme à l'extérieur de la cellule introduit des états libres n_f d'énergie continue. Le nombre d'électrons $\bar{Z}$ peuplant ces états libres définit l'ionisation moyenne du plasma. L'interaction effective $V_{ii}(r)$ entre les ions de charge $\bar{Z}$ dans le plasma peut ainsi être déterminée par l'écrantage du potentiel de Coulomb $V_C(r)$ causé par la densité d'électrons libres $n_f(r)$ telle que

$$V_{ii}(q) = -\bar{Z} V_C(q) + |n_f(q)|^2 / \chi_{ee}(q) \tag{1.13}$$

où les fonctions $V_{ii}(q), V_C(q)$ et $n_f(q)$ sont les transformée de Fourier respective de $V_{ii}(r), V_C(r)$ et $n_f(r)$ et où $\chi_{ee}(q)$ est la fonction de réponse des électrons. Le potentiel de paires de l'Eq.(1.13) est un résultat rigoureux provenant de la théorie des perturbations de deuxième ordre pour l'interaction de deux ions immergés dans le gaz homogène d'électrons.

Plus de détails sur la construction du potentiel interionique dans la section (2.3.3). Cependant, dans le régime de la MDC, les corrélations entre les électrons et l'ion central de la sphère sont généralement très importante et ne sont pas nulle à la surface de la sphère. Dans ce cas, il est préférable d'utiliser le modèle du pseudo-atome neutre (PAN) (connu en anglais sous *Neutral Pseudo-Atom*) proposé par Perrot et Dharma-wardana [61, 62, 63, 64] où l'on utilise plutôt une sphère de corrélation avec un rayon bien plus grand $r_c \approx$ 5-10 $\times r_{ws}$. Ce modèle s'avère être l'outil principal utilisé dans cette thèse et sera décrit en détail dans la section (2.3).

1.5. Structure de la thèse

L'étude de la MDC nécessite l'utilisation de plusieurs outils théoriques propres à chaque sous-système et seront décrit en détail dans le chapitre 2. Dans un premier temps, les méthodes de physique statistique permettant la description des propriétés statiques et dynamiques du système ionique classique seront présentées. Par la suite, la description de la TFD, en particulier son application aux systèmes à température finie, sera présentée comme l'approche de prédilection pour traiter le système électronique quantique. Finalement, le modèle de pseudo-atome neutre, dont l'utilisation à la MDC constitue le cœur de cette thèse, sera expliqué en détail. Cette thèse est présentée sous la forme d'un recueil d'articles publiés ou soumis à des revues scientifiques qui forment les principales sections de résultats de cet ouvrage. Les chapitres 3 et 4 se concentrent sur la description de la MUR au travers le calcul de spectres de phonons ainsi que d'équations d'état à partir du modèle du PAN. L'hypothèse du durcissement des phonons est discutée afin de déterminer si le concept de phonons est toujours valide dans ce régime. Le chapitre 5 concerne principalement le calcul de spectres de diffusion élastique de rayons X de systèmes compressés par chocs. L'hypothèse que ces systèmes soient dans un état à deux températures est mise de l'avant pour expliquer les spectres mesurés expérimentalement. Les propriétés dynamiques, telles que la vitesse du son et la relation de dispersion des modes acoustiques, ainsi que les propriétés quasi thermodynamiques des systèmes à deux températures, sont étudié dans le chapitre 6. Finalement, le chapitre 7 porte principalement sur le calcul de la conductivité électrique dans la MDC. La comparaison entre différentes méthodes de calculs illustre la complexité de ce problème et la nécessité d'obtenir davantage de résultats expérimentaux.

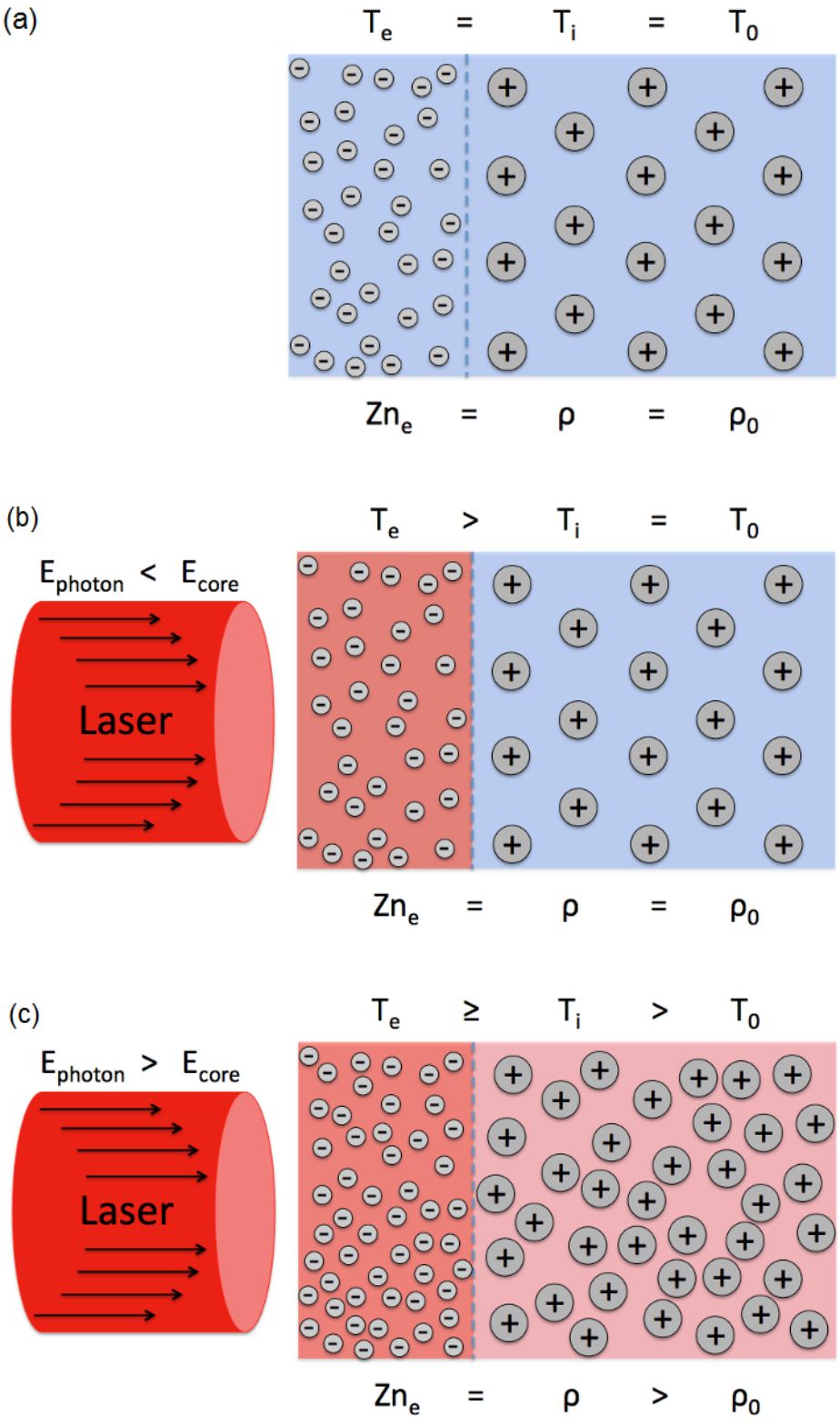

Figure 1.2. Schématisation d'un système métallique dans son état initial (a), dans le régime de la matière ultra-rapide (MUR) (b) et dans le régime de la matière compressée sous choc (MCC) (c) où E_{core} est la plus faible énergie de liaison d'un électron de cœur au noyau et E_{photon} est l'énergie des photons du laser incident.

Chapitre 2

MÉTHODOLOGIE

L'objectif de ce chapitre est de décrire de façon concrète les outils théoriques qui sont utilisés au travers des articles constituant cet ouvrage puisqu'ils recouvrent plusieurs disciplines distinctes. D'une part, dans le régime de MCC, le système ionique se trouve généralement dans une phase fluide et peut être traité de façon classique par les méthodes de physique statistique. Dans le cas particulier de la MUR, les ions sont gardés dans la phase solide où le mouvement collectif des ions peut être décrit en termes de phonons. D'autre part, le système électronique doit toujours être traité de façon quantique et l'outil utilisé sera la TFD à température finie. L'utilisation de codes standards de TFD, tels que ABINIT [38] ou VASP [40], pour étudier les systèmes en phase liquide nécessite des cellules de simulation de taille importante combinée à de la DM. Puisque de tels calculs sont énormément coûteux, l'utilisation d'un modèle plus simple est préférable lorsqu'il est nécessaire d'effectuer les simulations pour plusieurs conditions de température et de densité. Le modèle du PAN sera ainsi décrit en détail à la fin de ce chapitre.

2.1. Système ionique

2.1.1. Matière ultra-rapide

Dans le cas particulier de la MUR, les ions sont gardés à la température ambiante $T_i = T_r$ et la position des ions est fixée en dans une structure cristalline. La position de chaque ion peut alors être écrite comme $\mathbf{r}(\mathbf{R}) = \mathbf{R} + \mathbf{u}(\mathbf{R})$ où $\mathbf{u}$ est le déplacement autour de la position d'équilibre $\mathbf{R}$. Dans notre cas particulier, l'interaction inter-ionique sera décrite en termes d'un potentiel de paires V tel que l'énergie potentielle totale U est la somme de toutes les contributions de paires

$$U = \frac{1}{2}\sum_{\mathbf{R}\mathbf{R}'} V(\mathbf{r}(\mathbf{R}) - \mathbf{r}(\mathbf{R}')) = \frac{1}{2}\sum_{\mathbf{R}\mathbf{R}'} V(\mathbf{R} - \mathbf{R}' + \mathbf{u}(\mathbf{R}) - \mathbf{u}(\mathbf{R}')). \tag{2.1}$$

Puisque le mouvement des ions $\mathbf{u}$ est très petit, il est possible de développer U autour de son minimum

$$\begin{aligned} U =& \frac{N}{2}\sum_{\mathbf{R}} V(\mathbf{R}) + \frac{1}{2}\sum_{\mathbf{R}\mathbf{R}'}(\mathbf{u}(\mathbf{R}) - \mathbf{u}(\mathbf{R}')\cdot\nabla V(\mathbf{R}-\mathbf{R}') \\ &+ \frac{1}{4}\sum_{\mathbf{R}\mathbf{R}'}[(\mathbf{u}(\mathbf{R}) - \mathbf{u}(\mathbf{R}')\cdot\nabla]^2 V(\mathbf{R}-\mathbf{R}') + \mathcal{O}(\mathbf{u}^3). \end{aligned} \tag{2.2}$$

Puisque le terme linéaire est nul pour la structure cristalline, on obtient l'énergie potentielle totale dans *l'approximation harmonique* : $U = U_{\text{eq}} + U_{\text{harm}}$ telle que

$$U_{\text{eq}} = \frac{N}{2}\sum_{\mathbf{R}} V(\mathbf{R}) \qquad U_{\text{harm}} = \frac{1}{2}\sum_{\mathbf{R}\mathbf{R}',\mu\nu} u_\mu(\mathbf{R}) D_{\mu\nu}(\mathbf{R}-\mathbf{R}') u_\nu(\mathbf{R}') \tag{2.3}$$

où μ,$\nu \equiv x$,y,z et où l'on a défini la matrice harmonique

$$D_{\mu\nu}(\mathbf{R}-\mathbf{R}') = \left.\frac{\partial^2 U}{\partial u_\mu(\mathbf{R})\partial u_\nu(\mathbf{R}')}\right|_{u=0}. \tag{2.4}$$

Les $3N$ équations du mouvement

$$m\ddot{\mathrm{u}}_\mu(\mathbf{R}) = -\frac{\partial U_{\text{harm}}}{\partial u_\mu(\mathbf{R})} = -\sum_{\mathbf{R}'\nu} D_{\mu\nu}(\mathbf{R}-\mathbf{R}') u_\nu(\mathbf{R}') \tag{2.5}$$

ou, en utilisant une notation matricielle plus compacte ($u_\mu \to \mathbf{u}$ et $D_{\mu\nu} \to \mathbf{D}$),

$$m\ddot{\mathbf{u}}(\mathbf{R}) = -\sum_{\mathbf{R}'} \mathbf{D}(\mathbf{R}-\mathbf{R}')\mathbf{u}(\mathbf{R}') \tag{2.6}$$

ont comme solutions des ondes planes $\mathbf{u}(\mathbf{R},t) = \mathbf{v}\exp[i(\mathbf{k}\cdot\mathbf{R} - \omega t)]$ où $\mathbf{v}$ est le vecteur de polarisation du mode normal qui détermine la direction dans laquelle les ions effectuent leurs mouvements. En substituant $\mathbf{u}(\mathbf{R},t)$ dans l'Eq.(2.6), l'équation du mouvement est transformée en un problème aux valeurs propres en trois dimensions

$$m\omega^2\mathbf{v}(\mathbf{k}) = \left(\sum_{\mathbf{R}} \mathbf{D}(\mathbf{R}) e^{-i\mathbf{k}\cdot\mathbf{R}}\right)\mathbf{v}(\mathbf{k}) \equiv \mathbf{D}(\mathbf{k})\mathbf{v}(\mathbf{k}), \tag{2.7}$$

où l'on a défini la *matrice dynamique* $\mathbf{D}(\mathbf{k})$. La matrice $\mathbf{D}(\mathbf{R})$ possède les symétries particulières

$$D_{\mu\nu}(\mathbf{R}-\mathbf{R}') = D_{\mu\nu}(\mathbf{R}'-\mathbf{R}) \qquad \text{et} \qquad D_{\mu\nu}(\mathbf{R}-\mathbf{R}') = D_{\nu\mu}(\mathbf{R}-\mathbf{R}') \tag{2.8}$$

qui permettent d'obtenir une forme réelle pour la matrice dynamique

$$\mathbf{D}(\mathbf{k}) = \frac{1}{2}\sum_{\mathbf{R}} \mathbf{D}(\mathbf{R})^{-i\mathbf{k}\cdot\mathbf{R}} + e^{i\mathbf{k}\cdot\mathbf{R}} - 2] = -2\sum_{\mathbf{R}} \mathbf{D}(\mathbf{R})\sin^2\left(\frac{1}{2}\mathbf{k}\cdot\mathbf{R}\right). \tag{2.9}$$

Ces symétries impliquent qu'elle possède trois vecteurs propres réels $\mathbf{v}_j$ (j = 1,2,3) satisfaisant l'équation

$$\mathbf{D}(\mathbf{k})\mathbf{v}_j(\mathbf{k}) = \lambda_j(\mathbf{k})\mathbf{v}_j(\mathbf{k}) \tag{2.10}$$

où les valeurs propres λ_j décrivent la relation de dispersion de chaque mode normal tel que

$$\omega_j(\mathbf{k}) = \sqrt{\lambda_s(\mathbf{k})/m}. \tag{2.11}$$

Celle-ci peut être mesurée directement par la diffusion de neutrons ou de rayons X par le cristal et joue un rôle très important dans la capacité calorifique ainsi que dans la conductivité thermique et électronique. Elle s'avère être un très bon test lors de la construction de potentiels de paires puisqu'elle dépend de la dérivée seconde du potentiel.

À basse température, les potentiels construits selon l'Eq.(1.13) possèdent un caractère oscillatoire à très longue portée, connu sous le nom d'oscillations de Friedel, puisqu'ils dépendent directement de la densité électronique autour d'un ion. Pour illustrer cet effet, prennons la théorie à température nulle de Lindhard (voir chapitre 17 de Ref.[65]) qui prédit que, lorsqu'on plonge une impureté chargée dans le gaz d'électrons homogènes, ce dernier se réorganise de façon à écranter la charge de l'impureté. Cela résulte en une densité électronique $n(\mathbf{r})$ autour d'un ion

$$n(\mathbf{r}) \sim n_0 + \delta n \frac{\cos(2k_F|\mathbf{r}|)}{|\mathbf{r}|^3}, \tag{2.12}$$

dont les oscillations sont directement transmises dans le potentiel. Pour ce type de potentiels, la somme sur les positions des ions de l'Eq.(2.9) doit être effectuée sur une très grande distance afin d'obtenir une énergie d'interaction convergée. Dans le cas de l'aluminium à densité ambiante, cela correspond approximativement à la distance de la 25$^{\text{e}}$ couche de voisins. Les éléments de cette section jouent un rôle important dans les chapitres 3 et 4.

2.1.2. Matière compressée par choc : propriétés statiques

2.1.2.1. *Fonctions de distribution spatiale*

Au-delà de certaines conditions de température et de densité, la structure cristalline n'est plus stable et le système effectue un changement de phase vers l'état liquide ou plasma. Il n'est plus possible d'utiliser le concept de phonons et il est nécessaire d'utiliser les outils de la physique statistique pour décrire adéquatement notre système. Dans un premier temps, uniquement les méthodes statiques seront abordées puisqu'elles contiennent énormément d'information sur le système.

D'une part, la densité locale à un point $\mathbf{r}$ du système est définie par

$$\rho(\mathbf{r}) = \sum_{i=1}^{N} \delta(\mathbf{r} - \mathbf{r}_i), \tag{2.13}$$

où $\mathbf{r}_i$ est la position du i-ième ion. La corrélation entre deux densités séparées par une distance $\mathbf{r}$ est décrite par la *fonction autocorrélation densité-densité statique*

$$G(\mathbf{r}) = \frac{1}{N} \int \langle \rho(\mathbf{r}' + \mathbf{r}) \rho(\mathbf{r}) \rangle \, d\mathbf{r}' = \frac{1}{N} \left\langle \sum_{i \neq j}^{N} \delta(\mathbf{r} + \mathbf{r}_j + \mathbf{r}_i) \right\rangle + \delta(\mathbf{r}) = \rho g(\mathbf{r}) + \delta(\mathbf{r}) \tag{2.14}$$

où le terme $\delta(\mathbf{r})$ représente l'autocorrélation lorsque $i = j$, où $\langle \cdots \rangle$ représente une moyenne d'ensemble et où l'on a défini la fonction de distribution de paires (FDP) $g(\mathbf{r})$. Dans les système liquide ou plasma, il est généralement possible de supposer un système isotrope $\mathbf{r} \to r$ et de définir la fonction de distribution radiale (FDR) $g(r)$. Cette fonction contient énormément d'information sur la structure du système et permet d'obtenir directement les propriétés thermodynamiques d'un système interagissant par un potentiel de paires $V(r)$. L'énergie interne par atome U est fournie par

$$U = \frac{3}{2} k_b T + 2\pi \int_0^{\infty} r^2 V(r) g(r) \, dr, \tag{2.15}$$

tandis que la pression $P \equiv -\partial U / \partial V$ est obtenue par

$$P = \frac{\rho}{\beta} - \frac{2\pi\rho^2}{3} \int_0^{\infty} r^3 \left(\frac{dV(r)}{dr} \right) g(r) \, dr, \tag{2.16}$$

où V est le volume du système.

D'autre part. il est possible d'écrire la densité ionique en série de Fourier où les coefficients prennent la forme

$$\rho(\mathbf{k}) = \int e^{-i\mathbf{k}\cdot\mathbf{r}} \rho(\mathbf{r}) \, d\mathbf{r} = \sum_{i=1}^{N} e^{-i\mathbf{k}\cdot r_i}, \tag{2.17}$$

et de définir une fonction d'autocorrélation dans cet espace

$$S(\mathbf{k}) = \frac{1}{N} \langle \rho(\mathbf{k}) \rho(-\mathbf{k}) \rangle. \tag{2.18}$$

On remarque que le FSS $S(\mathbf{k})$ est la transformée de Fourier de la FDP

$$S(\mathbf{k}) = 1 + \frac{1}{N} \left\langle \sum_{i \neq j}^{N} e^{-i\mathbf{k}\cdot(\mathbf{r}_i - \mathbf{r}_j)} \right\rangle \tag{2.19}$$

$$= 1 + \frac{1}{N} \left\langle \sum_{i \neq j}^{N} \int e^{-i\mathbf{k}\cdot(\mathbf{r} - \mathbf{r}')} \delta(\mathbf{r} - \mathbf{r}_i) \delta(\mathbf{r}' - \mathbf{r}_j) \, d\mathbf{r} d\mathbf{r}' \right\rangle \tag{2.20}$$

$$= 1 + \rho \int e^{-i\mathbf{k}\cdot\mathbf{r}} g(\mathbf{r})\ d\mathbf{r}. \tag{2.21}$$

Dans le cas isotrope $\mathbf{k} \to k$, elle prend la forme particulière

$$S(k) = 1 + 4\pi\rho \int r^2 g(r) \frac{\sin kr}{kr}\ dr. \tag{2.22}$$

À titre d'exemple, on présente la FDP et le FSS à la Fig.2.1.

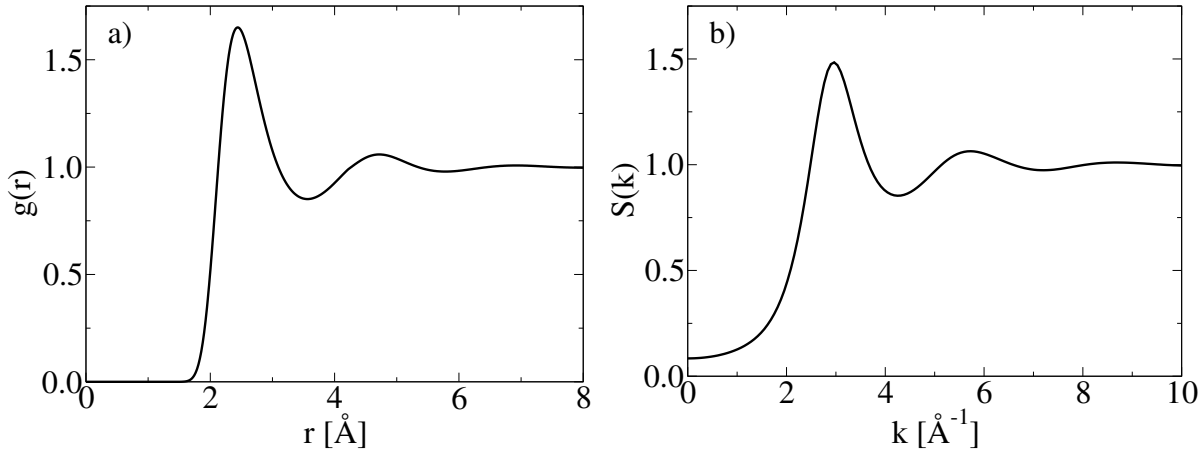

Figure 2.1. a) Fonction de distribution de paires $g(r)$ et b) facteur de structure statique $S(k)$ pour l'aluminium à T=1 eV et $\rho = 2.7$ g/cm^3 obtenues par le modèle PAN.

Une propriété importante du FSS est sa limite lorsque $k \to 0$ qui, selon la *règle de somme de la compressibilité* [66], permet de lier $S(0)$ à la compressibilité κ tel que

$$S(0) = \rho k_B T \kappa. \tag{2.23}$$

Cette relation sera particulièrement importante pour le chapitre 5 et 6 où κ sera comparée utilisant différentes approches. Malgré l'importance fondamentale de la fonction $g(r)$, c'est généralement la fonction $S(k)$ qui est la plus utilisée puisqu'elle peut directement être mesurée expérimentalement.

2.1.2.2. *Équation d'Ornstein-Zernike*

Dans mes travaux, les fonctions $g(r)$ et $S(k)$ ont principalement été calculées en utilisant l'équation intégrale de Ornstein-Zernike (OZ). Ceux-ci proposent [67] que la fonction de corrélation totale $h(r_{12}) \equiv g(r_{12}) - 1$, qui décrit l'influence de la particule 1 sur la particule 2 à une distance r_{12}, est divisée en deux contributions distinctes telles que

$$h(r_{12}) = c(r_{12}) + \rho \int c(r_{13}) h(r_{32})\ dr_3. \tag{2.24}$$

Le terme de corrélation *directe* $c(r_{12})$ décrit l'interaction immédiate entre la particule 1 et 2 tandis que le terme de corrélation *indirecte*, c'est-à-dire le reste de l'Eq.(2.24) , décrit l'influence de la particule 1 sur une particule 3 qui à son tour influence directement et indirectement la particule 2. La fonction de corrélation directe $c(r)$ est généralement très différente de la fonction de corrélation totale telle que présentée à la Fig.2.2

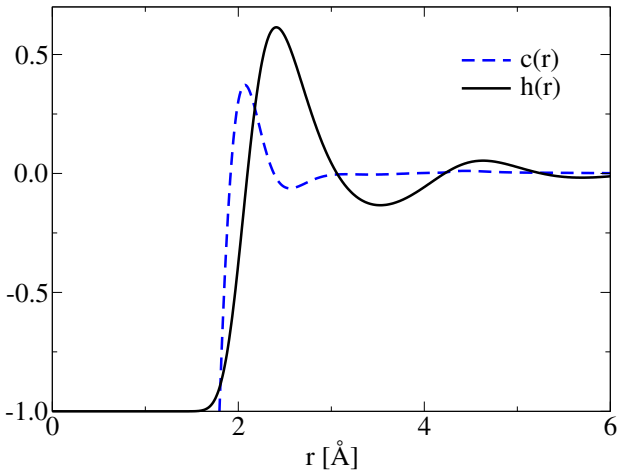

Figure 2.2. Comparaison entre la fonction de corrélation directe $c(r)$ et totale $h(r)$ pour l'aluminium à $T = 1$ eV et $\rho = 2.7$ g/cm^3 obtenues par le modèle PAN.

L'équation peut ainsi être résolue récursivement

$$h(r_{12}) = c(r_{12}) + \rho \int c(r_{13})c(r_{32})\ dr_3 + \rho^2 \int c(r_{13})c(r_{34})c(r_{42})\ dr_3 dr_4 + \ \cdots . \tag{2.25}$$

Cependant, en utilisant la forme isotrope de l'Eq.(2.24)

$$h(r) = c(r) + \rho \int c(|\mathbf{r} - \mathbf{r}'|)h(r')\ d\mathbf{r}' \equiv c(r) + \rho[c\ \star\ h](r), \tag{2.26}$$

on remarque que le deuxième terme peut être écrit en termes d'une convolution. En effectuant la transformée de Fourier, on obtient finalement une équation algébrique liant la corrélation totale à la corrélation directe

$$h(k) = c(k) + \rho c(k)h(k). \tag{2.27}$$

Il est alors possible d'isoler $h(k)$ ou $c(k)$ tel que

$$h(k) = \frac{c(k)}{1 - \rho c(k)} \qquad \text{ou} \qquad c(k) = \frac{h(k)}{1 + \rho h(k)}. \tag{2.28}$$

L'équation de OZ peut être vue comme une définition formelle de la corrélation directe et totale. Pour être en mesure de déterminer ces fonctions, il est nécessaire d'utiliser une relation

supplémentaire. Cette relation de *fermeture* prend la forme exacte

$$h(r) - 1 = g(r) = \exp[-\beta V(r) + h(r) - c(r) + B(r)] \tag{2.29}$$

où $B(r)$ est le terme de pont qui ne possède généralement pas de solution analytique. L'approche la plus simple, l'approximation *hyper-netted-chain* (HNC), consiste à poser $B(r) = 0$. La procédure numérique pour déterminer les fonctions $h(r)$ et $c(r)$ à partir de l'Eq.(2.28) et de l'Eq.(2.29) est détaillée dans l'annexe B. Pour des potentiels à courte portée ou pour des systèmes à faibles corrélations, l'approximation HNC est excellente et reproduit fidèlement des simulations de DM. Pour la MDC, le système est généralement fortement corrélé et il est nécessaire d'utiliser l'approximation *modified-hyper-netted-chain* (MHNC) qui consiste à introduire un terme de pont non nul $B(r) \neq 0$. La méthode utilisée dans cet ouvrage adopte le formalisme de Lado, Foiles et Ashcroft (LFA) [68] qui utilise la fonction de pont $B_{\rm hs}(r,\eta)$ d'un système auxiliaire de sphères dures avec un coefficient d'empilement compact η . En effet, en utilisant les résultats numériques très précis de Verlet et Weis [69] ainsi que de Henderson et Grundke [70] pour les fonctions $h_{\rm hs}(r,\eta)$ et $c_{\rm hs}(r,\eta)$, il est possible de déterminer $B_{\rm hs}$ directement à partir de l'Eq.(2.29). Le coefficient η est déterminé en utilisant la relation obtenue par LFA

$$\int \frac{\partial B_{\rm hs}(r,\eta)}{\partial \eta}[g(r) - g_{\rm hs}(r)]\ dr = 0 \tag{2.30}$$

Finalement, lorsque le coefficient η est déterminé pour un potentiel de paires particulier $V(r)$, les Eq.(2.24) et Eq.(2.29) permettent directement de calculer les fonctions $g(r)$ et $S(k)$ pour la MDC telles que présentées à la Fig.2.3.

2.1.3. Matière compressée par choc : propriétés dynamiques

2.1.3.1. *Fonctions de distributions spatio-temporelles*

Dans la section précédente, on a présenté la fonction $g(r)$ qui décrit la corrélation spatiale de la densité du fluide à des moments fixes dans le temps ainsi que sa transformée de Fourier $S(k)$ qui peut être directement mesurée expérimentalement par la diffusion *élastique* de neutrons. Dans plusieurs types d'expériences, par exemple la diffusion *inélastique* de neutrons ou la diffusion de lumière spectralement résolue, il est nécessaire de connaître les corrélations temporelles de la densité. Pour cela, il est possible d'utiliser un formalisme similaire en introduisant la densité locale à un point $\mathbf{r}$ et à un temps t tel que

$$\rho(\mathbf{r},t) = \sum_{i=1}^{N} \delta(\mathbf{r} - \mathbf{r}_i(t)) \tag{2.31}$$

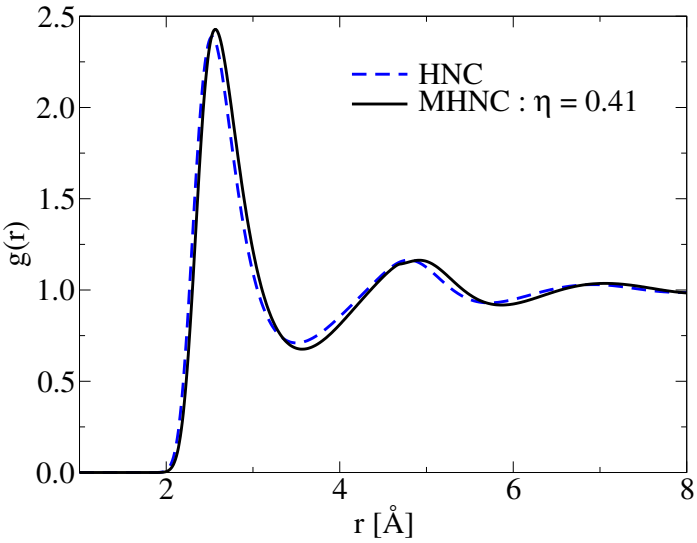

Figure 2.3. Comparaison entre la fonction de distribution de paires $g(r)$ dans l'approximation HNC ($\eta = 0$) et MHNC ($\eta = 0.41$) pour l'aluminium à $T = 0.15$ eV et $\rho = 2.7$ g/cm^3 obtenues par le modèle PAN.

où $\mathbf{r}_i(t)$ est la position du i-ième ion au temps t. La généralisation de la PDF, incluant les corrélations temporelles, est nommée la fonction de van Hove

$$G(\mathbf{r},t) = \frac{\langle \rho(\mathbf{r},t)\rho(\mathbf{0},0)\rangle}{\rho} = \frac{1}{N}\left\langle \sum_{i=1}^{N}\sum_{j=1}^{N} \delta[\mathbf{r} - \mathbf{r}_j(0) - \mathbf{r}_i(t)] \right\rangle . \tag{2.32}$$

En effectuant la transformée de Fourier spatiale de $G(\mathbf{r},t)$, on obtient la *fonction intermédiaire de diffusion* (FID)

$$F(\mathbf{k},t) = \int G(\mathbf{r},t) e^{-i\mathbf{k}\cdot\mathbf{r}} d\mathbf{r} \tag{2.33}$$

qui permet finalement d'obtenir le FSD $S(\mathbf{k},\omega)$ en prenant la transformée de Fourier temporelle de la FID

$$S(\mathbf{k},\omega) = \frac{1}{2\pi}\int_{-\infty}^{\infty} F(\mathbf{k},t)\ e^{i\omega t} dt. \tag{2.34}$$

Le FSD est directement lié au FSS par la relation

$$S(k) = F(k,0) = \int_{-\infty}^{\infty} S(k,\omega)\ d\omega \tag{2.35}$$

qui permet généralement de tester la cohérence lors du calcul de ces fonctions. Dans la limite hydrodynamique $k \to 0$, il est possible d'obtenir une forme analytique du FSD contenant une grande quantité d'information sur le système. En effet,

$$S(k \to 0,\omega) = \frac{S(k)}{2\pi}\left[\left(\frac{\gamma - 1}{\gamma}\right)\frac{2D_T k^2}{\omega^2 + (D_T k^2)^2}\right. \tag{2.36}$$

$$+ \frac{1}{\gamma}\left(\frac{\Gamma k^2}{(\omega - c_s k)^2 + (\Gamma k^2)^2} + \frac{\Gamma k^2}{(\omega + c_s k)^2 + (\Gamma k^2)^2}\right)\Bigg]$$

où D_T est le coefficient de diffusion thermique, Γ est le coefficient d'atténuation sonore, $\gamma \equiv c_P/c_V$ est le ratio de la capacité calorique à pression constante c_P et à volume constant c_V et c_s est la vitesse du son adiabatique. Dans cette limite, la fonction est caractérisée par trois contributions particulières soit la raie de Rayleigh (située à $\omega = 0$) et les raies de Brillouin (situées à $\omega = \pm c_s k$) telle que présentée à la Fig.2.4.

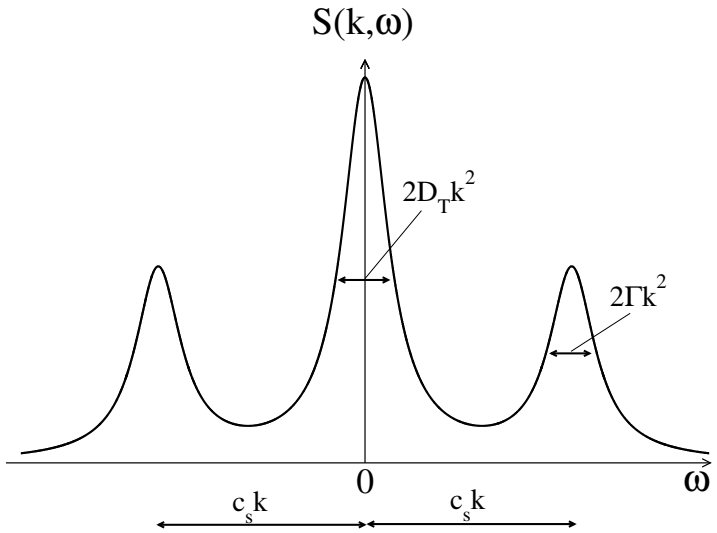

Figure 2.4. Facteur de structure dynamique dans la limite hydrodynamique $k \to 0$ illustrant la raie de Rayleigh ($\omega = 0$) et les raies de Brillouin ($\omega = \pm c_s k$)

La position des raies de Brillouin permet de déterminer la relation de dispersion des modes acoustiques dans le fluide $\omega_s(k)$ qui devient linéaire dans la limite hydrodynamique $\omega_s(k \to 0) = c_s k$. Celle-ci est d'une grande importance puisqu'elle peut être mesurée expérimentalement. Pour calculer le FSD, il n'est pas possible d'utiliser une méthode similaire a la procédure HNC et il est généralement nécessaire d'effectuer simulations de dynamique moléculaire.

2.1.3.2. *Dynamique moléculaire*

La dynamique moléculaire est un type de simulations numériques extrêmement utilisé pour l'étude des liquides et des plasmas qui consiste à résoudre les équations du mouvement classique pour un ensemble de N particules de masse m. Pour le cas particulier d'un potentiel

de paires $V(r)$, les équations de Newton pour les N particules prennent la forme

$$m\ddot{\mathbf{r}}_i(t) = \mathbf{F}_i(t) = -\nabla_i \sum_{i=1}^{N} \sum_{j>i}^{N} V(|\mathbf{r}_i(t) - \mathbf{r}_j(t)|) \tag{2.37}$$

Pour une configuration initiale, la méthode DM consiste à calculer la force sur chaque particule suivant l'Eq.(2.37) et à intégrer les équations du mouvement pour chaque particule afin d'obtenir la nouvelle position de chaque ion $\mathbf{r}_i(t + \Delta t)$ après une itération d'un pas de temps Δt. L'intégration des équations du mouvement est effectuée grâce à l'algorithme de Verlet [71] qui est présentée en détail dans l'annexe D. Il est primordial de choisir un pas de temps Δt suffisamment petit pour que l'algorithme d'intégration conserve l'énergie totale du système. Pour les simulations de cette thèse, on a utilisé différents pas d'intégration ($\Delta t = 0.5 \sim 2.5$ fs) selon la température ionique étudiée. Cette dernière est introduite dans la simulation en initialisant les vitesses aléatoirement suivant la distribution de Maxwell-Boltzmann. Cependant, cette procédure n'est pas suffisante pour maintenir la température désirée tout au long de la simulation. En effet, à partir de son état initial, le système va généralement relaxer de telle sorte que son énergie potentielle va diminuer. Puisque l'algorithme d'intégration conserve l'énergie totale, l'énergie cinétique du système accroît par la même quantité augmentant ainsi la température au-dessus de la valeur désirée. Pour contrer ce problème, on a utilisé le thermostat de Nosé-Hoover [72, 73] qui permet de simuler un ensemble statistique du type NVT, c'est-à-dire avec le nombre de particules N, le volume V et la température T conservés. L'idée générale est d'introduire un terme de friction ξ aux équations du mouvement qui permet de ralentir ou d'accélérer les particules jusqu'à l'obtention de la température désirée. Les équations du mouvement incluant le thermostat prennent la forme

$$m\ddot{\mathbf{r}}(t) = \mathbf{F}_i(t) - \xi(t) m\mathbf{v}_i(t) \tag{2.38}$$

$$\frac{d\xi(t)}{dt} = \frac{1}{Q}\left(\sum_{i=1}^{N} \frac{m\mathbf{v}_i(t)^2}{2} - \frac{3N+1}{2} k_b T\right) \tag{2.39}$$

où Q est le paramètre déterminant la vitesse de la relaxation. Les étapes de l'algorithme de Verlet-Nosé-Hoover sont ainsi modifiées et sont présentées dans l'annexe D. En utilisant cette méthode, la température n'est pas fixe au cours de la simulation, mais tend, tout en oscillant, vers la valeur désirée. Il est donc nécessaire d'adapter la valeur de Q et la longueur de la période de relaxation afin d'obtenir une température, une énergie potentielle et cinétique stable. À la fin de cette période, le thermostat est retiré et le reste de la simulation est

effectuée avec l'algorithme original de Verlet. C'est à partir de ce moment qu'il est possible de calculer les fonctions de distribution $G(r,t)$ et $S(k,\omega)$.

D'un point de vue pratique, il n'est pas nécessaire de calculer la fonction $G(r,t)$ afin d'obtenir $S(k,\omega)$. En effet, la fonction intermédiaire de diffusion $F(\mathbf{k},t)$ est accessible directement de la simulation DM puisqu'on connait analytiquement la transformée de Fourier spatiale de $\rho(\mathbf{r},t)$

$$F(\mathbf{k},t) = \frac{1}{N}\langle \rho(\mathbf{k},t)\rho(-\mathbf{k},0) \rangle \qquad \rho(\mathbf{k},t) = \sum_i^N e^{i\mathbf{k}\cdot\mathbf{r}_i(t)}. \tag{2.40}$$

Le facteur de structure dynamique est ensuite calculé en effectuant uniquement la transformée de Fourier temporelle comme présentée à l'Eq.(2.34). Cela permet d'éviter le calcul de la transformée de Fourier spatiale de $G(r,t)$ qui peut être problématique en raison de la taille finie de la simulation DM.

Finalement, les méthodes théoriques présentées dans cette section permettent une compréhension du système ionique et d'en prédire plusieurs propriétés physiques à condition d'avoir un potentiel de paires adéquat pour le régime de la MDC. Dans les métaux, l'interaction ion-ion est grandement modifiée par le nuage électronique entourant chaque ion. Il est donc nécessaire d'avoir une description fiable de la structure électronique dans ce régime complexe.

2.2. Système électronique

La description du système électronique interagissant s'avère d'une très grande complexité puisqu'il est toujours nécessaire de le traiter quantiquement. En général, on considère les électrons dans un potentiel extérieur produit par le système ionique. Il est fréquent d'utiliser l'approximation de Born-Oppenheimer, c'est-à-dire de considérer les ions comme immobiles par rapport aux électrons. Il est alors possible de décrire le système de N électrons interagissant par une fonction d'onde stationnaire $\Psi \equiv \Psi(\mathbf{r}_1, \cdots, \mathbf{r}_N)$ et de résoudre l'équation de Schrödinger indépendante du temps

$$\hat{H} \tag{2.41}$$

$$phi = \left[\hat{T} + \hat{V} + \hat{U}\right]\Psi = \left[\sum_i^N \left(-\frac{\hbar^2\nabla_i^2}{2m}\right) + \sum_i^N V(\mathbf{r}_i) + \sum_{i<j}^N U(\mathbf{r}_i,\mathbf{r}_j)\right]\phi = E\phi, \tag{2.42}$$

où E est l'énergie totale du système, $\hat{T}$ est l'énergie cinétique, $\hat{U}$ est l'interaction de Coulomb inter électron et $\hat{V}$ est le potentiel extérieur provenant des ions. Le terme d'interaction $\hat{U}$

complexifie grandement le problème et il est impossible de résoudre analytiquement l'hamiltonnien de l'Eq.(2.42). Depuis plusieurs décennies, une technique pour calculer la structure électronique s'est démarquée et est maintenant grandement utilisée en physique et chimie.

2.2.1. Théorie de la fonctionnelle de la densité à $T = 0$

La TFD, introduite dans les années 1960 par Hohenberg et Kohn (HK) [34], est dorénavant la méthode la plus utilisée pour décrire le système d'électrons interagissant. La méthode se base sur un théorème fondamental formulé par ces derniers.

2.2.1.1. *Théorème de Hohenberg-Kohn*

Le théorème énonce que le potentiel externe $V(\mathbf{r})$ de l'hamiltonien de l'Eq.(2.42) est une fonctionnelle unique de la densité électronique de l'état fondamental

$$n_0(\vec{r}) = N \int d\mathbf{r}_2 \cdots \int d\mathbf{r}_N \ \Psi_0^*(\mathbf{r},\mathbf{r}_2,\cdots,\mathbf{r}_N)\Psi_0(\mathbf{r},\mathbf{r}_2,\cdots,\mathbf{r}_N). \tag{2.43}$$

Ce dernier énonce qu'une densité $n(\mathbf{r})$ ne peut pas provenir de deux potentiels extérieurs $V(\mathbf{r})$ différents excepté si ceux-ci diffèrent uniquement l'un de l'autre par une constante. Un avantage marqué d'utiliser la densité comme variable est de diminuer grandement le nombre de variables spatiales de la théorie. En effet, celle-ci dépend uniquement de 3 coordonnées de l'espace tandis que la fonction d'onde électronique dépend de $3N$ coordonnées. Puisque la relation (2.43) est inversible, la fonction d'onde de l'état fondamental est alors nécessairement une fonctionnelle unique de la densité $\Psi_0 = \Psi[n_0]$. Par le fait même, la valeur moyenne de l'énergie de l'état fondamental est aussi une fonctionnelle unique de n_0 telle que $\langle \hat{H} \rangle_0 \equiv E[n_0]$. Dans le cas où la densité de l'état fondamental est inconnue, la fonctionnelle de l'énergie prend la forme

$$\begin{aligned} E[n] &= \langle \Psi[n] | \hat{T} + \hat{U} + \hat{V} | \Psi[n] \rangle \\ &= \langle \Psi[n] | \hat{T} + \hat{U} | \Psi[n] \rangle + \langle \Psi[n] | \hat{V} | \Psi[n] \rangle \\ &= F[n] + \int d\mathbf{r} \ V(\mathbf{r}) n(\mathbf{r}) \end{aligned} \tag{2.44}$$

où $F[n] \equiv T[n] + U[n]$ est une fonctionnelle unique de la densité $n(\mathbf{r})$ de N électrons interagissant. Celle-ci est la même, peu importe le potentiel extérieur $V(\mathbf{r})$ appliqué sur le système, et doit être calculée une seule fois. À condition de connaître explicitement la fonctionnelle $F[n]$, l'énergie de l'état fondamental $E[n_0]$ s'obtient alors en minimisant l'énergie $E[n]$ par rapport à la densité électronique $n(\mathbf{r})$.

D'un point de vue fondamental, deux conditions supplémentaires sont nécessaires pour s'assurer qu'il existe bel et bien une correspondance biunivoque entre la densité $n(\mathbf{r})$ et le potentiel externe $V(\mathbf{r})$. Premièrement, le problème de la représentabilité-N met en doute la certitude que la fonction $n(\mathbf{r})$ puisse assurément être représentée sous la forme de l'Eq.(2.43), c'est-à-dire en termes d'une fonction d'onde antisymétrique à N-corps $\Psi_0(\mathbf{r}, \cdots, \mathbf{r}_N)$. Deuxièmement, le problème de la représentabilité-V met en doute la certitude que la densité $n(\mathbf{r})$, satisfaisant la première condition, soit bel et bien la densité de l'état fondamentale d'un potentiel local $V(\mathbf{r})$. En effet, le théorème de HK garantit qu'il ne peut pas y avoir plus d'un potentiel, à une constante près, produisant une densité particulière, mais n'exclue pas la possibilité qu'aucun potentiel soit associé à cette densité. Dans cette thèse, ces enjeux fondamentaux de la TFD ne seront pas discutés, mais plus de détails sur ces sujets sont disponibles dans Ref.[74, 75, 76].

2.2.1.2. *Formulation de Kohn-Sham*

Le théorème de Hohenberg-Kohn démontre rigoureusement qu'il est possible d'utiliser uniquement la densité électronique comme variable afin de déterminer l'énergie de l'état fondamental d'un système de N électrons interagissant. Par contre, malgré l'élégance de la théorie, celle-ci n'offre pas de méthodes explicites pour effectuer les calculs. La formulation de la TFD par Kohn-Sham [35] offre une méthode auto cohérente afin d'obtenir l'énergie de l'état fondamental du système. La méthode consiste à utiliser un système de N électrons non interagissant soumis à un potentiel $V_s(\mathbf{r})$ tel que la densité de l'état fondamental de ce système soit identique à celle du système en interaction.

Soit l'hamiltonien du système sans-interactions $H_s = T_s + V_s$ qui permet d'écrire la fonctionnelle de l'énergie

$$E_s[n] = T_s[n] + \int d\mathbf{r}\ V_s(\mathbf{r}) n(\mathbf{r}) \tag{2.45}$$

où $T_s[n]$ est la fonctionnelle de l'énergie cinétique du système non interagissant, qui est différente de celle pour le système en interaction $T[n]$. La densité de l'état fondamental est alors donnée par

$$n(\mathbf{r}) = \sum_i^N |\phi_i(\mathbf{r})|^2, \tag{2.46}$$

où les fonctions d'onde $\phi_i(\mathbf{r})$ sont les N solutions de plus basse énergie E_i de l'équation de Schrödinger d'une seule particule soumise au potentiel $V_s(\mathbf{r})$

$$\left[-\frac{\hbar^2 \nabla_i^2}{2m} + V_s(\mathbf{r}) \right] \phi_i(\mathbf{r}) = E_i \phi_i(\mathbf{r}). \tag{2.47}$$

L'astuce consiste à réécrire la fonctionnelle de l'Eq.(2.44) en ajoutant et soustrayant la fonctionnelle de l'énergie cinétique $T_s[n]$ et la contribution de Hartree à l'énergie électrostatique afin d'obtenir

$$E[n] = T_s[n] + \frac{e^2}{2}\int d\mathbf{r}d\mathbf{r}'\ \frac{n(\mathbf{r})n(\mathbf{r}')}{|\mathbf{r}-\mathbf{r}'|} + \int d\mathbf{r}\ V(\mathbf{r})n(\mathbf{r}) + E_{\rm xc}[n] \tag{2.48}$$

où l'on a défini la fonctionnelle d'énergie d'échange et corrélation

$$E_{\rm xc}[n] \equiv T[n] + U[n] - T_s[N] - \frac{e^2}{2}\int d\mathbf{r}d\mathbf{r}'\ \frac{n(\mathbf{r})n(\mathbf{r}')}{|\mathbf{r}-\mathbf{r}'|}. \tag{2.49}$$

Toute l'information inconnue à propos de l'interaction entre électrons est alors comprise dans le terme $E_{\rm xc}[n]$. En effectuant la dérivée fonctionnelle des équations (2.45) et (2.48),on identifie le potentiel V_s nécessaire à la méthode

$$V_s(\mathbf{r}) = V(\mathbf{r}) + e^2\int d\mathbf{r}'\ \frac{n(\mathbf{r}')}{|\vec{r}-\mathbf{r}'|} + \frac{\delta E_{\rm xc}[n]}{\delta n(\mathbf{r})}. \tag{2.50}$$

Il est alors possible de débuter un calcul auto cohérent en insérant une densité initiale d'essai $\tilde{n}$ dans l'Eq.(2.50). À partir du potentiel initial $\tilde{V}_s(\mathbf{r})$ obtenu, on détermine les fonctions d'onde $\phi_i(\mathbf{r})$ en résolvant l'équation de Schrödinger (2.47) pour calculer la nouvelle densité électronique à partir de l'équation (2.46). Finalement, en répétant suffisamment ce processus, on obtient la densité $n_0(\mathbf{r})$ de l'état fondamental du système d'électrons en interaction. À priori, la méthode exposée est formellement exacte à condition de connaître explicitement la fonctionnelle d'énergie d'échange et corrélation $E_{\rm xc}[n]$. Puisque celle-ci est inconnue, plusieurs approximations ont été proposées et seront discutées dans la section (2.2.3). Cependant, puisque les électrons sont à de très hautes températures dans le régime de la MDC, il est nécessaire de modifier légèrement la TFD pour inclure les effets de température.

2.2.2. Théorie de la fonctionnelle de la densité à $T \neq 0$

La généralisation de la TFD à température finie est proposée par Mermin [77] dès 1965 et se base sur un théorème semblable à celui de Hohenberg et Kohn. Soit la fonctionnelle

$$\Omega[\rho] = \mathrm{Tr}\left[\rho\left(H - \mu N + \frac{1}{\beta}\ln\rho\right)\right], \tag{2.51}$$

qui permet de déterminer le grand potentiel (l'équivalent de l'énergie de l'état fondamental)

$$\Omega = -\frac{1}{\beta}\ln \mathrm{Tr}\left[e^{-\beta(H-\mu N)}\right] \tag{2.52}$$

par la fonctionnelle $\Omega[\rho_0]$ où ρ_0 est la matrice de densité de l'ensemble grand canonique

$$\rho_0 = \frac{e^{-\beta(H-\mu N)}}{\mathrm{Tr}\left[e^{-\beta(H-\mu N)}\right]}. \tag{2.53}$$

De façon similaire à Hohenberg et Kohn, il démontre que, dans l'ensemble grand canonique, la densité électronique $n(\mathbf{r})$ détermine uniquement le potentiel extérieur $V(\mathbf{r})$ qui à son tour détermine uniquement la matrice de densité ρ_0. Puisque $\rho_0[n]$ est une fonctionnelle unique de la densité, il est alors possible de réécrire l'Eq.(2.52) tel que

$$\Omega[n] = F[n] + \int d\mathbf{r}\ V(\mathbf{r})n(\mathbf{r}) \tag{2.54}$$

où la fonctionnelle universelle $F[n]$ prend maintenant la forme

$$F[n] = \mathrm{Tr}\left[T + U + \frac{1}{\beta}\ln\rho_0\right]. \tag{2.55}$$

Lorsque $n(\mathbf{r})$ est la densité à l'équilibre soumise au potentiel $V(\mathbf{r})$, la fonctionnelle $\Omega[n]$ est égale au grand potentiel Ω. Cependant, de façon similaire au cas $T = 0$, cette formulation du problème n'offre pas de méthode pour effectuer des calculs directement et il est nécessaire d'utiliser une méthode semblable à celle proposée par Kohn et Sham. Par contre, deux difficultés majeures surviennent lorsqu'on tente de reproduire la procédure présentée dans la section précédente.

Premièrement, lorsque la température est non-nulle, la densité de l'Eq.(2.46) prend plutôt la forme

$$n(\vec{r}) = \sum_i^N f(E_i)|\phi_i(\mathbf{r})|^2 \qquad \text{où} \qquad f(E_i) = \frac{1}{1+e^{\beta(E_i-\mu)}}. \tag{2.56}$$

L'ajout du facteur d'occupation de Fermi $f(E_i)$ augmente grandement le temps de convergence du calcul puisqu'il est nécessaire de résoudre l'équation de Schrödinger pour beaucoup plus d'état d'énergie E_i. Puisque le temps de simulation pour l'orthogonalisation de N fonctions d'ondes ϕ_i d'énergie T_i augmente comme le cube de ce dernier N^3, l'utilisation de la TFD à température finie devient rapidement impraticable à haute T_e. Deuxièmement, dans la formulation de Khon-Sham, il est nécessaire de connaître l'énergie d'échange et corrélation afin de pouvoir utiliser la méthode. La difficulté est alors de déterminer celle-ci en fonction de la température.

2.2.3. Fonctionnelle d'échange et corrélation

L'approximation la plus simple pour déterminer E_{xc} est l'approximation de la densité locale (ADL) (connue en anglais sous *Local Density Approximation*). Celle-ci consiste à ignorer

toutes les propriétés non locales de la fonctionnelle et décrire celle-ci sous la forme

$$E_{\rm xc}^{\rm ADL}[n] = \int \epsilon_{\rm xc}(n(\mathbf{r}))\ n(\mathbf{r})\ d\mathbf{r}. \tag{2.57}$$

où $\epsilon_{\rm xc}[n]$ est l'énergie d'échange et corrélation par particule du gaz homogène d'électrons de densité n. L'approximation sous-entendue dans la ADL est que la densité du système inhomogène varie suffisamment lentement de tel sorte que l'énergie d'échange et corrélation est localement celle du système homogène. Des simulations Monte Carlo quantiques [78] ont calculé l'énergie d'échange et corrélation permettant d'obtenir $\epsilon_{\rm xc}[n]$ sur tout le domaine de n tout en respectant les limites analytiques pour $n \ll 1$ et $n \gg 1$. On note que dans certains cas, il est nécessaire d'aller au-delà de l'approximation ADL et d'autres approximations sont utilisées telles que l'approximation du gradient généralisé (connue en anglais sous *Generalized Gradient Approximation*) qui prend en compte la variation locale de la densité telle que

$$E_{\rm xc}^{\rm AGG}[n,\nabla n] = \int \epsilon_{\rm xc}(n(\mathbf{r},\nabla n(\mathbf{r}))\ n(\mathbf{r}) d\mathbf{r}. \tag{2.58}$$

Une des formes les plus utilisées pour $\epsilon_{\rm xc}(n,\nabla n)$ fût proposée par Perdew, Burke et Ernzerhof [79]. Cependant, ces approximations ont initialement été développées pour l'étude des solides à température nulle. Il existe certaines méthodes pour évaluer l'énergie d'échange et corrélation dépendante de la température dont l'évaluation de diagrammes à bulle à température finie [80, 81], la paramétrisation de Iyetomi-Ichimaru (IYI) [82] ainsi que la méthode de la *Classical-map Hyper Netted Chain* (CHNC) proposée par Dharma-wardana [83]. En général, la méthode consiste à faire une application du liquide quantique d'électrons vers un liquide classique d'électrons interagissant pour la force de Coulomb modifiée λ/r. En utilisant la procédure HNC pour obtenir les fonctions de distribution électron-électron, il est possible d'extraire une fonctionnelle d'échange et corrélation à température finie selon la formule

$$f_{\rm xc} = \frac{n}{2}\int_0^1 \frac{d\lambda}{2\lambda}\int d\mathbf{r}\ \frac{\lambda}{r}\left[h_{11}(r,\lambda) + h_{12}(r,\lambda)\right]. \tag{2.59}$$

Une paramétrisation simple de cette fonctionnelle fût proposée par Perrot et Dharma-wardana [84]

$$f_{\rm xc}(n,T) = \frac{\epsilon_{\rm xc}(n,T_e=0) - P_1(n,T_e)}{P_2(n,T_e)} \tag{2.60}$$

où $\epsilon_{\rm xc}(n,T=0)$ est la fonctionnelle à température nulle et où P_i sont des fonctions de la densité électronique n et de la température électronique T_e. Cette fonctionnelle est utilisée dans le formalisme ADL de l'Eq.(2.57). Une description plus détaillée de la méthode CHNC et de la paramétrisation de $f_{\rm xc}(n,T)$ est présentée dans l'annexe C. Lors des simulations utilisant ABINIT ou VASP, on a utilisé les fonctionnelles à température nulle fournies avec

ces logiciels tandis que la fonctionnelle à température finie fût utilisée pour tous les calculs utilisant le modèle PAN.

2.2.4. Forces ioniques *ab initio*

Lorsque la densité électronique $n(\mathbf{r})$ est obtenue par TFD pour une configuration ionique donnée, il est possible de calculer la force $\mathbf{F}_a$ que subit un ion a à la position $\mathbf{R}_a$ submergé dans le potentiel créé par les électrons et les autres ions. Pour $T = 0$, cela permet d'effectuer une relaxation du système afin d'obtenir la structure cristalline minimisant l'énergie totale, tandis que pour $T \neq 0$, ces forces peuvent être utilisées pour effectuer de la dynamique moléculaire *ab initio*.

2.2.4.1. *Forces ioniques à température nulle*

À température nulle $T = 0$, la force $\mathbf{F}_a$ est calculée à partir du théorème d'Hellmann-Feynman [41, 42]

$$\mathbf{F}_a(T=0) = -\frac{\partial E}{\partial \mathbf{R}_a} = -\frac{\partial}{\partial \mathbf{R}_a}\langle\phi|H|\phi\rangle \tag{2.61}$$

$$= -\left[\langle\frac{\partial\phi}{\partial \mathbf{R}_a}|H|\phi\rangle + \langle\phi|H|\frac{\partial\phi}{\partial \mathbf{R}_a}\rangle + \langle\phi|\frac{\partial H}{\partial \mathbf{R}_a}|\phi\rangle\right] \tag{2.62}$$

$$\equiv \mathbf{F}_{a,\mathrm{P}} + \mathbf{F}_{a,\mathrm{HF}} \tag{2.63}$$

où H est l'hamiltonien du système donné par l'Eq.2.42 et $|\phi\rangle$ est la fonction d'onde du système. Le terme $\mathbf{F}_\mathrm{P}$ est connu sous la force de Pulay [85] qui dépend du type de fonction d'onde choisi, tandis que le terme F_HF est la force d'Hellmann-Feynmann qui décrit la force électrostatique classique produite par la densité électronique $n(\mathbf{r})$ et par les autres ions aux positions $R_{b\neq a}$. En inspectant l'Eq.2.42, on remarque qu'il y a uniquement deux termes de l'hamiltonien qui dépendent de $\mathbf{R}_a$ ce qui permet d'obtenir

$$\mathbf{F}_{a,\mathrm{HF}} = -\frac{\partial}{\partial \mathbf{R}_a}\left[\int \frac{Z_a n(\mathbf{r})}{|\mathbf{r}-\mathbf{R_a}|}d\mathbf{r} - \sum_b \frac{Z_a Z_b}{|\mathbf{R}_b - \mathbf{R}_a|}\right]. \tag{2.64}$$

Lorsque l'état $|\phi\rangle$ est une fonction propre de l'hamiltonien $H|\phi\rangle = E|\phi\rangle$, la force de Pulay est trivialement nulle

$$\mathbf{F}_{a,\mathrm{P}} = \langle\frac{\partial\phi}{\partial \mathbf{R}_a}|H|\phi\rangle + \langle\phi|H|\frac{\partial\phi}{\partial \mathbf{R}_a}\rangle = E[\langle\frac{\partial\phi}{\partial \mathbf{R}_a}|\phi\rangle + \langle\phi|\frac{\partial\phi}{\partial \mathbf{R}_a}\rangle] \tag{2.65}$$

$$= E\frac{\partial}{\partial \mathbf{R}_a}\langle\phi|\phi\rangle = 0, \tag{2.66}$$

où l'on a utilisé l'orthonormalisation de la fonction d'onde $\langle\phi|\phi\rangle = 1$. Dans la situation où $|\phi\rangle$ n'est pas une fonction propre de l'hamiltonien et qu'il est nécessaire de la développer sur une base de fonctions propres $|\phi\rangle = \sum_i a_i\psi_i$, il est possible d'utiliser la correction $\mathbf{F}_{a,\text{cor}}$ proposée par Bendt et Zunger [86]

$$\mathbf{F}_{a,\text{cor}} = -2\text{Re}[\sum_i a_i\langle\frac{\partial\psi_i}{\partial\mathbf{R}_a}]|(H-E)|\phi\rangle. \tag{2.67}$$

De façon générale, il est possible d'obtenir un développement suffisamment complet de la fonction $|\phi\rangle = \sum_i a_i\psi_i$ dans nos simulations pour que la correction $\mathbf{F}_{a,\text{cor}}$ soit négligeable.

2.2.4.2. *Forces ioniques à température finie*

À température finie $T \neq 0$, la force $\mathbf{F}_a$ s'obtient en prenant la dérivée de l'énergie libre $F = E - TS$, qui inclut l'entropie S en plus de l'énergie interne E

$$\mathbf{F}_a = -\frac{\partial F}{\partial\mathbf{R}_a} = -\frac{\partial}{\partial\mathbf{R}_a}(E - TS) \equiv \mathbf{F}_{a,E} + \mathbf{F}_{a,S}, \tag{2.68}$$

où l'on a définit la force provenant de l'énergie interne $\mathbf{F}_{a,E}$ et de l'entropie $\mathbf{F}_{a,S}$.

Lorsque $T \neq 0$, l'énergie interne du système est donnée par la relation $E = \sum_i f(E_i)E_i$ où E_i est l'énergie associée à l'état propre $|\phi_i\rangle$ et où $f(E_i)$ est l'occupation de Fermi-Dirac définie à l'Eq.(2.56). Puisque $f(E_i)$ dépend de $\mathbf{R}_a$ par le biais de E_i, la force provenant de l'énergie interne prend la forme

$$\mathbf{F}_{a,E} = -\frac{\partial}{\partial\mathbf{R}_a}\left(\sum_i f(E_i)E_i\right) = -\sum_i\frac{\partial f(E_i)}{\partial\mathbf{R}_a}E_i - \sum_i f(E_i)\frac{\partial E_i}{\partial\mathbf{R_a}}. \tag{2.69}$$

Premièrement, en négligeant les forces de Pulay, il est possible d'appliquer le théorème d'Hellmann-Feynmann à chacun des termes de la série du dernier terme de l'Eq.(2.69) pour obtenir

$$\mathbf{F}_{a,E} = -\sum_i\frac{\partial f(E_i)}{\partial\mathbf{R}_a}E_i + \mathbf{F}_{a,\text{HF}}, \tag{2.70}$$

où $\mathbf{F}_{a,\text{HF}}$ est la force d'Hellmann-Feynmann définie à l'Eq.(2.64) en utilisant la densité électronique à température finie $n(\mathbf{r}) = \sum_i f(E_i)|\psi_i(\mathbf{r})|^2$. Deuxièmement, l'entropie du système dépend uniquement de la fonction $f(E_i) \equiv f_i$ et prend la forme

$$TS = T\sum_i[f_i\ln f_i + (1-f_i)\ln(1-f_i) - \beta\mu f_i] \tag{2.71}$$

$$= T\sum_i\int\ln\left(\frac{f_i}{1-f_i} - \beta\mu\right)\,df_i \tag{2.72}$$

$$\equiv T\sum_i\int\mathcal{F}(f_i)\,df_i \tag{2.73}$$

$$= \sum_i \int E_i \; df_i. \tag{2.74}$$

où l'on a utilisé $\mathcal{F}(f_i) = E_i$. La force provenant de l'entropie prend alors la forme

$$\mathbf{F}_{a,S} = \frac{\partial(TS)}{\partial \mathbf{R}_a} = \sum_i \frac{\partial f(E_i)}{\partial \mathbf{R}_a} \frac{\partial}{\partial f_(E_i)} \left(\int E_i \; df_i \right) = \sum_i \frac{\partial f(E_i)}{\partial \mathbf{R}_a} E_i, \tag{2.75}$$

où l'on a utilisé le résultat de l'Eq.(2.71). Finalement, en combinant les résultats de l'Eq.(2.75) et de l'Eq.(2.69), on observe que les contributions provenant de la dérivée de l'occupation des états $|\phi_i\rangle$ s'annulent et que la force ressentit par l'ion a provient uniquement du terme d'Hellmann-Ferynman à température finie

$$\mathbf{F}_a(T \neq 0) = \mathbf{F}_{a,\mathrm{HF}}. \tag{2.76}$$

2.3. Modèle du pseudo-atome neutre

2.3.1. Théorie de la fonctionnelle de la densité totale

Le modèle du pseudo-atome neutre, initialement proposé par Ziman [87] et grandement utilisé par Dagens [88, 89, 90] ainsi que par Perrot et Dharma-wardana [61, 62, 63, 64], est une approche développée pour l'étude des métaux solides, des liquides métalliques et des plasmas qui s'avère être idéale pour l'étude de la MDC. L'idée générale du modèle consiste à décomposer la densité électronique totale en termes d'une superposition de la densité autour de chaque site ionique tel que généralement fait pour l'étude des métaux $n(\mathbf{r}) = \sum_i n_i(\mathbf{r})$. Du point de vue de la TFD, cette superposition peut être considérée comme l'élaboration d'un modèle d'atome-moyen exact et non pas une approximation. En effet, la TFD stipule que l'énergie libre totale $F[n,\rho]$ est une fonctionnelle unique de la densité électronique $n(\mathbf{r})$ *et* de la densité ionique $\rho(\mathbf{r})$. L'énergie libre doit ainsi satisfaire les conditions stationnaires suivantes

$$\delta F[n,\rho]/\delta n = 0 \tag{2.77}$$

$$\delta F[n,\rho]/\delta \rho = 0. \tag{2.78}$$

Tandis que la TFD conventionnelle utilise l'Eq.(2.77) pour construire un potentiel "quantique" de Kohm-Sham affectant des pseudo-électrons non interagissant, l'Eq.(2.78) définit un ensemble de pseudo-ions sans-interactions soumis à un potentiel "classique" de Kohn-Sham. Pour satisfaire ces équations, il est nécessaire de connaître la fonctionnelle d'échange et corrélation pour les électrons $F_{\mathrm{xc}}^{ee}[n]$, mais aussi la fonctionnelle de corrélation pour les ions $F_{\mathrm{c}}^{ii}[\rho]$ qui ne comporte pas de composante d'échange puisque les ions sont traités de façon classique dans notre régime d'intérêt. Pour les métaux simples étudiés dans cette

thèse, la procédure MHNC incluant les corrections de pont s'avère suffisante pour inclure les corrélations ion-ion. La solution du problème consiste à effectuer les étapes suivantes jusqu'à l'obtention de solutions auto cohérentes :

1. Calcul de la densité électronique $n(r)$ par TFD à température finie pour une densité ionique d'essai $\rho^0(r)$ autour d'un nucléon de charge Z. L'équation de KS à température finie est utilisée. La fonction $\rho^0(r)$ doit être consistante avec une densité ionique moyenne d'essai ρ_0 et une densité électronique moyenne d'essai n_0 telle que $n = \bar{Z}_0\rho$ avec $\bar{Z}_0$ une ionisation moyenne d'essai.
2. À partir de la densité électronique totale $n(r) = n_f(r) + n_b(r)$, la densité d'électrons liés $n_b(r)$, constituant le cœur de l'atome, permet d'obtenir le nombre d'électrons liés Z_b ainsi que la nouvelle ionisation moyenne du système $\bar{Z} = Z - Z_b$. Cette valeur de $\bar{Z}$ est utilisée de nouveau dans l'étape 1 jusqu'à ce que plusieurs règles de somme soient satisfaites. Ces contraintes, telles que la règle de somme f et la règle de somme de Friedel sont décrites en détail dans la section (7.5.2).
3. la densité d'électrons libres $n_f(r)$ est utilisée pour construire un potentiel de paires ion-ion $V_{ii}(r)$ à partir de l'Eq.(1.13). En utilisant ce potentiel, la FDP ion-ion $g_{ii}(r)$ est calculée par la procédure MHNC et permet d'obtenir la nouvelle densité ionique $\rho(r) = \rho g_{ii}(r)$.
4. Reprise de l'étape 1 à l'aide de la nouvelle densité ionique $\rho(r)$.

Lorsqu'elle est convergée, cette procédure fournit les densités centrées sur un site ionique tel que schématisé à la Fig.2.5. Tout le système est ainsi compris à l'intérieur d'une "sphère

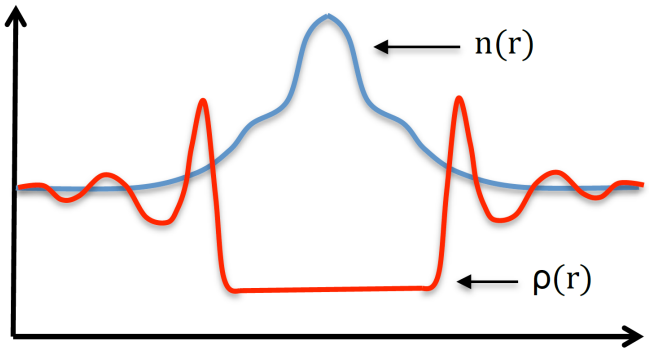

Figure 2.5. Schéma de la densité électronique $n(r)$ et ionique $\rho(r)$ autour d'un site ionique obtenue de façon auto cohérente par la théorie de la fonctionnelle de la densité totale.

de corrélation" de rayon R_c telle que toutes les corrélations sont nulles pour $r \to R_c$. Généralement, un rayon de corrélation $R_c \sim$ 5-10r_{ws} est suffisant pour contenir la densité électronique $n(r)$ et la densité ionique $\rho(r)$ formant ainsi un objet neutre nommé le "pseudo-atome neutre". Pour les métaux simples, la procédure converge rapidement et il est possible d'effectuer seulement une fois les étapes 1 à 3 comme première approximation.

2.3.2. Densité électronique

Le potentiel extérieur agissant sur les électrons est produit par le système ionique tel que

$$V_{\text{ext}}(\mathbf{r}) = \sum_i \int \frac{-Z\delta(\mathbf{r}' - \mathbf{r}_i)}{|\mathbf{r} - \mathbf{r}'|}\, d\mathbf{r}' \tag{2.79}$$

où $\mathbf{r}_i$ est la position des noyaux atomiques de charge Z. L'objectif est de décrire la densité électronique totale en termes d'une superposition de densités partielles autour de chaque ion

$$n(\mathbf{r}) = \sum_i \Delta n(\mathbf{r} - \mathbf{r}_i)) \equiv \sum_i \Delta n_i(\mathbf{r}). \tag{2.80}$$

Le potentiel (2.79) produira des états liés n_b et des états de valence quasi libre n_f

$$\Delta n_i(\mathbf{r}) = \Delta n_{b,i}(\mathbf{r}) + \Delta n_{f,i}(\mathbf{r}) \tag{2.81}$$

où l'ionisation $\bar{Z}$ du système est déterminé par les conditions

$$\bar{Z} = \int_\infty \Delta n_f(\mathbf{r})\, d\mathbf{r} = Z - \int_\infty \Delta n_b(\mathbf{r})\, d\mathbf{r} = Z - \int_{r_{ws}} \Delta n_b(\mathbf{r})\, d\mathbf{r}. \tag{2.82}$$

où la dernière égalité illustre que les états liés sont fortement localisés à l'intérieur de la sphère de Wigner-Seitz de rayon r_{ws}. Cependant, le potentiel (2.79) est un "diffuseur fort" ayant une somme de Friedel égale à $\bar{Z}$, c'est-à-dire qu'il déplace une densité d'électron quasi libre normalisée à $\bar{Z}$. Cela est un problème puisqu'il fut démontré [91] que le développement de la fonctionnelle d'énergie cinétique $T[\sum_i \Delta n_i]$, nécessaire au calcul de l'énergie totale du système en TFD, converge très lentement pour une somme de Friedel non-nulle. Il est possible de contrevenir à ce problème en introduisant une fonction d'écrantage auxiliaire $c_i(\mathbf{r})$ autour de chaque noyau. Cette fonction joue le rôle de notre densité ionique initiale $\rho^0(\mathbf{r})$ dont le choix le plus simple est une cavité sphérique de rayon r_{ws} et de charge totale $\bar{Z}$

$$c_i(\mathbf{r}) = nH(|\mathbf{r} - \mathbf{r}_i| - r_{ws}) \equiv \rho^0(\mathbf{r}) \tag{2.83}$$

avec $H(r)$ la fonction de Heaviside comme illustrée à la Fig.2.6. Le potentiel extérieur du système auxiliaire

$$V^*_{\text{ext}}(\mathbf{r}) = \sum_i \int \frac{-Z\delta(\mathbf{r}' - \mathbf{r}_i) + c_i(\mathbf{r}')}{|\mathbf{r} - \mathbf{r}'|}\, d\mathbf{r}' \tag{2.84}$$

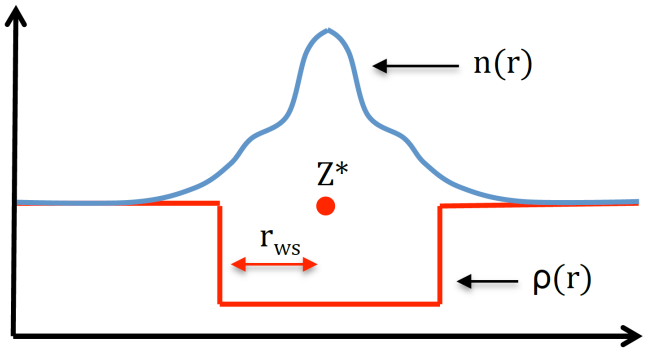

Figure 2.6. Schéma de la densité électronique $n(r)$ et de la cavité sphérique $c(r)$ utilisée comme densité ionique initiale $\rho^0(r)$.

produira la densité électronique du système auxiliaire

$$n^*(\mathbf{r}) = n + \sum_i \Delta n_i^*(\mathbf{r}) \tag{2.85}$$

tel que le potentiel total écranté est finalement donné par

$$V^*(\mathbf{r}) = \sum_i \int \frac{-Z\delta(\mathbf{r}' - \mathbf{r}_i) + c_i(\mathbf{r}') + \Delta n_i^*(\mathbf{r}')}{|\mathbf{r} - \mathbf{r}'|}\, d\mathbf{r}' = \sum_i V_i^*(\mathbf{r}). \tag{2.86}$$

Avec ce choix de fonction d'écrantage, la somme de Friedel de V_i^* et Δn_i^* est maintenant nulle et on s'attend à ce que l'approximation de superposition soit particulièrement bonne. Il est alors possible de résoudre les équations de la TFD uniquement pour le potentiel autour d'un site ionique V_i^* et d'obtenir la densité électronique Δn_i^*. Pour obtenir la densité électronique Δn du système exact en termes du système auxiliaire, on remarque que

$$\delta V_{\text{ext}}(\mathbf{r}) = V_{\text{ext}}(\mathbf{r}) - V_{\text{ext}}^*(\mathbf{r}) = \sum_i \int \frac{c_i(\mathbf{r}')}{|\mathbf{r} - \mathbf{r}'|}\, d\mathbf{r}' \tag{2.87}$$

est un "faible diffuseur" par construction et qu'il est ainsi possible d'utiliser la théorie de la réponse linéaire pour obtenir la correction

$$\delta n(\mathbf{r}) = \sum_i [\Delta n_i(\mathbf{r}) - \Delta n_i^*(\mathbf{r})] = \sum_i m_i(\mathbf{r}) - n. \tag{2.88}$$

La fonction de réponse linéaire χ^* du système arbitraire est impossible à calculer, mais puisque δV_{ext} est non-nul uniquement à l'extérieur de la cavité, c'est-à-dire où la densité électronique est essentiellement uniforme, on utilise la fonction de réponse linéaire du système uniforme d'électrons interagissant χ pour obtenir

$$m(\mathbf{r}) = \frac{1}{(2\pi)^3} \int \chi(q) V(q) c(q) e^{-i\mathbf{q}\cdot\mathbf{r}}\, d\mathbf{q} \tag{2.89}$$

où $V(q) = 4\pi/q^2$ est la transformée de Fourier du potentiel de Coulomb. On utilise la fonction de réponse statique à température finie

$$\chi(q,T) = \frac{\chi^0(q,T)}{1 - V(q)[1 - G(q)]\chi^0(q,T)} \tag{2.90}$$

où $\chi^0(q,T)$ est la fonction de Lindhard à température finie et où, pour aller au-delà de l'approximation de phase aléatoire (de l'anglais "Random Phase Approximation"), un facteur de correction locale (de l'anglais "Local Field Correction") à température finie $G(q)$ est utilisé

$$G(q) = \left(1 - \frac{\gamma_0}{\gamma}\right)\left(\frac{q^2}{k_{\mathrm{TF}}}\right)^2. \tag{2.91}$$

Dans l'Eq.(2.91), $k_{\mathrm{TF}} = \sqrt{6\pi n/E_f}$ est le vecteur d'onde de Thomas-Fermi avec E_F l'énergie de Fermi du système. De plus, γ est la compressibilité à température finie du système électronique interagissant

$$\frac{1}{\gamma} = n^2 \frac{\partial^2}{\partial n^2}(n\ f_{\mathrm{ghe}}(n,T)) \tag{2.92}$$

où $f_{\mathrm{ghe}}(n'T)$ est l'énergie libre par électron du gaz homogène d'électrons (plus de détails dans la section suivante) incluant la contribution d'échange et corrélation f_{xc} de l'Eq.(2.60). La compressibilité du système non interagissant γ_0 est obtenue en posant $f_{\mathrm{xc}} = 0$. La fonction de Lindhard $\chi^0(q,T)$ est donnée par la relation

$$\chi^0(q,T) = -\frac{1}{(2\pi)^3}\int \frac{f_{\mathbf{k}-\mathbf{q}} - f_{\mathbf{k}}}{E_{\mathbf{k}-\mathbf{q}} - E_{\mathbf{k}}}\ d\mathbf{k} \tag{2.93}$$

où

$$f_{\mathbf{k}} = \frac{1}{1 + \exp[\beta(E_{\mathbf{k}} - \mu)]} \qquad \text{et} \qquad E_{\mathbf{k}} = \frac{\hbar^2|\mathbf{k}|^2}{2m}. \tag{2.94}$$

Finalement, la densité électronique du système exact est obtenue par

$$n(\mathbf{r}) = \sum_i [\Delta n_i^*(\mathbf{r}) + m_i(\mathbf{r})] = \sum_i [\Delta n_{b,i}(\mathbf{r}) + \Delta n_{f,i}^*(\mathbf{r}) + m_i(\mathbf{r})] \tag{2.95}$$

puisque la densité électronique liée Δn_b est insensible au changement de premier ordre de δV_{ext}. Lorsque la densité électronique du système auxiliaire $n^*(\mathbf{r})$ est calculée en TFD, il est possible d'obtenir l'énergie libre totale du système.

2.3.3. Énergie libre totale

Dans un premier temps, on présente la formulation de l'énergie libre électronique F_e du système PAN pour une distribution ionique $\{\mathbf{r}_1, \cdots, \mathbf{r}_N\}$ particulière et fixe. Pour la suite,

on utilise la notation simplifiée

$$f(\mathbf{r}) \circ g(\mathbf{r}) = \int_\infty f(\mathbf{r}) g(\mathbf{r})\ d\mathbf{r} \qquad \text{et} \qquad f(\mathbf{r}) \star g(\mathbf{r}) = \int_\infty f(\mathbf{r}-\mathbf{r}') g(\mathbf{r}')\ d\mathbf{r}'. \tag{2.96}$$

On définit la fonctionnelle $G[n]$ qui inclut la contribution de l'énergie cinétique des électrons ainsi que l'échange et corrélation. L'énergie libre comporte alors 5 contributions distinctes :

1. La contribution de la fonctionnelle G :

$$G[n^*(\mathbf{r})] = G\left[n + \sum_i \Delta n_i^*(\mathbf{r})\right]\ ; \tag{2.97}$$

2. L'énergie d'interaction des électrons avec le potentiel externe V_{ext}^* :

$$\left(n + \sum_i \Delta n_i^*(\mathbf{r})\right) \circ \frac{1}{\mathbf{r}} \star \left(\sum_j -Z\delta_j(\mathbf{r}) + c_j(\mathbf{r})\right)\ ; \tag{2.98}$$

3. L'interaction électron-électron entre tous les pseudo-atomes :

$$\frac{1}{2}\left(n + \sum_i \Delta n_i^*(\mathbf{r})\right) \circ \frac{1}{\mathbf{r}} \star \left(n + \sum_j \Delta n_j^*(\mathbf{r})\right); \tag{2.99}$$

4. La correction perturbative de deuxième ordre provenant de δV_{ext} :

$$\left(n + \sum_i \Delta n_i^*(\mathbf{r})\right) \circ \frac{1}{r} \star \left(\sum_j c_j(\mathbf{r})\right) + \frac{1}{2}\left(\sum_i m_i(\mathbf{r}) - n\right) \circ \frac{1}{\mathbf{r}} \star \left(\sum_j c_j(\mathbf{r})\right); \tag{2.100}$$

5. L'interaction de Coulomb nucléon-nucléon :

$$\frac{1}{2}\sum_{i\neq j} \frac{Z^2}{|\mathbf{r}_i - \mathbf{r}_j|}. \tag{2.101}$$

Le problème principal consiste à calculer la contribution de G lorsque les densités électroniques se recouvrent. Cependant, la construction précédente en termes du système auxiliaire permet d'effectuer le développement

$$G\left[n + \sum_i \Delta n_i^*(\mathbf{r})\right] = G[n] + \sum_i G_i + \frac{1}{2}\sum_{i\neq j} G_{ij} + \cdots \tag{2.102}$$

$$G_i = G[n + \Delta n_i^*(r)] - G[n] \tag{2.103}$$

$$G_{ij} = G[n + \Delta n_i^*(\mathbf{r}) + \Delta n_j^*(\mathbf{r})] - G_i - G_j - G[n]. \tag{2.104}$$

Pour les métaux simples, le développement au deuxième ordre est suffisante et on note que G_{ij} tend vers zéro pour des paires d'ions éloignés. En séparant les termes $i = j$ et $i \neq j$, il est possible d'isoler les contributions propres à chaque site i de ceux qui dépendent de la structure ion-ion $i \neq j$. On redéfinit alors les 5 contributions à l'énergie libre totale sous la

forme intuitive

$$F_e = \sum_i \left[F_i^{\text{ghe}} + F_i^{\text{emb}} + F_i^{\text{cav}}\right] + \sum_{i \neq j} E_{ij}^{\text{ion}}. \tag{2.105}$$

où chaque terme est décrit ci-dessous.

1) Le terme F^{ghe} est l'énergie libre du gaz homogène d'électrons interagissant

$$F_i^{\text{ghe}} = G[n] = \bar{Z} f_{\text{ghe}}[n,T] = \bar{Z}[f_0(n,T) + f_{\text{xc}}(n,T)] \tag{2.106}$$

où f_0 est l'énergie libre du gaz homogène d'électrons sans-interactions et f_{xc} est l'énergie d'échange et corrélation. L'énergie f_{xc} est calculée en utilisant l'Eq.(2.60) tandis que f_0 est obtenue par la relation thermodynamique $f_0 = \Omega_0/V + \mu_0$ où Ω_0 est le grand potentiel et μ_0 est le potentiel chimique du système sans-interactions. Le potentiel chimique est obtenu en inversant la relation

$$n = \sqrt{\frac{2T^3}{\pi^4}} I_{1/2}(\mu_0/T) \tag{2.107}$$

qui permet de calculer le grand potentiel

$$\frac{\Omega_0}{V} = \sqrt{\frac{8T^5}{9\pi^4}} I_{3/2}(\mu_0/T) \tag{2.108}$$

où I_ν est la l'intégrale de Fermi-Dirac d'ordre ν

$$I_\nu(x) = \frac{1}{\Gamma(\nu+1)} \int_0^\infty \frac{t^\nu}{e^{t-x}+1}\, dt \qquad \nu > 0 \tag{2.109}$$

avec $\Gamma(x)$ la fonction gamma.

2) Le terme F^{emb} correspond à l'énergie nécessaire pour incorporer (de l'anglais "embedding") le PAN dans le gaz homogène d'électrons. Elle est définie comme la différence entre l'énergie libre du gaz d'électrons incluant et n'incluant pas le PAN

$$\begin{aligned} F_i^{\text{emb}} &= G[n + \Delta n_i^*(\mathbf{r})] - G[n] \\ &\quad - \left(\frac{Z}{\mathbf{r}} \circ [\Delta n_i^*(\mathbf{r}) + c_i(\mathbf{r})]\right) + \left(\frac{1}{2}[\Delta n_i^*(\mathbf{r}) + c_i(\mathbf{r})] \circ \frac{1}{\mathbf{r}} \star [\Delta n_i^*(\mathbf{r}) + c_i(\mathbf{r})]\right). \end{aligned} \tag{2.110}$$

3) Le terme F^{cav} est la correction pour l'introduction de la cavité artificielle

$$F_i^{\text{cav}} = \left(c(\mathbf{r}) \circ \frac{1}{\mathbf{r}} \star [-Z\delta_i(\mathbf{r}) + c_i(\mathbf{r}) + \Delta n_i^*(\mathbf{r})]\right) - \left(\frac{1}{2} c_i(\mathbf{r}) \circ \frac{1}{\mathbf{r}} \star [c_i(\mathbf{r}) - m_i(\mathbf{r})]\right). \tag{2.111}$$

4) Le terme E^{ion} est la contribution binaire entre les sites ioniques, c'est-à-dire l'interaction ion-ion pour une configuration ionique particulière

$$E_{ij}^{\text{ion}} = G_{ij} + \Big([-Z\delta_i(\mathbf{r}) + \Delta n_i^*(\mathbf{r})] \circ \frac{1}{\mathbf{r}} \star [-Z\delta_j(\mathbf{r}) + \Delta n_j^*(\mathbf{r})] \Big) - \Big(c_i(\mathbf{r}) \circ \frac{1}{\mathbf{r}} \star m_j(\mathbf{r}) \Big) \quad (2.112)$$

Puisque le terme de second ordre pour l'énergie cinétique ainsi que d'échange et corrélation G_{ij} est inconnue, il est nécessaire d'effectuer une approximation supplémentaire pour calculer l'énergie d'interaction ion-ion E^{ion}. Généralement, les électrons de cœur Δn_b sont fortement liés au noyau et il est possible de traiter le problème comme un ensemble d'ions de charge $\bar{Z}$ au lieu de traiter les nucléons de charge Z. L'astuce consiste à supposer qu'il existe un pseudo-potentiel électron-ion V_{ei} qui produit la densité d'électron libre Δn^* en réponse linéaire, c'est-à-dire

$$V_{ei}(q) = \frac{\Delta n^*(q)}{\chi(q)} \quad (2.113)$$

où χ est la fonction de réponse de l'Eq.(2.90). Cette hypothèse est valide à condition que $V_{ei}(q)/(-\bar{Z}V(q)) \leq 1$ pour toutes valeurs de q. Dans ce cas, il est possible de construire un potentiel de paires ion-ion

$$V_{ii}(q) = -\bar{Z}^2 V(q) + |V_{ei}(q)|^2 \chi(q). \quad (2.114)$$

L'énergie inter ionique pour la configuration ionique particulière $\{\mathbf{r}_1, \cdots, \mathbf{r}_N\}$ est alors obtenue

$$E^{\text{ion}} = \frac{1}{2} \sum_{i \neq j}^{N} V_{ii}(|\mathbf{r}_i - \mathbf{r}_j|) \quad (2.115)$$

en utilisant le potentiel de l'Eq.(2.114). Pour obtenir l'énergie libre totale du système F, il est nécessaire de prendre la moyenne thermodynamique sur l'ensemble des configurations ioniques possibles. Cependant, uniquement le dernier terme de l'Eq.(2.105) dépend de la structure ionique et l'on définit alors l'énergie libre ionique par atome

$$F^{\text{ion}} = F^{\text{paire}} + F^{\text{id}}. \quad (2.116)$$

Le terme $F^{\text{id}} = k_b T[\ln(\rho/\rho_Q) - 1]$ est l'énergie libre du gaz idéal avec $\rho_q = [mk_bT/2\pi\hbar^2]^{3/2}$ et où l'énergie libre du gaz ionique interagissant est donnée par

$$\beta F^{\text{paire}} = \frac{3 - 2\eta}{(1-\eta)^2} - 3 + \beta F_r[h(\mathbf{r})] - \beta F_r[h_{\text{hs}}(\mathbf{r})] + \beta F_q[h(\mathbf{q})] - F_q[h_{\text{hs}}(\mathbf{q})], \quad (2.117)$$

$$\beta F_r[h(\mathbf{r})] = -\frac{\rho}{2} \int (g(\mathbf{r})c(\mathbf{r}) - h(\mathbf{r})^2/2)\, d\mathbf{r} \quad (2.118)$$

$$\beta F_q[h(\mathbf{q})] = -\frac{1}{2\rho(2\pi)^3}\int(\ln[1+\rho h(\mathbf{q})] - \rho h[\mathbf{q}])\ d\mathbf{q}. \tag{2.119}$$

Les fonctions de corrélation $h(r)$, $c(r)$ et $g(r)$ sont déterminées par la méthode MHNC présentée dans la section (2.1.2.1) avec η le coefficient d'empilement compact déterminé par l'Eq.(2.30) et avec $h_{\rm hs}(r)$, $c_{\rm hs}(r)$ et $g_{\rm hs}(r)$ les fonctions de corrélation du système de sphères dures. Puisque la somme des trois premiers termes de l'Eq.(2.105) est identique pour chaque site i, l'énergie libre totale par atome est finalement donnée par

$$F = F^{\rm ghe} + F^{\rm emb} + F^{\rm cav} + F^{\rm ion}. \tag{2.120}$$

2.3.4. Énergie interne et pression

Lorsque l'énergie libre totale F est calculée pour une densité n et température T, il est possible de déterminer l'énergie interne par la relation

$$E = \frac{\partial(\beta F)}{\partial\beta} \tag{2.121}$$

ainsi que la pression

$$P = n^2\frac{\partial F}{\partial n}. \tag{2.122}$$

Bien qu'il soit possible d'obtenir certaines contributions de E et P analytiquement [63], il est nécessaire d'effectuer les dérivées numériquement pour le terme $F^{\rm paire}$. On a ainsi choisi d'effectuer le calcul numériquement en s'assurant que la précision numérique utilisée permettait bien de retrouver les résultats analytiques. Il est a noter que pour un système en quasi-équilibre avec $T_e \neq T_i$, il est nécessaire de modifier l'Eq.(2.121)

$$E(T_e, T_i) = \frac{\partial(\beta F)}{\partial\beta} \equiv F + \left.\frac{\partial F}{\partial\beta_e}\right|_{T_i} + \left.\frac{\partial F}{\partial\beta_i}\right|_{T_e}, \tag{2.123}$$

qui reproduit bien l'énergie interne à l'équilibre lorsque $T_e = T_i$.

Chapitre 3

ARTICLE I : PROPRIÉTÉS DE LA MATIÈRE ULTRA-RAPIDE I

Cet article a été publié à la revue *Contributions to Plasma Physics* **55**, 144 (2015).

Contexte

Ce premier article présente mes premières applications du modèle de pseudo-atome neutre à la matière dense et chaude dans le contexte particulier de la matière ultra-rapide. On y décrit la construction de potentiels de paires dépendant de la température électronique pour l'aluminium, le sodium et le potassium. Leur validité est illustrée en calculant les spectres de phonons à l'équilibre qui s'avèrent être en très bon accord avec les résultats expérimentaux et avec des calculs *ab initio*. Le durcissement des phonons, c'est-à-dire l'augmentation des fréquences de vibrations des modes propres avec la température électronique, est démontré à l'aide de nos potentiels. Cet article fait partie du *proceeding* de la conférence *Strongly Coupled Coulomb Systems* qui eut lieu à Santa Fe, Nouveau Mexique, USA en 2014.

Contributions

— Utilisation du code de "Neutral Pseudo Atom" de Chandre Dharma-wardana pour créer des potentiels de paires pour les métaux simples dans le régime de la matière dense et chaude

— Calcul des spectres de phonons à deux températures grâce aux PP ainsi qu'à l'aide de méthodes *ab initio* avec le code ABINIT.

— Vérification de l'importance de la correction locale dans la fonction de réponse pour la construction de potentiel de paires.

— Rédaction de la première version de l'article.

Two-temperature pair potentials and phonon spectra for simple metals in the warm dense matter regime

Louis Harbour[1], M. W. Chandre Dharma-wardana[2], Dennis D. Klug[2], Laurent J. Lewis[1]

[1]*Département de Physique and Regroupement Québécois sur les Matériaux de Pointe, Université de Montréal, C.P. 6128, Succursale Centre-Ville, Montréal, Québec, Canada H3C 3J7*

[2]*National Research Council of Canada, Ottawa, On., Canada K1A 0R6*

Abstract

We develop ion-ion pair potentials for Al, Na and K for densities and temperatures relevant to the warm-dense-matter (WDM) regime. Furthermore, we emphasize non-equilibrium states where the ion temperature T_i differs from the electron temperature T_e. This work focuses mainly on ultra-fast laser-metal interactions where the energy of the laser is almost exclusively transferred to the electron sub-system over femtosecond time scales. This results in a two-temperature system with $T_e > T_i$ and with the ions still at the initial room temperature $T_i = T_r$. First-principles calculations, such as density functional theory (DFT) or quantum Monte Carlo, are as yet not fully feasible for WDM conditions due to lack of finite-T features, e.g. pseudopotentials, and extensive CPU time requirements. Simpler methods are needed to study these highly complex systems. We propose to use two-temperature pair potentials $U_{ii}(r, T_i, T_e)$ constructed from linear-response theory using the non-linear electron density $n(\mathbf{r})$ obtained from finite-T DFT with a *single* ion immersed in the appropriate electron fluid. We compute equilibrium phonon spectra at T_r which are found to be in very good agreement with experiments. This gives credibility to our non-equilibrium phonon dispersion relations which are important in determining thermophysical properties, stability, energy-relaxation mechanisms and transport coefficients. **Keywords:** Warm Dense Matter, Pair Potential, Phonon, Two-temperature

3.1. Introduction

Warm dense matter (WDM) is a region of the phase diagram located at the conjuncture of the plasma state and the condensed-matter state. The density is high enough that ions are strongly correlated and can be found in a mixture of different ionization states. The ion temperature T_i can be different from the electron temperature T_e which can be as high as the Fermi temperature or even more, and hence the electrons can be partially degenerate. Such WDM states are of great interest at the fundamental level, but also for their technological applications such as laser ablation [92], inertial-confinement fusion [93], Coulomb explosion [94], etc., and are also of relevance to astrophysics [95, 96]. It is a great challenge to predict the two-temperature quasi-thermodynamic properties or transport and radiative processes of such basically non-thermodynamic states. The interest for WDM in the theoretical physics community has greatly increased since the advent of the possibility of creating these extreme conditions in the laboratory. However, the experimental techniques required for this purpose have the crucial particularity of always producing two-temperature WDM with $T_i \neq T_e$, which is problematic in the current theoretical framework. The present work focuses on the case where $T_e > T_i$, which can be observed when a femtosecond laser pulse interacts with a thin metal foil [97, 98]. Since the electron-ion mass ratio is very small, the laser energy is almost totally transferred to the electron system, thus increasing the electron temperature from the equilibrium initial temperature to T_e. Meanwhile, since the transfer of energy from the laser to the electron subsystem, as well as the equilibration of the latter, happens much faster than the electron-ion energy relaxation, the ion temperature T_i remains at room temperature T_r with the ionic-lattice structure staying intact as the ions have no time to move. Using a two-temperature model (TTM) [99, 10] to describe the electron-ion energy relaxation, it has been determined that the electron-ion relaxation time τ_{ei} is of the order of picoseconds, while τ_{ee} and τ_{ii} are orders of magnitude shorter. The challenge then is to develop theoretical tools designed for such non-equilibrium and strongly-correlated systems.

Within the framework of density functional theory (DFT) [34], the total free energy of a system of electrons and ions $F[n(\mathbf{r}),\rho(\mathbf{r})]$ can be written as a functional of the one-electron density $n(\mathbf{r})$ and the one-ion density $\rho(\mathbf{r})$. The energy minimization results in a set of two coupled equations for $n(\mathbf{r})$ and $\rho(\mathbf{r})$. The first set is the integral equations for the ion distribution $\rho(\mathbf{r})$ which obeys classical physics, and hence can be solved using the hypernetted-chain (HNC) approximation within the Ornstein-Zernike (OZ) equation if the ion-ion pair potential $U_{ii}(\mathbf{r})$ is known. The second set is the Kohn-Sham [35] equations for electrons in the external potential caused by $\rho(\mathbf{r})$. The HNC approximation, or its modified

version with bridge corrections, provides the correlation potentials for the ion subsystem which does not have exchange effects. However, a key element in the DFT-equations of the electron subsystem is the exchange and correlation (xc) free energy functional $F_{xc}[n,T_e]$ and its density derivative which is the xc-potential. Major DFT codes — e.g. ABINIT [38] — are designed for ground-state calculations using ground-state adapted pseudopotentials and do not include many finite-T features. They offer a large variety of ground state xc-functionals $E_{xc}[n]$ but do not currently implement finite-T xc-functionals. Since DFT calculations can be quite sensitive to the choice of $E_{xc}[n]$ in certain regimes, it seems very important to use a finite-T functional $F_{xc}[n,T_e]$ to adequately study WDM systems. Furthermore, in the DFT extension to finite-T by Mermin [77], it is required to include the Fermi distribution $f(E_i,T_e)$ into the finite-T electron density $n(r,T_e)$ calculation. Since T_e can be very high in the WDM regime, it requires many excited Kohn-Sham-Mermin eigenfunctions in each part of the self-consistent procedure which considerably increases the calculation time. Moreover, standard DFT simulations are designed for crystal or molecular structures, which excessively limit the range of T_i accessible to study WDM.

Higher ion temperatures can be studied using molecular dynamics (MD) simulations. MD is a powerful method to study the ion system in the liquid, gaseous or plasma phases. It has been highly parallelized to make it possible to simulate very large systems. The main input of MD simulations is the ion-ion pair potential which is required for each interaction in the system. However, most pair potentials, as implemented in comprehensive MD packages such as LAMMPS [100], are semi-empirical constructions. A particular example is the embedded-atom method (EAM) [101], fitted to reproduce particular properties under ambient conditions while failing at predicting other ones, especially those of interest in two-temperature WDM.

In the following, we propose to construct ion-ion two-temperature pair potentials (TTP) $U_{ii}(r,T_i,T_e)$ based on fundamental considerations. The first part of this paper explains how we construct the non-equilibrium electron-ion pseudopotentials $U_{ei}(r,r_s,T_{ei})$, which depend on both temperature $T_{ei} \equiv (T_e, T_i)$ and density via the electron Wigner-Seitz radius r_s. The most important quantity to compute is the free electron density $n_f(r,T_{ei})$ around an ion of effective charge $\bar{Z}$. This density is then used to construct the pseudopotential from linear-response theory, going beyond the random phase approximation (RPA) by adding a finite-T local-field correction (LFC). The second part explains how to construct the pair potential U_{ii} from U_{ei} and shows the importance of the LFC. The total ion-ion interaction is obtained by adding the direct-ion Coulomb interaction to the indirect interaction through the electron subsystem. In the last part, we compute the equilibrium and non-equilibrium phonon spectra

$\omega_\mu(k,T_{ei})$ of three simple metals to test our TTP $U_{ii}(r,T_{ei})$. We examine aluminum as well as sodium and potassium which are typical free-electron metals under the conditions studied.

3.2. Non-equilibrium electron-ion pseudopotentials

According to the original formulation of DFT by Hohenberg and Kohn [34], the electron density $n(\mathbf{r})$ rather than the many-body wavefunction is considered to be the fundamental quantity describing a quantum system so that *all* physical properties of interest can be expressed as a functional of $n(\mathbf{r})$. The self-consistent scheme proposed by Kohn and Sham [35] enables one to reduce the many-body system to an effective "one-electron" problem by putting all the missing information about the electron-electron interactions in the xc-functional $E_{xc}[n]$. However, since electrons in the WDM regime are far from zero temperature, it is crucial to use the extension of DFT to finite temperatures. Furthermore, one could wonder if using the DFT for systems with $T_i \neq T_e$ is in contravention with the fundamentals of DFT, but since calculations are done for a single fixed ion surrounded by its T_i-dependent density which is immersed in an electron liquid at T_e, the applicability of DFT is satisfied.

3.2.1. Electron density from finite-T DFT

In extending the work of Hohenberg and Kohn to finite-T, Mermin showed that the electron density defines uniquely the external potential $V(r)$ of the system [77]. The Mermin-Kohn-Sham equations reduce the finite-T many-electron problem to a one-electron problem, giving the interacting electron density $n(\mathbf{r},T_e)$.

$$n(\mathbf{r},T) = n_b(\mathbf{r}) + n_f(\mathbf{r}) = \sum_i^N f(\epsilon_i,T)|\phi_i(\mathbf{r})|^2, \qquad \text{where} \qquad f(\epsilon_i,T) = \frac{1}{1+\exp[\beta(\epsilon_i-\mu^0)]}, \tag{3.1}$$

with $n_b(\mathbf{r})$ and $n_f(\mathbf{r})$ the bound and free electron density, $f(\epsilon_i)$ the Fermi occupation function, $\mu^0(T)$ the non-interacting chemical potential, $\beta = 1/k_bT$ the inverse temperature (with $k_b = 1$ in our units), and $\phi_i(\mathbf{r})$ the Mermin-Kohn-Sham wavefunction of eigenvalue ϵ_i. At $T = 0$, μ^0 is the Fermi energy ϵ_F. As mentioned in the introduction, the presence of the Fermi occupation factors, and the need for high angular-momentum states, greatly increase the CPU time since the convergence of the energy is quadratic in the number of bands needed. One way to decrease the simulation time and make it accessible to WDM conditions is to reduce the number of electrons in the system by introducing the effective ion charge

$\bar{Z}$ which appears in the pseudopotential. However, the formulation of finite-T pseudopotentials remains largely unexplored, and standard codes simply use the zero-T ones which are inadequate for many WDM applications [102].

3.2.2. Effective charge $\bar{Z}$ and the neutral pseudoatom approximation

The main objective is to replace the nuclear charge Z by an effective charge $\bar{Z} \equiv Z - n_b$ where n_b is the number of bound electrons. This is calculated by integrating the bound electron density $n_b(\mathbf{r})$ over the ion sphere [63, 54]. The main difficulty is to determine how to split the total charge density into a bound and a free part $n(\mathbf{r}) = n_b(\mathbf{r}) + n_f(\mathbf{r})$ since bound electrons may extend beyond the Wigner-Seitz radius r_s. In this study, there is no ambiguity in the value of $\bar{Z}$ for Al, Na and K in the given density and temperature range. Using $\bar{Z}$, one may attempt to construct an electron-ion pseudopotential which reproduces the free electron wavefunctions outside a core radius r_c. However, a large number of continuum wavefunctions are needed in the WDM regime associated with finite-T problems [102], and a large number of ions have to be included in the simulation box of the usual type of DFT calculations, increasing significantly the CPU time. We simplify the problem using two key ideas from DFT. (i) Only one nucleus at the origin is considered, and spherical symmetry can be exploited; hence $\mathbf{r}$ will be replaced by r when appropriate. The charge density $n(r)$ around the central nucleus, rather than its wavefunctions are considered. (ii) Instead of including every ion at their locations $\mathbf{r}_i$ we consider only the one-ion charge distribution $\rho(\mathbf{r}) = \sum_i \delta(\mathbf{r} - \mathbf{r}_i)$. Here we follow the correlation-sphere-DFT model of Dharma-wardana and Perrot and compute the electron density around only one ion of effective charge $\bar{Z}$ surrounded by the self-consistently calculated spherically averaged ion density *distribution* $\rho(r)$[61]. Once the free electron charge density $n_f(r)$ at an ion in the given WDM environment is determined, a simple local pseudopotential can be extracted as explained in Sec. 3.2.4.

For the elements that we study in this work, it is possible to simplify the calculation of $n_f(r)$ even more by using the neutral-pseudoatom (NPA) approximation [88, 89, 90]. The NPA approach is valid for solids, liquids and plasmas at low or high densities and temperatures as long as $\bar{Z}$ can be clearly defined so that core-electrons are not important in the ion-ion interaction. Thus, the ion density is replaced by a uniform positive background (jellium) except for a spherical neutral cavity of radius $r_{\rm WS}$ (ion Wigner-Seitz radius) around the central ion. In this model, the ion temperature T_i is merely a parameter which determines the value of $r_{\rm WS}$ from the density of the material at T_i. All these simplify greatly the solution of the Kohn-Sham-Mermin equations.

3.2.3. The exchange and correlation free energy functional

To compute $n(\mathbf{r})$ around the single ion, the finite-T xc-potential given by Perrot and Dharma-wardana is used in the Kohn-Sham-Mermin equations. It has been constructed as follows. The fully non-local xc free energy per electron $f_{xc} = F_{xc}/N$ is given by the integral of the spin-dependent electron-electron correlation function $h_{ij}(\mathbf{r}) = g_{ij}(\mathbf{r})$-1 over the coupling constant λ

$$f_{xc} = \frac{n}{2}\int_0^1 \frac{d\lambda}{2\lambda}\int d\mathbf{r}\frac{\lambda}{r}[h_{\uparrow\uparrow}(\mathbf{r},\lambda) + h_{\uparrow\downarrow}(\mathbf{r},\lambda)]. \tag{3.2}$$

Using the classical-map hypernetted-chain (CHNC) [103] method, $h_{ij}(r)$ and f_{xc} have been calculated by Perrot and Dharma-wardana for different electron densities r_s and temperatures T_e. Their results appear to be in good agreement with the $T = 0$ and finite-T quantum Monte Carlo (QMC) calculations [104], thereby supporting the use of the CHNC approximation for problems where QMC data are not available. The method consists in mapping the quantum electron-fluid onto a classical Coulomb fluid using an effective electron-electron potential and an effective electron temperature to simulate quantum effects. It makes it possible to solve the OZ integral equations with the HNC approximation so as to get the finite$-T$ interacting $h_{ij}(\mathbf{r}, \lambda, r_s, T_e)$. The $f_{xc}(r_s,T_e)$ obtained this way has been parametrized to a simple form [84] which makes it very practical.

3.2.4. Electron-ion pseudopotentials from linear response theory

Once the effective charge $\bar{Z}$ and the free electron density $n_f(r)$ have been calculated for a particular r_s and T_{ei}, it is possible to construct a weak local ($s-$wave) electron-ion pseudopotential $U_{ei}(r)$ using linear response theory [105]. In q-space, it takes the form

$$U_{ei}(q,r_s,T_{ei}) = n_f(q,r_s,T_{ei})/\chi_{ee}(q,r_s,T_e), \tag{3.3}$$

with χ_{ee} the finite-T interacting electron linear response. Only the $q <\sim 3k_F$ region is relevant as the ion-core is excluded. To go beyond the RPA, we include a local-field correction G_q so that χ_{ee} is given by

$$\chi_{ee}(q,r_s,T_e) = \frac{\chi_0(q)}{1 - V_q(1 - G_q)\chi_0(q)} \quad \text{with} \quad V_q = \frac{4\pi}{q^2}, \quad G_q = \left(1 - \frac{\gamma_0}{\gamma}\right)\left(\frac{q}{k_{TF}}\right)^2. \tag{3.4}$$

Here $\chi_0(q)$ is the non-interacting finite$-T$ Lindhard function which may use an effective electron mass m^* if needed [105]. The LFC is used in the local-density approximation (LDA) and is evaluated from the ratio of the non-interacting and interacting finite$-T$ compressibilities γ_0 and γ respectively of the electron subsystem. The interacting compressibility can be

evaluated from the finite-T xc-potential. It is important to note that the NPA approach is valid if resulting pseudopotentials satisfy $U_{ei}(q)/(-\bar{Z}V_q) \leq 1$.

3.3. Two-temperature ion-ion pair potentials

3.3.1. The ion-ion pair potentials

It is now possible to construct two-temperature pair potentials by adding the direct ion-ion interaction to the indirect interaction through the electron fluid such that

$$U_{ii}(q,r_s,T_{ei}) = \bar{Z}^2(T_i)V_q + |U_{ei}(q,r_s,T_{ei})|^2\chi_{ee}(q,r_s,T_e). \tag{3.5}$$

The extension to a mixture of ions of different types or different ionizations is discussed in Ref. [64]. In the present work, we present two-temperature pair potentials resulting from this procedure for three different simple metals. We examine aluminum, which is the "standard" free electrons metal with three valence electrons ($\bar{Z} = 3$), followed by sodium and potassium, which are alkali metals with one valence electron ($\bar{Z} = 1$). Since most laser pulse-probe experiments are done at room temperature, we computed pair potentials with $T_i = T_r = 0.026$ eV whereas T_e is increased up to some value, e.g. 6 eV, that is experimentally relevant. The resulting TTP for Al, Na and K are presented in Fig. 3.1. The pseudopotentials used to construct these TTP are fitted to a Heine-Abarankov form (HA). A simple discussion of HA may be found in Shaw and Harrison [106]. The local HA pseudopotentials use a core radius r_c and a constant core-potential A for $r < r_c$, while the potential for $r > r_c$ is $\bar{Z}/r$. The equilibrium lattice parameter at room temperature a_L resulting from such potentials is usually 1-3% in error. We have slightly modified the r_c and A parameters to obtain nearly the correct a_L. This is justified since the ion positions are held fixed at their room-temperature values in the WDM studied here.

An important characteristic of these pair potentials is the presence of long-range oscillations which result from the Friedel oscillations in the electron density. These are related to the discontinuity in the Fermi distributions in WDM and zero-T systems. They are clear non-linear effects included in our model from the self-consistently calculated electron density and exist even in linear response theory which is used to construct the pseudopotentials. Since even the first minimum is basically a Friedel oscillation, it is very important to accurately calculate their amplitude. It has been shown that fitting pair potentials to elastic constants or phonon dispersion curves results in non-unique amplitudes [107]. We can see that the screening effect depends greatly on the number of valence electrons as the amplitudes of oscillations in the Na and K potentials damp much faster than in the Al case.

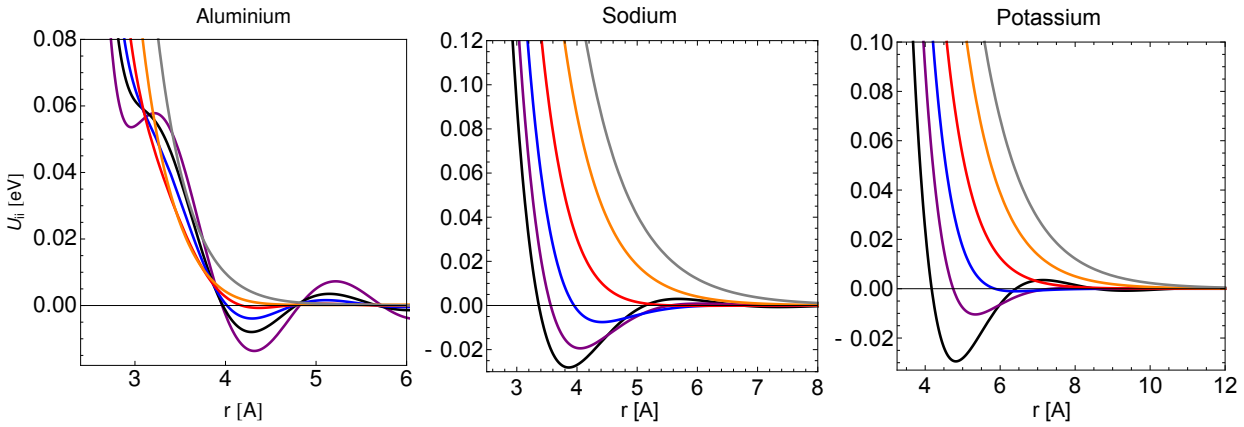

Figure 3.1. Two-temperature pair potentials for Al, Na and K. Ions are at $T_i = 0.026$ eV and the electrons at $T_e = 0.026$ eV (black), 1.25 eV (purple), 2.00 eV (blue), 3.00 eV (red), 4.50 eV (orange) and 6.00 eV (gray).

Furthermore, as T_e increases, the electron screening becomes less and less Friedel-like and the pair potentials exhibit only the repulsive behavior typical of Yukawa potentials. At such T_e, the crystal structure usually looses its stability, resulting in a Coulomb explosion or melting of the metal, depending on the heating time scales.

3.3.2. The importance of the local-field correction

To illustrate the importance of going beyond the RPA form of the screening function χ, we computed the pair potential for Al at $T_{ei} = T_r$ with and without the LFC; the results are presented in Fig.3.2.

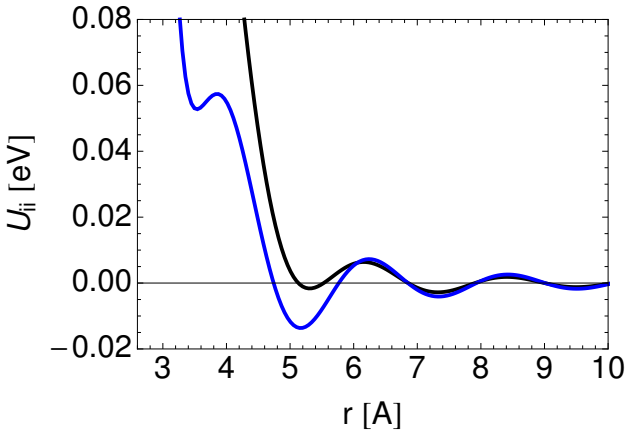

Figure 3.2. Comparison between Al pair potential at $T_{ei} = T_r$ obtained using the RPA (black line) and with the LFC included (blue line) in the screening function.

We observe a notable difference between the two pair potentials. The RPA-potential does not exhibit the first minimum shown by the LFC potential. This difference is crucial since this first minimum defines the nearest-neighbour position in the crystal; thus the RPA does not give a realistic description of solid Al.

3.4. Phonon spectrum of laser-heated simple metals

Using the TTP, it is possible to compute the phonon energies by constructing the dynamical matrix [65]:

$$\mathbf{D}(\mathbf{q}) = \sum_i \mathbf{D}(\mathbf{r}_i) e^{-i\mathbf{k}\cdot\mathbf{r}_i} \qquad \text{with} \qquad \mathbf{D}(\mathbf{r_i}) = \left. \frac{\partial^2 U_{ii}(\mathbf{r}_i - \mathbf{0})}{\partial \mathbf{u}(\mathbf{r}_i)\, \partial \mathbf{u}(\mathbf{0})} \right|_{\mathbf{u}=0} . \tag{3.6}$$

Here $\mathbf{u}$ is the small displacement in the position of ions at $\mathbf{r}_i$ and at the origin $\mathbf{0}$. Phonon frequencies are then given by $\omega_\mu(\mathbf{q}) = \sqrt{\lambda_\mu(\mathbf{q})/M}$, with $\lambda_\mu(\mathbf{q})$ the eigenvalues of the dynamical matrix. Using pair potentials, it is extremely rapid to compute the phonon dispersions for any crystal structure. To validate our simple model, we compare it with a more fundamental linear-response method using the ABINIT package [38]. The latter is, strictly speaking, only applicable to systems in equilibrium, with $T_i = T_e$. Determining phonon spectra in DFT is usually done using the response function [39, 108] method where the first derivative of every wavefunction is computed. This requires even more CPU time. Typically, while the ABINIT phonon calculation for aluminum may take many hours on a computer cluster, the pair potential approach is nearly 'instantaneous' on a laptop.

The ions in the ultra-fast laser-heated solid are not at their equilibrium positions but frozen in their 'old' positions. The phonon description assumes that the elementary excitations are oscillations of the ions about their equilibrium positions, with the first derivative of the potential, i.e., the force, equal to zero. This is increasingly invalid as T_e exceeds T_i. However, this 'harmonic approximation' is assumed in both the ABINIT and the pair-potential phonon calculation given here. In reality, the first derivative (i.e., the Hellman-Feynman force on each ion) is large and will lead to an explosive acceleration of the ions outwards rather than generating harmonic oscillations. A consideration of the time scale for one oscillation, and the time scale for the motion of an ion by about a wavelength, suggest that only the higher frequency modes can have a physical meaning. Nevertheless, we present the full phonon spectra in order to compare with similar efforts of other workers (using *ab initio* codes) who have provisionally assumed the existence of these non-equilibrium phonons. Besides the first-derivative being negligible, the second derivative of the total potential, being the elastic constant for the harmonic motion, must be positive at the ion positions. The

higher derivatives give anharmonic effects. Thus, at sufficiently high T_e, the phonon frequencies become purely imaginary, as the pair-potential becomes more like a Yukawa potential. It is extremely important to experimentally determine 'phonon spectra' of WDM systems to establish the scope and validity of the phonon description of the elementary excitations of these two-temperature solids.

3.4.1. Aluminum

At room temperature, aluminum exhibits a FCC crystal structure with an experimentally determined lattice parameter $a_{\rm Al} = 4.05$Å which is used as an input (via the density) into our TTP construction. On the other hand, our *ab initio* simulations are done using the LDA with the norm-conserving pseudopotential method. We used a 165 eV kinetic energy cutoff and a $20 \times 20 \times 20$ Monkhorst-Pack **k**-point grid to compute the planewave expansion of the pseudowavefunctions. The ground-state calculation gives us an equilibrium lattice parameter $a_{\rm Al}^{\rm DFT} = 4.01$Å and phonon frequencies, at $T_{ei} = T_r = 0.026$ eV, in very good agreement with our TTP model and with experiment [31], as presented in Fig. 3. We computed the phonon spectra for the laser-heated situation where ions are kept 'frozen' at their initial equilibrium position, and with $T_i = T_r$, whereas the electron temperature is increased up to $T_e = 6$ eV. The non-equilibrium phonon spectra obtained with our TTP model and with ABINIT-DFT, by simulating more electronic band and using the Fermi-Dirac occupation function to mimic finite-T effects , are also displayed in Fig. 3.

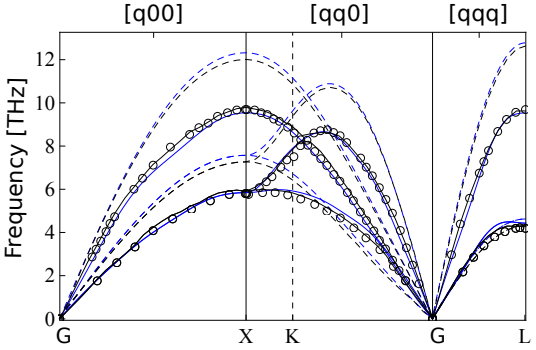

Figure 3.3. Equilibrium (full lines) and non-equilibrium (dashed lines) aluminum phonon dispersion relations computed with the TTP model (blue) and ABINIT (black), compared with experimental data (circles).

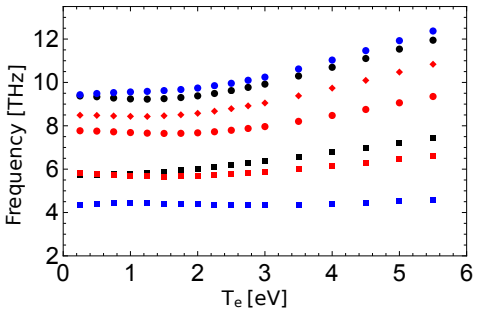

Figure 3.4. Phonon frequencies of laser-heated aluminum at $T_i = T_r \neq T_e$ for longitudinal (circles) and transverse (squares and diamonds) modes at symmetry points X (black), L (blue) and K (red).

As T_e increases, we find that both methods show phonon hardening. The TTP model predicts a maximum frequency increase of 29% at the symmetry point X passing from 9.54 THz to 12.32 THz for the longitudinal mode. As mentioned by Recoules *et al* [29], the transverse mode frequency at the symmetry point L is not really affected, passing from 4.43 THz to 4.62 THz. Nevertheless, our results clearly illustrate that all other branches are also modified by the laser-heating mechanism. At room temperature, the TTP model predicts frequencies lower than DFT calculations whereas at $T_e = 6$ eV they are higher. As T_e increase, finite$-T$ effects become more and more important; further studies are needed to understand if this difference comes from the finite$-T$ features which are absent in the ABINIT-DFT simulations. The fast computation of TTP by this method permits us to compute phonons for many different T_e as presented in Fig.4. The ability to calculate phonon spectra 'on the fly' can be of great utility in determining electron-ion energy relaxation and non-equilibrium transport properties such as the thermal and electrical conductivity.

3.4.2. Sodium and potassium

Sodium and potassium are alkali metals having a BCC crystal structure at room temperature with experimentally determined lattice parameters of $a_{\mathrm{Na}} = 4.23$Å and $a_{\mathrm{K}} = 5.23$Å, respectively, which will be used as input in the TTP construction. The ABINIT-DFT simulations have been done within the generalized-gradient approximation (GGA), a $24 \times 24 \times 24$ Monkhorst-Pack **k**-point grid and a 1360 eV kinetic energy cutoff for both Na and K. Ground state calculations result in lattice parameter $a_{\mathrm{Na}}^{\mathrm{DFT}} = 4.20$Å and $a_{\mathrm{K}}^{\mathrm{DFT}} = 5.25$Å, respectively, and yield phonon frequencies in agreement with our TTP model and with experiment [32, 33] as presented at Fig.5.

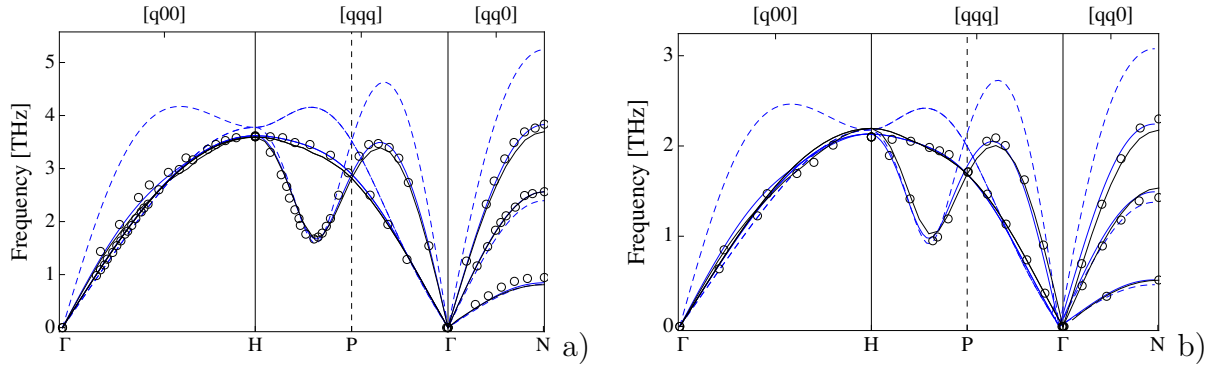

Figure 3.5. Equilibrium $T_e = T_i = T_r$ (full lines) and non-equilibrium $T_e = 6$ eV (dashed lines) phonon dispersions for **a**) sodium and **b**) potassium computed with the TTP model (blue) and ABINIT (black), compared with experiment (circles).

Once again, our TTP results are in excellent accord with experiment for the equilibrium case which gives us confidence in applying the method to the non-equilibrium situation. In the case of Na and K, we observe that most frequencies increase but also that the shape of the dispersion relation changes as T_e reaches 6 eV. We can see new maxima appearing between symmetry points $\Gamma - H$ and between $H - P$. In both cases, the maximum increase occurs at the point N with an augmentation for the frequency of the longitudinal branch of 37%. Finite$-T$ *ab initio* simulations for these metals are still not completed. Hence the comparison of the predictions of our TTP model with more fundamental calculations is not yet final for this case.

3.5. Conclusion

As WDM studies are becoming more and more topical and important in many fields of physics, we have addressed the problem of describing theoretically such highly-correlated systems via a simple model based on transparent physics. Furthermore, to compare predictions with experiment, it is necessary to describe non-equilibrium systems where $T_i \neq T_e$. Since *ab initio* simulations can be very time consuming in this regime, we have developed simple two-temperature pair potentials as the 'work-horse' of the method. They are constructed from fundamental considerations by computing the electron density from finite-T DFT and then using linear response theory with a finite-T local-field correction. Pair potentials resulting from this procedure produce long-range interactions resulting from the presence of Friedel oscillations in the electron density. These TTP were used to compute phonon dispersion relations for equilibrium Al, Na and K. The excellent accord with experiment and DFT simulations (using the ABINIT code) establishes support for the validity of our approach for the non-equilibrium case. In all cases, our model predicts an increase of the frequencies, which is different for each mode branch, supporting the phonon hardening hypothesis. At higher T_e, where thermal effects are more important, frequencies obtained for Al with the TTP model are found to be higher than the ones obtained by DFT simulations. This discrepancy might come from the non-implementation of a finite-T exchange and correlation energy functional and the lack of other finite-T features in *ab initio* codes like the ABINIT. To validate this hypothesis, further work will be done to implement our finite$-T$ xc-functional in a major DFT code. The possibility to quickly compute TTP for many different combinations of T_i and T_e could also be used to predict electron-ion energy relaxation and non-equilibrium transport properties. Another important application of our TTP is to incorporate it in laser ablation simulations where pair potentials dependent on both temperatures are needed. Finally, construction of two-temperature potentials for more complex metals, such as gold and

copper, would be of great interest since many WDM experiments [30] have been carried out with these metals.

Acknowledgments

This work has been supported by grants from the Canadian Natural Sciences and Engineering Research Council (NSERC) and the Fonds de Recherche Québec - Nature et Technologies (FQRNT). We are indebted to Calcul Québec for generous allocations of computer resources.

Chapitre 4

ARTICLE II : PROPRIÉTÉS DE LA MATIÈRE ULTRA-RAPIDE II

Cet article a été publié dans la revue *Physical Review E* **95**, 043201 (2017).

Contexte

Ce deuxième article est la suite de notre étude sur les propriétés de la matière ultra-rapide. Le durcissement des phonons prédit par le modèle de pseudo-atome neutre est validé par des simulations *ab initio* qui prédisent une augmentation des fréquences en très bon accord avec les prédictions du modèle. Puisque la matière ultra-rapide est fortement hors d'équilibre, on s'est questionné sur la stabilité d'un tel système lorsqu'une énorme pression interne est induite par l'augmentation de la température électronique. De plus, dans ce régime, le concept même de phonons s'avère discutable et la validité de cette interprétation est étudié en détail. On s'est aussi interrogé sur l'importance d'utiliser une fonctionnelle d'échange et corrélation dépendante de la température pour ces conditions particulières. Finalement, on s'est intéressé à comprendre la différence entre la matière dense et chaude à l'équilibre avec la matière ultra-rapide en calculant leurs équations d'état.

Contributions

— Calcul des spectres de phonon à deux températures pour l'aluminium, le lithium et le sodium grâce au code NPA ainsi qu'au code ABINIT.

— Calcul de la pression en fonction de la température électronique et du paramètre de maille du cristal pour le régime de la matière ultra-rapide ainsi qu'à l'équilibre.

— Démonstration que le concept de phonon n'a plus de sens physique en comparant le temps d'ablation de la surface des métaux avec le temps d'une oscillation du phonon le plus rapide.

— Évaluation de l'importance des corrections à température finie dans la fonctionnelle d'échange et corrélation pour le calcul de la pression.

— Rédaction de la première version de l'article.

Equation of state, phonons, and lattice stability of ultra-fast warm dense matter

Louis Harbour[1], M. W. Chandre Dharma-wardana[2], Dennis D. Klug[2], Laurent J. Lewis[1]

[1]*Département de Physique and Regroupement Québécois sur les Matériaux de Pointe, Université de Montréal, C.P. 6128, Succursale Centre-Ville, Montréal, Québec, Canada H3C 3J7*

[2]*National Research Council of Canada, Ottawa, On., Canada K1A 0R6*

Abstract

Using the two-temperature model for ultrafast matter (UFM), we compare the equation of state, pair-distribution functions $g(r)$, and phonons using the neutral pseudoatom (NPA) model with results from density-functional theory (DFT) codes and molecular-dynamics (MD) simulations for Al, Li and Na. The NPA approach uses state-dependent first-principles pseudopotentials from an 'all-electron' DFT calculation with finite-T XCF. It provides pair potentials, structure factors, the 'bound' and 'free' states, as well as a mean ionization $\bar{Z}$ unambiguously. These are not easily accessible *via* DFT+MD calculations which become prohibitive for T/T_F exceeding $\sim$ 0.6, where T_F is the Fermi temperature. Hence, both DFT+MD and NPA methods can be compared up to $\sim$ 8 eV, while higher T can be addressed *via* the NPA. The high-T_e phonon calculations raise the question of UFM lattice stability and surface ablation in thin UFM samples. The ablation forces in a UFM slab are used to define an "ablation time" competing with phonon formation times in thin UFM samples. Excellent agreement for all properties is found between NPA and standard DFT codes, even for Li where a strongly non-local pseudopotential is used in DFT codes. The need to use pseudopotentials appropriate to the ionization state $\bar{Z}$ is emphasized. The effect of finite-T exchange-correlation functional is illustrated via its effect on the pressure and the electron-density distribution at a nucleus.

Keywords: Phonon, Equation of state, Warm Dense Matter

4.1. Introduction

The equation of state (EOS) of common thermodynamic phases of matter is well understood. However, recent laser and shock-wave experiments have accessed novel ultrafast regimes of density and temperature which are of great theoretical and technological interest. The same physics appears during the injection of hot carriers in field-effect transistors and other nanostructures. Topics like inertial-confinement fusion [93], Coulomb explosions [94], space re-entry shielding, laser machining and ablation [92] involve such regimes of warm dense matter (WDM). However, elementary approaches cannot be applied since the Coulomb coupling constant Γ, i.e., the ratio of the Coulomb energy to the kinetic energy, is larger than unity. The electrons may range from degenerate to Boltzmann-like, with $T/E_F \sim 1$ or larger, where T is electron temperature in energy units, while E_F is the Fermi energy. This causes a prohibitive increase in basis sets that span the many excited electronic states. WDMs pose a theoretical challenge for rapid accurate computations of properties like pressure, heat capacity, phonons and conductance needed even for equilibrium WDMs.

A class of WDMs known as ultra-fast matter (UFM) is produce when energy is deposited using an ultrafast pulsed laser on a metal surface [12]. The light couples strongly to the mobile electrons which equilibrate on femtosecond timescales, to a temperature T_e (as high as many eV) while the much heavier ions and their strongly-bound core electrons remain essentially at their initial temperature T_i, i.e., usually the room temperature T_r. This two-temperature WDM ($2T$-WDM) phase with $T_e > T_i$ remains valid for timescales t such that $\tau_{ee} < \tau_{ii} < t < \tau_{ei}$, where τ_{ee}, τ_{ii} and τ_{ei} are the electron-electron, ion-ion and electron-ion temperature relaxation times, respectively. It has been shown for near-solid densities that τ_{ei} is of the order of picoseconds, and orders of magnitude longer than τ_{ee} and τ_{ii} [99, 10]. For WDMs with $\theta = T/E_F$ small, similar relaxation times hold as seen in calculations for typical systems [109]. Experiments using femtosecond pump-probe techniques [95, 96] provide data for quasi-equilibrium analogues of free energy and pressure, transport and relaxation processes. While many UFM samples do not conform to the $2T$ model (e.g., as in Medvadev *et al.* [110]), the $2T$ model provides a great simplification when it holds. Even for UFMs, theory and experiment are quite challenging as the system transits rapidly from a solid to a plasma depending on the pump energy. Hence a theoretical model that encompasses a wide range of material conditions is needed to describe the time evolving system as a series of static $2T$ systems. The 'quasi-equilibrium' theory is applied to each static picture of the time evolving system.

In this work, we use the neutral pseudoatom (NPA) model, in the form given by Perrot and Dharma-wardana [88, 89, 63, 64, 111, 54], to study the $2T$-WDM regime of a few nominally *simple metals*, *viz.*, aluminum, lithium and sodium. These are "simple" at ambient conditions since their valence electrons are "free-electron like" and energetically separated from the core electrons. The number $\bar{Z}$ of valence electrons per atom (mean ionization) for Al, Li, and Na is 3, 1, and 1, respectively. Furthermore, if the matter density is ρ, each ion can be assigned a spherical volume with the Wigner-Seitz (WS) radius $r_{ws} = (3/4\pi\rho)^{1/3}$, and it can be shown for Al, Li, Na that the bound-electron core has a radius r_c such that it is well inside the WS sphere for the temperatures studied here (see Sec. 4.2.1). In such cases, the definition of $\bar{Z} = N - n_b$, where n_b is the number of bound electrons in the core, is unambiguous, clear and is a physically measurable quantity, e.g., using X-ray Thomson scattering [2]. In the case of equilibrium WDM, the NPA-calculated $\bar{Z}$ for Al and Li remains 3 and 1 in the range $0 < T_e < 8$ eV whereas in the case of sodium, $\bar{Z}$ rises to 1.494 by T=8 eV and 1.786 by 10 eV. The case of Na provides us an example of a typical variation of $\bar{Z}$ very common in equilibrium WDM systems and handled without any ambiguity and with thermodynamic consistency by the NPA approach coupled with determinations of the ion-ion $g(r)$ using the NPA pair-potentials. However, in the case of UFM which is the scope of this work, $\bar{Z}$ is kept unchanged for all three elements through the $0 < T_e < 8$ eV temperature range.

The NPA model replaces the interacting *many-nuclear* and *many-electron* problem by an effective non-interacting *single-nuclear* and *single-electron* formulation where the many-body problem is reduced using finite-T density functional theory (DFT) [34, 35]. The NPA charge densities are used to construct $2T$ pseudopotentials and effective ion-ion pair potentials. The method takes into account particle correlations at the pair-density level and beyond using density-functional methods via exchange-correlation functionals for electrons, and ion-correlation functionals for ions in a decoupled step which uses a classical integral equation or molecular dynamics. The NPA framework is well adapted to treating metallic systems ranging from solids to liquids or plasmas at very high or low compressions, and from T=0 to several keV. The importance and relevance of the NPA lies in its accuracy, flexibility, and computational rapidity compared to DFT coupled to molecular dynamics (MD) methods (DFT+MD). However, the NPA, as used here, is inapplicable when inner-shell electrons (e.g., d-electrons) play a role in the ion-ion interactions (e.g., as in transition metals). A simple metal becomes 'complex' when its electronic bound states extends beyond its WS radius r_{ws}. This is not a short-coming but a strength of the model which signals the need for multi-ion contributions into the theory in such ranges of temperature and pressure. In such

regimes, discontinuities in $\bar{Z}$ where some are spurious may appear unless suitable electron-ion XC-correlation potentials are included in the theory [112]. Furthermore *transient* molecule formation can be successfully handled [113] within the NPA as it allows for binary ion-ion correlations.

We compare our $2T$-NPA predictions with those from solid-state DFT electronic-structure codes such as ABINIT [38] and VASP [40], which use MD to evolve the finite-T ionic structures. These codes are primarily designed for $T_i = T_e = 0$ situations, and solve the *multi-nuclear* Kohn-Sham equations in a plane-wave basis, using $T = 0$ pseudopotentials to reduce the number of electrons needed in the simulations. The solid, liquid or plasma is treated as a *periodic solid* in a simulation box ("supercell") containing N nuclei, with N being $\sim$100. A finite T_e Fermi-Dirac distribution for electron occupation numbers is used, along with $T = 0$ pseudopotentials and $T = 0$ exchange-correlation functionals (XCF). The number of electronic bands required to access high T_e increases rapidly with T_e and becomes prohibitive for T_e/E_F greater than ~ 1. This method generates energy bands for the periodic solid where as in reality there are *no such band structure* in liquids and plasmas. This artifact is overcome by generating electronic-structure calculations for many static ionic configurations via MD simulations and averaging over a large number of them.

DFT+MD provides only a "mean ionization" for the whole N-ion supercell; it cannot provide, e.g., the composition of an equilibrium mixture of specific charge states of ions in a C, H "plastic" at, say, 1 eV. Furthermore, VASP and ABINIT currently only implement the zero-T XCF even though finite-T parametrizations have been available for some time, e.g., the evaluation of finite-T bubble diagrams [80, 81], from the work of Iyetomi and Ichimaru [82], Perrot and Dharma-wardana (PDW) [84] and from Feynman-path methods by Brown *et al* [104] parametrized recently by Karasiev *et al* [114]. The present NPA calculations are done with the PDW finite-T XCF which is in close agreement with the quantum simulations of Brown *et al.* [115]. In most cases finite-T XC effects contribute only small corrections and DFT+MD provides valuable benchmarks for testing other methods.

The NPA method is summarized in section 4.2 where we emphasize its application to the $2T$ regime. Resulting $2T$ pair potentials ($2T$PP), quasi-equilibrium phonon dispersions and pair distribution functions (PDF) $g(r)$ are presented in Sec. 4.3. The phonon calculations confirm the results and also validate the meV accuracy of the NPA method. The NPA $g(r)$ calculations for normal and compressed Li ($\sim$ up to a compression of 2) show that the *local* pseudopotential for Li is successful. Here we compare the ion-ion structure factor $S(k)$ with the simulations of Kietzmann *et al.* Having confirmed the accuracy of the pseudopotentials and pair potentials, the $2T$-thermodynamic properties, such as the quasi-pressure, are also

presented. These are compared with the values for systems in thermal equilibrium. Discussions about phonon formation times in $2T$ systems, the role of finite-T XC-contributions in the $2T$-EOS calculation, and the choice of suitable pseudopotentials in *ab initio* finite-T simulations are also presented.

4.2. The neutral pseudoatom model.

4.2.1. General description of the model

Several average-atom models and NPA models have been proposed, even in the early literature [87]. Many of these are intuitive cell models and are not true DFT models. A rigorous DFT formulation of a NPA model at $T = 0$ was first used for solids by Dagens [88, 89]. There the treatment of the ion distribution was developed in the traditional manner as providing a fixed external potential; Dagens showed that the NPA results at $T = 0$ agree closely with the band-structure codes available at the time. A finite-T version was given in several papers by Perrot [63] and Dharma-wardana [61, 62, 105]. In Ref. [61], the ion distribution $\rho(r)$ itself was treated within DFT using the property that the free energy $F[n,\rho]$ is a functional of *both* $n(r)$ and $\rho(r)$ simultaneously. A classical DFT equation for the ions and an ion-correlation functional, $F_c^{ii}(\rho)$, approximated as a sum of hypernetted-chain (HNC) diagrams plus bridge diagrams, was introduced, *without* invoking a Born-Oppenheimer approximation or treating the ions as providing a fixed external potential [116]. Exchange-correlation functionals $F_{xc}^{ei}(\rho)$ for electron-ion interactions were also introduced although neglibible in common materials. This puts the NPA approach on a very rigorous DFT footing where approximations enter in modeling the ion-correlation functional, just as in the case of the electron DFT problem for the electronic XCF.

However, in the following we present the theory in terms of the more familiar superposition picture. We consider a system of ions located at sites $\mathbf{R}_i$ at temperature T_i and average density ρ, interacting with a system of electrons at temperature T_e and average density n. The *multi-center* problem is reduced to a simplified *single-center* problem where the total electron density $n(r)$ is regarded as the superposition of single-site densities such that $n(r) = \sum_i n_i(r - \mathbf{R}_i)$. In contrast to ion-sphere (IS) models like those used in Purgatorio [51], or Piron and Blenski [50], Starrett and Saumon [55], the single-site free-electron density $n_f(r)$ extends over the whole of space, approximated by a correlation sphere [61] of radius R_c which is of the order of 10 ionic Wigner-Seitz radii. All particle correlations are assumed to have died out when $r \to R_c$. This R_c is similar to the linear dimension of the simulation box of a DFT+MD simulation which has to be as big as possible. However,

in practice the charge distribution used in DFT+MD simulations spreads over a volume of about 100 ions. In contrast, the NPA correlation sphere with $R_c \simeq 10r_{ws}$ extends over $\{R_c/r_{ws}\}^3$, i.e., the volume covered by ∼1000 ions. The calculation of course uses only one nucleus, but its charge density overlaps the space of some 1000 atoms, and this is crucial to getting the right pair-potentials with long-range Friedel oscillations, and to satisfy the Friedel sum rule [61]. The IS-models cannot satisfy the Friedel sum rule. At higher temperatures where particle correlations are weak, r_c may be reduced to, e.g., $5r_{ws}$, but the results are independent of R_c, and R_c is *not* an optimization parameter.

The ion distribution $\rho(r) = \rho g_{ii}(r)$ contains the full ion-ion PDF, $g(r)$, when seen from any site taken as the origin. It is found that in most cases it is sufficient, as far as the bound-electron structure is concerned, to approximate $g(r)$ by a spherical cavity $c(r)$ of radius r_{ws} and total charge $\bar{Z}$ centered on the ion, followed by a uniform positive density ρ for $r > r_{ws}$. As mentioned below, unlike in IS-models, its effect will be subtracted out (as a "cavity correction") to obtain the response of a uniform electron gas to the nucleus. Thus have:

$$c(r) = n[H(0) - H(r - r_{ws})], \tag{4.1}$$

where $H(r)$ is the Heaviside step function. Initially $\bar{Z}$ is unknown but its value is obtained self-consistently from the iterative Kohn-Sham procedure. The single-site electron density is written as $n_i = \Delta n_i + m_i$ where m_i is the cavity correction and Δn_i is the electron pile-up obtained by the DFT calculation for the electrons in the external potential $V_{\rm ext}$ given by

$$V_{\rm ext}(r) = -\frac{Z}{r} + \frac{1}{|\mathbf{r} - \mathbf{r}'|} \star c(\mathbf{r}') \tag{4.2}$$

where the symbol $\star$ means integration over all space. Here $Z = Z_n$ is the nuclear charge. The positive background with the WS-cavity, the nucleus at its center and the free-electron charge density filling the whole correlation sphere constitute the neutral pseudoatom [62]. The WDM system is made up of superpositions of such neutral-pseudo atoms correlated to give the ion-ion $g(r)$, with the cavity contributions subtracted out.

For simple metallic systems, this cavity model that defines the extent of the bound states is sufficient to produce physically accurate results and is mathematically convenient, as shown in the papers by Dagens or those of Perrot and Dharma-wardana cited above. Thus, to compute the cavity correction $m(r)$, we assume that the electrons respond linearly to the cavity $c(r)$, *viz.*, in Fourier space,

$$m(q) = -V(q)c(q)\chi_{ee}(q, n, T_e). \tag{4.3}$$

Here, $V(q) = 4\pi/q^2$ is the Coulomb potential and χ_{ee} is the interacting-electron response function at the electron density n and temperature T_e. To go beyond the random phase approximation (RPA), we use the following finite-T response function:

$$\chi_{ee}(q, n, T_e) = \frac{\chi_0(q,n,T_e)}{1 - V(q)[1 - G(q)]\chi_0(q,n,T_e)}, \tag{4.4}$$

with χ_0 the finite-T Lindhard function and $G(q) = G(q,T_e)$ a local-field correction (LFC) defined as:

$$G(q) = \left(1 - \frac{\gamma_0}{\gamma}\right)\left(\frac{q}{k_{\rm TF}},\right)^2. \tag{4.5}$$

In the above, the Thomas-Fermi wave vector $k_{\rm TF} = \sqrt{6\pi n/E_F}$, is defined by the Fermi energy of the system $E_F = 1/(\alpha r_s)$ where r_s is the electron WS radius and $\alpha = (4/9\pi)^{1/3}$. The finite-T interacting electron compressibility $1/\gamma = n^2\partial^2[nf(r_s,T_e)]/\partial n^2$ is determined from the homogenous electron gas free energy per electron $f(r_s,T_e)$, as given in Eq.4.13, which include a finite-T XC contribution f_{xc}. The non-interacting electron compressibility γ_0 is obtained by setting $f_{xc} = 0$.

The simplicity of the NPA model rests on decomposing the total charge distribution into a superposition of single-center distributions. If the ion-ion structure factor $S_{ii}(q)$ is known, any total electron charge distribution $n_t(q)$ can always be written as a convolution of the $S_{ii}(q)$ with some effective single-center charge distribution $n(q)$, even for transition metals or systems with resonant levels; but partitioning the electron contributions from states that extend beyond their WS cells without correctly including the physical interactions is not sufficient. Furthermore, a 'simple metal' at one temperature may behave as a 'transition-metal' at another temperature when a shell of electrons begins to transit to the continuum, and *vice versa*. If the system is of such low density that r_{ws} is larger than the bond length of a possible dimer (e.g., Li_2), then the dimer itself will be contained within the WS sphere, and in such cases the NPA model fails; a more elaborate "neutral-pseudomolecule" approach or the use of suitable electron-ion XC-potentials $F^{ei}_{xc}(n,\rho)$ is then needed. We do not examine such non-simple WDMs in this study. Similarly, at high densities, WDM-Li shows complex phases containing persistent Li_4 clusters [117], and the simple NPA model needs modifications. In the present case, a single-center decomposition is physically transparent if the bound electron core is unambiguously confined within the WS sphere of the ion. We discuss in the results section (sec. 4.2.1) the variation of the $\bar{Z}$ of Na which changes from unity at low T to 1.49 by $T = 8$ eV. The occupation number in the $2p$ level begins to decrease, while its radius slightly decreases, and hence there is no ambiguity in estimating $\bar{Z} = Z - n_b$ where n_b are all the bound electrons compactly contained well inside the WS-sphere. That is, the electron

density pileup Δn_i can be clearly divided into bound and free parts such that $\Delta n_i = n_b + n_f$. Once this division is achieved the interaction of an electron with the nucleus plus its core can in most cases be replaced by a pseudopotential U_{ei} which is a weak scatterer because it is constructed using linear response; this is given by:

$$U_{ei}(q) = n_f(q)/\chi_{ee}(q,r_s,T_e), \tag{4.6}$$

where χ_{ee} is provided by Eq. 4.4.

Even though linear response is used, the resulting pseudopotential includes non-linear effects since $n_f(q)$ is the fully non-linear free-electron density obtained from DFT. Only a range of q between zero to slightly above $2k_F$ (depending on T_e) needs to be included as the large-q behavior (short-range in r, i.e., inside the core) is not relevant. The resulting pseudopotential is valid only if it satisfies the relation $U_{ei}/(-\bar{Z}V(q)) \leq 1$. Unlike the pseudopotentials used in VASP, ABINIT and similar DFT codes, this linear-response pseudopotential does not require solving a Schrödinger equation. It is a state-dependent *local* pseudopotential that can be fitted to, say a Heine-Abarankov form for convenience (see Shaw and Harrison [118]). This has a constant core potential $V_{\rm HA} = D$ for $r < r_c$ and it is Coulomb-like, $V_{\rm HA} = -\bar{Z}/r$ for $r > r_c$. However, such a fitting is not needed except to conveniently report the pseudopotential and to quantify the core radius associated with the potential. In our NPA calculations we use the numerical form of $U_{ei}(q)$ directly.

The pseudopotential calculated at T_i can be used to form a $2T$ ion-ion pair potential ($2T$PP) with ions at T_i and electrons at T_e, since it is a sum of the direct Coulomb interaction and the indirect interaction via the displaced-electron charge, *viz.*

$$U_{ii}(q,T_i,T_e) = -\bar{Z}^2(T_i)V(q) + |U_{ei}(q)|^2\chi_{ee}(q,T_e). \tag{4.7}$$

This procedure is valid because $\bar{Z}$ remains unchanged in UFM since the bound core of electrons remains at the initial ion temperature for times $t < \tau_{ei}$. If T_e is large enough to change $\bar{Z}$, be it for UFM or equilibrium systems, then the pseudopotential has to be re-calculated using an NPA calculation at the needed temperature.

At low T_e, the Friedel oscillations in the electron density resulting from the sharp discontinuity at $k = 2k_F$ in $\chi_{ee}(q)$ produce oscillations in the pair potential $U_{ii}(r)$. These lead to multiple minima in the ion-ion energy which contribute to the maxima in $g(r)$. Such physically important features are not found in "Slater-sum" approaches [119] to finite-T potentials, in 'Yukawa-screening' models [65, 120, 109], or in Gordon-Kim models [121]. Furthermore, the charge densities restricted to the WS-sphere used in IS-models cannot capture such long-range effects. Our NPA pair potential can be used to study phonons in the system or to

generate the ion-ion $g_{ii}(r)$ and corresponding structure factor $S_{ii}(k)$ when necessary. The ion subsystem in a UFM is clamped at $T_i \sim 300$K when Al, Li, and Na are crystalline metals. Hence the ion-ion pair distribution function is simply given by the relation

$$g_{ii}(\mathbf{r}) = \frac{1}{4\pi\rho} \sum_{\{i\}} \delta(\mathbf{r} - \mathbf{R}_i). \tag{4.8}$$

The summation is over the crystal lattice, permitting a simple computation of the ion contribution to the quasi free energy and pressure from the $2T$ pair potential.

4.2.2. The NPA quasi thermodynamic relations

The total free energy F of the $2T$ system given by the NPA is

$$F = F_{\text{emb}} + F_{\text{cav}} + F_{\text{heg}} + F_{\text{ion}}, \tag{4.9}$$

where F_{heg}, F_{emb}, F_{cav}, and F_{ion} are respectively the free energy contribution of the interacting homogeneous electron gas (HEG), the embedding free-energy of the NPA into the electron gas, the correction from the cavity, and the ion-ion free energy. The only parameters of this model are the nuclear charge Z, electron temperature T_e and the HEG density n such that the average ion density $\rho = n/\bar{Z}$, itself determined by the ion temperature T_i. We discuss these four terms below, using Hartrees with $\hbar = m_e = |e| = 1$.

(i) The embedding energy F_{emb} is the difference between the free energy of the electron gas containing the central ion and the unperturbed HEG; thus

$$\begin{aligned} F_{\text{emb}} &= T[n + \Delta n(r)] - T[n] - \int \frac{\bar{Z}}{|\mathbf{r}|} \cdot [\Delta n(\mathbf{r}) + c(\mathbf{r}))] d\mathbf{r} \\ &+ \frac{1}{2} \int \frac{[\Delta n(\mathbf{r}) + c(\mathbf{r})]}{|\mathbf{r} - \mathbf{r}'|} \cdot [\Delta n(\mathbf{r}') + c(\mathbf{r}')] d\mathbf{r} d\mathbf{r}', \end{aligned} \tag{4.10}$$

with $T[n]$ is the electron kinetic energy.

(ii) The cavity correction F_{cav} is computed from the total screened Coulomb potential $V(r)$ resulting from the total electron displacement $\Delta n(r)$:

$$V_i^*(\mathbf{r}) = \int \frac{[c(\mathbf{r}') + \Delta n(\mathbf{r}') - \bar{Z}\delta(\mathbf{r}' - R_i)]}{|\mathbf{r} - \mathbf{r}'|} d\mathbf{r}'. \tag{4.11}$$

Since each cavity involves a charge deficit $\eta(r) = n - c(r)$, the cavity correction is

$$F_{\text{cav}} = -\frac{1}{2} \int \frac{\eta(\mathbf{r}) \cdot [c(\mathbf{r}') - m(\mathbf{r}')]}{|\mathbf{r} - \mathbf{r}'|} d\mathbf{r} d\mathbf{r}' + \int \eta(\mathbf{r}) \cdot V^*(\mathbf{r}) d\mathbf{r}. \tag{4.12}$$

(iii) The free energy of the HEG $F_{\rm heg}$ is written as

$$F_{\rm heg} = \bar{Z} f(n,T_e) = \bar{Z}[f_0(n,T_e) + f_{xc}(n,T_e)], \tag{4.13}$$

where f_0 and f_{xc} are respectively the non-interacting and exchange-correlation free energies per electron at the density n and temperature T_e. To compute f_0, we use the thermodynamic relation $f_0 = \Omega_0/nV + \mu_0$, where Ω_0 and μ_0 are the non-interacting grand potential and the chemical potential, respectively.

We emphasize that the NPA-Correlation-sphere model uses the non-interacting μ_0 associated with the mean electron density n as required by DFT theory. In IS models the known matter density defines the Wigner-Seitz cell, and the free electrons are confined in it, and the corresponding μ is determined by an integration within the WS-sphere (e.g., see Eq. 1 of Faussurier [122]), leading to a value of $\mu \neq \mu_0$. In contrast, the mean electron density n, the nuclear charge Z_n and the temperature T are the only inputs to the NPA code. The computation outputs the corresponding mean ion density ρ and $\bar{Z} = n/\rho$. A series of calculations are done in a range of n and the specific n which gives the physical ion density, viz., ρ is selected. For a given electron density n and temperature T_e, the non-interacting chemical potential μ_0 is obtained by satisfying the relation

$$n = (\sqrt{2}/\pi^2) T_e^{3/2}\ I_{1/2}(\mu_0/T_e), \tag{4.14}$$

while, using this μ_0, the non-interacting part of the grand potential is given by

$$\Omega_0/V = (2\sqrt{2}/3\pi^2) T_e^{5/2}\ I_{3/2}(\mu_0/T_e), \tag{4.15}$$

with $I_\nu(z)$ the Fermi-Dirac integral of order ν. Note that only the non-interacting chemical potential, viz., μ_0 appears in the DFT-level occupations of the NPA model since DFT theory maps the interacting electrons to a system of non-interacting electrons at the *interacting density* (see also Ref. [61]).

The XC contribution f_{xc} is computed directly from the PDW parametrization at the given r_s and T_e. The total free energy per electron of the interacting HEG is the sum of f_0 and f_{xc}.

(iv) The ion-ion interaction energy is given explicitly by the pairwise summation over the pair potential U_{ii} as defined at Eq.(4.7):

$$F_{\rm ion} = \frac{1}{V}\frac{1}{2}\sum_{\{i\neq j\}} U_{ii}(|\mathbf{R}_i - \mathbf{R}_j|), \tag{4.16}$$

where the sum is over the positions of the ions in their initial crystal configuration. This is the only term in F that depends explicitly on the ion structure.

Both the cavity correction and the embedding energy involve the ion with its bound core of electrons held at the temperature T_i, while the electrons are at T_e. The numerical results are insensitive to using a simple NPA calculation with even the core at T_e, if the the bound-state occupancies (and thus $\bar{Z}$) remain virtually unchanged.

The quasi-equilibrium pressure of the system is obtained by the appropriate density derivative of the ion-structure independent free energy terms while the structure-dependent ion-ion contribution is given by the viral equation

$$P = n^2 \frac{\partial}{\partial n}(F_{\rm heg} + F_{\rm emb} + F_{\rm cav}) - \int g_{ii}(\mathbf{r}) \left(\frac{3}{r}\frac{\partial}{\partial r} - n^2 \frac{\partial}{\partial n} \right) U_{ii}(\mathbf{r}) d\mathbf{r}. \tag{4.17}$$

The explicit electron-density dependence of the ion-ion pair potential is taken into account in computing the pressure [66]. Analytical results can be obtained for the terms

$$P_{\rm emb} = -\int \eta(\mathbf{r}) \cdot V^*(\mathbf{r}) d\mathbf{r} \tag{4.18}$$

$$P_{\rm cav} = -\bar{Z} V^*(r_{ws}) \tag{4.19}$$

whereas other derivatives have to be done numerically.

4.3. Results

We used the NPA model to determine the properties of $2T$-WDM as produced by femtosecond laser pulses interacting with three common metals in their usual solid state, viz., aluminum, lithium and sodium, with electron densities such that r_s is 2.07, 3.25, and 3.93 a.u., corresponding to $\bar{Z} = 3$, 1 and 1, respectively. Note that the $\bar{Z}$ for Na deviates from unity for $T > 3$ eV. The ion density is kept constant in the calculations for isochoric sodium. We present the $2T$ ion-ion pair-potentials, non-equilibrium phonon dispersion curves and pressures for varying T_e, while the ions remain cold at T_i =0.026 eV (300K).

4.3.1. Ion-ion pair potentials

The first step within our UFM model is to compute the equilibrium (at room temperature, $T_e = T_i = 0.026$ eV) free-electron density $n_f(q)$ from the NPA calculation. The pseudopotential $U_{ei}(q)$ at $T_e = T_i$ can then be obtained using Eq. 4.6. This pseudopotential is an atomic property that depends on $\bar{Z}$ and on the core radius given the ionic r_{ws}, which is then used to construct ion-ion pair potentials $U_{ii}(q,T_e)$ at any T_e via Eq. (4.7). For this the electron response at $T_e \neq T_i$ is used. This method is simpler and numerically almost indistinguishable from calculating the pseduopotential from a full $2T$-NPA procedure where the core electrons are held frozen at T_i and $n_f(q,T_e)$ is calculated from the Kohn-Sham equation,

with $\bar{Z}$ remaining unchanged. The agreement between the two different ways of calculating the $2T$ potentials provides a strong check on our calculations. Furthermore, while pair potentials cannot be easily extracted from *ab initio* calculations, the NPA model provide this physically important quantity.

Examples of NPA ion-ion pair potentials at different temperatures are presented in Fig. 4.1. At equilibrium or sufficiently low T_e, all three pair potentials display Friedel oscillations as discussed in section 4.2. Hence it requires many neighbor shells to compute the total pairwise ion-ion interaction energy with sufficient precision. For Li and Na, we used 8 shells whereas 30 shells were necessary for the Al-Al interaction. As T_e increases, the sharp Fermi surface breaks down, the discontinuity in $f(k)$ at $k = k_F$ broadens, and oscillations disappear, yielding purely repulsive Yukawa-screened potentials [65, 120].

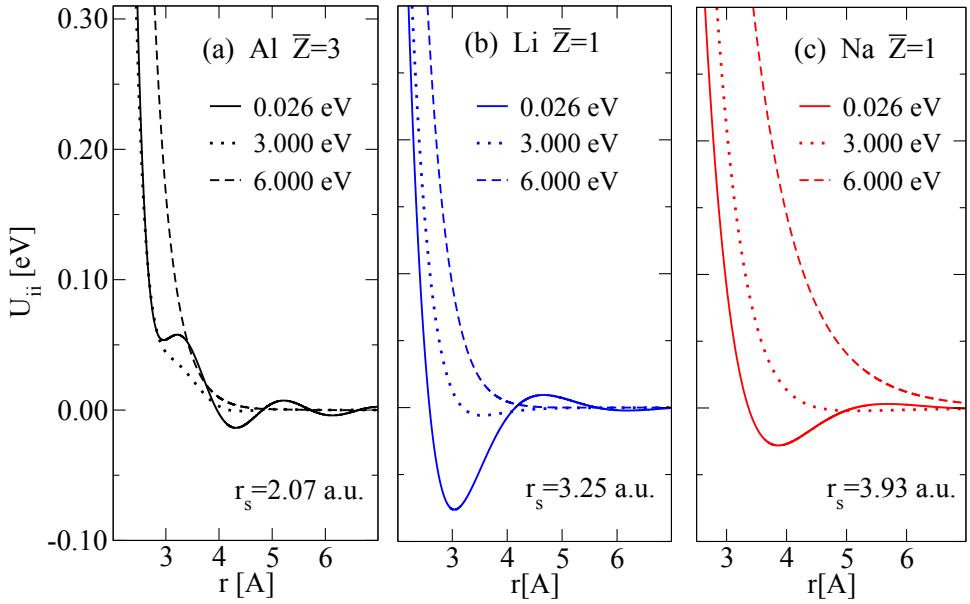

Figure 4.1. Two-temperature ion-ion pair potentials for electrons at three different temperatures and ions at $T_i = 0.026$ eV (300 K), for (a) Al, (b) Li, and (c) Na.

4.3.2. $2T$ quasi-equilibrium phonon spectra

As the electrons get heated, the screening weakens and inter-ionic forces become stronger; hence there is an interest in computing the phonon spectra although in many cases the phonon oscillation times may be comparable to the lifetime of the UFM system. Once the 2TPP is constructed for the desired T_e, the phonon spectra are easily calculated by the

diagonalization of the dynamical matrix [45]

$$\mathbf{D}(\mathbf{k}) = \sum_i \mathbf{D}(\mathbf{R}_i) e^{-i\mathbf{k}\cdot\mathbf{R}_i} \tag{4.20}$$

where the elements of the harmonic matrix $\mathbf{D}(\mathbf{R})$ are given by

$$D_{\mu\nu}(\mathbf{R}) = \frac{1}{2} \sum_j \frac{\partial^2 U_{ii}(\mathbf{R}_j)}{\partial u_\mu(\mathbf{R}) \partial u_\nu(\mathbf{0})} \tag{4.21}$$

with $\mathbf{R}_j$ the position of the jth atom and U_{ii} the pair-potential of Eq.4.7. From the s eigenvalues $\lambda_s(\mathbf{k})$ of $\mathbf{D}(\mathbf{k})$, the phonon frequencies are given by $\omega_s(\mathbf{k}) = \sqrt{\lambda_s(\mathbf{k})/M}$ with M the mass of the ion. The resulting phonons are compared with the results from ABINIT-DFT simulations employing density-functional perturbation theory [39, 108] (DFPT), which determines the second derivative of the energy using the first-order perturbation wavefunctions. We used the common crystal structure for each metal, i.e., face-centered cubic (FCC) for Al and body-centered cubic (BCC) for Li and Na, with their room temperature lattice parameters $a = 4.05$ Å, 3.49 Å, and 4.23 Å, respectively.

Quasi-equilibrium phonon dispersion relations at $T_e = 6$ eV using the two methods are presented in Fig. 4.2 with the NPA equilibrium phonons as reference to illustrate important modifications in the spectra. In addition, NPA quasi-equilibrium phonon spectrum at $T_e =$ 12 eV are also presented by which temperature DFPT becomes prohibitive. The excellent accord between the NPA and experimental equilibrium phonon spectra at low temperatures has already been demonstrated and shows the meV accuracy of the NPA calculations even at low temperatures [123]. This regime can be hard to model as noted by Blenski *et al.* [124] when, for example, working on Al at normal density and at low T within another model.

For the three systems in this study, the two methods (NPA and DFPT) predict very similar $2T$ phonon spectra, thus reconfirming the $2T$ NPA calculations and corroborating the DFPT calculations at finite T. This is important as there are as yet no experimental observations of UFM phonon spectra. In the case of Al, we observe a large increase in frequencies, as high as 32% for longitudinal (L) modes, which supports the "phonon hardening" theory. However, we notice that transverse (T) branches in the $\Gamma - L$ region are barely affected by the electron heating, as was also noted by Recoules [29]. In the case of Li and Na, we find that the spectral modifications are more complex than the 'homogeneous' increase found for Al; here, an important increase in the L-branch in the middle of the $\Gamma - H$ region takes place, whereas there is no change at the symmetry point H. No modifications to T-branches are noticed in this region. In the region $H - \Gamma$, the L-branch frequencies increase in the middle of the region $H - P$ but remain unchanged at the symmetry point H. For the T-branch,

an increase is noticeable at the maximum in the region $P-\Gamma$ whereas no change affects the minimum in the region $H-P$. In the region $\Gamma-N$ and for the L-branch, we observe the overall largest increase of 29% and 37% for Li and Na, respectively, whereas frequencies of T-modes are only slightly modified.

4.3.3. $2T$-quasi-equilibrium equation of state

A system in its initial equilibrium configuration ($T_i = T_e = T_r$) rapidly reaches a new UFM state with T_i remaining near T_r while T_e increases. However, since the ion motion within the time of arrival of the probe pulse is negligible, the pressure builds up essentially isochorically due to electron heating.

In Fig 4.3, we compare the pressure calculated with the NPA model with ABINIT and VASP simulations. In the latter, we used an energy cut-off of 1630 eV for the plane-wave basis, with 60 energy bands to capture finite-T effects. In ABINIT simulations, we used norm-conserving (NC) pseudopotentials with the $T = 0$ Perdew-Burke-Ernzerhof (PBE) XCF within the generalized gradient approximation (GGA). In VASP, we employed projected-augmented-wave (PAW) pseudopotentials with the PBE XCF for Li and Na, and the Perdew-Wang (PW) $T = 0$ XCF for Al. With both codes, pseudopotentials were chosen specifically to simulate $\bar{Z}$=3 valence electrons for Al, and $\bar{Z}$=1 for Li and Na as the core electrons remain bound, and at the ion temperature. This is an important aspect discussed in subsection 4.2.1.

We find that, for all three metals, calculations using NPA, ABINIT and VASP predict nearly identical pressures with small deviations only at high T_e. At $T_e = 8$ eV, the maximum difference between all model is 9 GPa, 4 GPa and 3 GPa for Al, Li, and Na, respectively. Thus, the results from the extension of the NPA model to the $2T$ regime confirms the usability of the solid-state codes at least up to 6 eV on the one hand, and on the the other hand the validity of the NPA approach. However, since NPA uses a finite-T XC-functional whereas *ab initio* simulations do not, the effect of such finite-T corrections will be reviewed in section 4.4.

The computational efficiency and accuracy of the NPA approach make it a valuable tool for studying WDM and other complex systems where iterative computations of materials properties like $2T$ EOS, $2T$ specific heat, transport properties, opacities, energy-relaxation times, etc., are needed as the system evolves with time, since mean ionization, pair-potentials and structure factors are readily obtained. A few minutes on a desktop computer is sufficient in NPA calculations to generate accurate results which require long and intensive computations with DFT+MD.

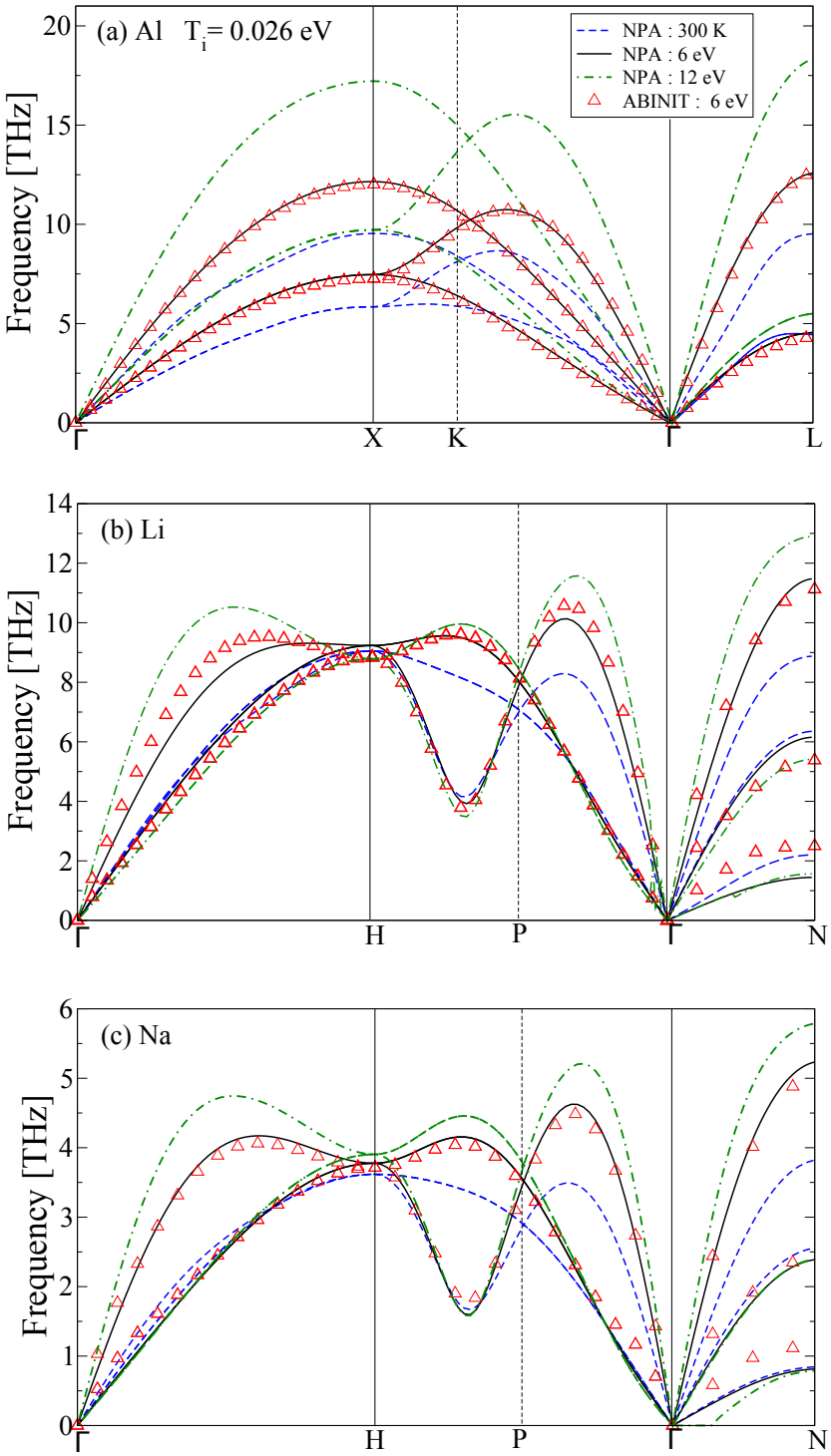

Figure 4.2. Quasi-equilibrium phonon spectra at $T_e = 6$ eV obtained with NPA and with ABINIT for (a) Al, (b) Li, and (c) Na. The NPA equilibrium phonon spectra at 300 K are shown to illustrate the effect of increasing T_e (dashed lines).

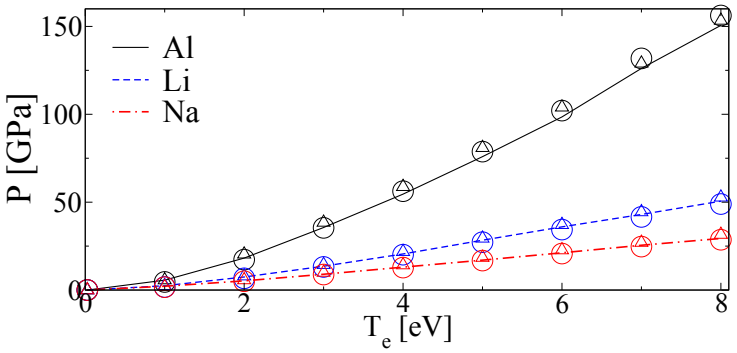

Figure 4.3. Quasi-equilibrium pressures obtained with the NPA (lines), ABINIT (circles), and VASP (triangles) for Al, Li, and Na.

4.4. Discussion

4.4.1. Crystal-lattice stability

As electrons absorb the laser energy (within fs timescales) and heat up to T_e, the internal pressure of the system becomes very high as discussed in section III-C. In metals, the thermal expansion is also caused by the free-electron pressure. We studied the crystal stability of the solids as a function of lattice expansion; the results are presented in Fig. 4.4.

For Al at $T_e = 2$ eV, we find that a moderate expansion $a/a_0 = 1.24$ is sufficient to reduce the pressure back to zero, indicating that the crystal may appear stable if the timescale needed for such lattice motion is available before the UFM breaks down. However, in all other cases, the pressure goes to zero only asymptotically with increasing lattice parameter, suggesting that such UFM crystals are unstable. Such thermal expansions or spontaneous fluctuations lead to the 'explosive' breakdown of the solid on ps timescales. However, since UFM conditions are reached in fs timescales, the ions remain essentially in their initial positions and (as already noted) no net linear forces act upon them due to crystal symmetry. They remain trapped in a stronger harmonic potential leading to hardening of most of the phonon branches. The physical reason for the hardening at increased T_e is the decreased screening of ion-ion interactions by the hotter electron gas.

4.4.2. "Phonons" and surface ablation

The UFM system is under very large pressure and the ion-ion $2T$PP is purely repulsive unless T_e is small (cf. Fig. 4.1). The discussion in terms of phonons may become inapplicable at higher T_e due to non-zero ablation forces acting on ions in typical UFM samples (0.1-1μm thick). An ideal periodic lattice implies that the linear derivative of the total potential is

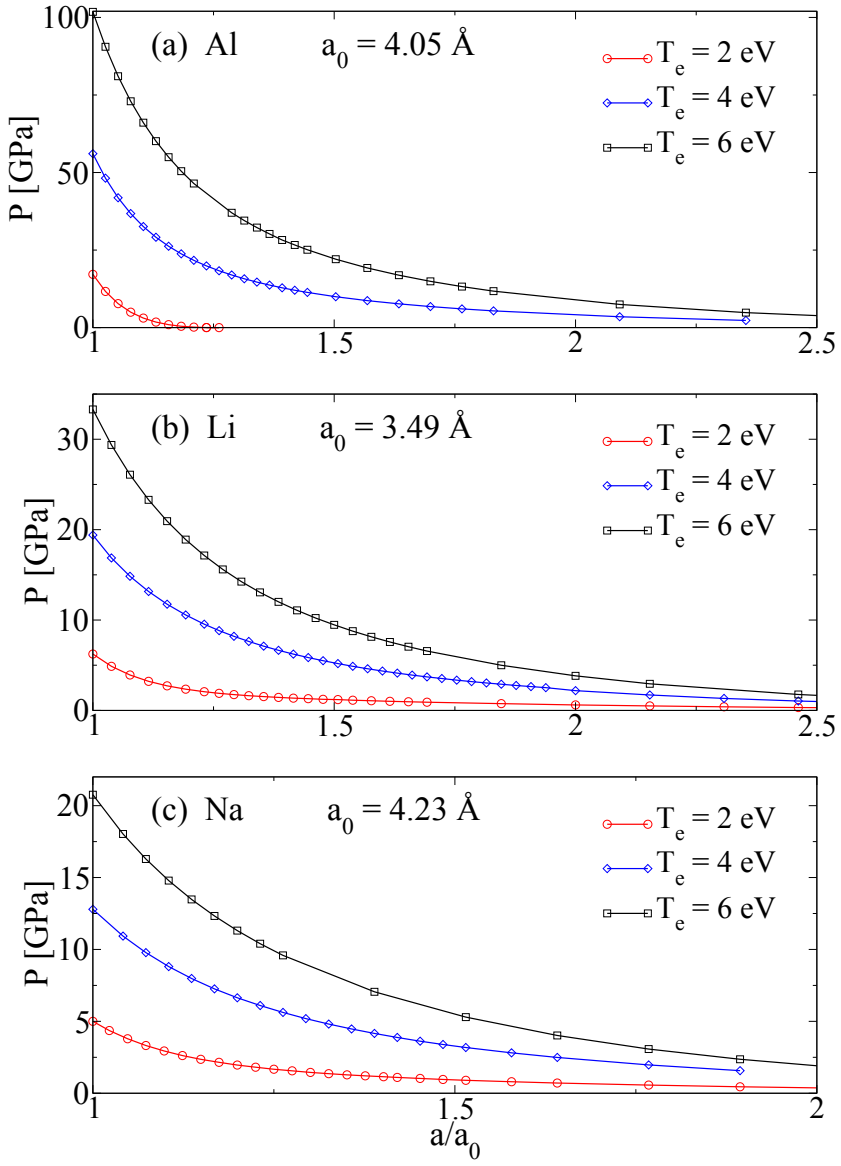

Figure 4.4. Total pressure of the solids as a function of the lattice parameter of the crystal relative to the room-temperature value a_0 for (a) Al, (b) Li, and (c) Na.

zero because the crystal is isochorically constrained by the external pressure. The phonons of UFM "exist" only within this artifice. Small thermal 'Debye-Waller' type ionic displacements u (with a mean value $\langle u \rangle = 0.2$Å at 300K for Al, retained in the UFM) do not render the periodic UFM unstable, and slightly split the degeneracy of transverse branches.

However, pump-probe experiments use very thin metal films. Crystal symmetry is broken and large uncompensated forces act at the surface of the films; as a result, the surface layer

and successive layers ablate. We calculated the ablation force $F_{\rm abl}^{\rm VASP}$ on an FCC-(100) Al surface and the two inner layers using the VASP code with the Al surface reconstructed as happens for the cold surface at 0K. Five layers of Al and 5 layers of vacuum were used for evaluating the Hellman-Feynman forces on the surface atoms. The NPA method is beyond its regime of validity since the charge density at a surface is not uniform. However, the NPA pressure is the force per unit area at the bounding (100) surface, with one ion per unit area. This is used as the NPA estimate of the ablation force $F_{\rm abl}^{\rm NPA}$. The forces on the inner neighbor and next-neighbor layers calculated from VASP at T_e =6 eV were 3% and 0.02% respectively of the force on the surface layer. The surface force $F_{\rm abl}$ determines an approximate "ablation time" $\tau_{\rm abl}$, the time needed for the surface plane to move by an inter-plane distance ($a/2$ in the case of Al). This $\tau_{\rm abl}$ estimate makes some assumptions, e.g., $F_{\rm abl}$ to be constant over $a/2$, with no movement of inner layers. To verify if phonons can form within such timescales, we compare $\tau_{\rm abl}$ with the shortest time for an ion oscillation τ_ω at the highest phonon frequency for the [100] direction; the results are presented in Table 4. I.

Table 4. I. The "ablation force" $F_{\rm abl}$ and the "ablation time" $\tau_{\rm abl}$ for the (100) surface of an Al slab from VASP and NPA at three different electron temperatures T_e and lattice temperature $T_i = 0.026$ eV. The fastest [100] phonon oscillation time τ_ω is also given for each T_e.

T_e	$F_{\rm abl}^{\rm NPA}$	$F_{\rm abl}^{\rm VASP}$	$\tau_{\rm abl}^{\rm NPA}$	$\tau_{\rm abl}^{\rm VASP}$	τ_ω
eV	eV/Å	eV/Å	fs	fs	fs
2.00	0.91	0.90	111	111	105
4.00	2.75	2.70	63.9	64.2	92.6
6.00	5.03	4.70	47.1	48.6	80.6

As T_e increases, phonons "harden" and $F_{\rm abl}$ increases. In order to observe the "hardening" of phonons on any measurement, a probe time $\tau_{\rm pr}$ such that $\tau_\omega < \tau_{\rm pr} < \tau_{\rm abl}$ is required. However, for sufficiently high T_e (e.g., above $\sim$ 2 eV for Al), the $F_{\rm abl}$ are strong enough to make $\tau_{\rm abl} < \tau_\omega$. Hence the ion oscillations have no time to build up and it is probably impossible to satisfy the time constraint enabling the observation of hardened phonons. The phonon concept itself becomes misleading for thin UFM films. Interpreting experiments when $\tau_{\rm pr} > \tau_{\rm abl}$ may require explicit inclusion of surface ablation corrections in the theory used for analyzing optical data (e.g., in the Helmholtz equations).

4.4.3. Finite-T exchange and correlation

In the NPA model, we used the finite-T XCF of PDW and assessed the importance of such corrections in the temperature regime studied here. The valence density, or "free"-electron density $n_f(r)$ of the solid at $T_e > T_i$ is the key quantity for the NPA model. In Fig. 4.5, we present the $n_f(r)$ obtained using the PDW finite-T XCF with that obtained from the zero-T XCF. Even though the correction is small, it may be of importance in some circumstances, e.g., x-ray Thomson scattering spectra, and hence there is no reason to neglect it. The difference between the $T = 0$ XCF and the finite-T XCF increases with $\theta = T/E_F$ at first, and it rapidly and asymptotically goes to zero as $\theta > 1$ and as $T \to \infty$. Hence the more important consequences of using finite-T XCF should occur in the partially degenerate regime $0 < \theta < 1$.

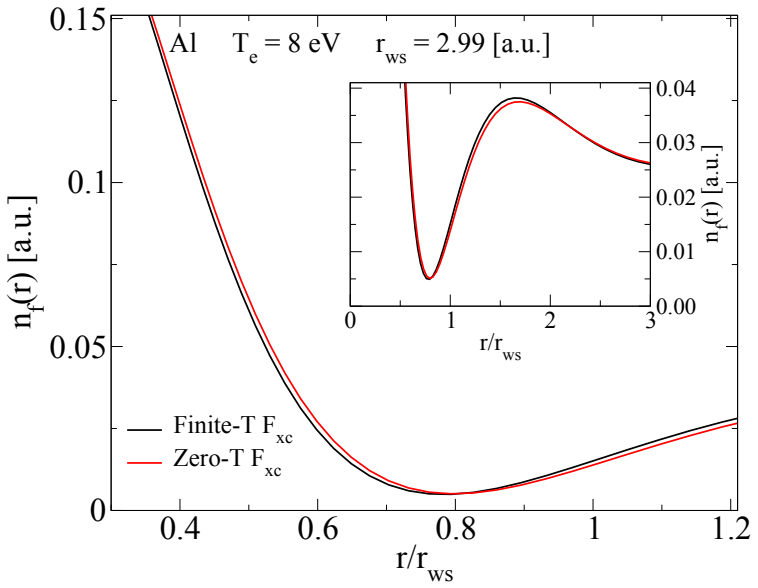

Figure 4.5. The NPA free-electron density $n_f(r)$ for Al^{3+} at density $\rho = 2.7$ g/cm^3, with $T_e = 8$ eV and $T_i = 0.026$ eV, calculated using XC at finite-T and at $T = 0$. The inset shows the density for larger $r/r_{\rm ws}$.

The finite-T XCF is present in two contributions to the pressure, namely the electron-electron interacting linear response function $\chi(k,T_e)$, which is used to construct the pseudopotential and the pair potential, and the HEG electron kinetic pressure. Although the finite-T XCF has noticeable effects on the pair potentials or on the energy spectrum of bound states, we observe that overall thermodynamic effects are only slightly sensitive to such finite-T corrections as can be seen in Fig. 4.6. In fact, at $T_e = 8$ eV, the finite$-T$ XCF

only decreases the pressure in Al by 4%. Since individual finite-T contributions are considerable, this insensitivity to XCF comes from the interplay of several terms. For instance, the electron pressure by itself differs by about 10% in the regime $\theta \sim 0.8$, but the overall pressures obtained from $T = 0$ and finite-T NPA calculations differ by less than 4%.

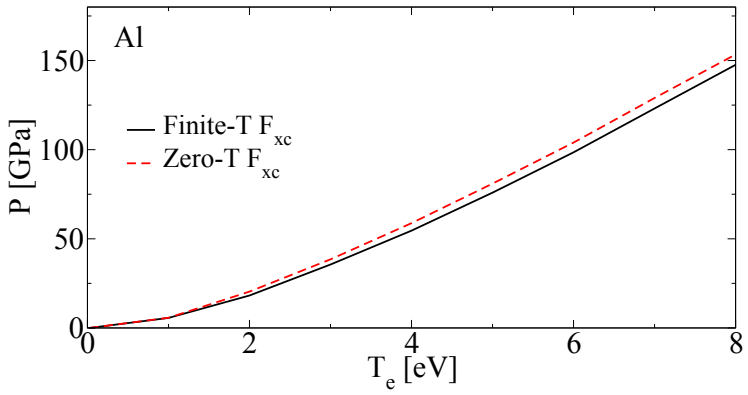

Figure 4.6. Comparison between the pressure of Al in the UFM regime computed via the NPA model with the finite-T F_{xc} and with the zero-T F_{xc}.

4.4.4. Pseudopotential and mean ionization

Here, we discuss the importance of choosing the proper pseudopotential for *ab initio* simulations of UFM systems in the $2T$ model. The pump-laser frequency is normally chosen such that core electrons are not excited and remain strongly bound to the 'cold' nuclei at temperature T_i. Thus, only the $\bar{Z}$ valence electrons on each ion are heated to T_e during the irradiation. In DFT calculations, the electron temperature is used in a Fermi-Dirac distribution for the occupation numbers of all electrons in the simulation. Thus, if the chosen pseudopotential includes more electrons than the typical number of valence electrons, these core electrons will also be "heated" even if they should not in order to simulate correctly UFM systems. Wrong predictions may result, e.g., for the 2T pressure of the given UFM and its electronic specific heat.

To illustrate this point, we carried out ABINIT simulations using PAW pseudopotentials which include $\bar{Z}$=3 and 9 valence electrons for Li and Na, respectively. We also did NPA-DFT calculations with *all* electrons at T_e. In the NPA model, the mean ionization $\bar{Z} = Z_n - n_b$ can be computed as in Ref. [62]. The $\bar{Z}$ as a function of T_e is not an integer in the NPA but represents an average over different ionization states as discussed in Ref. [64].

In the case of Al and Li, the NPA predicts that $\bar{Z}$ is unaffected for $T_e < 8$ eV, relevant to UFMs. Pressure should also be unchanged, which is exactly what we obtain with the

Table 4. II. Mean ionization $\bar{Z}$, the $2p$ Fermi factor, and the $2p$ mean radius (a.u) for sodium (normal solid density) are given as a function of the temperature T in eV. The WS radius r_{ws}=3.3912 a.u. and hence the core is compactly contained inside the WS sphere of Na for all values of T investigated here.

T	$\bar{Z}$	f_{2p}	$< r_{2p} >$
1.00	1.001	1.000	0.808
3.00	1.004	0.999	0.804
5.00	1.104	0.983	0.792
8.00	1.494	0.919	0.762
10.0	1.786	0.872	0.744

ABINIT simulations of Li using the all-electron PAW pseudopotential. However, in the case of Na, $\bar{Z}$ starts to increase around $T_e = 3$ eV up to $\bar{Z} = 1.49$ at $T_e = 8$ eV (see Table. 4. II). The increase in $\bar{Z}$ is accompanied by a decrease in the occupation of the $2p$ level as electrons are promoted to the continuum. The decreased screening in the core (both due to increase of T and due to the decrease in the number of core electrons) leads to a *decrease* in the radius of the n=2 shell. Hence, the increase of $\bar{Z}$ and the modification of the core levels do not lead to any ambiguity in specifying $\bar{Z}$.

We computed the pressure with the NPA model including the changed $\bar{Z}$ and compared it with the ABINIT simulations of Na using the nine-electron PAW pseudopotential. Results are presented in Fig. 4.7. We find that, at $T_e = 8$ eV, the pressure, when heating of some core electrons is included, is 54% higher than the correctly calculated value. The use of 'all-electron' codes for the study of UFM in the $2T$ state suffers from this pitfall of not

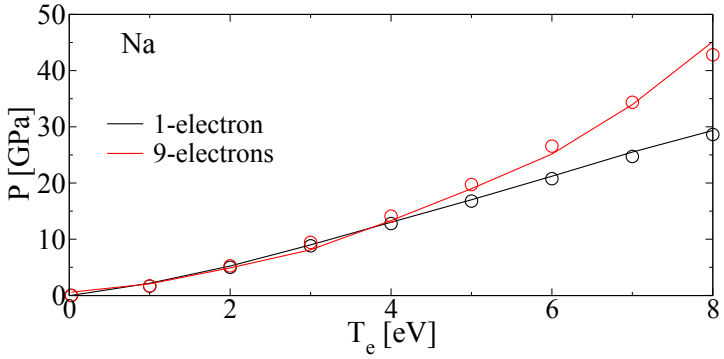

Figure 4.7. Comparison between the pressure computed with the NPA (line) and with ABINIT (circles) when heating is applied to the valence electron of Na only or to all electrons (9 electrons in the ABINIT simulations).

selecting the physically appropriate $\bar{Z}$ and the corresponding pseudopotential. When suitable pseudopotentials are not available for DFT+MD calculations, one possibility is to use only the relevant part of the electron density of states (DOS) that is assigned to the free electrons on the basis of $\bar{Z}$, when pressure and related properties are computed. For instance, when calculating the specific heat of 'free electrons' for use in UFM studies, the 'free-electron' DOS used in the calculations should be consistent with the number of actual free electrons that couple with the laser. In a metal like gold (not studied here), even though a pseudopotential with 11 valence electrons is needed, the DOS used for evaluating the electron specific heat for $T_e < 2$ should be only for $\bar{Z} = 1$. The optical properties of gold (see ref. [125]) show that the d-shell couples to light only when the interband threshold energy ($\sim$ 2 eV) is exceeded. In the case of gold, the $5d$ shell hybridizes with the continuum electrons (nominally made up of $6s$ electrons) and extends outside the Au-Wigner-Seitz sphere until the $s - d$ transition threshold ($\sim$2 eV) is reached. Hence, at low temperatures the NPA model with its 'one-center' formulation cannot be used for gold at normal density. Similarly, WDM systems with bound states extending outside the Wigner-Seitz sphere cannot be treated unless explicit multi-center electron-ion correlation terms are included.

4.4.5. Local pseudopotential for Li

The Li pseudopotential used in the NPA is a *local* pseudopotential, whereas it is widely found in the context of large DFT codes that Li almost always needs a non-local pseudopotential. Even in early studies of phonons, a nonlocal pseudopotential was used by Dagens, Rasolt, and Taylor [126], and yet the Li phonons at room temperature they obtained were less satisfactory than for, say, sodium. We have already shown that the NPA pair potential based on a local pseudopotential quite adequately reproduces the Li phonons at room temperature and high temperature at normal density, but not as accurately as for aluminum or sodium. Hence it is of interest to test the robustness of the Li pseudopotential and pair potential at higher compression by calculating the Li-Li $g(r)$ using the NPA potentials. Here we use the MHNC method where a bridge term is included using the Lado-Foiles-Ashcroft (LFA) criterion [127] which is based on the Gibbs-Bogoliubov inequality for the free energy of the system. The MHNC assumes radial symmetry and lim- its us to "simple-liquid" structures.

Since Li becomes a complex liquid with clustering effects at high compressions [117], we consider a compression of $\sim$ 1.6 and compute the PDF for Li at 0.85 g/cm^2 and at 2000K (0.173 eV) for which results are available from Kietzmann *et al.* [128]. The LFA criterion yields a hard-sphere packing fraction $\eta = 0.371$ to model the bridge function. The resulting NPA-MHNC $g(r)$ is displayed together with the $g(r)$ of Ref. [128] in Fig. 4.8. We find

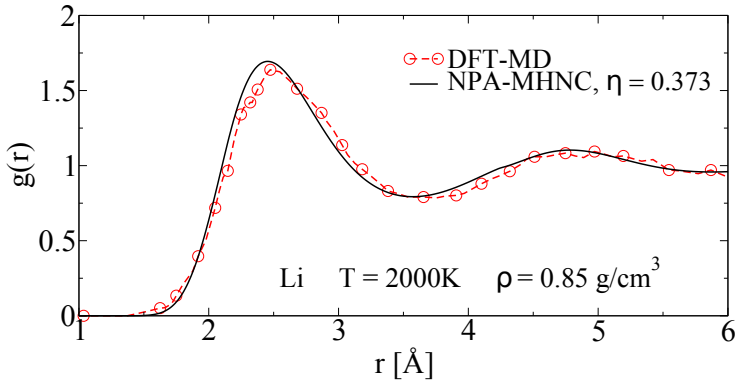

Figure 4.8. The Li-Li NPA-MHNC pair distribution function $g(r)$ at 2000K (0.173 eV), $\rho = 0.85$ g/cm^3, compared with the $g(r)$ of Ref. [128].

that the simple but state-dependent *local* pseudopotential constructed from the free-electron charge pileup at a Li nucleus is adequate to calculate phonons (i.e, requiring an accuracy of meV energies), as well as the Li-Li PDFs up to moderate compressions and high coupling constants Γ.

4.4.6. Comparison between equilibrium WDM and UFM EOS

In UFM, the internal pressure mainly results from the hot electron subsystem since ions remain close to their initial temperature T_r. Here, we investigate the difference in the pressure between the quasi-equilibrium UFM regime ($T_i \neq T_e$) and the equilibrium WDM regime which will usually be in a liquid or plasma state with $T_i = T_e$. In DFT codes it is possible to simulate liquids by computing forces among ions and the MD evolution of the positions of the N ions in the simulation cell. However, to obtain reasonable statistics, one needs to use a supercell containing as many ions as possible, thus reducing considerably the first Brillouin zone and increasing the required number of electronic bands to be included. As mentioned earlier, the number of bands needs to be even larger in order to simulate T_e via a Fermi-Dirac distribution. As examples, to obtain reasonably good band occupations for a system of 108 Al atoms at room density, 360 bands at $T_e = 1$ eV are required, and this number grows to 1200 at $T_e = 5$ eV. Thus, since computing repeatedly at every MD step a high number of bands in DFT codes is computationally very demanding, it becomes prohibitive at higher temperatures. Such a problem does not occur in the NPA model as only one DFT calculation at a single nucleus is required to construct the ion-ion pair potential. The structure factors may be computed using MD, or with MHNC equation for simple liquids.

The comparison of the pressure from UFM and equilibrium WDM is presented in Fig. 4.9. The equilibrium WDM pressure is much higher than the UFM value. Furthermore, the DFT-NPA calculation is in agreement with NPA up to $T_e = 5$ eV (the limit of our DFT+MD simulation). This mutually reconfirms the validity of the NPA as well as DFT+MD approaches in the WDM regime.

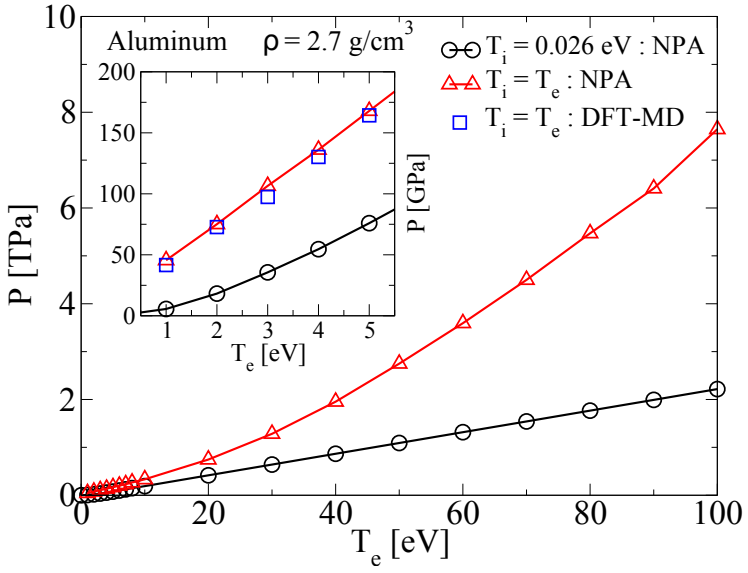

Figure 4.9. Comparison of the NPA isochoric pressures for the UFM system and the equilibrium liquid system. Inset : Comparison of the NPA pressures in the low-T regime where DFT+MD is practical.

Since $\bar{Z}$ reaches ~ 7 at T_e $\sim$100 eV, codes for simulating Al should employ pseudopotentials that include more electrons than the 3 valence electrons valid at low temperatures. Simulations with high $\bar{Z}$ values will greatly increase the computational load and such calculations become prohibitive. Hence NPA methods or orbital-free Hohenberg-Kohn methods become relevant [129]. The latter do not however provide energy spectra and details of the bound electrons.

4.5. Conclusion

In order to describe physical properties of UFM, we examined applications of the NPA model within the two-temperature quasi-equilibrium model. We computed phonons, as well as the pressure resulting from the heating of free electrons. The excellent accord between such NPA calculations and DFT simulations using the ABINIT and VASP codes reconfirms the use of the NPA in this regime. As the internal pressure increases due to the heating of

electrons by the ultrafast laser pulses, we explicitly showed that the phonon picture does not have much physical meaning, especially for thin WDM samples, even if frequencies could be computed using the harmonic approximation. As the NPA approach has negligible computational cost compared to standard DFT codes, it is a valuable tool for swiftly and accurately calculating important WDM properties such as mean ionization, pair potentials, structure factors, phonons, x-ray Thomson scattering spectra, electron-ion energy relaxation, conductivity, etc..

Acknowledgments.

This work was supported by grants from the Natural Sciences and Engineering Research Council of Canada (NSERC) and the Fonds de Recherche du Québec - Nature et Technologies (FRQ-NT). We are indebted to Calcul Québec and Calcul Canada for generous allocations of computer resources.

Chapitre 5

ARTICLE III : DIFFUSION THOMSON DES RAYONS X DE LA MATIÈRE COMPRESSÉE PAR CHOC

Cet article a été publié dans la revue *Physical Review E* **94**, 053211 (2016).

Contexte

Ce troisième article s'intéresse à la diffusion Thomson de rayons X de la MDC puisqu'il s'agit de la technique expérimentale la plus répandue pour obtenir les propriétés de la MCC. En particulier, la partie élastique du spectre de diffusion dépend directement du facteur de structure ion-ion qui est efficacement accessible par le modèle du PAN. La comparaison du modèle PAN avec des calculs de TFD-DM dans le cadre de quatre expériences de MCC permis d'illustrer la validité et l'efficacité du modèle. De plus, l'hypothèse que le système soit dans un état hors d'équilibre, même dans le cas de la MCC, fut proposé afin de reproduire les résultats expérimentaux de trois des expériences étudiés. L'utilisation de potentiels de paires est si efficace pour le calcul du FSS ion-ion qu'un potentiel semi-empirique fut intensivement utilisé par la communauté. Tandis que ce potentiel permet généralement de bien prédire le spectre de diffusion, celui-ci est inadéquat pour prédire d'autres propriétés physiques de la MCC contrairement aux potentiels du modèle PAN.

Contributions

— Calcul de la contribution élastique du spectre de diffusion de rayon-x pour l'aluminium et le béryllium compressés par une onde de choc à l'aide du code NPA.

— Démonstration que l'utilisation d'un potentiel empirique pour le calcul du spectre élastique prédit une mauvaise température et qu'il est possible de reproduire les résultats ab initio et expérimentaux en supposant un système à deux températures.

— Démonstration que le potentiel empirique n'est pas en mesure de prédire d'autres propriétés physiques du système tel que le spectre de phonon ainsi que la conductivité électrique tandis que les PP du modèle NPA sont en accord avec les calculs ab initio.

— Rédaction de la première version de l'article.

Pair potentials for warm dense matter and their application to x-ray Thomson scattering in aluminum and beryllium

Louis Harbour[1], M. W. Chandre Dharma-wardana[2], Dennis D. Klug[2], Laurent J. Lewis[1]

[1]*Département de Physique and Regroupement Québécois sur les Matériaux de Pointe, Université de Montréal, C.P. 6128, Succursale Centre-Ville, Montréal, Québec, Canada H3C 3J7*

[2]*National Research Council of Canada, Ottawa, On., Canada K1A 0R6*

Abstract

Ultrafast laser experiments yield increasingly reliable data on warm dense matter, but their interpretation requires theoretical models. We employ an efficient density functional neutral-pseudoatom hypernetted-chain (NPA-HNC) model with accuracy comparable to *ab initio* simulations and which provides first-principles pseudopotentials and pair-potentials for warm-dense matter. It avoids the use of (i) *ad hoc* core-repulsion models and (ii) "Yukawa screening", and (iii) need not assume ion-electron thermal equilibrium. Computations of the x-Ray Thomson scattering (XRTS) spectra of aluminum and beryllium are compared with recent experiments and with density-functional-theory molecular-dynamics (DFT-MD) simulations. The NPA-HNC structure factors, compressibilities, phonons and conductivities agree closely with DFT-MD results, while Yukawa screening gives misleading results. The analysis of the XRTS data for two of the experiments, using two-temperature quasi-equilibrium models, is supported by calculations of their temperature relaxation times.

Keywords: Pair potentials, X-ray Thomson Scattering, Warm Dense Matter

5.1. Introduction

High-energy deposition on matter using ultrafast lasers has opened the way to novel non-equilibrium regimes of density and temperature, raising issues of broad scientific interest [1]. These include hollow atoms, quasi-equilibrium solids and transient plasmas. The physics of warm dense matter (WDM) applies to hot carriers in nanostructures, space reentry, inertial confinement fusion [93, 130], Coulomb explosion, laser machining, surface ablation [131, 132, 94] and astrophysical environments, etc. The interactions in the WDM regime are characterized by the effective coupling parameter Γ, viz., the ratio of the Coulomb energy to the kinetic energy, which is bigger than unity. Simple approaches based on perturbation theory from a known "ideal" state thus become inapplicable.

Recent laser experiments on solid simple metals have reached WDM conditions through e.g., (i) ultrafast isochoric heating ($\rho = \rho_0$, where ρ_0 ρ are the initial and final densities, respectively) [99, 96, 26], and (ii) shock-compression ($\rho > \rho_0$) [48, 16, 49, 17, 19]. In situation (i) the optical laser directly interacts with a metallic target and couples to the free electrons causing their temperature T_e to reach many eV, while ions remain approximately at their initial temperature T_i. In situation (ii) the laser may pre-couple to the covalent electrons (bonds) of a non-metallic driver layer placed prior to the target material. This sets up a shock wave that can both heat and compress the target material which is usually metallic. If the driver layer is thick enough, the T_i attained by the target exceeds T_e as the shock wave does not directly couple to the electrons. A third and more complex situation (iii) arises if the insulating driver layer creates a shock wave as before, but in addition the laser penetrates through it and deposits energy directly in the metallic target layer. The electron temperature T_e can then exceed the ion temperature T_i even in shock-compression experiments. Finally, the state of the WDM encountered by the probe beam also depends on the time delay τ_d between the pump laser and the probe laser [96, 133]. If τ_d significantly exceeds the electron-ion temperature relaxation time τ_{ei}, T_e and T_i would then relax to a common equilibrium temperature T. It should be noted that as T_e approaches T_i, the temperature relaxation becomes increasingly slower, and coupled-mode formation begins (on phonon timescales) and the process is further slowed down [133]. Hence the tacit assumption of thermal equilibrium in WDM created by laser-shock techniques can produce misleading interpretations of experiments, as we show in what follows.

In the discussion above we have assumed the simplest non-equilibrium paradigm, viz., the well-known two-temperature ($2T$) model [134]. However, this may be too simplistic. The laser may create spatial and thermal inhomogeneous distributions which are hard to interpret.

On short timescales (e.g., <100 fs) or in more complex situations, even the electrons may not equilibrate to a common, unique temperature T_e [110].

X-ray Thomson scattering (XRTS) is a key method for studying WDM as it yields T_e, T_i, the ion density ρ, the mean electron density n_e, and details of ionic and electronic correlations. The XRTS signal is directly proportional to the total electron-electron dynamic structure factor $S_{ee}(k,\omega)$, which naturally follows a decomposition in terms of free-free, bound-bound and bound-free contributions from all "*single ion sites*", as discussed by Chihara [21]. Such a decomposition is not available *directly* via density-functional theory (DFT) calculations, which use an N-ion simulation cell, since the electron density $n(r)$ calculated by such methods is the property of all the N ions. However, by combining DFT with molecular-dynamics (MD) simulations (DFT-MD), the known ionic positions permit the calculation of the static ion-ion, ion-electron structure factors and the electron density at a "*single ionic center*".

The work of Vorberger *et al.*[135] demonstrates the interest in simpler methods to obtain such 'single-ion' properties as charge densities $n(q)$ for WDM studies. In Ref. [135] $n(q)$ is calculated from an *externally obtained* pseudopotential (for Al). Since such potentials are not available for WDM conditions, the authors use an Ashcroft empty-core potential $U^{emp}(q)$ [136, 137]. However, such $U^{emp}(q)$ are applicable only for a few metals like Al at normal density and temperatures. The advantages and shortcomings of the empty-core pseudopotential even for aluminum at normal density and temperature are well known, and more complex transferable pseudopotentials are used in DFT-MD codes. The alternative of deconvoluting the N-ion charge density obtained from DFT-MD into a single-center charge density is a computationally demanding complex process. Instead, the neutral-pseudoatom (NPA) method directly constructs density- and temperature-dependent pseudopotentials *in situ* (without using transferable potentials) via an all-electron calculation. It is a rigorous DFT formulation that uses an *effective* single-ion model of the electron-ion system to provide all the required quantities directly in order to predict, say, the XRTS signal, with negligible computational cost. The only term that depends directly on T_i is the contribution to XRTS from the isotropic *ion feature* $W(k,\omega)$, sometimes referred to as the Rayleigh feature (see e.g. Refs. [2, 138]); it is given by

$$W(k,\omega) = |f(k) + q(k)|^2 S_{ii}(k,\omega), \tag{5.1}$$

$$S_{ii}(k,\omega) \simeq S_{ii}(k)\delta(\omega). \tag{5.2}$$

Here $f(k)$ and $q(k)$ are the form factors of bound $n_b(r)$ and free $n_f(r)$ electron densities *at an individual ion*, and $S_{ii}(k,\omega)$ is the dynamic structure factor of the ions. Current XRTS experiments cannot resolve ion dynamics (at meV energy scales); hence it is approximated

by the static structure factor $S_{ii}(k)$, denoted hereafter as $S(k)$. Thus, while T_e and n_e are determined via the inelastic part of the XRTS signal, a determination of T_i is required to obtain the ion-ion $S(k)$.

Such computations of the XRTS signal have mostly been done with electronic-structure codes [40, 38] based on DFT Kohn-Sham calculations for a fixed set of N ions held in a simulation box, coupled with MD to move them and generate ensemble averages for observable properties. Results from these computationally intensive DFT-MD simulations are themselves fitted to intermediate quantities, e.g., simple "physically-motivated" pair potentials, to ease computations. Such intuitive models usually have hidden pitfalls but become entrenched as accepted practice unless corrected.

The objective of the present study is to employ the DFT-based NPA approach to provide simple first-principles calculations of the electron densities, $n(k)$, pseudo-potentials, $U_{ei}(k)$, and ion-ion pair interactions, $V_{ii}(k)$. Here, by 'first-principles' we mean calculations that do not recourse to *ad hoc* intermediate models, but use only results flowing from the initial Kohn-Sham Hamiltonian of the NPA formulation. Admittedly, in calculating $S_{ii}(k)$ using an integral equation, a hard-sphere bridge parameter η is invoked. But it is determined by an optimization procedure internal to the method; or it may be avoided altogether by using MD with the NPA pair-potentials, as discussed below.

The pair-potentials when coupled with a hypernetted-chain (HNC) integral equation or MD yield structure factors $S(k)$ which can be use to calculate all other physical properties of WDM when used with the pseudopotentials and charge densities. In particular, all quantities needed for computing XRTS spectra, transport properties, energy relaxation, equation of state (EOS) etc., become available and may be used to investigate recent experiments as well as the quality of their interpretations employing popular "physically-motivated" *ad hoc* models. Since the NPA-HNC method is typically as accurate as DFT-MD, while orders of magnitude more efficient, it permits the rapid computation of $W(k)$ for several T_i in a very effective manner, enabling us to examine different $2T$-models and their consistence with experiment.

In particular, the need for a simple potential has led to the use of an intuitive model that has come into vogue with WDM studies, viz. the "Yukawa + short-ranged repulsive (YSRR) potential" [48, 49, 139],

$$\beta_i V_{ii}^{\rm ysrr}(r) = \sigma^4/r^4 + \beta_i \exp(k_s r)/r, \tag{5.3}$$

introduced in Ref. [47]. Here, $\beta_i = 1/T_i$ is the inverse ion temperature, k_s is a screening wavevector and σ is a parameter fitted to MD data. We examine the validity of the YSRR approach using first-principles models and XRTS data for $2T$ systems ($T_e \neq T_i$) as well as

for equilibrium systems. The YSRR potential is found to yield misleading conclusions about T_e and T_i, incorrect compressibilities (i.e., a property of the EOS), incorrect phonons and incorrect electrical conductivities.

The utility of the NPA-HNC and the possibility of two-temperature systems in laser-generated WDM is illustrated below by re-analyzing experiments on Al and Be. For Al, we examine shock-compressed systems by (i) Fletcher *et al.* [48] at $\rho/\rho_0 = 2.32$ and $T_e = 1.75$ eV and by (ii) Ma *et al.* [49] at $\rho/\rho_0 = 3.0$ and $T_e = 10$ eV with $\rho_0 = 2.7$ g/cm^3; for Be, we examine the shock-compressed system by (iii) Lee *et al.* [17] at $\rho/\rho_0 = 2.99$ and $T_e = 13$ eV and the isochorically-heated system by (iv) Glenzer *et al.* [19] at $\rho/\rho_0 = 1$ and $T_e = 12$ eV with $\rho_0 = 1.85$ g/cm^3.

5.2. The NPA-HNC model

An XRTS $W(k)$ calculation needs the electron density at an ion and the structure $S(k)$ of the system. The NPA approach [88, 89, 61, 63] decomposes the total density into a superposition of effective one-center densities combined *via* structure factors and provides a comprehensive scheme based on DFT. However, this is not intrinsically a superposition *approximation*; rather, this is a rigorous method in DFT which is often not recognized as such, with a tendency to consider it as a mean-field average-atom model. In effect, DFT provides a route to an *exact* average-atom description of an arbitrary electron-ion system. As discussed in Ref. [61], DFT asserts that the free energy $F[n,\rho]$ is a functional of the one-body electron density $n(\mathbf{r})$, and the one-body ion density $\rho(\mathbf{r})$, irrespective of the existence of complex interactions (e.g., superconductive associations for electrons), and complex covalent-bonding structure, d-bonds etc., for ions. Furthermore, the functional derivatives of $F[n,\rho]$ satisfy the following stationary conditions:

$$\delta F[n,\rho]/\delta n = 0, \tag{5.4}$$

$$\delta F[n,\rho]/\delta \rho = 0. \tag{5.5}$$

Standard DFT uses the first stationary condition to construct a Kohn-Sham one-body potential acting on an effective "one-electron" density $n(\mathbf{r})$. Similarly the stationary condition on the ion density, Eq. 5.5, defines a set of non-interacting "Kohn-Sham ions" moving in the classical form of the DFT potential acting on a "single ion" representative of $\rho(\mathbf{r})$. The ions can be regarded as classical spinless particles for our purposes. In Ref. [61] the potential acting on the "average ion" was identified with the "potential of mean-force" used in the theory of classical liquids [66]. Such an approach requires corrections beyond mean-field theory which are included in the exchange-correlation functional $F_{xc}^{ee}[n]$ for the electrons *and*

in the ion-ion correlation functional $F_c^{ii}[\rho]$ for the ions. The ions are classical and do not have exchange (see Eq. 1.13, in Ref. [140]). Only pair-interactions between the DFT average-ions appear in the theory and the burden of approximating effects beyond pair-interactions falls on constructing these correlation functionals. It has in fact been shown that such an approach is successful even for liquid carbon with transient multi-center covalent bonding where carbon-carbon interactions are usually handled with multi-center "reactive bond-order potentials" [113].

However, here we study Al and Be in regimes where they are expected to be 'simple liquids'. A sum of hypernetted-chain diagrams and bridge diagrams has been used to model $F_c^{ii}[\rho]$. The usual DFT-MD codes do not use Eq. 5.5 nor F_c^{ii} and F^{ei} since the ion many-body problem is not reduced to a one-body problem for the ions, unlike in the NPA. Instead, standard DFT uses a Born-Oppenheimer approximation where N ions in a simulation box are explicitly enumerated and provide an "external potential" to the Kohn-Sham electrons. In contrast, the NPA uses only the one-body ion distribution $\rho(\mathbf{r})$. Given a good ion-correlation functional $F_c^{ii}(\rho)$, enormous computational simplifications follow from this full-DFT approach compared to the standard method which calculates the Kohn-Sham eigenfunctions of a simulation cell containing typically $N = 64$ - 128 ions. Thus the "single-center" NPA is a *rigorous* DFT average-atom approach, and its approximations lie in the construction of F_c^{ii} and F_{xc}^{ee}. The other advantage is that the NPA naturally provides "single-ion" properties like the mean ionization $\bar{Z}$, charge density $n(\mathbf{r})$ at a single ion, and the separation of the bound-electron and free-electron spectra (needed in XRTS theory) consistent with the exchange and correlation potentials used in the theory.

Several NPA models are described in the literature [24], e.g., those using ion-sphere models and other prescriptions not completely based on DFT theory. These different formulations affect how the chemical potential is treated and how the bound and free electrons are identified [63, 57, 51, 50, 141, 54]. We employ the NPA model of Perrot and Dharmawardana [63, 64, 115] which includes a cavity of radius r_{ws}, with $r_{ws} = \{3/(4\pi\rho)\}^{1/3}$ the ion Wigner-Seitz radius, around the central nucleus to mimic, in a simplified way, the ion-density $\rho(r)$ of the plasma contained in a "correlation sphere" of radius $R_c \sim 10r_{ws}$. This is equivalent to using $(4/3)\pi(R_c/r_{ws})^3$, i.e., about 4200 particles in an MD simulations; in contrast, typical DFT-MD simulations use about 250 particles. The full ion distribution is subsequently evaluated by an HNC or modified-HNC (MHNC) procedure although MD may also be used, especially if low-symmetry situations are envisaged. The R_c is such that the pair-distribution functions (PDF), viz., ion-ion $g_{ii}(r)$ and ion-electron $g_{ie}(r)$ have asymptotically reached unity as $r \to R_c$. The electron-electron PDF g_{ee} can be shown to also reach

the asymptotic limit when $r \to R_c$ as the e-e coupling is comparatively much weaker. The electron chemical potential is for non-interacting electrons at the interacting mean density n_e and temperature T_e, as required by DFT. The finite-T DFT calculations are done using a finite-T exchange-correlation functional F_{xc}^{ee} [84]. The free-electron density $n_f(r)$ is calculated using Mermin-Kohn-Sham wave functions which are orthogonal to the core states. Core-valence Pauli blocking, core-repulsions as well as core-continuum exchange-correlation effects are naturally included in the model. The NPA is an all-electron calculation and yields bound-state energies, bound-electron densities, as well as continuum densities and phase shifts which satisfy the Friedel sum rule.

The NPA free-electron pileup $n_f(k)$ around the NPA-nucleus is the key quantity in constructing electron-ion pseudopotentials $U_{ei}(k)$ and ion-ion pair potentials $V_{ii}(k)$, given in terms of the fully interacting static electron response function $\chi(k,T_e)$ as follows :

$$U_{ei}(k) = n_f(k)/\chi(k,T_e), \tag{5.6}$$

$$\chi(k,T_e) = \frac{\chi_0(k,T_e)}{1 - V_k(1-G_k)\chi_0(k,T_e)}, \tag{5.7}$$

$$G_k = (1-\kappa_0/\kappa)(k/k_{\rm TF}); \quad V_k = 4\pi/k^2, \tag{5.8}$$

$$k_{\rm TF} = \{4/(\pi\alpha r_s)\}^{1/2}; \quad \alpha = (4/9\pi)^{1/3}, \tag{5.9}$$

$$V_{ii}(k) = \bar{Z}^2 V_k + |U_{ei}(k)|^2 \chi_{ee}(k,T_e). \tag{5.10}$$

Here χ_0 is the finite-T Lindhard function, V_k is the bare Coulomb potential and G_k is a local-field correction (LFC). Hence the electron response goes beyond the random-phase approximation (RPA). The finite-T compressibility sum rule is satisfied since κ_0 and κ are the non-interacting and interacting electron compressibility, respectively, with κ matched to the F_{xc} used in the Kohn-Sham calculation. In Eq. 7.9, $k_{\rm TF}$ appearing in the LFC is the Thomas-Fermi wavevector. We use a G_k evaluated at $k \to 0$ for all k instead of the more general form (e.g., Eq. 50 in Ref. [84]) since the k-dispersion in G_k has negligible effect for the WDMs treated in this study. Note that the "Yukawa form" of the pair-potential is obtained from the above equations at sufficiently high temperatures since the Lindhard function can be approximated by its $k \to 0$ limit under such Debye-Hückel-like conditions, while G_k goes to zero. Such approximations are largely invalid in the WDM regime; Friedel oscillations in the pair-potentials contribute to defining the peak positions in the $g(r)$ and hence their relevance to observed properties is well-known experimentally and theoretically. Furthermore the need for finite-k screening instead of the Yukawa form is the norm for systems with $T/E_F < 1$ and normal densities. In fact the pair-potentials, PDFs, XRT features, conductivities and

phonons will be incorrect if calculated from the $k \to 0$ Yukawa form for the given conditions. Hence all the observable properties studied here can be regarded as examples of observations of finite-k screening (see, e.g., Ref [142]).

The pseudopotential $U_{ei}(k)$ is a *local* potential which contains non-linear effects as the $n_f(k)$ was calculated from the Kohn-Sham equations. However, since it is forced to be linear in the response, the pair-potential Eq. 7.10 is trivially constructed. The regime of validity of this procedure is discussed in Ref. [105]. Outside the regime of validity it becomes increasingly more approximate, but as no *ad hoc* models extraneous to the calculation are invoked, it remains a first-principles method for constructing the pseudopotential from the all-electron single-center Kohn-Sham calculation. The structure factor $S(k)$ is computed (for uniform systems) from the modified hypernetted-chain (MHNC) equation which includes a bridge term $B(\eta,r)$ modeled using a Percus-Yevick hard-sphere fluid with a packing fraction η. The packing fraction is determined by the Lado-Foiles-Ashcroft *et al.* (LFA) criterion [68, 143] based on the Gibbs-Bogoluibov inequality. Although we use the MHNC equation, we refer to the general method as NPA-HNC, or occasionally as NPA-MHNC when we wish to emphasize the use of the MHNC procedure over the HNC one. It should also be noted that any ambiguity in the choice of the bridge function, or the use of a hard-sphere model for the bridge function, can be avoided if the NPA pair-potential is used directly in MD to generate $g(r)$. Such NPA+MD calculations were not deemed necessary in the present study.

Since the NPA pair-potential accurately predicts phonons (i.e., meV scales of energy) for common $2T$ WDM systems [123], even the dynamical $S_{ii}(\mathbf{k},\omega)$ can be predicted when XRTS data at meV accuracy become available. Furthermore, since all the PDFs and interaction potentials are available, the Helmholtz free energy F, and hence EOS properties, specific heats etc., as well as linear transport properties, can be calculated rapidly and in a parameter-free manner. Many such calculations have been presented in the past, as reviewed in Ref. [115]. Here we illustrate this for XRTS experiments on an equilibrium system and on a $2T$-quasi-equilibrium system.

5.3. Aluminum

5.3.1. Shock-compressed Aluminum - I

Using XRTS, Fletcher *et al.* [48] have studied compressed aluminum evolving across the melting line into a WDM state (named Al-I hereafter). From their inelastic data, they determined the aluminum density and temperature to be $\rho/\rho_0 = 2.32$ and $T_e = 1.75$ eV, respectively. This density corresponds to a Wigner-Seitz radius $r_{ws} = 2.255$ a.u. for the

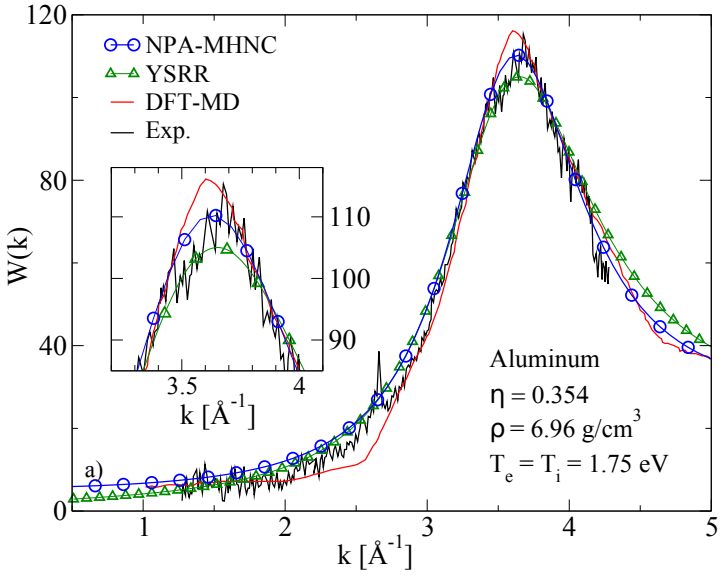

Figure 5.1. The XRTS ion feature $W(k)$ of Ref. [48] for Al-I, and from the DFT-MD, NPA-MHNC and YSRR models, as indicated. The inset magnifies the peak region.

ions and $r_s = 1.564$ a.u. for the electrons since the mean ionization $\bar{Z}$ is found to be 3 from the NPA calculation. They used two 4.5 J laser beams on both sides of a 50 μm-thick Al foil coated with a 2 μm-thick layer of Parylene. A probe-pulse delay of $\tau_d = 1.9$ ns is used. Hence the assumption of thermal equilibrium ($T_e = T_i$) seems justified. The NPA free-electron charge density $n_f(r)$ at an Al^{3+} ion in the WDM system directly provides the pseudopotential U_{ei} and the pair-potential $V_{ii}^{\rm NPA}(r)$. For the Yukawa screening of the YSRR potential, Fletcher *et al.* used the zero-T value of the Thomas-Fermi wavevector (Eq. 7.9). We find the value of σ to be 4.9 a.u., correcting what may be an error in Ref. [48] where σ= 9.4 a.u. is quoted [144]. The $S(k)$ corresponding to the NPA or the YSRR pair-potential can be calculated using an HNC or MHNC procedure, as appropriate, and used in Eq. 5.1 to compute the XRTS-signal $W(k)$.

In Fig. 5.1, the $W(k)$ computed from NPA and YSRR are compared with the experimental XRTS $W(k)$. In the NPA case, a bridge function $B(\eta,r)$ with $\eta = 0.354$ is obtained from the LFA criterion. The NPA-MHNC $W(k)$ is in good agreement with experiment and also confirms thermal equilibrium with $T_i = 1.75$ eV. No bridge correction is used for the YSRR since its $S(k \to 0)$ limit is already strongly inconsistent with the compressibility sum rule as will be illustrated below in the discussion (section 5.3.4). Since the conditions of the Fletcher experiment produce a near-degenerate electron gas ($T_e/E_F = 0.085$), the pair potential $V_{ii}^{\rm NPA}(r)$ displays Friedel oscillations as can be seen in Fig. 5.2(a). The $S(k)$ from NPA-HNC

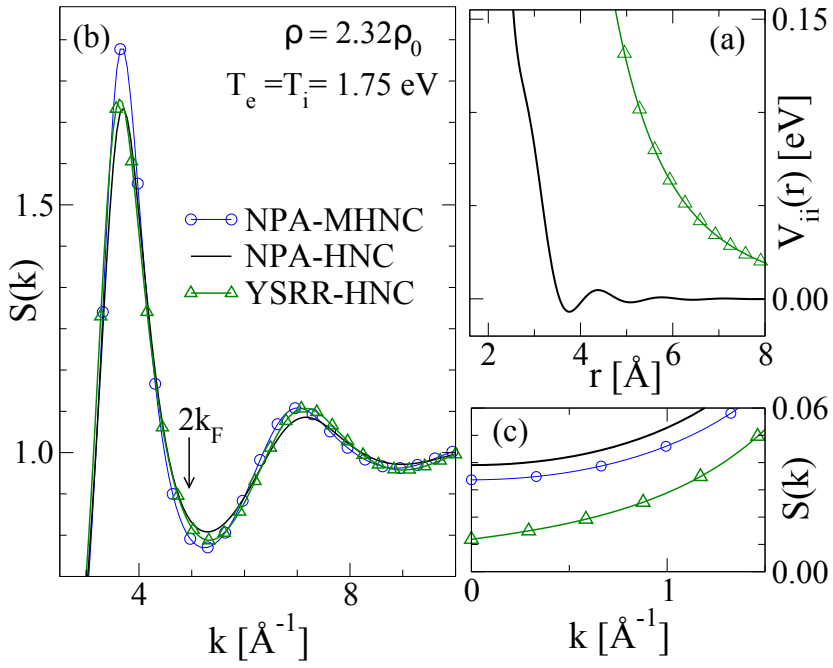

Figure 5.2. (a) NPA and YSRR potentials for Al-I (cf. experiment of Ref. [48]); (b) $S(k)$ from the $V_{ii}(r)$ using HNC and MHNC; (c) $k \to 0$ region of $S(k)$.

and YSRR-HNC are shown in Fig. 5.2(b). The NPA-HNC $S(k)$ is very similar to the YSRR-$S(k)$ but differs in the $k \to 0$ region and near $2k_F$ (panel (c)), and this will affect some EOS properties.

5.3.2. Shock-compressed Aluminum - II

From inelastic data for shock-compressed Al (hereafter Al-II), Ma *et al.* [49] determined the experimental conditions in the target to be $\rho/\rho_0 = 3.0$ and $T_e = 10$ eV. This density corresponds to $r_{ws} = 2.07$ a.u. for the ions and r_s=1.435 a.u. for the electrons. A set of nine pump beams, with a total energy of 4.5 kJ deposited in 1 ns, were aimed directly at the 125 μm-thick Al foil without any protective shield. The shock compression heats up the ion subsystem on the picosecond timescale, but the coupling of the laser to the free electrons in aluminum raises the electron temperature much more rapidly, within femtoseconds, creating a $2T$-system with $T_i < T_e$ initially. If the data are collected after a sufficient time delay, an equilibrium temperature $T = T_i = T_e$ will be reached. Calculations using the YSRR potential with $T_i = T_e = 10$ eV show good agreement with the XRTS ion feature. However, this turns out to be misleading since the ion feature of the system at $T_i = 10$ eV determined

by the DFT-MD simulation of Rüter *et al.*[145] disagrees with the XRTS data of Ma *et al.* as shown at Fig. 5.3.

Using an "orbital-free" approach, viz. a Thomas-Fermi model with Weiszäcker corrections, Clérouin *et al.* [146] arrived at a $2T$ model with $T_i = 2$ eV and $T_e = 10$ eV in order to obtain good agreement with the XRTS data. They claimed that, since their method involves all electrons, the core-repulsion term included in the YSRR model is non-physical. Our NPA Kohn-Sham calculations — which are all-electron, parameter-free and include core and continuum states — confirm the conclusions of Clérouin *et al.*. Using the NPA-potential for this case, a MHNC calculation with $\eta = 0.367$ predicts an excellent fit to the Ma *et al.* data with $T_i = 1.8$ eV and $T_e = 10$ eV, as can be seen in Fig. 5.3. In Fig. 5.4 (a)-(c), the NPA and YSRR $S(k)$, pair-potentials $V_{ii}(r)$ and the $k \to 0$ limit of $S(k)$ are shown. There are no Friedel oscillations in $V_{ii}^{\mathrm{NPA}}(r)$ as T_e is nearly six times higher than in the conditions prevailing in Al-I. The disagreement between the NPA-$S(k)$ and the YSRR-$S(k)$ for $k \to 0$ should again be noted.

The high-k shoulders of the $W(k)$ curves from the $2T$ NPA-HNC and from the YSRR calculations are washed-out in the experiment, suggesting more complexity than in a $2T$ system. The ion subsystem may be cold (at 1.8 eV), but containing an unknown high-T component as well. On the other hand, it has been pointed out by Souza *et al.* [24] that the high intensity peak around $k \sim 4\text{Å}^{-1}$ might be anomalous and caused by a non-Gaussian and/or broadened probe beam. The DFT-MD as well as the NPA results for the equilibrium case ($T_e = T_i = 10$ eV) both predict a peak height of ~ 65, in strong contrast to the YSRR model, while the actual experimental peak height is ~ 106.

Evidently, the XRTS data cannot be consistent with an equilibrium model. Since the aluminum target is pumped directly with a laser, the system would initially begin with $T_e > T_i$, and the possibility that the system has $T_e = 10$ eV, with the ion subsystem at $T_i \sim 2$ eV, is an entirely reasonable result. More complex non-equilibrium features [147] may also be envisaged, and may be useful for explaining the wings of the XRTS data. A model of the hot electrons involving a high-energy tail, energy bumps etc., would involve additional parameters that fit the observed $W(k)$, but without independent information to confirm them. Since the main XRTS $W(k)$ profile can be explained well within a $2T$-model, this WDM is best regarded as being in a state with cold ions and hot electrons,but this by no means excludes more complicated situations which can be assessed only if more details of the experimental configuration and the pulsed heating process are available.

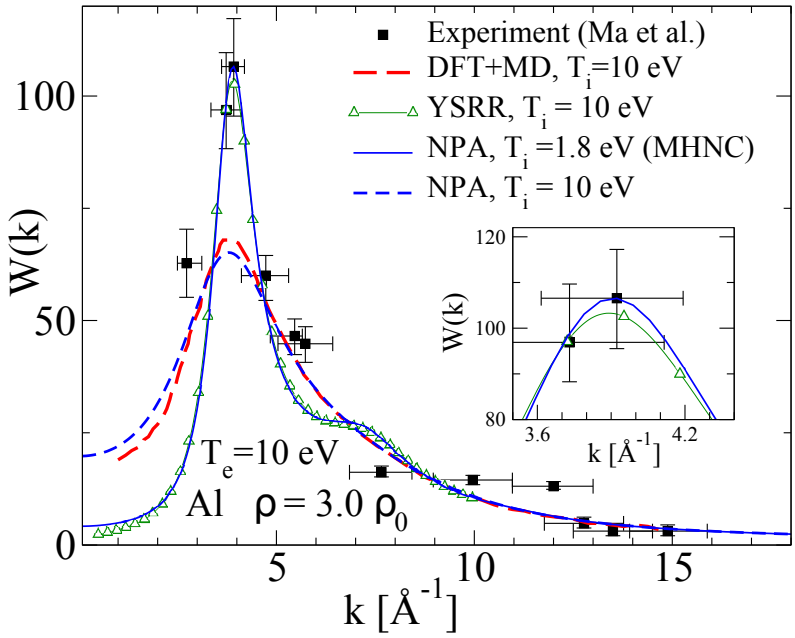

Figure 5.3. The XRTS ion feature $W(k)$ of Ma *et al.* [49] for Al-II, compared with the $W(k)$ from YSRR, NPA, the DFT-MD calculation of Rütter *et al.* with $T_i = T_e$, and our $2T$-NPA calculation with $T_i = 1.8$ eV and $T_e = 10$ eV; the inset magnifies the peak region.

5.3.3. Temperature relaxation in Al-II

In this section, our objective is to estimate the temperature relaxation time τ_{ei} in order to determine if the system has reached equilibrium within the pulse-probe delay. Assuming the $2T$ model with $T_e = 10$ eV and $T_i = 1.8$ eV, we can use the NPA electron-ion pseudopotential to calculate the temperature relaxation rate [133] via the Fermi Golden Rule (FGR). Since the FGR estimate of τ_{ei} was already sufficiently informative, we did not need a more detailed energy-relaxation model such as the coupled-mode description which is known to make the relaxation-time estimates somewhat longer. For this purpose we define the form factor M_k of the pseudopotential by

$$M_k = U_{ei}(k)/\bar{Z}(Z_e V_k); \quad Z_e = -1. \tag{5.11}$$

The energy-relaxation rate, i.e., the rate of transfer of energy from the hot electrons to the ions per unit volume, calculated within a number of simplifying approximations, is given by

$$\frac{dE_e}{dt} = \omega_{i,\mathrm{p}}^2 (T_e - T_i)$$

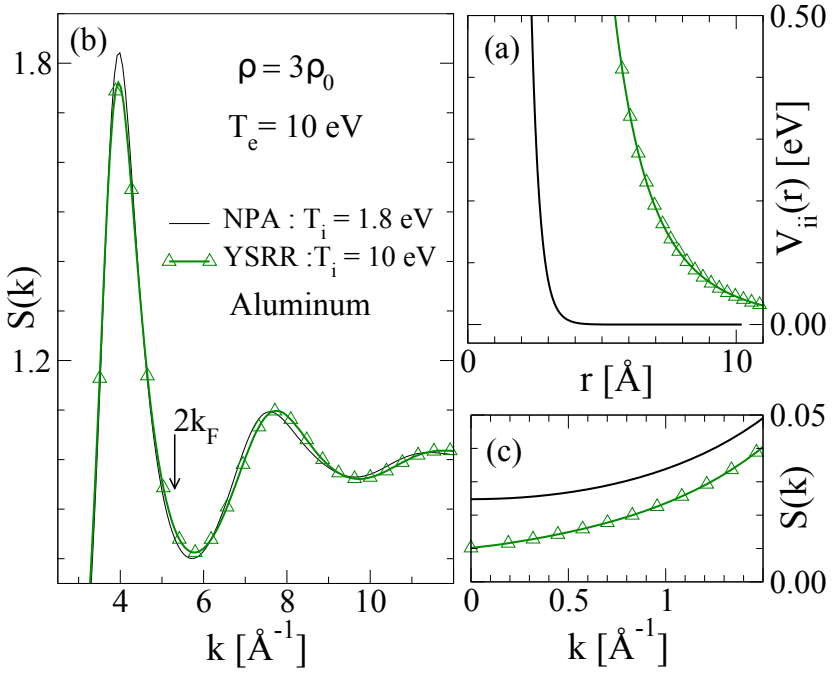

Figure 5.4. (a) The NPA-HNC and YSRR pair potentials for Al-II; (b) corresponding $S(k)$; (c) the $k \to 0$ limit of $S(k)$.

$$\times \int \frac{d^3\vec{k}}{(2\pi)^3}\, V_k \left|M_{\vec{k}}\right|^2 \mathrm{Im}\left[\frac{\partial}{\partial\omega}\chi^{ee}(\vec{k},\omega)\right]_{\omega=0}, \tag{5.12}$$

where E_e is the energy in the hot electron subsystem at time t, $\omega_{i,\mathrm{p}}$ is the ion plasma frequency and χ^{ee} is the fully interacting dynamic electron response function. The f-sum rule has been used to eliminate the dependence on the ionic structure [148] and hence provides an estimate of the energy relaxation which is superior to those obtained by using models for $S_{ii}(k,\omega)$, if the other assumptions made in the above theory hold. For instance, a difference of Bose factors of the form $N(\omega/T_e) - N(\omega/T_i)$, where $N(x) = 1/(\exp(x) - 1)$, for the density fluctuations in the electron system and the ion system respectively, has been approximated as $(T_e - T_i)/\omega$ in order to calculate a temperature relaxation rate. If T_i is assumed to be fixed (at least for a short timescale), we can use Eq. 5.12 for the energy relaxation rate of the electrons to determine a temperature relaxation rate. It requires a relation between the internal energy of an interacting warm-dense electron fluid and its temperature. Here we use the property that $F = F_0 + F_{xc}$, and the internal energy $E = \partial\{\beta F\}/\partial\beta$ as presented in Ref. [84] where the needed parametrizations are given. The replacement of the Bose factors by a temperature difference is not quite valid for the $T_i = 1.8$ eV and $T_e = 10$ eV estimated to prevail in the Ma *et al.* experiment since the electrons are partially degenerate.

Nevertheless, one can obtain a *grosso modo* estimate of the temperature-relaxation time τ_{ei}. It is found to be 300-400 ps depending on various assumptions. This timescale is sufficient for the formation of phonons, and hence the temperature relaxation towards equilibrium will be further slowed down by the formation of coupled modes (i.e., the conversion of ion-density fluctuations by electron screening into ion acoustic modes). This slows down the relaxation time by more than an order of magnitude. An actual estimate of the temperature relaxation of the target material (Al-II) will also have to account for the fact that the ion subsystem looses energy to its holding structure and the environment. These considerations independently support our conclusion, and that of Clérouin *et al.*, that $T_i < T_e$ is a possible scenario, contrary to the 'equilibrium model' indicated by the YSRR model.

5.3.4. Discussion of Al results

DFT simulations treat the WDM sample as a periodic crystal made up of N nuclei whose positions in the simulation box evolve via MD and provide "single-electron" Kohn-Sham spectra. However, it provides no simple method for computing electron properties that can be attributed to a "single" nucleus, e.g., the mean ionization $\bar{Z}$ arising from the bound and free parts of the spectrum, or pair interactions resulting from the single ions. The latter, if available, provides a convenient means of obtaining $S(k)$ and related properties of the WDM in a computationally efficient manner. The YSRR model potential was justified by Wunsch *et al.* [47] as a suitable way of inverting a given $g(r)$ obtained from DFT-MD simulations in WDM conditions; it contains a Yukawa-like screening term based on an externally provided $\bar{Z}$ and an explicit "core-repulsion" term.

The NPA approach rigorously constructs the effective Kohn-Sham "single-electron" density via the "single-ion" DFT description of the electron-ion system, as implied by the Euler-Lagrange equations given by Eq. 5.4 and Eq. 5.5. Thus, unlike DFT codes which treat the ions as an external potential, the NPA directly provides single-ion/single-electron properties as well as the pair potentials. The NPA calculation for Al-I, for the experiment of Fletcher *et al.*, shows that the mean radius of the $n = 2, l = 0$ bound shell in Al, which reflects the radius of the bound core, is 0.3552 Å. The YSRR potential reaches large values already by 2 Å, i.e., at a radius nearly 6 times larger than the actual core size; thus the short-range repulsive part $(\sigma/r)^4$ is not appropriate. The claim in Ref. [48, 49] that the YSRR potential "accounts for the additional repulsion from overlapping bound-electron wavefunctions" is certainly not confirmed by the shell structure of Al^{3+} in the plasma. Note that even the Wigner-Seitz radius, i.e., the sphere radius for an ion for aluminum at a compression of 2.32, is 2.255 a.u.= 1.193 Å , and hence the YSRR model is clearly unphysical. The core-core

interaction in Al can be calculated from the Al^{3+} core-charge density as in Appendix B of Ref. [64]. It is totally negligible for Al at compressions of 2.32 (in Al-I) or 3 (in Al-II) studied here. It should be noted that, as far as $S(k)$ is concerned, core-core interaction effects lead to an *attraction* due to core polarization, as was also discussed in Ref. [64]. This too can be neglected in aluminum.

The liquid-metal community of the 1980s found that the inverse problem of extracting a potential from the $S(k)$ given in a limited k-range, obtained from MD or from experiment, is misleading and not unique [149, 150, 151, 152]. A parametrized physically-valid model (e.g., a pair potential $V_{ii}(r)$ constrained via an atomic pseudopotential) together with a good $B(\eta,r)$ [143] can successfully invert the MD data. However, the DFT-MD step is unnecessary in most cases since the $V_{ii}^{\rm NPA}(r)$ and the $S(k)$ that provide the physics are easily evaluated from a rapid parameter-free NPA calculation. The YSSR potential is fitted to a limited range in r-space as in Wunsch *et al*. But the Fourier transform to obtain k- space quantities involves information on all of r-space. This leads to serious and uncontrolled errors unless a physically valid potential is used to extend the simulation $g(r)$ data to all r and hence to all relevant k. We note the following. (a) The YSSR is proposed in Fletcher *et al.* for the computation of the EOS. Small-k behaviour is very important for EOS properties and we bring this out via the compressibility calculation. (b) Behaviour near $2k_F$ is important for transport and scattering processes and we bring this out via the resistivity calculation. (c) Other intermediate k-values are sampled by the phonons and we show that YSSR fails for most-k in the phonon dispersion. Hence even when YSSR 'seems to work' for one property, one cannot attribute any physical significance to it. Thus, besides the XRTS ion feature, we tested the validity of NPA and YSRR models under WDM conditions by computing three key physical quantities, namely (i) compressibility κ, (ii) phonon spectra, and (iii) resistivity R, as we discuss below.

(i) To determine κ we assume that the sum rule $S(0) = \rho T_i \kappa$ holds for $2T$ systems under certain restrictions [153]. We computed κ using NPA, YSRR and ABINIT, and obtained respectively 26, 9.6 and 30 a.u. for Al-I at a compression of 2.32 and $T_i = T_e = 1.75$ eV. The corresponding values for aluminum (Al-II) at a compression of 3, $T_i = 1.8$ eV and $T_e = 10$ eV, are 14, 1.1 and 16.4 a.u. In both cases, the results from the NPA are in close agreement with ABINIT whereas the YSRR gives a much lower compressibility. Here, the YSRR-$S(k)$ is calculated from the HNC without a bridge term, i.e. $B(\eta,r) = 0$, since a bridge term would make the compressibility even more erroneous. Thus, even in equilibrium, the YSRR model is not trustworthy enough for EOS properties like the compressibility.

(ii) Even though the ionic system is clearly melted in both Al-I and Al-II conditions, a good test of the quality of the pair potential is the computation of the phonon spectrum for its low-T crystal structure (face-centered-cubic (FCC) for Al) which is a particular ionic configuration of the system even in the melt. In fact, the short-range structure of strongly coupled ionic fluids as reflected in the $S(k)$ is known to correspond closely to the $S(k)$ of the crystal structure below the melting point. The comparison of phonons obtained via the pair potential approach with those from *ab initio* calculations permits the validation of the energy landscape created by the pair potential for this particular ionic configuration. Such tests have already been done for other systems showing that the NPA predicts equilibrium and non-equilibrium phonons in good accord with *ab initio* simulations [123], which illustrates its meV-level of accuracy. The examination of phonon modes is relevant for ultra-fast-matter (UFM) studies where electron temperatures will rise significantly more rapidly than that of the nuclei. The limiting case where the nuclei are at low temperature is where phonon stability is relevant The excellent agreement between the NPA and ABINIT longitudinal phonons in Al-I (Ref. [48]) and Al-II (Ref. [49]) is displayed in Fig 5.5 and further validates the NPA pair potentials in the WDM regime. The unphysical "stiffness" of the YSRR potential leads to high phonon frequencies and a sound velocity much larger than the NPA and ABINIT predictions.

(iii) We tested the validity of the Yukawa component in the YSRR model and the validity of the YSRR-$S(k)$ by calculating the electrical resistivity R. The Yukawa pair potential $\bar{Z}^2 \exp(-k_s r)/r$ arises from the Yukawa pseudopotential $U_{ei}^y(q) = -4\pi\bar{Z}/q^2$ screened by the $k \to 0$ RPA dielectric function, i.e., $\epsilon(q) = 1 + (k_s/q)^2$. We use the Ziman formula in the form given in Ref. [64], Eq. (31) to calculate the resistivity. Computing R for the NPA and YSRR model, we obtain respectively 15.0 and 145 $\mu\Omega$·cm for Al-I while the corresponding values for Al-II are 9.65 and 99.4 $\mu\Omega$·cm. Thus, in both cases, the resistivity predicted by the YSRR is about 10 times higher than the NPA value. Such larger-than-expected resistivities have also been obtain by Sperling *et al.*[26] while using an even simpler model than YSRR. The resistivities predicted by Sperling *et al.* are known to be in strong disagreement with the DFT-MD Kubo-Greenwood resistivity calculations of Sjostrom *et al.* [154]. These issues are discussed at length in Ref. [155] where it is concluded that the Sperling calculation of the static conductivity is likely to be inapplicable. In Fig.5.6, we show that this behavior is also observed for various densities in equilibrium with $T = 1.75$ eV. The Ziman formula in conjunction with the NPA-HNC model, which includes a self-consistently generated $U_{ei}(k)$, $S(k)$ and a screening function $\chi(k)$ containing an LFC that satisfies the compressibility sum rule, is a well-tested method for many systems (for a review, see Ref. [115]) including

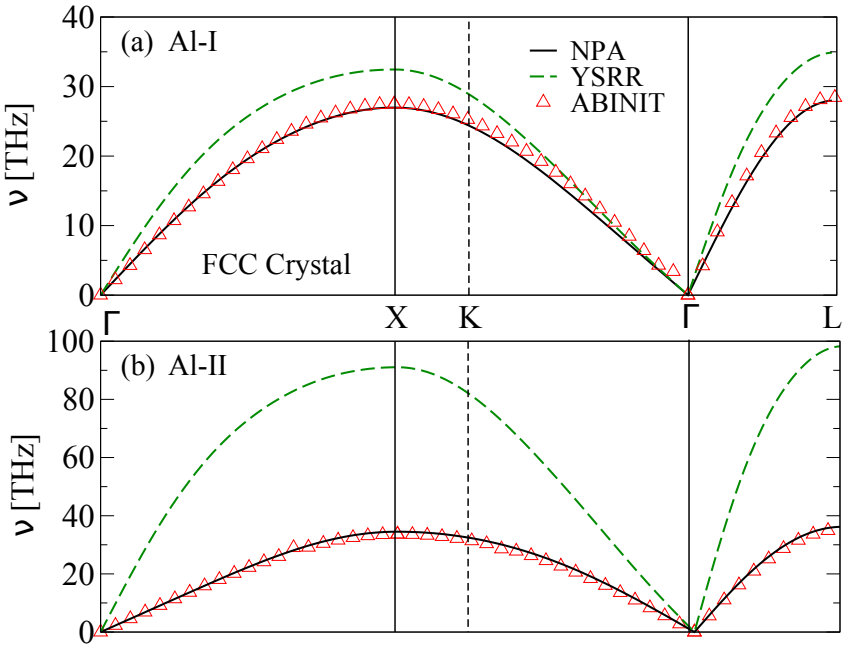

Figure 5.5. The longitudinal phonon spectrum for the FCC crystal of a) Al-I, i.e. compression of 2.32 and $T_e = T_i$ =1.75 eV, Ref. [48]; b) Al-II, i.e. compression of 3.0, T_i=1.8 eV, and T_e = 10 eV, Ref. [49]. The Γ, X, K and L point are symmetry points of the first Brillouin zone of the FCC crystal.

aluminum [64, 156]. Thus, while it may be thought that additional *ab initio* or experimental resistivity data are required to confirm the NPA and Ziman formula results in the WDM regime, it is unlikely that the NPA resistivities are in error by an order of magnitude, given the excellent track record of NPA-resistivity predictions [156]. In our view, the Yukawa part of the YSSR calculation is responsible for the erroneous estimate of the resistivity.

In summary, through the calculation of phonons, compressibilities and resistivities, we showed that the short-ranged-repulsive and the Yukawa parts of the YSRR model are individually untenable. In contrast, the correct physics is quite simply obtained from the NPA-HNC for both the equilibrium and the $2T$ situation.

5.4. Beryllium

5.4.1. Shock-compressed Beryllium

Beryllium has been of recent interest (e.g., Ref. [157]) for many reasons including its potential applications as an ablator material in inertial-confinement fusion studies. Lee *et al.* [17] studied compressed beryllium by applying 12 pump beams, each with an individual

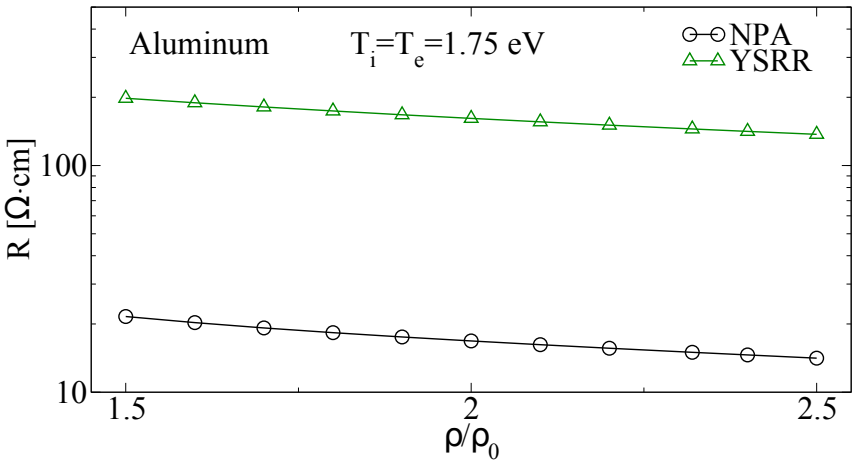

Figure 5.6. The electrical resistivity of Al at T=1.75 eV for different compressions calculated using NPA and YSRR.

energy of 480 J in 1 ns, directly on a 250 μm-thick Be foil without any coating. The pump-probe laser delay is $\sim$ 4.5 ns, and may appear to be enough for electron-ion equilibration. We will examine this by a calculation of the τ_{ei}, as was done for aluminum. From an analysis of the XRTS data they concluded that Be is in a compressed state with $\rho/\rho_0 = 2.99$ and $T_e = 13$ eV (Be-I hereafter). Figure 5.7 compares the ion feature $W(k)$ from the NPA-HNC model with the experimental data of Ref. [17] and with the detailed and careful DFT-MD simulations of Plagemann *et al.* [158]. Even though NPA-HNC and DFT-MD do not predict exactly the same spectrum, both approaches agree in not confirming the first experimental point at $k = 1.3$ Å^{-1} under the equilibrium condition $T_i = T_e = 13$ eV. By re-analyzing the original data (indicate as 'Exp (re-fitted)' in Fig. 5.7 and in Fig. 5.10), Plagemann *et al.* found that a $2T$-system with $T_i = 9$ eV and $T_e = 13$ eV was able to reproduce the spectrum. The NPA-HNC calculation does not predict the second experimental point at $k = 4.3$ Å^{-1} as it shows higher values than DFT-MD for all values of k. To understand this difference between DFT-MD and NPA-HNC, we compared individually the two contributions to the ion feature, namely the static ion-ion structure factor $S(k)$ and the total electron form factor $N(k) = f(k) + q(k)$. In Fig. 5.8, a comparison of the $S(k)$ at different equilibrium temperatures shows excellent accord between NPA-HNC and DFT-MD. However, Fig. 5.9 reveals important differences in the core-electron form factor $f(k)$ starting around $k = 4$ Å^{-1}. To determine $f(k)$, Plagemann *et al.* used snapshots of the DFT-MD simulation from the VASP code and post-processed in the ABINIT code using a "superhard" pseudopotential accounting for all four electrons. In contrast, NPA-HNC is an all-electron atomic calculation including corrections from the ion environment which

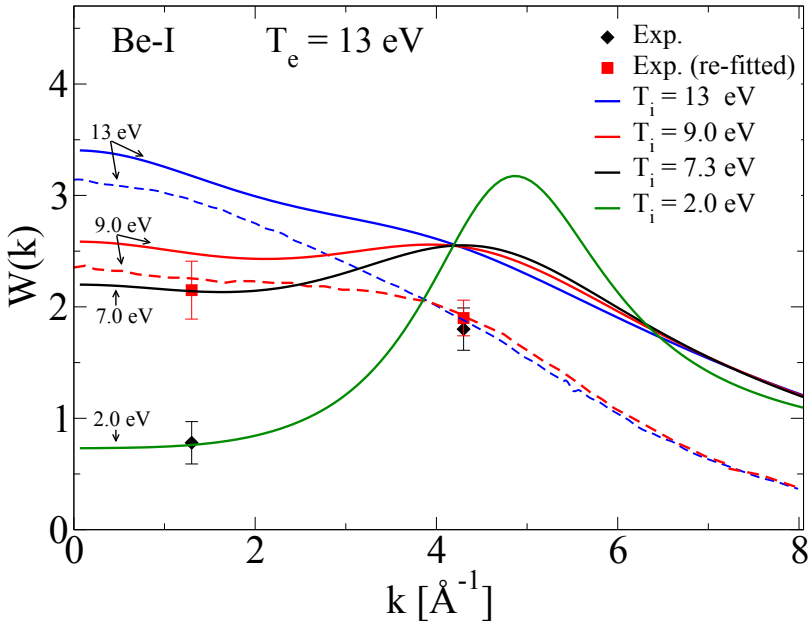

Figure 5.7. The XRTS ion feature $W(k)$ of Lee *et al.* [17] compared with the NPA-HNC $W(k)$ (full lines) and with DFT-MD results (dashed lines) of Plagemann *et al* [158] for equilibrium and for $T_e \neq T_i$, as indicated.

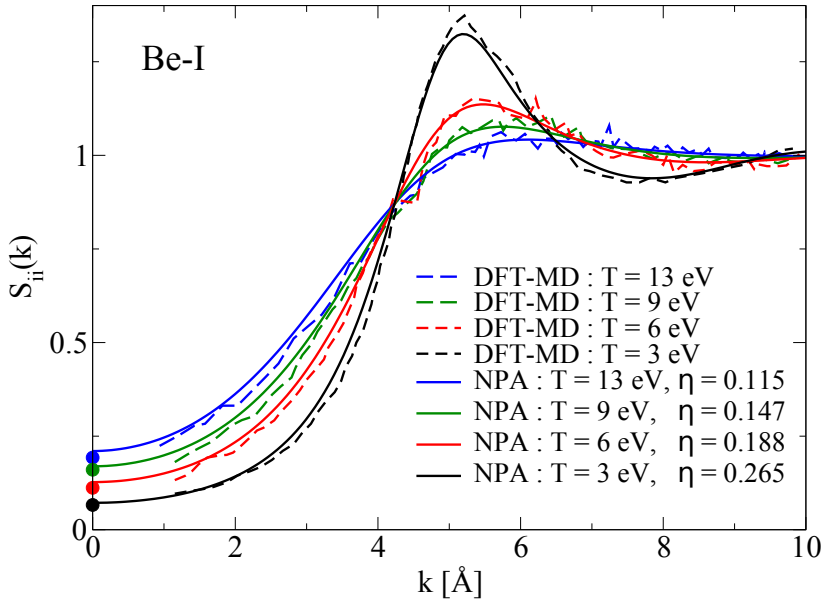

Figure 5.8. Static ion-ion structure factor $S(k)$ for Be-I from the NPA-HNC and DFT-MD simulation of Plagemann *et al* [158], including their $k = 0$ value marked as dots, for different equilibrium temperatures.

predicts an $f(k)$ similar to the independent pseudo-atom calculation of Souza *et al.* [24]. Since the discrepancy starts around $k = 4\text{Å}^{-1}$, i.e., already deep into the core, it is possible that the "superhard" pseudopotential used does not reconstruct correctly the core electron density close to the nucleus. Further investigation should be done of this possibility which would account for the differences in the calculation of $W(k)$ from NPA-HNC and DFT-MD. Finally, using the NPA-HNC model while keeping $T_e = 13$ eV, the best fit to the re-analyzed experimental $W(k)$ is obtained with $T_i = 7.3$ eV while it requires $T_i = 2$ eV to reproduce the original data. Given $T_i = 7$ eV and $T_e = 13$ eV, the Be-target is better equilibrated than if one were to posit $T_i = 2$ eV, and $T_e = 13$ eV.

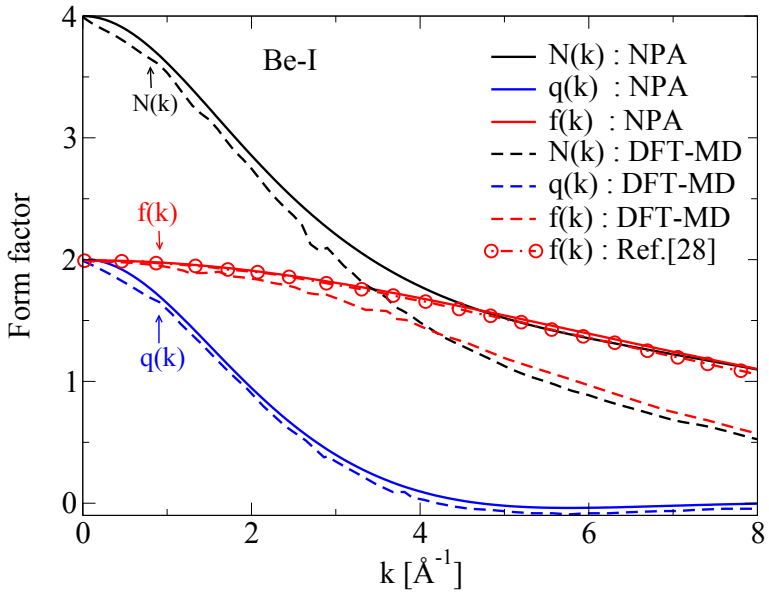

Figure 5.9. Total $N(k)$, bound-electron $f(q)$ and free-electron $q(f)$ form factor for the Be-I conditions

5.4.2. Isochorically-heated Beryllium

Glenzer *et al.* [19] created an isochorically heated ($\rho/\rho_0 = 1$) WDM Be sample (named Be-II hereafter) by aiming 20 pump beams, with a total energy of 10 kJ over 1 ns, onto a 300 μm-thick Be cylinder coated by a protective 1 μm-thick silver layer. They determined that $T_e = 12$ eV while the pump-probe delay of 0.5 ns was considered sufficient to achieve thermal equilibrium between ions and electrons. In Fig. 5.10, the $W(k)$ from the NPA-HNC model is compared with the experimental data of Ref. [19] and with the DFT-MD simulations of Plagemann *et al.* [158]. The NPA-HNC and the DFT-MD calculations do not reproduce

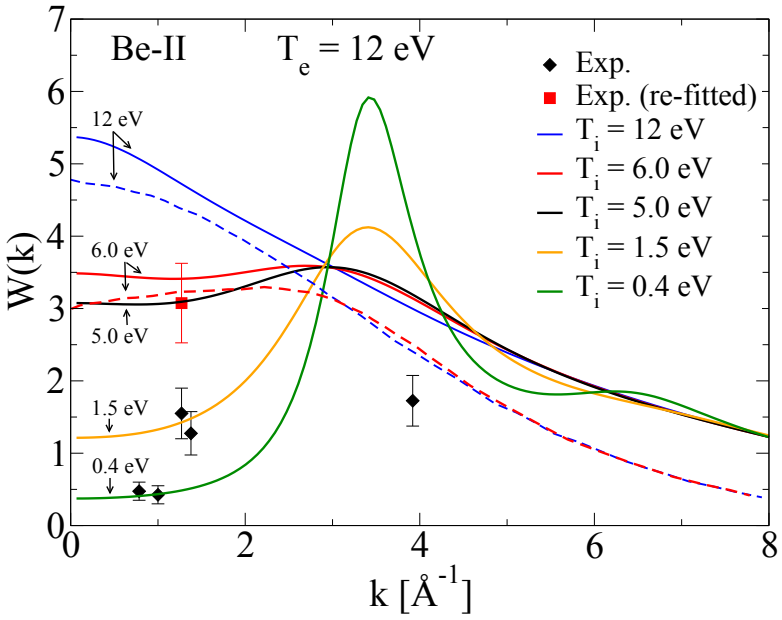

Figure 5.10. The XRTS ion feature $W(k)$ of Glenzer *et al* [19] compared with the $W(k)$ of the NPA-HNC model (full lines) and with the DFT-MD simulation (dashed lines) of Plagemann *et al* [158] for the equilibrium and $2T$ situations.

the original experimental data of Glenzer *et al.* nor the re-analyzed data using equilibrium conditions with $T_i = T_e = 12$ eV. By keeping $T_e = 12$ eV, Plagemann *et al.* found that it was possible to reproduce their (single) re-analyzed data point by setting $T_i = 6$ eV. In order to reproduce this point, the NPA-HNC model requires a slightly lower ion temperature of $T_i = 5$ eV. Within the NPA, it was impossible to reproduce all four original experimental points for $k < 2\text{Å}^{-1}$ with a single T_i. However, the first two points could be obtained with $T_i = 0.4$ eV while the two next points required $T_i = 1.5$ eV. Both models are not able to reproduce the point at $k = 3.9\text{Å}^{-1}$ since it is too low to be reproduced with any T_i. As in the case of isochoric compressed Be studied by Lee *et al.* [17], the NPA-HNC model predicts higher $W(k)$ values than DFT-MD simulations for all k. A comparison between the NPA-HNC and the DFT-MD $S(k)$ is shown in Fig. 5.11, demonstrating close agreement between results from the NPA pair potential and DFT-MD. Hence, in this case also the difference in $W(k)$ between the two methods comes from the difference in the core electron form factor $f(k)$, which is essentially similar to the compressed-Be case presented in Fig. 5.9. Whether the "superhard" pseudopotential used by Plagemann *et al.* or other plasma effects included in the NPA treatment, but not in the DFT-MD, may be responsible for differences in the

core electron density near the nucleus is unclear at present. We again note that the NPA is an "all-electron" method.

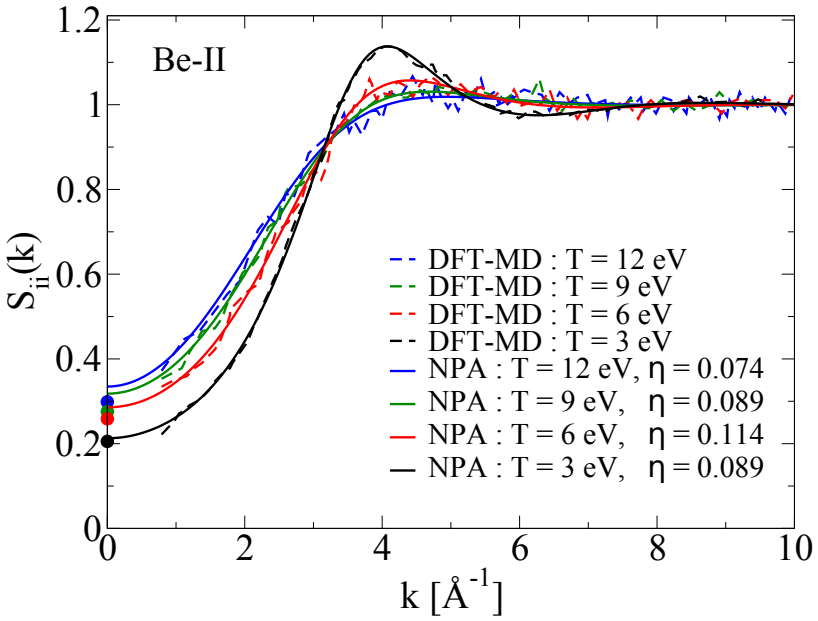

Figure 5.11. Static ion-ion structure factor $S(k)$ for Be-II from the NPA-HNC model and from the DFT-MD simulations of Plagemann *et al* [158], including the $k = 0$ values marked as dots, for different equilibrium temperatures.

5.4.3. Discussion of Be results

In addition to the differences between NPA-HNC and DFT-MD in the $k > 4$ Å^{-1} region for $W(k)$, we also observe a disparity at $k = 0$ for both Be systems studied here. Since the total electron form factor $N(k = 0) = 4$ is equal to the total number of electrons per ion, the divergence between the two models comes from the structure factor $S(k = 0)$ as shown in Figs. 5.9 and 5.11. It is very difficult to reach such low k values from DFT-MD simulations (because of the finite size of the simulation cell) and Plagemann *et al.* extracted them from independent thermodynamic calculations. As mentioned before, this quantity is important since it is linked to the compressibility κ via the sum rule $S(k = 0) = \rho T_i \kappa$. It should be noted that an accurate value of the compressibility κ should be determined from an EOS calculation, while the $S(k \to 0)$ limit, from an MHNC calculation, matches the EOS-κ only when the bridge contribution is optimal. Table 5. I compares calculations from the NPA-HNC method and from DFT-MD by Plagemann *et al.*. In both situations, the NPA-HNC

Table 5. I. Compressibilities κ (in a.u.) of WDM beryllium calculated using DFT-MD and NPA-HNC.

System	Be-I (Ref. [17])	Be-II (Ref. [19])
T_i $[eV]$	13.0, 9.00, 6.00, 3.00	12.0, 9.00, 6.00, 3.00
κ (DFT-MD)	3.72, 4.47, 4.69, 5.54	18.6, 22.8, 32,1, 50.1
κ (NPA-HNC)	3.89, 4.73, 5.32, 6.01	20.8, 26.3, 35.5, 52.8

compressibility is slightly higher than the DFT-MD, which is enough to affect the small-k region of the $W(k)$. This emphasizes the importance of experimental data for $k = 0$ in order to validate theoretical models and thermodynamics for WDM. On the other hand, we saw that, in the Be-II case, the two models are unable to predict the $k = 3.9$ Å^{-1} data and that it is impossible to reproduce all four original experimental points for $k < 2$Å^{-1} using one single-ion temperature. The extraction of $W(k)$ is highly dependent on how the other terms in the Chihara decomposition, in particular the free-free electron-electron structure factor $S^0_{ee}(k,\omega)$, are computed. The $S^0_{ee}(k,\omega)$ is directly linked to the imaginary part of the response function χ and most authors have been using the Mermin [159] formulation while including electron-ion collisions in the Born approximation. It has been recently pointed out that the Mermin approximation is not applicable to UFM systems because of inherent assumptions behind the model [155]. Recently, time-dependent-DFT-MD simulations have been done for Be [160] and it would be of interest to compare the total electron-electron dynamic structure factor $S_{ee}(k,\omega)$, including the bound-free contribution, in the WDM regime from these different models. Until a satisfactory model for $S_{ee}(k,\omega)$ is validated, it is hard to determine T_i via $W(k)$ but it should be kept in mind that a two-temperature system or other more complex situations might occur in laser-generated WDMs.

5.4.4. Temperature relaxation in Be

We consider the energy relaxation rate for the isochorically-heated beryllium (Be-II) where $\rho/\rho_0 = 1$, and for the particular $2T$-case with $T_e = 12$ eV and $T_i = 6$ eV. Here the electron-sphere radius $r_s \simeq 1.92$ and T_e is close to the Fermi energy $E_F^{\text{Be-II}} = 16.6$ eV. Hence this system is far less degenerate than the Al-I and Al-II systems discussed above. The Fermi golden-rule calculation using the f-sum rule gives a temperature relaxation time of 150-200 ps. Coupled-mode formation may slow this down by an order of magnitude. Hence the claimed delay of about 500 ps may not be enough to achieve equilibration. The difficulties in matching the experimental data with simulations also indicate that we do not have a properly equilibrated WDM-Be sample.

In the case of the compressed Be sample with $T_e = 13$ eV (Be-I), the f-sum-based relaxation time is nearly five times faster than for Be-II. Hence temperature-equilibration shortcomings cannot be an explanation for the difficulties encountered in modeling the data using a $2T$ approach. Difficulties in reproducing the $W(k)$ using NPA-HNC and DFT-MD suggest that the experimental characterization requires further attention.

5.5. Conclusion

We have presented parameter-free all-electron NPA-HNC calculations of the charge densities, pseudo-potentials, pair potentials and structure factors that are required to interpret XRTS experiments. Compressibilities, phonons, resistivities as well as temperature-relaxation times for relevant cases have been presented, using the NPA pseudopotentials and structure factors where needed. Re-analyzing recent WDM experiments enabled us to (a) investigate the validity of the commonly-used YSRR model by showing that both its short-ranged part and its screening part yield misleading predictions; (b) expose pitfalls in inverting structure data to obtain effective pair potentials; (c) examine possible $2T$-models and their temperature relaxation to examine the interpretations of $W(k)$ data from XRTS, emphasizing the need for caution in assuming thermal equilibrium in laser-generated WDM; and (d) demonstrate the accuracy of the NPA calculations of physical properties of electron-ion systems, from ambient temperatures and compressions to high temperatures and high compressions. The computational rapidity of the NPA-HNC model permits 'on-the-fly' testing-out of possible values of T_i, T_e and compressions that may rapidly fit an experiment, while this is time-consuming or impossible with DFT-MD simulations of properties like the ion feature $W(k)$ of WDM systems.

Acknowledgments

This work was supported by grants from the Natural Sciences and Engineering Research Council of Canada (NSERC) and the Fonds de Recherche du Québec - Nature et Technologies (FRQ-NT). We are indebted to Calcul Québec and Calcul Canada for generous allocations of computer resources.

Chapitre 6

ARTICLE IV : PROPRIÉTÉS DYNAMIQUES DE LA MATIÈRE COMPRESSÉE PAR CHOC

Cet article a été publié dans la revue *Physical Review E* **97**, 043210 (2018).

Contexte

Dans ce quatrième article, on s'intéresse aux propriétés dynamiques de la matière compressée par choc dans un régime à deux températures. Le FSD ion-ion contient énormément d'information sur les propriétés dynamiques du système et intervient dans la diffusion de rayons X. En effet, la structure du FSD à petites valeurs d'impulsion permet d'obtenir la vitesse du son ainsi que la relation de dispersion des modes acoustiques du fluide. Puisque le calcul du FSD s'obtient généralement à l'aide de simulations de DM, l'accessibilité à cette région du spectre nécessite une très grande cellule de simulation ce qui favorise l'utilisation de potentiels de paires au lieu d'utiliser la TFD pour calculer les forces interioniques.Dans le cas de systèmes à deux températures, ses propriétés dynamiques auront un sens physique à condition que les corrélations ion-ion spatio-temporelles disparaissent dans un temps inférieur au temps de thermalisation électron-ion. Finalement, la comparaison entre les équations d'état de la matière à l'équilibre et celle à deux températures illustre les importantes différences de ces deux régimes.

Contributions

— Calcul du facteur de structure dynamique (FSD) pour l'aluminium à l'équilibre et en quasi-équilibre avec les potentiels de paires du modèle NPA et comparaison avec des calculs ab initio de la littérature.

— Vérification que les corrélations spatio-temporelles disparaissent suffisamment rapidement pour établir un régime à deux températures.

— Comparaison entre la vitesse du son obtenue par le FSD et par la compressibilité.

— Calcul de l'énergie libre, de l'énergie interne et de la pression pour la système à deux températures et comparaison avec le système à l'équilibre.

— Rédaction de la première version de l'article

Ion-ion dynamic structure factor, acoustic modes and equation of state of two-temperature warm dense aluminum

Louis Harbour[1], Daniel Förster[1], M. W. Chandre Dharma-wardana[2], Laurent J. Lewis[1]

[1]*Département de Physique and Regroupement Québécois sur les Matériaux de Pointe, Université de Montréal, C.P. 6128, Succursale Centre-Ville, Montréal, Québec, Canada H3C 3J7*

[2]*National Research Council of Canada, Ottawa, On., Canada K1A 0R6*

Abstract

The ion-ion dynamical structure factor and the equation of state of warm dense aluminum in a two-temperature quasi-equilibrium state, with the electron temperature higher than the ion temperature, are investigated using molecular-dynamics simulations based on ion-ion pair potentials constructed from a neutral pseudoatom model. Such pair potentials based on density functional theory are parameter-free and depend directly on the electron temperature and indirectly on the ion temperature, enabling efficient computation of two-temperature properties. Comparison with *ab initio* simulations and with other average-atom calculations for equilibrium aluminum shows good agreement, justifying a study of quasi-equilibrium situations. Analyzing the van Hove function, we find that ion-ion correlations vanish in a time significantly smaller than the electron-ion relaxation time so that dynamical properties have a physical meaning for the quasi-equilibrium state. A significant increase in the speed of sound is predicted from the modification of the dispersion relation of the ion acoustic mode as the electron temperature is increased. The two-temperature equation of state including the free energy, internal energy and pressure is also presented.

Keywords: Dynamic structure factor, ion accoustic modes, speed of sound, equation of state, two-temperature system

6.1. Introduction

The challenge of modeling warm dense matter (WDM) — a system of strongly-coupled classical ions and partially degenerate electrons at high temperature and high density — is central to understanding many physical systems such as the interior of giant planets [161], laser machining and ablation [92], and inertial-confinement fusion [162]. In WDM, neither the kinetic energy nor the potential energy can be treated as a perturbation. Hence the usual theoretical techniques of classical plasma physics or solid-state physics become inapplicable. In the laboratory, WDM can be created through the interaction of high-energy short-pulse lasers with simple metals such as aluminum [48, 49] and beryllium [17], with densities ρ several times the room density ρ_0 and temperatures of the order of 1 eV. The importance of treating these systems as two-temperature WDM systems rather than equilibrium systems has not always been appreciated in analyzing the experimental results [155, 109].

The ion-ion dynamic structure factor (DSF) $S(\mathbf{k},\omega)$ is a key quantity for understanding the WDM regime. For instance, it contains information on the longitudinal waves propagating in the system. The DSF can be measured by neutron scattering and indirectly via X-ray Thomson scattering (XRTS) [2]. The Chihara decomposition [21] has been applied to describe the XRTS signal by partitioning the total electron-electron DSF $S_{ee}(\mathbf{k},\omega)$ in the following form :

$$S_{ee}(\mathbf{k},\omega) = S^0_{ee}(\mathbf{k},\omega) + N(\mathbf{k})S_{ii}(\mathbf{k},\omega) + S^{fb}_{ee}(\mathbf{k},\omega). \tag{6.1}$$

Here S^0_{ee} is the free electron-electron DSF, S^{fb}_{ee} is the contribution from transitions between bound and free electrons, $N(\mathbf{k}) = n_b(\mathbf{k}) + n_f(\mathbf{k})$ is the total electron form factor split into a bound part n_b and a free part n_f, and S_{ii} is the ion-ion DSF. Using this decomposition, simulations combining standard density functional theory (DFT) with molecular dynamics (MD) simulations have been used [48, 49, 145, 146] to extract properties of WDM systems such as the free electron density per ion n_e (i.e., $\bar{Z}$), the ion density ρ, the electron temperature T_e and the ion temperature T_i. Since these simulations are computationally expensive, the use of a simpler approach such as the neutral pseudoatom (NPA) model is appropriate. The NPA is well adapted to extract the ion part of the XRTS signals [109] and will be the principal method used in this work, where we show that the NPA also has the needed accuracy. The XRTS spectrum can be computed in the NPA, and also by other means without using the Chihara decomposition [135, 163] but its discussion is not needed for this work.

However, the separation between ion acoustic modes $\Delta\omega = 2\hbar\omega_p$, with ω_p the ion-plasma frequency, is of the order of 1 meV, significantly lower than the bandwidth of any X-ray probe laser used experimentally at the moment. Thus, the ion-ion DSF is usually approximated by

its static form $S(k,\omega) = S(k)\delta(\omega)$ in describing the XRTS signal. Nevertheless, the ion-ion DSF contains important information about the ion transport properties linked to electron-ion equilibration, formation of coupled modes, interaction with projectiles, etc., which makes it a key quantity for fully understanding the WDM regime. With X-ray laser sources being improved, the ion-ion DSF should become available from future experiments, motivating its calculation for both equilibrium and quasi-equilibrium situations.

Furthermore, in the limit of small wavevectors, $k \to 0$, the ion-ion DSF can be described in a hydrodynamic framework [66] (see below), providing important physical quantities such as the adiabatic velocity of sound, the ion acoustic dispersion relation, the thermal diffusivity and the sound attenuation coefficient. In addition, in the case of simple metals commonly probed in most XRTS experiments, the laser interacts mainly with the free-electron subsystem, creating a non-equilibrium system where the electron temperature T_e is higher than the initially cold ions at temperature T_i. It has been shown that, when the shock wave resulting from the laser pulse has propagated through the sample and reaches the probing location, the system might still be in a two-temperature ($2T$) state [109, 155]. Since the ion-ion interactions in simple metals are related to the screening of the free-electron subsystem, the quasi-equilibrium properties of the total system with $T_e \neq T_i$ differ significantly from the equilibrium ones. The hardening of the phonon spectra in ultra-fast matter [123, 164, 29], where T_e is about 1 eV while T_i remains at room temperature T_r, is an example of how the ion dynamics can be affected drastically in such conditions. Transport properties of Al in the two-temperature regime, such as self-diffusion and shear viscosity, are also significantly modified [165].

The ion-ion DSFs for WDM have been calculated mainly using DFT coupled to classical molecular dynamics (MD) [145] simulations. Since DSF calculations require a large number of particles and long simulation times, DFT-MD calculations are computationally very intensive. In addition, the finite-T treatment of the electronic subsystem in DFT requires the solution of the Kohn-Sham equations for many electronic bands to take thermal excitations according to the Fermi-Dirac distribution into account. Orbital-free (OF) DFT simulations do not require electronic wave functions, but require a Hohenberg-Kohn kinetic-energy functional as well as a finite-T generalization thereof. Such procedures are less accurate than the Kohn-Sham method, but make the simulations practical [46]. The full DFT-MD simulations when feasible can be used to benchmark simpler methods like the NPA or OF approaches which are easily applied over a wider range of temperatures and densities.

In the present work, we compute the ion-ion DSF using classical MD simulations based on pair potentials (PP) constructed from the NPA model, which is a fully based on DFT.

The NPA approach has already been used to predict the DSF of strongly-coupled hydrogen plasmas [166] and provides the sound velocity, the thermal diffusivity, the specific-heat ratio, and the viscosity. The NPA-PPs are free of *ad hoc* parameters and are accurate to within a few meV as established by the prediction of accurate experimental phonon spectra for simple WDM solids [123, 164]. The NPA-PP-predictions for static structure factors (SSF) obtained using the modified-hyper-netted-chain (MHNC) approximation are in agreement with DFT-MD simulations for WDM systems (typical examples are Be and Al [109] ; for a review of the NPA, see Ref. [115]).

Furthermore, in the quasi-equilibrium case, i.e. when T_e is different from T_i, the extension of the NPA approach to two-temperature ($2T$) situations has enabled the construction of $2T$-PPs which reproduce *ab initio* calculations of quasi-equilibrium phonon spectra [164], quasi-equilibrium XRTS signals [109], and frequency-dependent $2T$ plasmon profiles [155] and conductivities of ultra-fast matter [167]. The objective of the present study is to determine the DSF $S(k,\omega,T_e,T_i)$ in the $2T$ regime. In addition, we evaluate the $2T$ equation of state (EOS). All calculations are carried out for aluminum at the 'room temperature' density of $\rho_0 = 2.7$ g/cm^3 with the ion temperature fixed at $T_i = 1$ eV while the electron temperature T_e is varied between 1 and 10 eV.

6.2. Methods

6.2.1. Neutral-pseudoatom model

The NPA model [88, 89, 63] is a rigorous all-electron DFT average-atom approach where the ion distribution is also treated in DFT [61]. Given the mean free-electron density n and electron temperature T_e, it determines the total electron density around a *single Kohn-Sham ion* constructed from a nucleus of charge Z_n embedded in the plasma environment of mean density ρ. A classical Kohn-Sham equation for the ions determines the one-body ion distribution $\rho(r) = \rho g_{ii}(r)$, where $g_{ii}(r)$ is the ion pair distribution function (PDF), abbreviated to $g(r)$. The classical Kohn-Sham equation for the ions is identified as a type of hyper-netted chain (HNC) integral equation bringing in ion-ion correlations beyond the mean-field approximation. The Kohn-Sham-Mermin solutions are obtained in the local-density approximation using a finite-T_e free-energy exchange-correlation (XC) functional $F_{xc}[n,T_e]$ [84]. The available finite-T XC-functionals, fitted to quantum Monte-Carlo results or to the classical-map HNC results (used here), yield numerically equivalent results in WDM applications [168].

In order to simulate the effect of the ion-density $\rho(r)$ on the electronic states, a uniform positive neutralizing background with a spherical cavity of radius $r_{\rm ws}$, with the nucleus at

the origin, is used. Here, $r_{\rm ws} = [3/(4\pi\rho)]^{1/3}$ is the Wigner-Seitz radius of the ion. This lowest-order model for $\rho(r) = \rho g(r)$ is sufficient for calculating the Kohn-Sham energy levels of "simple metal" ions immersed in a warm dense electron fluid, as has been discussed in a recent review [115]. The adjustment of the ion distribution to the electron distribution is accomplished by the optimization of a single parameter, viz. $r_{\rm ws}$, subject to the finite-T Friedel sum rule [61]. Although, strictly speaking, an electron-ion exchange-correlation functional is also needed [112], it is neglected here.

An advantage of the NPA model is that it directly provides single-ion properties such as the mean ionization $\bar{Z}$ and the electron density around the nucleus $n(r) = n_b(r) + n_f(r)$, with n_b and n_f the bound and free electron densities, respectively. In simple metals, n_b is found to be localized within a radius much smaller than $r_{\rm ws}$, such that $n_b(r \to r_{\rm ws}) = 0$, which enables a clear definition of the mean ionization $\bar{Z} = n - n_b$. Note however, that the free-electron distribution is *not* restricted to the WS-sphere, as is done in many average-atom (AA) models, as reviewed by, e.g., Murillo *et al.* [54].

The free electrons occupy the whole space, modeled by a large correlation sphere of radius R_c of about 10 WS radii, usually sufficient to include all particle correlations associated with the central nucleus. Unlike in AA models, the mean number of free electrons per ion, viz. $\bar{Z}$, is an unambiguously defined quantity subject to the Friedel sum rule, and experimentally measurable using XRTS [2], static conductivities, Langmuir probes, etc. The interaction among ions of charge $\bar{Z}$ is screened by the free electron subsystem which is assumed to respond linearly to the electron-ion pseudopotential

$$U_{ei}(k,T_e) = n_f(k)/\chi(k,T_e). \tag{6.2}$$

Since $n_f(k)$ is determined by the Kohn-Sham calculation which goes beyond the linear response to $\bar{Z}/r$, the above pseudopotential actually includes all the non-linear DFT effects within a linearized setting. The limits of validity of this procedure are discussed in Ref. [105].

With $n_f(k)$ at hand, U_{ei} is constructed using the finite-T interacting electron response function

$$\chi(k,T_e) = \frac{\chi_0(k,T_e)}{1 - V(k)[1 - G(k,T_e)]\chi_0(k,T_e)} \tag{6.3}$$

with χ_0 the finite-T non-interacting Lindhard function, $V(k) = 4\pi/k^2$ the bare Coulomb interaction, and G a finite-T local-field correction [123] which depends directly on F_{xc}. Finally, the screened ion-ion pair interaction is given by

$$V_{ii}(k,T_e) = \bar{Z}^2 V(k) + |U_{ei}(k,T_e)|^2 \chi(k,T_e); \tag{6.4}$$

This pair potential is the NPA input to the classical MD calculations.

It should be noted that the NPA uses a pair-potential for the ions and does not attempt to include multi-ion potentials, as is customary in effective medium (EM) approaches that have been successfully used for metals and semiconductors, especially at ambient temperature and compression. The EM method is at best a non-selfconsistent DFT approach [169] which includes two-body, three-body and other multi-ion effects. It is often further extended by fitting to empirical and calculational databases. However, recent attempts to use such models for, e.g., WDM carbon, have not been very successful [170]. The NPA approach exploits the fact that the grand potential $\Omega[n,\rho]$ is a functional of *both* the one-electron distribution $n(r)$ and the one-ion distribution $\rho(r)$. Hence a single-ion description (which allows a pair potential) is the only rigorously necessary information for a full DFT description of the system. In practice, pair potentials are sufficient if linear-response pseudopotentials could be constructed, as in Eq. 7.6. However, this approach now needs, not only an XC-functional for the electrons, but also a correlation functional for the classical ions. These are constructed via classical integral equations, or automatically via MD simulations. Detailed discussions of these issues and the NPA method may be found in Refs. [116, 115]. In this context, we remark that standard implementations of DFT-MD in codes like ABINIT and VASP [38, 40] use only the one-electron density-functional property, and *not* the one-ion density functional, as it chooses to implement a full N-ion Kohn-Sham simulation with N typically of the order of 100 or more.

Furthermore, the multi-center nature of the simulations implies a highly non-uniform electron density requiring sophisticated gradient-corrected XC-functionals. In contrast, the NPA uses a relatively smooth single-center electron distribution for which the local-density approximation (LDA) is found to work very well, even for sensitive properties like the electrical conductivity [167] and plasmon spectral line shapes [155]. The LDA form of the finite-T XC-functional of Perrot and Dharma-wardana [84] is used in this study.

6.2.2. Dynamic Structure Factor

The ion-ion spatial and temporal correlations are determined from the van Hove function

$$G(\mathbf{r},t) = \frac{\langle \rho(\mathbf{r},t)\rho(\mathbf{0},0)\rangle}{\rho} = \frac{1}{N}\left\langle \sum_{i=1}^{N}\sum_{j=1}^{N} \delta[\mathbf{r} - \mathbf{r}_j(0) - \mathbf{r}_i(t)] \right\rangle \tag{6.5}$$

with $\langle \cdots \rangle$ the ensemble and time average (over many different time origins) calculated from classical MD simulations of a N-particle system, ρ the mean ion density, and $\mathbf{r}_i(t)$ the position

of the i-th ion at time t. The ion-ion DSF

$$S(\mathbf{k},\omega) = \frac{1}{2\pi}\int_{-\infty}^{\infty} F(\mathbf{k},t)\ e^{i\omega t}dt \tag{6.6}$$

is the time Fourier transform of the intermediate scattering function $F(\mathbf{k},t)$, which is itself the spatial Fourier transform of the Van Hove function

$$F(\mathbf{k},t) = \int G(\mathbf{r},t)e^{-i\mathbf{k}\cdot\mathbf{r}}d\mathbf{r}. \tag{6.7}$$

While $G(\mathbf{r},t)$ contains much information relevant to $2T$ situations, $F(\mathbf{k},t)$ is also directly accessible in MD simulations via the relation

$$F(\mathbf{k},t) = \frac{1}{N}\langle\rho_{\mathbf{k}}(t)\rho_{-\mathbf{k}}(0)\ \rangle \tag{6.8}$$

where

$$\rho_{\mathbf{k}}(t) = \sum_{i}^{N} e^{i\mathbf{k}\cdot\mathbf{r}_i(t)}, \tag{6.9}$$

thus avoiding the calculation of the spatial Fourier transform which can add spurious high-frequency oscillations to $F(\mathbf{k},t)$ due to the finite size of the MD simulation cell. Under WDM conditions, the averaged system properties are those of an isotropic fluid; thus important structural quantities are spherically-symmetric in real space, $|\mathbf{r}| = r$, and in reciprocal space, $|\mathbf{k}| = k$.

In the hydrodynamic limit, $k \to 0$, the DSF takes the so-called 'three-peak' form

$$\begin{aligned} S(k,\omega) = \frac{S(k)}{2\pi}\Bigg[\left(\frac{\gamma-1}{\gamma}\right)\frac{2D_T k^2}{\omega^2 + (D_T k^2)^2} \\ + \frac{1}{\gamma}\left(\frac{\Gamma k^2}{(\omega - c_s k)^2 + (\Gamma k^2)^2} + \frac{\Gamma k^2}{(\omega + c_s k)^2 + (\Gamma k^2)^2}\right)\Bigg] \end{aligned} \tag{6.10}$$

with D_T the thermal diffusivity, Γ the sound attenuation coefficient, $\gamma = c_P/c_V$ the ratio of the constant pressure to the constant volume specific heats, c_p and c_V, and c_s adiabatic speed of sound. The second and third terms of Eq. 6.10 are the Brillouin peaks whose positions provide the acoustic dispersion relation $\omega_s(k)$, which is linear at small k, $\omega_s(k \to 0) = c_s k$, and is measurable experimentally. In addition, it is also possible to compute c_s from the SSF $S(k)$ using the compressibility κ sum rule $S(0) = \rho\kappa T_i$ which leads to $c_s = \sqrt{T_i/S(0)}$. Once the PP is constructed, the SSF can be easily calculated via the MHNC procedure, independent of MD simulations.

6.2.3. Equation of State

The total free energy per atom in the NPA model is given by

$$F = F_e^0(T_e) + F_{\rm emb}(T_e) + F_{ii}(T_i,T_e) + F_i^0(T_i), \tag{6.11}$$

with contributions F_e^0 from the interacting homogeneous electron gas, $F_{\rm emb}$ from the embedding of the pseudoatom into the uniform system, F_{ii} from the interacting ion-ion system, and F_i^0 from the ideal ion gas. A more detailed description of each term of the NPA free energy is given in Refs. [63, 64]. For the equilibrium system, the pressure is obtained via the density derivative of the free energy while the internal energy is obtained by taking the temperature derivative :

$$P = n^2\frac{\partial F}{\partial n}, \qquad E = \frac{\partial(\beta F)}{\partial \beta} \tag{6.12}$$

with $\beta = 1/T$. For quasi-equilibrium systems, the internal energy must be computed taking into account the temperature derivative of each contribution in Eq.6.11. Note that the term F_{ii} depends on both T_i and T_e. Thus, the total derivative of the $2T$ internal energy reads

$$E(T_e,T_i) \equiv \frac{\partial(\beta F)}{\partial \beta} = F + \left.\frac{\partial F}{\partial \beta_e}\right|_{T_i} + \left.\frac{\partial F}{\partial \beta_i}\right|_{T_e} \tag{6.13}$$

which recovers the correct equilibrium internal energy when $T_i = T_e$.

6.3. Results

All DSF have been calculated from MD simulations using the NPA pair potentials. The initial configuration was a face-centered cubic crystal containing 5324 particles arranged in a cubic simulation cell. This corresponds approximately to a linear dimension of 17 to 18 Wigner-Seitz radii, i.e., significantly larger than typical ion-ion correlations seen in the ion-ion pair distribution of aluminum even at its melting point. Simulations were carried out over 0.5 ns with a timestep of 0.5 fs. The first 50,000 steps have not been used as they pertain to the initial equilibration period. From the remaining simulation, configurations have been extracted every 1 fs for the calculation of $G(r,t)$ and $F(k,t)$ which have been calculated up to 3000 fs. The ion temperature was kept constant throughout the simulation using a Nosé-Hoover thermostat. The electron temperature no longer appears in the dynamics, so no electron thermostat is needed ; T_e only intervenes in the construction of the NPA pair potential, which is the essential 'quantum input' to the classical MD simulation.

In the range of T_e studied in this work, i.e. from 1 to 10 eV, the mean ionization calculated from the NPA model remained essentially unchanged from the room temperature value of

$\bar{Z}$ = 3.0000 to 3.0163 for the normal density of 2.7 g/cm^3. Given a Fermi energy (i.e, approximately the chemical potential) of $\sim$ 12 eV, no significant change in $\bar{Z}$ is in fact expected. There is even less of a change at the higher density of 5.2 g/cm^3 used by Rüter *et al* [145], as the Fermi energy is correspondingly higher. The value of $\bar{Z}$ for Al begins to increase only from about 20 eV, and the consistency of the NPA evaluated $\bar{Z}$ even at higher temperatures is shown from its successful prediction of electrical conductivities of aluminum under a variety of WDM conditions [167, 171].

6.3.1. Static properties

We first review the results for several key static properties, viz. pair-potentials, PDFs, and structure factors.

6.3.1.1. *Pair-potentials*

The easily computed NPA ion-ion pair-potentials described by Eq. 6.4 are the starting point of our study of the aluminum DSF, using classical molecular dynamics with the NPA-PPs as the input. Hence, in Fig. 6.1 we show typical Al-Al pair potentials that are relevant to our study. These pair potentials are the simplest that can be constructed from the NPA density, while the NPA calculation provides enough data to construct more complex non-local pseudopotentials, or potentials designed to recover phase shifts, etc. However, such elaborations need to be invoked only if such potentials are really required. We have found that this elementary approach works well for simple metallic fluids in regimes of compressions of 0.5 to about 2.5, and from low temperatures (e.g., melting point) to higher temperatures (where the model works better). In the present study (aluminum at 2.7 g/cm^3, and 5.2 g/cm^3, at T=1 eV and 5.4 eV, the model is eminently applicable, as we show by comparisons with more microscopic simulations for the PDFs and other properties given below. Panels (a), (b) show the crucial role played by the Friedel oscillations in the potentials. These are evident in the potential at T_e = 1 eV and more weakly in the 3.5 eV potential. At high T_e, they are damped out and the potentials become more Yukawa-like. The NPA model faithfully reproduces these potentials to good accuracy, whereas many commonly-used average-atom models do not. The location of these oscillations, as well as packing effects in the fluid, are controlled by $r_{\rm ws}$. Hence the plot using $r/r_{\rm ws}$ as the x-coordinate brings potentials at different densities to a comparable footing. We also show the pair-potential at 5.2 g/cm^3 and T=3.5 eV calculated using the T=0 XC-functional that is customarily implemented in DFT-MD simulations, showing a small and probably negligible difference. However, it should

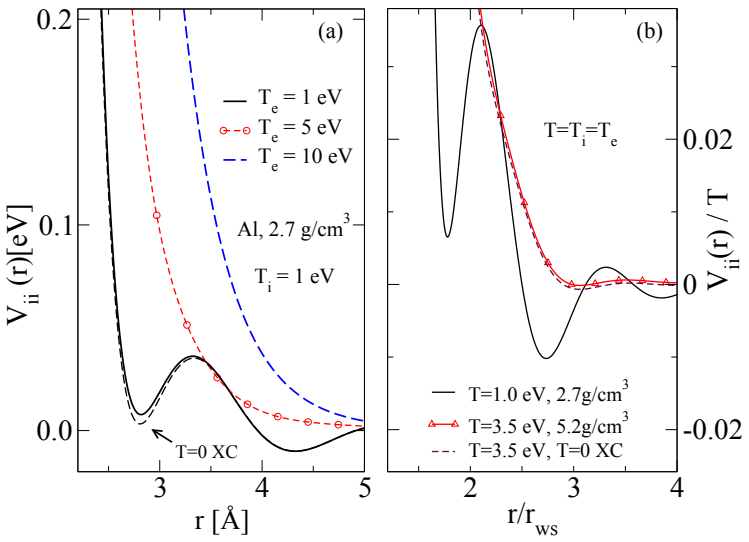

Figure 6.1. (color online) (a) Ion-ion pair potentials constructed from the NPA model at electron temperatures of T_e = 1, 5, and 10 eV, while the ion temperature is held at T_i = 1 eV. (b) The $T_i = T_e$ = 1 eV potential for the 'room temperature' Al density 2.7 g/cm^3, as well the pair potential at 5.2 g/cm^3 and T=3.5 eV relevant to the work of Rüter Rütter and Redmer [145]. Note that in panel (b) we have plotted the potentials in terms of physically relevant variables $r/r_{\rm ws}$ and $V_{ii}(r)/T$, where the nominal WS radii $r_{\rm ws}$ are 2.991 a.u. and 2.404 a.u, respectively.

be always remembered that standard DFT-MD simulations can be used to benchmark other calculations only when the $T = 0$ XC approximation holds.

6.3.1.2. *Pair Distribution Function*

The NPA-PPs are known to closely reproduce the ion-ion PDF $g(r)$ and the corresponding static structure factor $S(k)$ for most systems studied so far, for compressions of 0.5 to about 2.5. Some examples are :
(i) Al (a) at normal density $\rho = 2.7$g/cm^3 and at the melting point, and (b) at an expanded density $\rho = 2.0$ g/cm^3 with T = 1,000K and 5,000K [172],
(ii) Li at $T = 2000$ K and $\rho = 0.85$ g/cm^3[164],
(iii) Be at densities of $\rho = 1.85$ g/cm^3 and $\rho = 5.53$ g/cm^3 for various two-temperature situations [109], and
(iv) C, Si and Ge in the WDM state [113, 173]. Here, because of the high electron density ($\bar{Z} = 4$) the NPA model works even at 12 g/cm^3, i.e, close to six times the graphite density.

While liquid metal PDFs can be obtained from MD simulations using multi-center potentials such as those available from EM theory [169], embedded-atom model (EAM) approaches [174], or bond-order potentials [175], they have not been applied in an intensive way to the WDM regime. The effect of T_e on the ion-ion interaction is not included except in limited cases [176]. Kraus *et al.* [170] examined the use of multi-ion bond-order potentials for WDM carbon but found them to be unsuitable and extremely difficult to formulate for finite-T usage. In contrast, the NPA-PPs are simple to compute and are at finite-T from the outset. Here we show that the PDFs obtained from them agree closely with those from DFT-MD for the systems studied here.

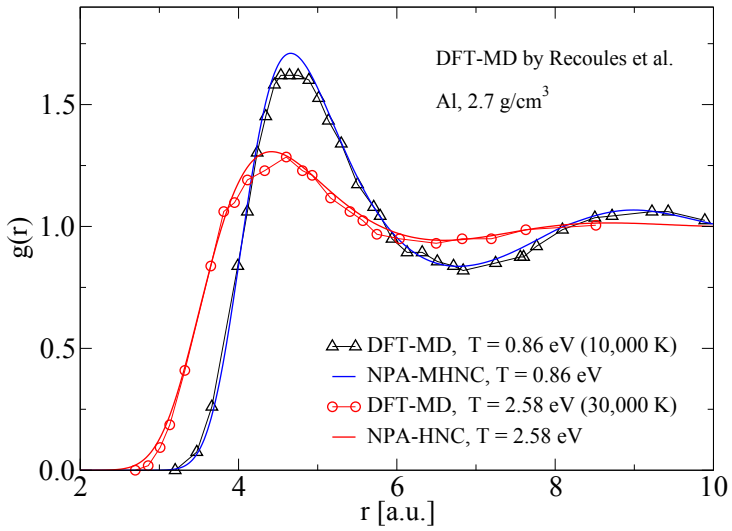

Figure 6.2. (color online) A comparison of the $g(r)$ from the NPA-MD and from DFT-MD simulations (Recoules *et al.* [177] for Al at the normal density ρ_0 and at 10,000K and 30,000K. No bridge terms are needed at the higher T case, where HNC and MHNC become equivalent).

In Fig.6.2 NPA PDFs for aluminum at the 'normal' density ρ_0 are compared with DFT-MD simulations from Recoules *et al* at 10,000 K and 30,000 K [177]. The agreement is relatively good. The slight disagreement ($\sim$ 4%) noted near the main peak is a common feature in this type of comparison, arising from statistical noise in MD simulations with, say $N \sim 100$ atoms. Here one may expect fluctuations of $\sim 1/\sqrt{N}$. In reality, the need to take an ensemble average of every quantity in DFT-MD simulations adds to the labour and cost. In Fig.6.3, we compare the PDF for Al obtained from the NPA pair potentials with that from Kohn-Sham DFT-MD simulations for two cases. The first case (panel (a) in

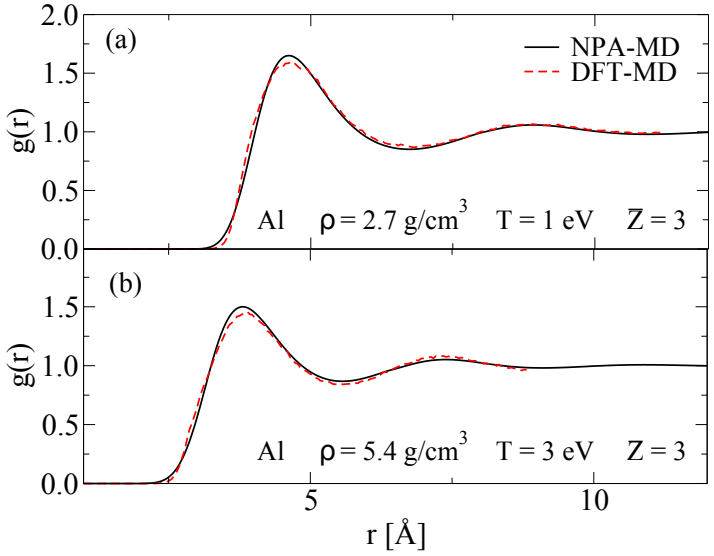

Figure 6.3. (color online) Comparison of the $g(r)$ from the NPA-MD and from DFT-MD simulations for two Al WDM states : (a) ρ at the room temperature density of 2.7 g/cm^3, $T = 1$ eV, and (b) $\rho = 5.4$ g/cm^3, $T = 3$ eV.

Fig.6.3) is for the room temperature density $\rho = 2.7$ g/cm^3 at a temperature $T = 1$ eV, which gives one of the equilibrium WDMs used in this study. The second case (panel (b) in Fig.6.3) is for the compressed density $\rho = 5.4$ g/cm^3 at a temperature $T = 3$ eV which is close to the conditions used by Rüter and Redmer [145] in their DFT-MD calculation of the aluminum DSF. The latter is used in section 6.3.2 to compare with our NPA-MD DSF. Our DFT-MD simulations were done with the ABINIT package using a cell of 108 atoms with a norm-conserving pseudopotential and the $T = 0$ Perdew-Burke-Ernzerhof exchange and correlation functional within the generalized gradient approximation. In this case, the position of the first maxima in $g(r)$ are within 1% of each other for the first case (a) and within 2% at for the second case (b). The height of the first peak differs by about 3% in both cases showing the good aggreement between DFT-MD and NPA-MD simulations. The use of pair potentials to perform classical MD simulations requires a considerably shorter amount of time illustrating the advantage of employing the NPA model.

6.3.1.3. *Static Structure Factor*

As indicated in Sec.6.2.2, c_s can also be calculated from the SSF using the compressibility sum rule. In Fig. 6.4, we compare the $S(k)$ computed from HNC, MHNC and MD simulations all using the same pair potential. We note that the MHNC SSF and the MD SSF agree very

well, while the HNC predicts a slightly lower maximum and a slightly different $k = 0$ limit. This suggests that the differences may be due to the use of a hard-sphere model within the Lado-Foiles-Ashcroft criterion for modeling the bridge function [68]. In principle, more accurate bridge functions can be extracted from MD simulations.

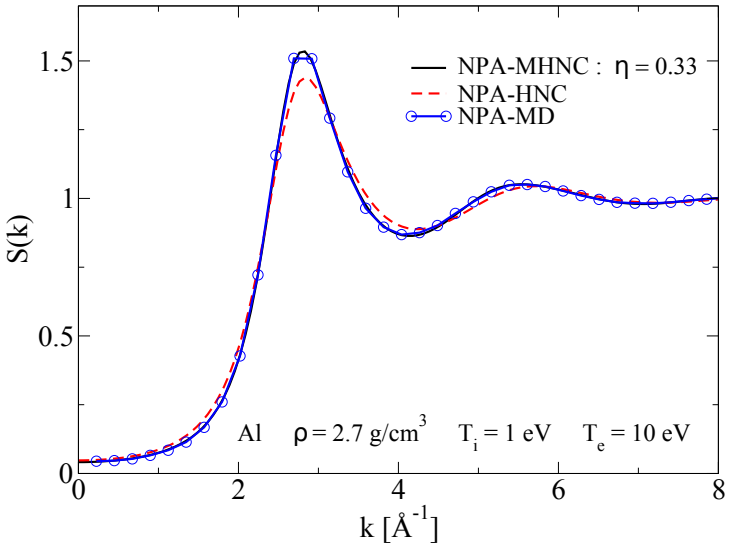

Figure 6.4. (color online) $S(k)$ computed from MHNC (continuous line), HNC (red dashed line) and MD (blue circles and blue line) simulations at T_i=1 eV and T_e=10 eV.

6.3.2. Dynamical properties

6.3.2.1. *Dynamical Structure Factor : Equilibrium system*

In this section, the DSF for equilibrium Al, $T_i = T_e$, obtained from the NPA-PP, is compared with other DSF calculations. First we consider the results of Rüter and Redmer [145] who used Kohn-Sham DFT-MD to study Al at a density of $\rho = 5.2$ g/cm^3 (compression ~ 2) and $T = 3.5$ eV, i.e., $T/E_f \simeq 0.19$. In Fig.6.5, the NPA-MD DSF is compared with the DFT-MD DSF for $k = 0.42$ Å^{-1} and $k = 0.69$ Å^{-1}. The position and profile of the Brillouin peak obtained from the NPA-MD agree closely with results from DFT-MD. Furthermore, the speed of sound obtained by Rüter and Redmer, $c_s = 10.38$ km/s, and the NPA value of $c_s = 10.62$ km/s are within 2.3% of each other. In this case, the NPA calculation satisfies the f-sum rule to within 96% over the range of k studied.

Since a full Kohn-Sham DFT-MD calculation as given by Rüter *et al.* [145] for the the DSF is extremely costly, simpler approaches based on average-atom models as well as orbital-free

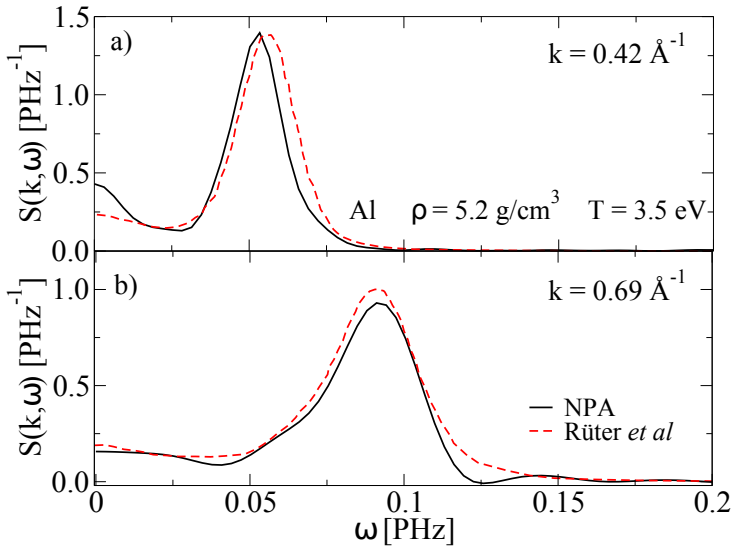

Figure 6.5. A comparison of the dynamic structure factors obtained from NPA-MD (this work) and DFT-MD [145] at two different wavevectors. In NPA-MD, the pair potential (Eq. 6.4) is the input to simulation.

methods have been used to compute the ion-ion DSF. Here we compare the results from the NPA-MD with corresponding results from the pseudoatom model of Starrett and Saumon [57](PA-SS), and with OF-DFT-MD simulations, for Al at the density ρ_0 and $T = 5$ eV. A comparison of our NPA-MD calculations with the OF-DFT-MD simulations of White *et al.* [46] and those of Gill *et al.* [178], using the PA-SS and MD, is presented in Fig. 6.6 for wavevectors $k = 0.45$ Å^{-1} and 0.96 Å^{-1}. White *et al.* used 108 ions in a cubic supercell in an OF-DFT approach. Gill *et al.* presented an OF model calculation with a classical simulation with 10,000 ions, and also a Kohn-Sham (KS) approach within their PA-SS model. Since our NPA model uses the KS procedure, only the KS-PA-SS results are compared in Fig. 6.6.

The positions of the Brillouin peak for $k = 0.45$ Å^{-1} coincide for OF-DFT-MD and NPA-MD, and the peak heights differ by ∼4%. The adiabatic speed of sound $c_s = \omega_s/k$ was obtained by a linear fit to the dispersion relation $\omega_s(k)$ for small value of k. The OF-DFT-MD predicts an adiabatic speed of sound of 10.4 km/s, very close to the NPA-MD value of 10.2 km/s whereas the PA-SS-MD predicts a higher value of 12.7 km/s. Once again, we ensured that the NPA calculation satisfies the f-sum rule to within 97% over the range of k studied. The good agreement between the equilibrium DSF calculated via the NPA-MD and OF-DFT-MD mutually confirm the extent of validity of these methods and of the NPA-MD approach. We already noted the good agreement with the fully microscopic calculations

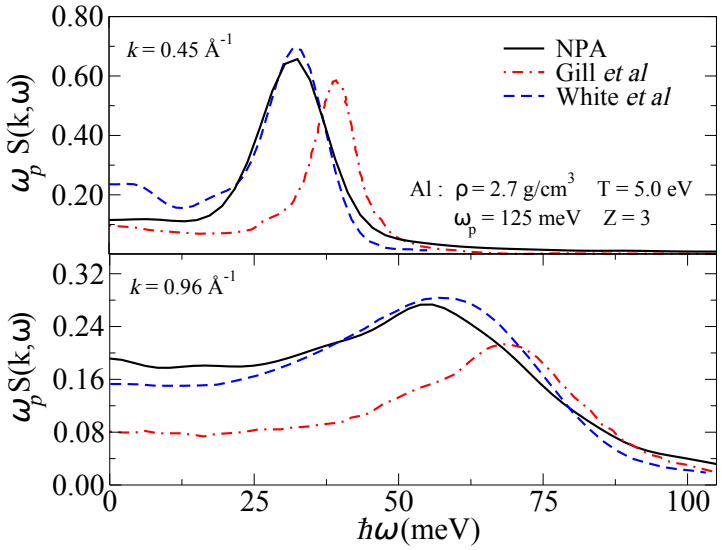

Figure 6.6. (color online) The equilibrium DSF of Al at density $\rho = \rho_0$ and $T = 5$ eV, for wavevector $k = 0.45$ Å^{-1} (upper panel) and 0.96 Å^{-1} (lower panel) : NPA (black continuous line), PA-SS [178] (red dot-dashed line) and OF-DFT-MD [46] (blue dashed line).

of Rüter *et al* [145]. All these encourage us to apply $2T$-NPA-PP to investigate dynamical properties of quasi-equilibrium systems where $T_e \neq T_i$.

6.3.2.2. *Dynamical Structure Factor : Quasi-equilibrium system*

In order to study the ion dynamics in the quasi-equilibrium system with $T_e > T_i = 1$ eV, we employ the ion-ion pair potential $V_{ii}(r,T_e)$ constructed from the NPA calculation which explicitly depends directly on T_e. The dependence on T_i comes in via the ion density and the ionization state $\bar{Z}$ of the ions, and hence is implicitly included in the NPA calculation. In Fig. 6.1(a) we present the potentials for the cases $T_e = 1$, 5, and 10 eV. At $T_e = 1$ eV, the potential exhibits Friedel oscillations with several minima, whereas it becomes purely repulsive at higher temperatures since the Fermi energy at 2.7 g/cm^3 is 11.65 eV.

To ensure that the two-temperature DSF of the quasi-equilibrium system is physically relevant, we must verify that all spatial correlations vanish in a time τ_c smaller than the ion-electron relaxation time τ_{ei}, which is of the order of hundreds of picoseconds [133]. The Van Hove function has been calculated for the specific case $T_i = 1$ eV and $T_e = 10$ eV and its time evolution is presented in Fig. 6.8. We find that at $\tau_c = 125$ ps, all spatial correlations have vanished, such that $\tau_c < \tau_{ei}$, implying that dynamical properties can be meaningfully calculated for the quasi-equilibrium system.

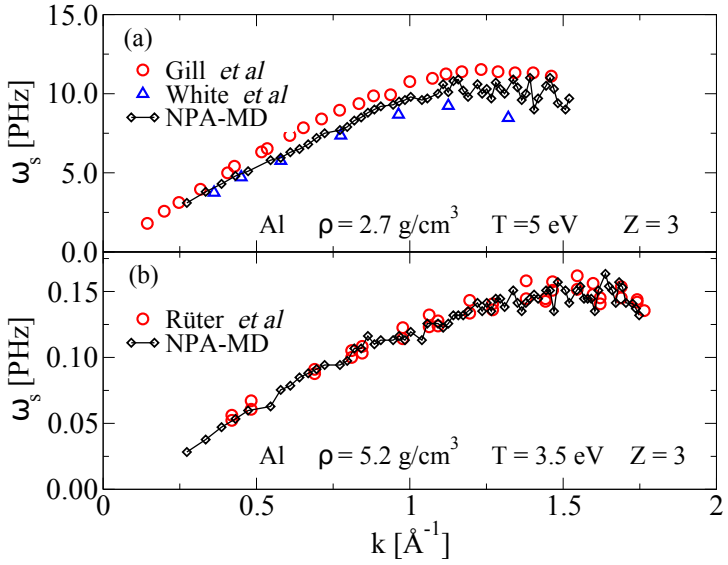

Figure 6.7. (color online) A comparison of the equilibrium acoustic dispersion relation of Al for (a) density $\rho = \rho_0$ and $T = 5$ eV as in the OF-DFT-MD calculations of White *et al* [46] and as in the PA-SS calculations of Gill *et al* [178], and (b) $\rho = 5.2$ g/cm^3 and $T = 3.5$ eV as in Rüter *et al* [145].

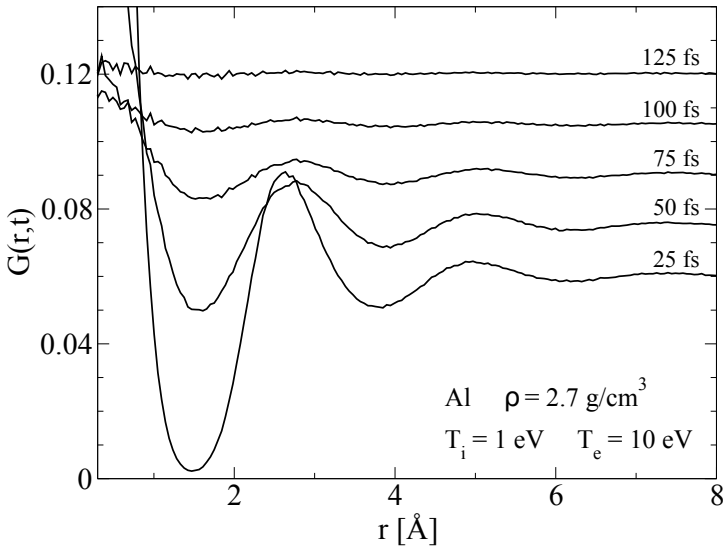

Figure 6.8. The Van Hove function for different times for the case $T_i = 1$ eV and $T_e = 10$ eV. For clarity, each curve is shifted vertically by 0.015 from the previous one while the curve for $t = 25$ fs is unshifted.

The $2T$-DSF at $\rho = \rho_0$, computed with the NPA-based PP, is presented in Fig. 6.9 for $T_i = 1$ eV and $T_e = 1, 5$ and 10 eV and wavevector $k = 0.45$ Å^{-1}. The position of the

Brillouin peak shifts to higher ω as T_e increases while the value at $\omega = 0$ is drastically lowered. Furthermore, the shape of the peak is narrower for higher T_e.

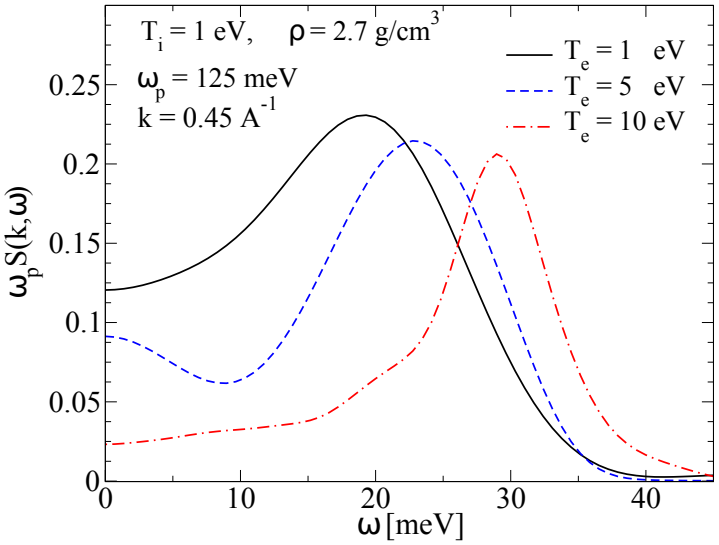

Figure 6.9. (color online) The quasi-equilibrium DSF of Al at density ρ_0, $T_i = 1$ eV and $T_e = 1, 5$, T= 10 eV, for wavevector $k = 0.45$ Å^{-1}.

The dispersion relation $\omega_s(k)$ for $T_e = 1, 5$ and 10 eV can be deduced from the position of the Brillouin peak. It is displayed in Fig. 6.10.

The dispersion relation begins to be noisy and unphysical at different values of wavevector k as T_e is increased. Thus the position of the Brillouin peak could be confidently determined only up to $k = 0.8$, 1.2, and 1.5 Å^{-1} for $T_e = 1$, 5, and 10 eV, respectively. Establishing that collective excitations still exist for higher values of k becomes more difficult as the Brillouin peak merges back with the Rayleigh peak at $k = 0$. This makes it hard to evaluate the full width at half maximum of the Brillouin peak, ideally needed to establish the survival of longitudinal modes at higher k and higher T_e. Instead, we decided to include the position of the peak as long as its height is at least 20% higher than the value at $k = 0$. Using the same procedure for each combination of T_i and T_e enables us to treat them in a comparable manner. Longer MD simulations would yield better results for $\omega_s(k)$; however the current results are sufficiently precise to conclude that there exist more ion longitudinal modes at $T_e = 10$ eV than at lower T_e ; this may be due to the lower compressibility of the electron subsystem as well as the ion subsystem with a more repulsive pair potential, as shown in Fig. 6.1, the ion temperature being identical. These dispersion relations will be used to determine the speed

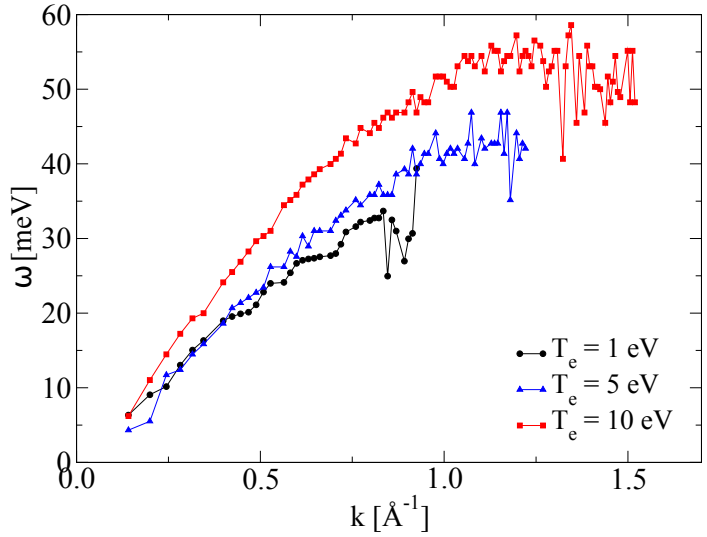

Figure 6.10. (color online) The two-temperature dispersion relation $\omega_s(k)$ calculated from the position of the Brillouin peak for $T_i = 1$ eV and $T_e = 1$, 5, and 10 eV.

of sound c_s as a function of T_e. Predictions of the speed of sound computed from the DSF, the MHNC-SSF and the HNC-SSF are compared in Fig. 6.11.

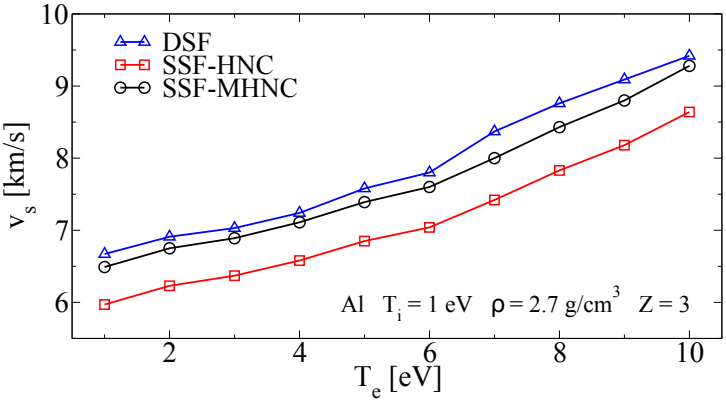

Figure 6.11. (color online) Comparison of the speed of sound in the $2T$-system calculated from the SSF and from the DSF with $T_i = 1$ eV.

The speed of sound calculated from the DSF is slightly and systematically higher than the MHNC-SSF value through the entire range of T_e, with a maximum difference of 4.6% occurring at $T_e = 7$ eV ; both methods predict a 43% increase from $T_e = 1$ to 10 eV. These results also confirm the phenomenon of phonon hardening [29]. It should be noted that the HNC-SSF value is considerably lower than the value from other methods, illustrating the

importance of using a bridge term in the integral equation for the ion distribution at these coupling strengths.

6.3.3. Quasi-Equation of State

The NPA model allows a rapid calculation of the EOS of Al in equilibrium conditions, which was intensively investigated by Sjostrom *et al* [179], but also for $2T$ situations. In Fig. 6.12 we present a comparison between the equilibrium and the quasi-equilibrium Helmholtz free energy F, internal energy E, and total pressure P. At the highest electronic temperature ($T_e = 10$ eV) that we have studied, the equilibrium F is lower than that of the quasi-equilibrium system by 2.3% while the internal energy is higher by 0.25%. The internal energy in both cases has a maximum in the range of $T_e = 6 - 7$ eV and has a similar shape. While F and E are only slightly modified in the $2T$ regime, the equilibrium pressure is higher than that obtained at quasi-equilibrium by as much as 56 % at T_e=10 eV. Even though the changes in the free energy and internal energy are small, such variations could considerably affect EOS-dependent properties such as specific heats, conductivities, energy relaxation rates and other coupling coefficients that enter into more macroscopic WDM simulations. The efficiency and rapidity of computing such $2T$-EOS via the NPA model allows to obtain them on the fly for simulations of shocked or laser-driven systems, for most combinations of T_i and T_e where a significant density of free electrons is available to make the NPA approach valid, and where no persistent chemical bonds are formed.

6.4. Conclusion

Taking aluminum as an example, we demonstrated that the NPA pair potentials can be used to compute efficiently and accurately the equilibrium dynamic structure factor via MD simulations, and established that it is in close agreement with DFT-MD results. We explored the two-temperature system and showed that all ion-ion correlations vanish in a time shorter than typical electron-ion relaxation times, validating the concept of a $2T$-dynamic structure factor in this context.

We presented the $2T$-DSF and showed that the Brillouin peak shifts to higher energies as the electron temperature is increased. As a result, the ion acoustic mode dispersion relation is modified and the adiabatic speed of sound c_s is increased, in good agreement with its determination via the compressibility sum rule in the small-k limit of the static structure factor. The latter is independently obtained via the modified hyper-netted chain method and using the pair potentials generated via the neutral-pseudoatom method. The increase in the acoustic velocity is also consistent with the phenomenon of 'phonon hardening'.

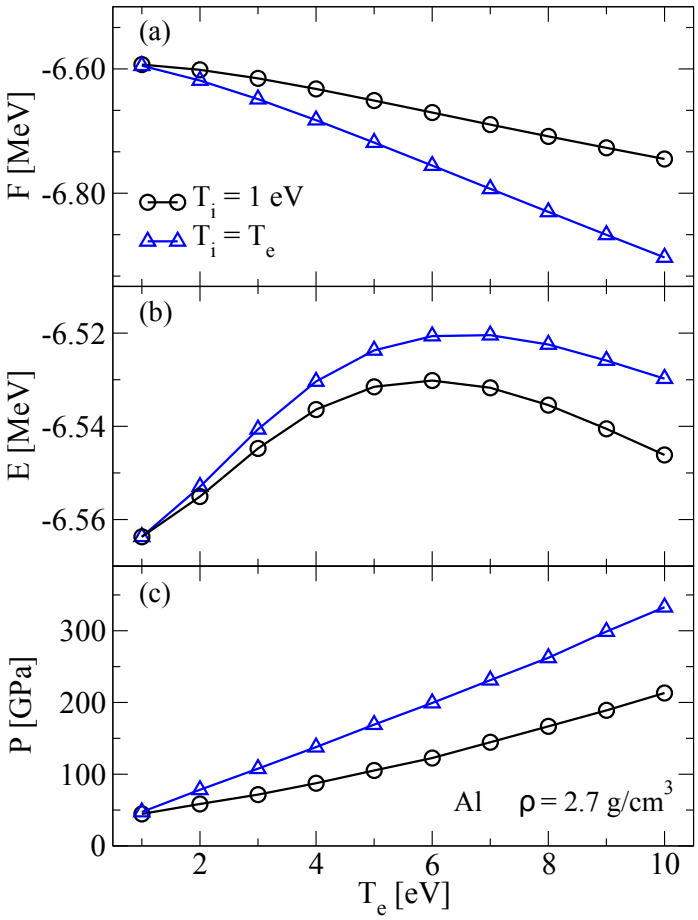

Figure 6.12. (color online) Comparison between the equilibrium and quasi-equilibrium free energy (a), internal energy (b), and pressure (c) of Al at density ρ_0. As T_i is held fixed at 1 eV for quasi-equilibrium time scales (or longer via a thermostat coupled only to the ions), the ionic lattice does not expand and the density remains fixed.

The comparison between the equilibrium and quasi-equilibrium EOS shows that the free energy and the internal energy are only weakly modified in the two-temperature system, while the pressure is significantly affected. The efficient calculation of the quasi-equilibrium EOS via the neutral pseudoatom method constitutes a powerful tool for exploring out-of-equilibrium systems via MD simulations.

Acknowledgments

This work was supported by grants from the Natural Sciences and Engineering Research Council of Canada (NSERC) and the Fonds de Recherche du Québec - Nature et Technologies

(FRQ-NT). Computations were made on the supercomputer Briarée, managed by Calcul Québec and Compute Canada. The operation of this supercomputer is funded by the Canada Foundation for Innovation (CFI), the ministère de l'Économie, de la science et de l'innovation du Québec (MESI) and the Fonds de recherche du Québec - Nature et technologies (FRQ-NT)

Chapitre 7

ARTICLE V : CONDUCTIVITÉ ISOCHORIQUE, ISOBARIQUE ET ULTRA-RAPIDE DE LA MATIÈRE DENSE ET CHAUDE

Cet article a été publié dans la revue *Physical Review E* **96**, 053206 (2017).

Contexte

Dans ce cinquième article, on étudie la conductivité électrique de la matière dense et chaude puisqu'il s'agit d'une des propriétés les plus importantes d'un point de vue technologique. En particulier, on s'intéresse à comprendre comment la conductivité est affectée par la température dans le régime isochorique, isobarique et ultra-rapide. D'une part, l'une des techniques les plus utilisées pour calculer théoriquement la conductivité est la formule de Kubo-Greenwood qui nécessite plusieurs simulations de TDF-MD extrêmement coûteuses. D'autre part, il est possible d'utiliser la formule de Ziman qui, couplée au modèle PAN, permet un calcul rapide de la conductivité. La comparaison entre ses différentes techniques et les valeurs expérimentales, lorsque disponibles, illustre bien la complexité du problème. De plus, il semble que le choix de la fonctionnelle d'échange et corrélation ait un effet important ce qui démontre la sensibilité du calcul. Finalement, les importantes différences entre les deux modèles théoriques démontrent la nécessité d'effectuer davantage d'expériences.

Contributions

- Simulations de TDF+DM de l'aluminium dans le régime isochorique et isobarique
- Calcul de la conductivité de l'aluminium par la méthode de Kubo-Greenwood
- Vérification des calculs de conductivité dans le modèle PAN
- Discussion sur l'interprétation de l'expérience de Gathers
- Discussion sur l'impact du choix de la fonctionnelle d'échange et corrélation dans le calcul de conductivité
- Calcul du spectre de diffusion de rayons X pour le lithium

Isochoric, isobaric and ultrafast conductivities of aluminum, lithium and carbon in the warm dense matter regime

M. W. Chandre Dharma-wardana[2], Dennis D. Klug[2], Louis Harbour[1], Laurent J. Lewis[1]

[1]*Département de Physique and Regroupement Québécois sur les Matériaux de Pointe, Université de Montréal, C.P. 6128, Succursale Centre-Ville, Montréal, Québec, Canada H3C 3J7*

[2]*National Research Council of Canada, Ottawa, On., Canada K1A 0R6*

Abstract

We study the conductivities σ of (i) the equilibrium isochoric state ($\sigma_{\rm is}$), (ii) the equilibrium isobaric state ($\sigma_{\rm ib}$), and also the (iii) non-equilibrium ultrafast matter (UFM) state ($\sigma_{\rm uf}$) with the ion temperature T_i less than the the electron temperature T_e. Aluminum, lithium and carbon are considered, being increasingly complex warm dense matter (WDM) systems, with carbon having transient covalent bonds. First-principles calculations, i.e., neutral-pseudoatom (NPA) calculations and density-functional theory (DFT) with molecular-dynamics (MD) simulations, are compared where possible with experimental data to characterize $\sigma_{\rm ic}, \sigma_{\rm ib}$ and $\sigma_{\rm uf}$. The NPA $\sigma_{\rm ib}$ are closest to the available experimental data when compared to results from DFT+MD, where simulations of about 64-125 atoms are typically used. The published conductivities for Li are reviewed and the value at a temperature of4.5 eV is examined using supporting X-ray Thomson scattering calculations. A physical picture of the variations of σ with temperature and density applicable to these materials is given. The insensitivity of σ to T_e below 10 eV for carbon, compared to Al and Li, is clarified. **Keywords:** Conductivity, Isobaric, Isochoric, Ultrafast, Warm Dense Matter

7.1. Introduction

Short-pulsed lasers as well as shock-wave techniques can probe matter in hitherto experimentally inaccessible regimes of great interest. These provide information needed for understanding normal matter and unusual states of matter, in equilibrium or in transient conditions [180, 99]. Similar 'hot-carrier' processes occur in semiconductor nanostructures [181, 182]. Such warm dense matter (WDM) systems include not only equilibrium systems where the ion temperature T_i and the electron temperature T_e are equal, but also systems where $T_i \neq T_e$, or highly non-equilibrium systems where the notion of temperature is inapplicable [110]. While the prediction of a quasi equation of state (EOS) and related static properties for two-temperature ($2T$) systems [164] is satisfactory, the conductivity calculations using standard codes, even for sodium at the melting point, require massive quantum simulations with as much as ∼1500 atoms and over 56 k-points (according to Ref. [183]), whereas even theories of the 1980s evaluated the sodium conductivities successfully via a momentum relaxation-time ($\tau_{\rm mr}$) approach [184], which can also be used in Drude fits to the Kubo-Greenwood (KG) formula used with density-functional theory (DFT) and molecular dynamics (MD) methods. The KG-formula and its scope are discussed further in the Appendix.

The static electrical conductivities of WDM equilibrium systems (i.e., $T_i = T_e$), as well as $2T$ quasi-equilibrium systems, are the object of the present study. We distinguish the isobaric equilibrium conductivity $\sigma_{\rm ib}$ and the isochoric equilibrium conductivity $\sigma_{\rm ic}$ from the ultrafast matter (UFM) quasi-equilibrium (isochoric) conductivity $\sigma_{\rm uf}$. The $2T$ WDM states exist only for times shorter than the electron-ion equilibration time $\tau_{\rm ei}$ and may be accessed using femtosecond probes.

We consider three systems of increasing complexity above the melting point: (a) a 'simple' system, viz., WDM-aluminum at density ρ =2.7 g/cm^3; (b) WDM-lithium at 0.542 g/cm^3; and (c) WDM-carbon (2.0-3.7 g/cm^3) including the low-T covalent-bonding regime. As experimental data are available for the isobaric evolution of Al and Li starting from their nominal normal densities and down to lower densities of the expanded fluid, we calculate $\sigma_{\rm ib}$ for Al and Li. The ultrafast conductivity $\sigma_{\rm uf}$ is calculated for all three materials, as $\sigma_{\rm is}$ is conveniently accessible via short-pulse laser experiments.

The electrons in WDM-Li are known to be non-local with complex interaction effects. For instance, clustering effects may appear [117] as the density is increased. WDM-carbon is a complex liquid with transient covalent bonding where the C-C bond energy E_{cc} may reach ∼ 8 eV in dilute gases. The three conductivities $\sigma_{\rm ic}$, $\sigma_{\rm ib}$, and $\sigma_{\rm uf}$ for Al, Li and C, are calculated

via two first-principles methods where, however, both finally (i) the neutral pseudoatom (NPA) method as formulated by Perrot and Dharma-wardana [164, 115, 64, 63] together with the Ziman formula, and (ii) the DFT+MD and KG approach as available in codes such as VASP and ABINIT [40, 38], enabling us to assess the extent of the agreement among these theoretical methods and the available experiments. The liquid-metal experimental data are still the most accurate data on WDM systems available; they are used where possible to compare with calculations.

Accurate experimental data for the isobaric liquid state of Al [185, 186] and Li [27] are available, and provide a test of the theory. No reliable isobaric carbon data are available; carbon at 3.7-3.9 g/cm^3 and 100-175 GPa was studied recently by x-ray Thomson scattering (XRTS) [170]. Hence we evaluate only $\sigma_{\rm ic}$ and $\sigma_{\rm ib}$ in this case, for ρ in the range of XRTS experiments and related simulations [187]. The conductivity across a recently-proposed phase transition [113] in low-density carbon ($\sim$ 1.0 g/cm^3) near $T \simeq 7$ eV is not addressed here.

DFT+MD methods treat hot plasmas as a thermally evolved sequence of frozen solids with a periodic unit cell of N atoms — typically $N \sim 100$, although order-of-magnitude larger systems may be needed [183] for reliable transport calculations. The static conductivity σ is evaluated from the $\omega \to 0$ limit of the KG $\sigma(\omega)$ using a phenomenological model (e.g., the Drude $\sigma(\omega)$ [183, 29] or modified Drude forms [157]). More discussion of these issues is given in the Appendix. The N-ion DFT+MD model does not allow an easy estimate of single-ion properties, e.g., the mean number of free electrons per ion ($\bar{Z}$) or ion-ion pair potentials.

The NPA methods, e.g., that of Perrot and Dharma-wardana, reduce the many-electron, many-ion problem to an effective one-electron, one-ion problem using DFT [61, 64, 115]. A Kohn-Sham (KS) calculation for a nucleus immersed in the plasma medium provides the bound and free KS states. While bound states remain localized within the Wigner-Seitz (WS) sphere of the ion for the regime studied here, the free electron distribution $n_f(r)$ of each ion resides in a large "correlation sphere" (CS) such that all $g_{ij}(r) \to 1$ as $r \to R_c$. We typically use $R_c = 10 r_{ws}$, i.e., a volume of some 1000 atoms. Several average-atom models [54, 124] have similarities and significant differences among them and with the NPA method. These are reviewed in the Appendix and in Ref. [113]. The NPA method applies for low T systems even with transient covalent bonding. Hence, it differs from Blenski *et al.* [124] who hold that "... all quantum models seem to give unrealistic description of atoms in plasma at low T and high plasma densities". But in reality, the earliest successful applications of the NPA were for solids at $T = 0$. Here we treat very low-T WDMs, e.g., Al, ρ=2.7 g/cm^3, $T/E_F < 0.01$, using the NPA, E_F being the Fermi energy and obtain very good agreement

for equations of state (EOS) data [164] and even for transport properties, e.g., the electrical conductivity.

The NPA static conductivity is evaluated from the Ziman formula using the NPA pseudopotential $U_{ei}(k)$ and the ion structure factor $S(k)$ [64] generated from the NPA pair potential $V_{ii}(r)$. The latter is used in the hypernetted-chain (HNC) equation or its modified (MHNC) form inclusive of bridge functions, assuming spherical symmetry appropriate to fluids. HNC methods are accurate, fast and much cheaper than MD methods which fail to provide small k-information, i.e., less than $\sim 1/L_{bx}$ where L_{bx} is the linear dimension of the simulation box. The Ziman formula can be derived from the Kubo formula using the force-force correlation function and assuming a momentum relaxation time $\tau_{\rm mr}$. Zubarev's method can also be used [188] to derive the Ziman formula. Details regarding the conductance formulae and their limitations are given in the Appendix.

7.2. The conductivities of WDM aluminum

Surprisingly low static conductivities for UFM aluminum at 2.7 g/cm^3, extracted from x-ray scattering data from the Linac Coherent Light Source (LCLS), have been reported in Sperling *et al.*, Ref. [26]. Calculations of $\sigma_{\rm ic}$ using an orbital-free (OF) form of DFT and MD revealed sharp disagreement with the LCLS data [154]. Sperling *et al* [26] found the conductivity data of Gathers [185] to differs strikingly from the LCLS data and the OF results. In Fig. 4 of Ref. [26], they attempt to present a theoretical $\sigma_{\rm ic}$ at 2.7 g/cm^3 that agrees approximately with the Gathers data and to some extent with the LCLS data. The Gathers data are reviewed in the Appendix.

However, in our view, the LCLS, OF, and Gathers σ *should* indeed differ, in the physics involved as well as in the actual values, because:
(i) the Gathers data are for the *isobaric* conductivity $\sigma_{\rm ib}$ of liquid aluminum from $\rho = 1.7$ to 2.4 g/cm^3 (cf. region (a) in Fig. 7.1).
(ii) The orbital-free simulation [154] and the DFT+MD simulations [190] are for the *isochoric* equilibrium ($T_e = T_i$) $\sigma_{\rm ic}$ of Al at ρ=2.7 g/cm^3 (region (c) in Fig. 7.1).
(iii) The LCLS data applies to UFM-aluminum $\sigma_{\rm uf}$, $T_i \neq T_e$, with the ions 'frozen' at $T_i \simeq T_0$, as proposed in Ref. [155]. The UFM-conductivity is shown as region (b) in Fig. 7.1. The ultrafast conductivity $\sigma_{\rm uf}$ is essentially isochoric, with $T_i \simeq T_0$ at the density ρ_0. The timescales in UFM experiments are too short for (ρ, T_i) to differ significantly from (ρ_0, T_0). The evaluation of the ultrafast conductivity $\sigma_{\rm uf}$ was discussed in detail in Ref. [155], and here we extend our study of ufm-conductivities.

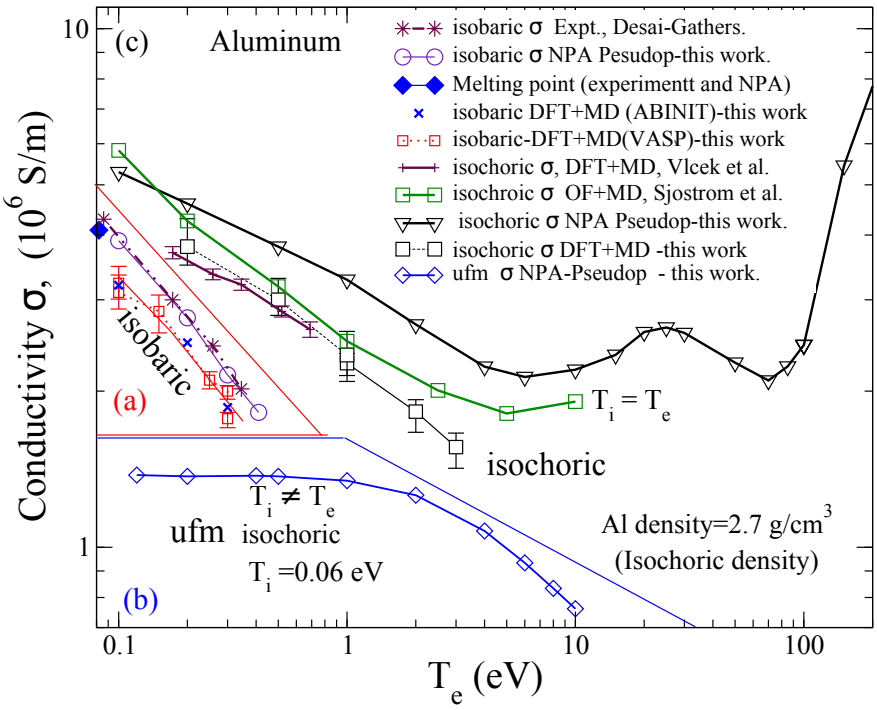

Figure 7.1. Static conductivities for Al from experiment and from DFT+MD and NPA calculations. The isobaric conductivity $\sigma_{\rm ib}$ is at densities $2.37 \leq \rho \leq 1.65$ g/cm^3 (cf. triangular region (a)). The isochoric ($\sigma_{\rm ic}$, region (c)) and UFM ($\sigma_{\rm uf}$, region (b)) conductivities are for a density of 2.7 g/cm^3. Enlarged views of regions (a) and (c) are given in the Appendix. The blue-filled diamond gives the conductivity of normal aluminum at its melting point (0.082 eV, 2.375 g/cm^3), viz. $\sigma = 4.16 \times 10^6$ S/m from experiment (quoted in Ref. [189]) and $\sigma = 4.09 \times 10^6$ S/m from the NPA.

7.2.1. Isobaric conductivity.

In Fig. 7.1, we globally compare our NPA-Ziman *isobaric* conductivities for aluminum with the isochoric and ufm conductivities, shown in regions (b) and (c). The three conductivities evolve in characteristic ways as a function of temperature.

The experimental data of Gathers for $\sigma_{\rm ic}$ are compared with our results in more detail in Fig. 7.2, and we find *excellent agreement* with our NPA calculation. DFT+MD calculations using a 108-atom simulation cell are shown in both figures for $\sigma_{\rm ib}$ and $\sigma_{\rm ic}$, where the PBE functional available in VASP and ABINIT was used; they fall below the experimental $\sigma_{\rm ib}$ or the NPA $\sigma_{\rm ib}$, a common trend for the DFT+MD+KG $\sigma_{\rm ic}$ as well, as discussed further in the Appendix. It should be noted that Gathers gives two isobaric resistivities in columns four and five of Table-II (Ref. [185]), causing some confusion; Gathers' results are further discussed in the Appendix.

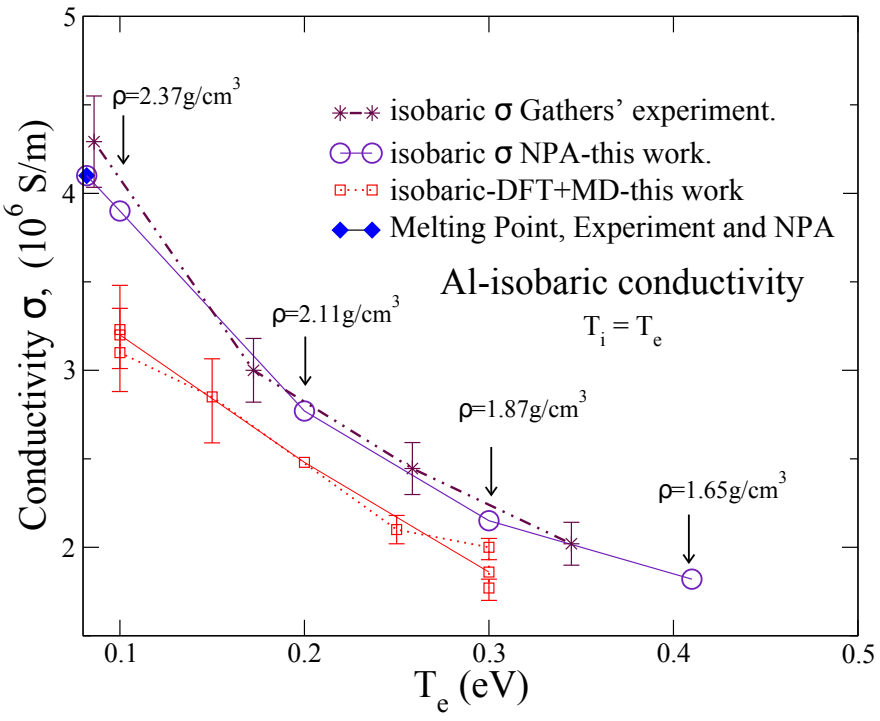

Figure 7.2. Isobaric conductivity of aluminum from near its melting point to about 0.4 eV, expanded from Fig.7.1 , comparing the NPA, experiment (Gathers) and DFT+MD results. The experimental conductivity of Al at its melting point (filled blue diamond) [189], with density 2.375 g/cm^3 is displayed and aligns with the NPA calculations for the Gathers data showing the very good agreement between the NPA and two independent experiments.

The *isochoric* conductivity of Al at 0.082 eV (nominal melting point) is $\approx 5 \times 10^6$ S/m; the experimental *isobaric* conductivity [189] at the melting point is $\sigma_{\rm ib} = 4.1 \times 10^6$ S/m, with density 2.375 g/cm^3 instead of the room-temperature density of 2.7 g/cm^3 due to thermal expansion. The value of 4.08 $\times 10^6$ S/m obtained from NPA for aluminum at 2.375 g/cm^3 is in excellent agreement with experiment. It is shown as a filled blue diamond symbol in figure 7.1. This value drops to 3.8 $\times 10^6$ S/m if a bridge contribution (MHNC) is not used in calculating the ion-ion structure factor.

7.2.2. Isochoric conductivity

The isochoric system, region (c) in Fig. 7.1, is at $\rho_0 = 2.7$ g/cm^3, $r_{ws} \simeq 2.98$ a.u. ($\hbar = |e| = m_e = 1$), for all $T = T_i = T_e$. The NPA value of $\sigma_{\rm ic}$ at $T = 0.082$ eV (nominal melting point) is $\approx 5 \times 10^6$ S/m; this is higher than the experimental value usually quoted [189] of $\sigma_{\rm ib} = 4.1 \times 10^6$ S/m as the density of normal aluminum becomes 2.375 g/cm^3 instead of 2.7 g/cm^3 due to thermal expansion. In region (c) we see the OF conductivity of Ref. [154]

going to a minimum at T ∼5 eV and subsequently rise as T increases; DFT+MD+KG becomes increasingly prohibitive at these higher temperatures. The NPA calculations show a first minimum at ∼ 6 eV, followed by a maximum at 25 eV, and another minimum at ∼ 70 eV. These features in the NPA results are due to the concurrent increase in $\bar{Z}$ as well as the competition between different ionization states. This effect — the conductance minimum or resistivity saturation — occurs when electrons become non-degenerate (i.e., $\mu_e \leq 0$), i.e. when all electrons (not just those near $E_F \sim 12$ eV) begin to conduct.

While we favour this explanation of the minimum in the conductivity and first presented it in our discussion [191] of the Milchberg experiment, some authors (e.g., R. M. More in Ref. [99], and also Faussurier et al. [192]) have proposed an explanation in terms of resistivity saturation, as in Mott's theory of minimum conductance in semiconductors. The electron "mean-free path" $\lambda = \bar{v}\tau_{\rm mr}$, where $\bar{v}$ is a mean electron velocity, is claimed to reduce to the mean interatomic distance at resistivity saturation. However, $\tau_{\rm mr}$ evaluated using the Ziman formula is a momentum-relaxation time associated with scattering within the thermal window of the Fermi distribution at the Fermi energy (more accurately, at an energy corresponding to the chemical potential). Since $2k_F$ is of the order of an inverse r_{ws}, it is not surprising that one can connect a length scale related to r_{ws} to λ. But it does not describe the right physics of the conductivity minimum. Even the simplest form of the Ziman formula already shows the conductivity minimum, and it is a single-center scattering formula using a Born approximation within a continuum model; it contains no information on the interatomic distance since one can even set $S(k) = 1$ and obtain the resistivity saturation. In contrast, the resistivity saturation seen in Fig. 7.1 for the NPA calculation manifests itself from approximately half the Fermi energy ($\simeq$ 6 eV) corresponding to $\bar{Z} = 3$, to about 70 eV corresponding to a much higher ionization of $\bar{Z} \approx 7$. The increased ionization prevents the chemical potential from becoming rapidly negative and delays the onset of the steep rise in conductivity. These features cannot be explained via a limiting mean free-path model. In fact, in an isochoric system the interionic distance does not change and one cannot have the complex structure shown in the NPA $\sigma_{\rm ic}$. For $T_e = 6$ eV to about $T = 25$ eV, $\bar{Z} = 3$ for aluminum and steadily converts to $\bar{Z} = 4$, and then a decline and a rise are accompanied by the conversion of $\bar{Z} = 4$ to $\bar{Z} \simeq 7$ by $T \sim 70$ eV.

Fig. 1 of Faussurier *et al.* [192] displays the isochoric resistivity for aluminum together with results from Perrot and Dharma-wardana [191]. However, the latter gives the scattering as well as the pseudopotential-based resistivity for aluminum where the mean *electron* density $\bar{n}$ is held constant, not the usual isochoric resistivity where the ion density $\bar{\rho}$ has to be held constant. Electron-isochoric and ion-isochoric conditions are equivalent initially and as long

as $\bar{Z} = 3$ for aluminum; but the comparison becomes misleading beyond $T \approx 15$ eV. Fig. 1 of Faussurier *et al.* [192] also displays the aluminum isochoric resistivity from Yuan *et al.* [193]. However, as explained in sec. 7.5.3 of the Appendix, both Faussurier and Yuan use an ion-sphere model which leads to ambiguities in the definition of $\bar{Z}$ and μ_0, leading to non-DFT features which are absent in the NPA model. Hence their resistivity estimates are not directly comparable to ours. Sufficiently accurate experiments are not yet available at such high temperatures to distinguish between different theories and validate one or the other. Such models should also be tested using cases where accurate experimental data are available (e.g., in the liquid-metal regime).

A further aspect of conductivity calculations is the need to account for multiply-ionized species. For $T > E_F/2$, $\bar{Z}$ begins to increase beyond 3 and departs substantially from an integer (e.g., $\bar{Z} = 3.5$ at 20 eV). It is thus clear that a multiple ionization model with several integral values of $\bar{Z}$, (e.g, a mixture $\bar{Z} = 3$ and $\bar{Z} = 4$) should be used, as implemented in 1995 by Perrot and Dharma-wardana [64], for lower-density aluminum. The isochoric data $\sigma_{\rm ic}$ reported in Fig. 7.1 uses the approximation of a single ionic species with a mean $\bar{Z}$.

7.2.3. Ultrafast conductivity

The nature of ultrafast matter and its properties are determined by the initial state of the system. That is, if the initial system were a room temperature solid, and if the experiment were performed with minimal delay after the pump pulse of the laser, then the ion subsystem would remain more or less intact. However, the initial state can also be the liquid state and this will lead to different results. Both these cases are studied to compare and contrast the resulting $\sigma_{\rm uf}$ for Al.

(i) For the case where the initial state is solid, we assume for simplicity that the ion subsystem structure factor $S(k)$ can be adequately approximated by its spherical average since aluminum is a cubic (FCC) crystal. The major Bragg contributions are included in such an approximation. In fact, the spherically-averaged $S(k)$ is taken to be the ion-ion $S(k)$ of the supercooled liquid at 0.06 eV as that is the lowest temperature (closest to room temperature) where the Al-Al $S(k)$ could be calculated. Furthermore, here we are using the simplest local (s-wave) pseudopotential derived from the NPA approach using a radial KS equation. Hence the use of a spherically average $S(k)$ is consistent, and probably within the large error bars of current LCLS experiments (see Fig.4, Ref.[26]). Currently, no DFT+MD+KG results for $\sigma_{\rm uf}$ are available for comparison. However, in the present model, the $\sigma_{\rm uf}$ at $T_e = T_i = 0.6$ eV does not match the conductivity of solid (crystalline) aluminum, but goes to a lower value, possibly consistent with that of a supercooled liquid. The lower conductivity, compared to

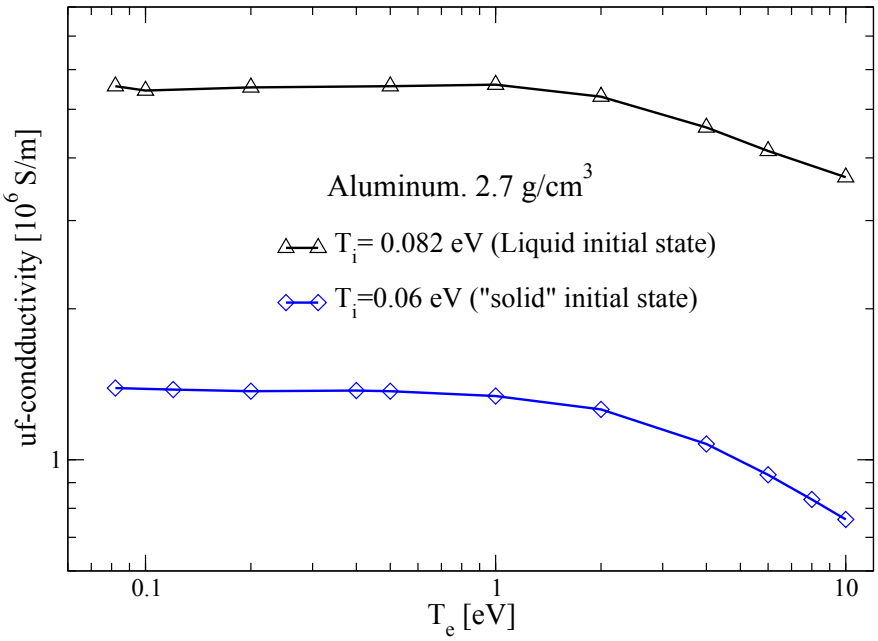

Figure 7.3. Ultrafast conductivity of Al at density 2.7 g/cm^3 for (i) solid initial state at 0.06 eV, and (ii) liquid initial state just above melting point 0.082 eV. Curve (i) was also displayed in Fig. 7.1 for comparison with σ_{ib} and σ_{ic}.

the FCC crystal is qualitatively consistent with the drop in the conductivity from the solid-state, room temperature, density = 2.7 g/cm^3 value of $\sigma \simeq 41 \times 10^6$ S/m to the liquid-state value at the melting point, 4 $\times 10^6$ S/m. The drop predicted by the NPA $\sigma_{\rm uf}$ is larger. Hence this calculation appears to need further improvement for $T < 1.0$ eV, e.g. using the structure factor of the FCC solid and including appropriate band-structure effects.

(ii) The second model we study has molten Al at its nominal melting point (0.082 eV) but at its isochoric density of 2.7 g/cm^3 as the initial state. This mimics the case where the pump pulse had warmed the ion subsystem to some extent. Then we use the $S(k)$ and pseudopotentials evaluated at 0.082 eV (nominal isobaric melting point), and regard that they remain unchanged while the electron screening and all properties dependent on the electron subsystem are evaluated at the electron temperature T_e. The resulting $\sigma_{\rm uf}$ is shown in Fig. 7.3, together with the case where the initial state was assumed to be a temperature (e.g.,the room temperature 0.026eV, or 0.06 eV) which is below the melting point. The two curves clearly suggest that the LCLS-experiments for Al are more consistent with the initial state (i.e., the state of matter at the peak of the laser pulse) being solid, and with no significant pre-melt.

7.2.4. XC-functionals and the Al conductivity

Using a DFT+MD+KG approach, Witte *et al.* [194] examined the σ for Al at $\rho = 2.7$ g/cm^3 and $T = 0.3$ eV computed with the exchange-correlation (XC) functionals of (i) Perdew, Burke, and Ernzerhof (PBE) [79] and (ii) Heyd, Scuseria, and Ernzerhof (HSE) [195]. Their results agree with those of Vlček *et al.* [190] for the PBE functional; our DFT+MD calculations also agree well with those of Vlček *et al.* as seen from the region (c) in Fig. 7.1. However, Witte *et al.* propose, from their Fig. 1, that their HSE calculation agrees [196] best with the experimental data of Gathers [185]. This is based on a calculation of the conductivity at 0.3 eV only ($\approx$ 3500 K), which is compared with the corresponding entry in Table II, column 4, of Ref. [185], viz. resistivity=0.451$\mu\Omega$m, i.e.,conductivity = 2.22 $\times 10^6$ S/m. However, this datum is given by Gathers for a volume dilation of 1.44 (column 3), i.e., $\rho = 1.875$ g/cm^3, and *not* 2.7 g/cm^3. Witte *et al.* incorrectly interpret column 4 of Gathers Table II as providing *isochoric* conductivities of Al at 2.7 g/cm^3. Gathers tabulation and the several resistivities given are indeed a bit confusing; we reconstruct them in Table 1 of the Appendix for convenience.

Columns 4 and 5 in Ref. [185] give two possible results for the isobaric conductivity of aluminum, with column 5 giving the experimental resistivity as a function of the nominal input enthalpy, i.e., "raw data". Column 4 gives the resistivity where in effect the input enthalpy has been corrected for volume expansion; this is *not* the isochoric resistivity of aluminum, as proposed by Sperling *et al.* [26] and by Witte *et al.* [194].

All the resistivities in Gathers' Table II, column 4 can be recovered accurately by our parameter-free NPA calculation using the isobaric densities. Also, the fit formula given in the last row of table 23 of Gathers' 1986 review [186] confirms that Table II, column 4 in Ref. [185] is indeed the final *isobaric* data at 0.3 GPa. In addition, our NPA calculation at the melting point accurately recovers the known isobaric conductivity [189] at 0.082 eV.

The HSE functional includes a contribution (e.g., 25%) of the Hartree-Fock exchange functional. If there is no band gap at the Fermi energy, the Hartree-Fock self-energy is such that several Fermi-liquid parameters become singular. Hence the use of this functional in WDM studies may lead to uncontrolled or unknown errors. Furthermore, previous studies, e.g., Pozzo *et al.* [183], Kietzmann *et al.* [128], show that the PBE functional successfully predict conductivities. Those conductivities, if recalculated with the HSE functional are most likely to be in serious disagreement with the experimental data.

DFT is a theory which states that the free energy is a functional of the one-body electron density, and that the free energy is minimized by just the physical density. It does *not*

claim to give, say, the one-electron excitation spectrum or the density of states (DOS). The spectrum and the DOS are those of a fictitious non-interacting electron system at the *interacting density*, and moving in the KS potential of the system. The KS potential is not a mean-field approximation to the many-body potential, but a potential that gives the exact physical one-electron density if the XC-functional is exact. Hence any claimed "agreement" between the DFT spectra and physical spectra is not relevant to the quality of the XC-functional, except in phenomenological theories which aim to go beyond DFT and recover spectra, DOS, bandgaps etc., by including parameters in 'metafunctionals' which are fitted to a wide array of properties. There is however no theoretical basis for the existence of XC-functionals which also simultaneously render accurate excitation spectra, DOS and bandgaps in a direct calculation.

7.2.5. The variation of the conductivity as a function of temperature

The evolution with temperature of the conductivity can be understood within the physical picture of electrons near the Fermi energy (chemical potential) undergoing scattering from the ions in a correlated way via the structure factor. This in turn invokes the relation of the structure factor to the Fermi momentum k_F, and the breakdown of the Fermi surface as T/E_F is increased, while breakdown is countered by ionization which increases the Fermi energy. At sufficiently high temperatures the chemical potential μ tends to zero and to negative values. The conductivity then becomes classical, and finally Spitzer-like. The conductivity minimum (resistivity plateau) in WDM systems occurs near the $\mu \approx 0$ region and is not related to the Mott minimum conductivity.

The differences between $\sigma_{\rm ic}$ and $\sigma_{\rm uf}$, both isochoric, arise because the structure factors $S(k,T_i)$ of the two systems are different, while $U_{ei}(k)$ and the Fermi-surface smearing for them are essentially the same at T_e, with $\bar{Z} \simeq 3$ for Al. The ion structure factor at different temperatures, calculated using the NPA pseudopotential $U_{ei}(k,T_e)$ and used for evaluating $\sigma_{\rm ic}$, are shown in Fig. 7.4 (a). The U_{ei} and $S(k)$, and hence σ, are first-principles quantities determined entirely from the NPA-KS calculation. If the initial temperature T_0 at the time of creation of the Al-UFM were 0.082 eV (i.e., ∼melting point), then the corresponding $S(k,T_0)$ is used in evaluating $\sigma_{\rm uf}$ at all T_e, together with the $U_{ei}(k,T_e)$. More details of $\sigma_{\rm uf}$ and comparison with LCLS data may be found in Ref. [155]. The isobaric system differs in density from the isochoric and ultrafast systems due to volume expansion. Hence the $S(k)$ and the U_{ei} are calculated at each 'expanded' density.

Degenerate electrons ($T_e/E_F < 1$) scatter from one edge (e.g. $-k_F$) of the Fermi surface to the opposite edge (k_F, with a momentum change $k \simeq 2k_F$ and their scattering contribution

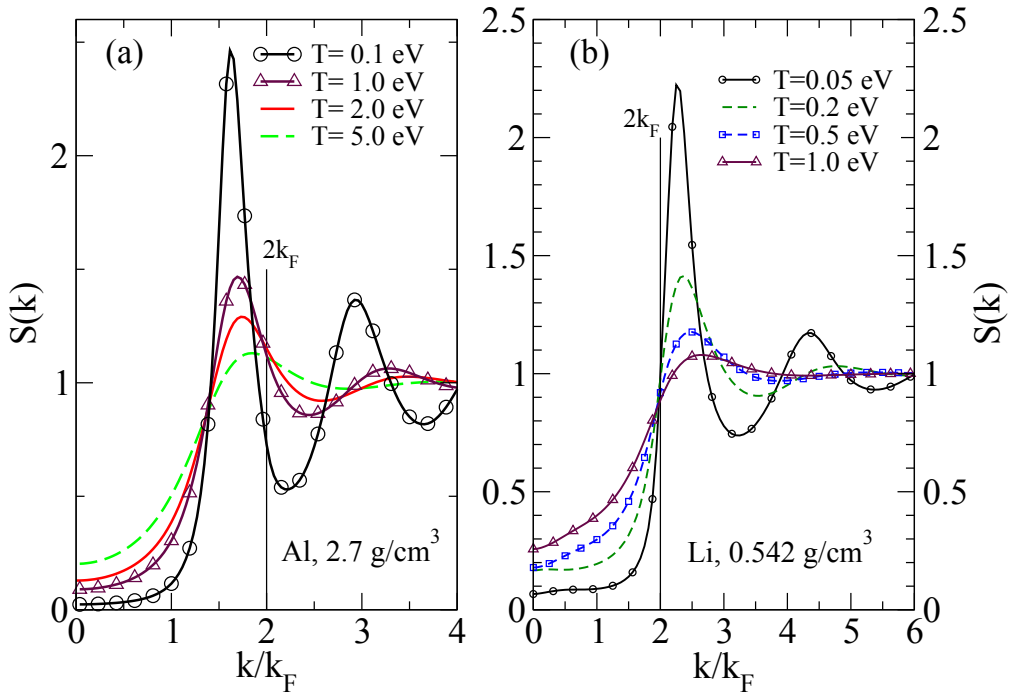

Figure 7.4. (a) Static structure factor $S(k)$ of isochoric aluminum WDM at different temperatures; $S(k)$ at $2k_F$ changes by 65% from $T = 0.1$ to $T = 5$ eV. In ultrafast aluminum $S(k)$ remains 'fixed' at the initial temperature, even when T_e changes. (b) Evolution of $S(k)$ for isochoric Li at 0.542 g/cm^3 as a function of temperature. As T increases, the peak broadens and shifts away from $2k_F$.

essentially determines σ. Thus the position of $2k_F$ with respect to the main peak of $S(k)$ and its changes with T_e explain the T_e dependence of $\sigma(T_e)$. For aluminum at $\rho = 2.7$ g/cm^3, $2k_F$ lies on the high-k side of the main peak, and as $T_i = T_e$ increases, the peak broadens into the $2k_F$ region (see Fig. 7.4(a)), resulting in increased scattering. In the isochoric UFM case both T_i and $S(k)$ do not change, but as T_e increases the window of scattering $f(k)(1-f(k))$ increases (here $f(k)$ is the finite-T Fermi occupation number), and $\sigma_{\rm uf}$ decreases.

Given that the NPA is a first-principles (i.e., 'parameter-free') DFT scheme, the excellent agreement between the NPA $\sigma_{\rm ib}$ and the Gathers aluminum data for $\sigma_{\rm ib}$ (see Fig. 7.2) confirms the accuracy of NPA pseudopotentials U_{ei} and structure factors, and enhances our confidence in the NPA predictions for $\sigma_{\rm ic}$. In addition, experiments at other density ranges were found to be in good agreement with NPA calculations [156] and with the DFT+MD calculations of Dejarlais *et al.* [197]. Furthermore, the NPA approach becomes more reliable at higher temperatures ($T/E_F > 1$) while the DFT+MD methods rapidly become impractical due to the large number of electronic states that are needed in the calculation due to the spread in

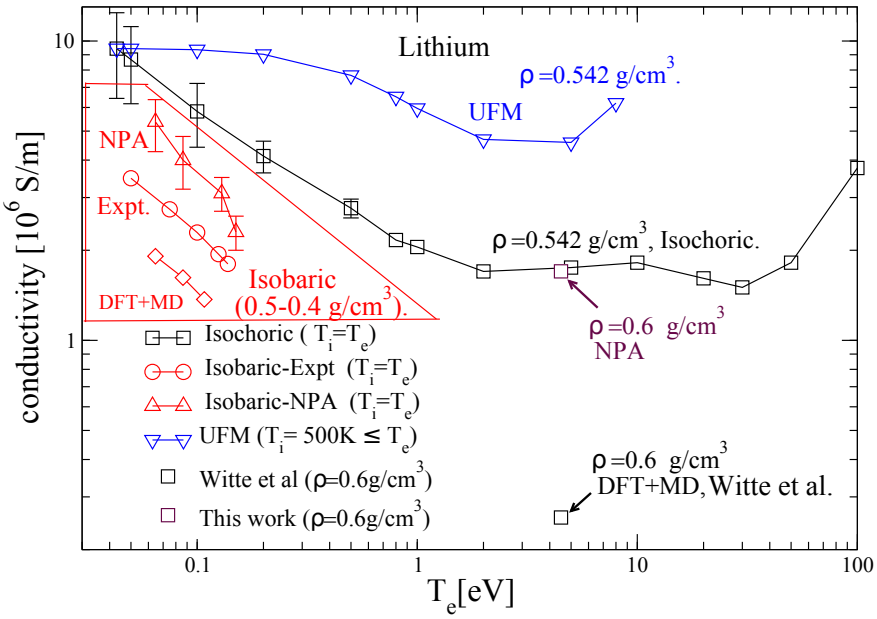

Figure 7.5. Isobaric ($\sigma_{\rm ib}$), isochoric($\sigma_{\rm ic}$), and ultrafast ($\sigma_{\rm uf}$) conductivities of Li at density 0.542 g/cm^3. Isobaric experimental conductivities $\sigma_{\rm ib}$ are for $0.5 \leq \rho \leq 0.4$ g/cm^3. The DFT+MD+KG $\sigma_{\rm ic}$ value of Witte *et al.* at 0.6 g/cm^3 and the NPA-Ziman value for $\sigma_{\rm ic}$ are also shown.

the Fermi distribution.. At lower T ion-ion correlations and interactions become important and DFT+MD treats them well. However, at low T, the higher conductivities imply longer mean free paths and the need for simulation cells with larger L_{bx} [198]. Good DFT+MD+KG results, when available, provide benchmarks for calibrating other methods.

7.3. The conductivities of WDM lithium

The three conductivities $\sigma_{\rm ic}$,$\sigma_{\rm ib}$, and $\sigma_{\rm uf}$ for Li are shown in Fig. 7.5. The isobaric data are in the triangular region. The isochoric conductivities $\sigma_{\rm ic}$ at a density of ρ=0.542 g/cm^3, i.e., $r_{ws} = 3.251$, are given for a range of T, while one value at ρ=0.6 g/cm^3 and $T_e = T_i$ =4.5 eV, is also given. This is for conditions reported by Witte *et al.* [199]. The experimental isobaric data from Oak Ridge [27] for $\sigma_{\rm ib}$ (0.5 g/cm^3 at 0.05 eV to 0.4 g/cm^3 at 0.1378 eV), as well as the NPA $\sigma_{\rm ib}$, are also shown. Unlike aluminum, Li is a "low electron-density" material with $\bar{Z} = 1$. Hence its $E_F \sim 5$ eV is small compared to that of aluminum. For Li, $2k_F$ lies on the low-k side of the main peak as can be seen in Fig. 7.4(b). The UFM conductivity $\sigma_{\rm uf}$ remains higher than the $\sigma_{\rm ic}$, and its temperature dependence can be understood, as discussed in sec. 7.2.5, by the position of k_F with respect to $S(k)$ as T_e varies.

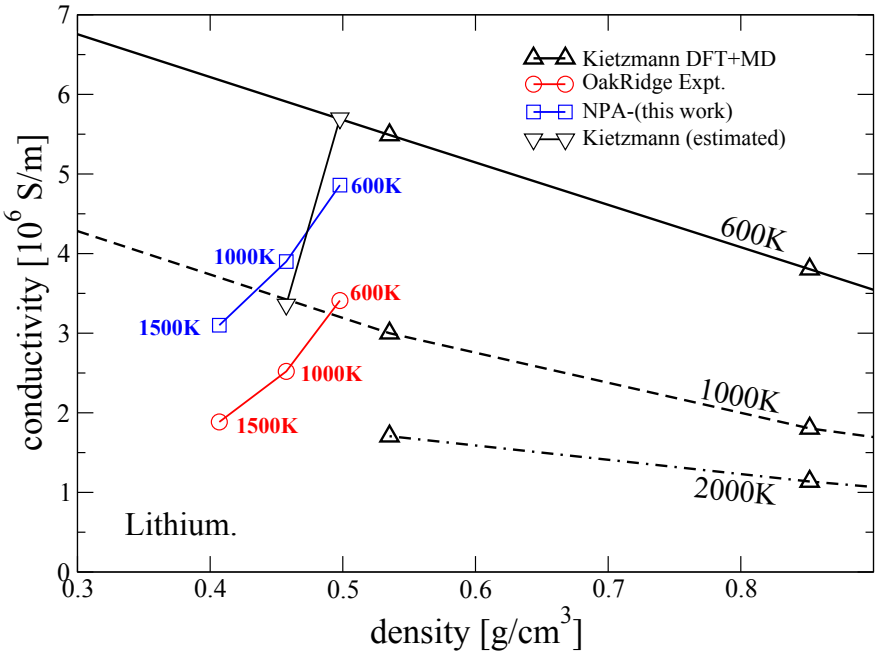

Figure 7.6. The Oak Ridge experimental data compared with the NPA and the DFT+MD+KG conductivity of Kietzmann *et al.* [128]. Their 600K and 1000K results have been slightly extrapolated to the low-density region covered by the experiments. The curve at 2000K given by Kietzmann *et al.* is above the boiling point of Li, and is not representative of the behaviour of Li at 1500K.

The agreement between the NPA-$\sigma_{\rm ib}$ and the Oak Ridge data for isobaric Li is moderate. The NPA-Li pseudopotential is the simplest local (s-wave) form and corrections (e.g., for the modified DOS) have not been used. In Fig. 7.6 we have attempted to compare the Oak Ridge experimental data for liquid lithium with the DFT+MD+KG calculations of Kietzmann *et al.* [128]. We use their calculations as a function of density for 600K and 1500K. The Kietzmann calculation at 2000K is also shown in Fig. 7.6, but since the boiling point of lithium under isobaric conditions is $\simeq$ 1600K, the calculation at 2000K cannot be justifiably used to estimate a value for 1500K from the data of Kietzmann *et al.* which also include the two points at 600K and 1000K. Nevertheless, their results are consistent with the observed trend and agree with our NPA results to the same extent as with the Oak Ridge data.

Disconcertingly, the NPA+Ziman and the DFT+MD $\sigma_{\rm ic}$ for ρ =0.6 g/cm^3 and T = 4.5 eV reported by Witte *et al.* [199] using a 64-atom simulation cell disagree by a factor of five. But the NPA-XRTS calculations for Li (see the Appendix) agree very well with the DFT-XRTS of Witte *et al.*. Furthermore, we had already shown that the pair-distribution functions

from NPA for Li for the density range of interest are in good agreement with the simulations of Kietzmann *et al.* (see Ref. [164]). However, at T=4.5 eV, $the chemical potential \mu$=0.035 a.u., i.e. the plasma is nearly classical. Hence , small-k scattering becomes important in determining σ. A simulation cell of length a=20.26 a.u., is applicable for 64 atoms; the smallest momentum accessible is $\pi/a = 0.16/(\text{a.u.})$ and fails to capture the smaller-k weighting of σ. These could contribute to the observed differences between the NPA and DFT+MD+KG results.

7.4. The conductivities of WDM carbon

Solid carbon is covalently bonded, with strong $sp3, sp2, sp$ bonding (with a bond energy of $\sim$ 8 eV) being possible. Hence efforts to create potentials extending to several neighbors, conjugation and torsional effects etc., have generated complex semi-empirical "bond-order" potentials parametrized to fit data bases but without any T dependence. Transient C-C bonds occur in liquid-WDM carbon. Normal-density liquid C near its melting point is a good Fermi liquid with four 'free' electrons per carbon ($\bar{Z}$ =4). An early comparison of Car-Parrinello calculations for carbon with NPA was reported by Dharma-wardana and Perrot in 1990 [112]. NPA successfully predicts the $S(k)$ and $g(r)$, inclusive of pre-peaks due to C-C bonding [113] as also obtained from DFT+MD simulations of WDM-carbon[170, 187]. The NPA and Path Integral Monte Carlo $g(r)$ [95] also agree closely [113]. No experimental $\sigma_{\rm ib}$ are available; hence we calculate only $\sigma_{\rm ic}$ and $\sigma_{\rm uf}$ to display the remarkable difference in the conductivities of complex WDMs with (transient) covalent bonding, compared to simpler WDMs like Al and Li.

Figure 7.7(a) displays $\sigma_{\rm ic}$ and $\sigma_{\rm uf}$ for isochoric carbon at 3.7 g/cm^3. Here E_F is $\sim$ 30 eV (for $\bar{Z} = 4$) and the WDM behaves as a simple metal, with σ dropping as T increases, and then increasing at higher T_e when μ_e becomes negative. The conductivity (for $T \leq 0.5E_F$) is determined mainly by the value of $S(k)$ at $2k_F$, shown in Fig. 7.7(b). This is set by the C-C peak in $S(k)$, which is relatively insensitive to T, and hence σ is also insensitive to temperature (compared to WDM Al or Li) in this regime. The insensitivity of $S(k = 2k_F)$to temperature also leads to the strikingly different behavior of the ultrafast conductivity for liquid carbon as compared to $\sigma_{\rm uf}$ and $\sigma_{\rm ic}$ of WDM-Al or Li. In WDM-carbon the ultrafast and isochoric conductivities are very close in magnitude. The DFT+MD $\sigma_{\rm ic}$ values for 3.7 g/cm^3 differ from the NPA at low-T where strong-covalent bonds dominate. The $N \sim 100$ atom DFT+MD simulations may be seriously inadequate due to such C-C bond formation. The NPA itself deals only in a spherically averaged way with the covalent bonding. That

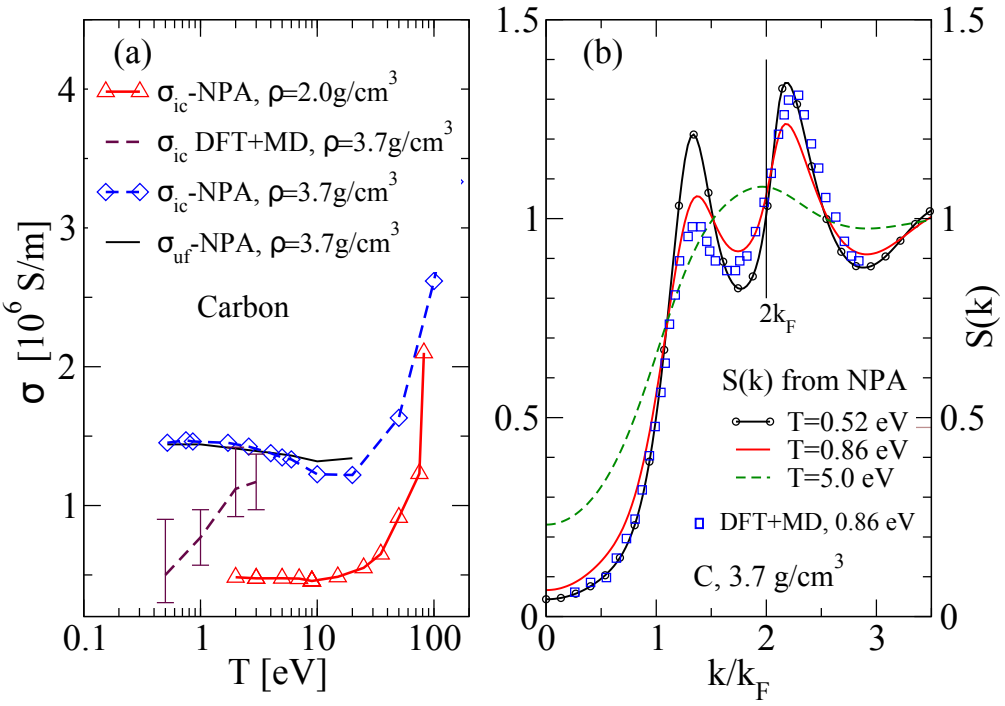

Figure 7.7. (a) Isochoric conductivity, $\sigma_{\rm ic}$, and ultrafast conductivity $\sigma_{\rm uf}$ for carbon at $\rho = 3.7$ g/cm^3 from NPA and DFT+MD, and isochoric conductivity from NPA for ρ=2.0 g/cm^3. (b) Ion-ion $S(k)$ for several temperatures; note nearly constant value of $S(k)$ at $2k_F$ (indicated by a vertical line).

approximation is probably sufficient for static conductivities if the bonding is truly transient. In any case, accurate experimental $\sigma_{\rm ib}$ data for liquid carbon are badly needed.

7.5. Conclusion

Although it is not necessary in principle to distinguish between isochoric and isobaric conductivities, as the specification of the density and temperature is sufficient, the use of such a distinction is useful in comparing experiment and theory. We see from our calculations that the temperature variations of the three conductivities have distinct features. Furthermore, the ultrafast conductivity is indeed a physically distinct property as the ion subsystem remains unchanged while only the electron subsystem is changed during the short time delay between the pump pulse and the probe pulse. Thus in this study we have found it useful to distinguish isochoric, isobaric and ultrafast conductivities of WDM systems, using Al, Li and C as examples. The NPA σ_{ib} are in excellent agreement with the isobaric aluminum data of Gathers [185], and in moderate agreement with Oak Ridge σ_{ib} for Li, as is also the case with DFT+MD+KG calculations. The carbon σ_{ic},σ_{uf} from NPA have a striking behaviour in the

regime of (normal) densities studied here, and differ from Al and Li. We attribute this to the effect of transient C-C bonds.

Appendix

This appendix addresses the following topics:
• Neutral pseudoatom (NPA) calculation of the X-ray Thomson scattering (XRTS) ion feature $W(q)$ for comparison with the density-functional-theory/molecular-dynamics (DFT+MD) calculations of Witte *et al.* [199], where the excellent agreement is in clear contrast to the disagreement for the conductivity datum for Li reported by Witte ıet al.
• Details of the neutral pseudoatom (NPA) model.
• Ziman formula for the conductivity using the NPA pseudopotential and the ion-ion structure factor $S(k)$.
•Examples of DFT+MD and KG calculations for Al, Li, and C, and Drude fits to the KG conductivity of Al and Li.
• Review of the isobaric and the isochoric conductivities of aluminum in the context of the experiment of Gathers, and the disagreement with the conductivity of Al reported in Fig.1 of Ref. [194] by Witte *et al.* using the Heyd, Scuseria, and Ernzerhof (HSE) functional.

7.5.1. X-ray Thomson Scattering calculation for Li at density $\rho = 0.6$ g/cm^3 and temperature $T = 4.5$ eV.

The calculation of XRTS of WDM using the NPA method has been described in detail in Ref. [109]. The XRTS ion feature $W(k)$ for Li at $T = 4.5$ eV and $\rho = 0.6$ g/cm^3 has been calculated (see Fig. 7.8) to compare our NPA results with the results from the DFT+MD simulations by Witte *et al.* (Ref. [199], Fig.8). This establishes the excellent agreement with the electronic structure part of the NPA calculation and the ionic part, $S_{ii}(k)$, resulting from the DFT+MD calculations, *irrespective* of the exchange-correlation (XC) functional used. That is, while we have used the local-density approximation (LDA) of the finite-T XC functional F_{xc} based on the classical-map hyper-netted-chain scheme (CHNC) [84], Witte *et al.* have used the $T = 0$ Perdew-Burke-Ernzerhof (PBE) XC functional [79] which includes gradient corrections.

The mean ionization $\bar{Z}$ for Li obtained in the NPA is unity, in agreement with that used by Witte *et al.*. They calculate the quantities $q(k), f(k), N(k)$, and $W(k) = N(k)^2 S(k)$. The quantity $q(k)$ is the 'screening cloud', i.e., the Fourier transform of the free-electron density

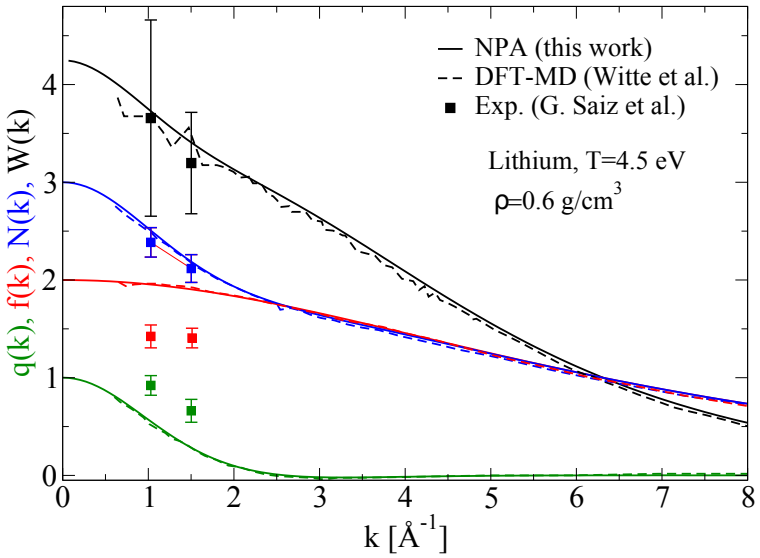

Figure 7.8. Comparison of quantities relevant to XRTS calculated using NPA+HNC (this work) and DFT+MD (Witte *et al.* [199]) for lithium. Values for k smaller than about 0.6/Å are not available from the DFT+MD simulation due to the finite size of the simulation cell. Here $q(k)$ is the Fourier transform of the free-electron density at the Li ion in the plasma, while $f(k)$ is the bound-electron form factor and $N(k) = f(k) + q(k)$. The *ion feature* $W(k) = N(k)^2 S(k)$ involves the ion-ion structure factor $S(k)$. Experimental points are from Saiz *et al.* (2008) cited in Witte *et al.*, Fig. 8

at the Li ion in the plasma, while $f(k)$ is the bound-electron form factor. Their sum is denoted by $N(k) = f(k) + q(k)$. Finally, $W(k) = N(k)^2 S(k)$ is the ion feature and involves the ion-ion structure factor $S(k)$.

The excellent accord between our XRTS calculation and that of Witte *et al.* establishes that our $S(k)$, electron charge distributions, and potentials $U_{ei}(k)$ and $V_{ii}(k)$ are fully consistent with the structure data and electronic properties coming from DFT+MD. The $S(k)$ and $U_{ei}(k)$ are the only inputs to the Ziman formula for σ_0. Nevertheless, our estimate of the conductivity disagrees strongly with the Kubo-Greenwood estimate of Witte *et al.*. Given the relatively good agreement that we found with the Oak Ridge experimental data, as well as with the Kietzmann data (see Fig. 7.6), this disagreement is *a priori* quite surprising; one possible contributory factor will be taken up in our discussion of the Kubo-Greenwood formula, viz., that it may be caused by the use of a small 64-atom DFT+MD simulation cell.

The conductivity estimate by Witte *et al.* for T=0.3 eV at 2.7 g/cm^3 is also problematic and it is taken up below, in our discussion of Gathers' results for aluminum.

7.5.2. Details of the NPA model and $\bar{Z}$.

The NPA model used here [63, 64] has been described in many articles; we summarize it again here for the convenience of the reader, as it should not be assumed that it is equivalent to various currently-available ion-sphere (IS) average-atom (AA) models such as Purgatorio [52] used in many laboratories. While these models are closely related, they invoke additional considerations which are outside DFT. We regard the NPA model as a rigorous DFT model based on the variational property of the grand potential $\Omega([n],[\rho])$ as a functional of both one-body densities $n(r)$ and $\rho(r)$, directly leading to two coupled KS equations where the unknown quantities are the XC-functional for the electrons and the ion-correlation functional for the ions [116]. Approximations arise in modelling those XC-functionals and decoupling the two KS equations for simplified numerical work.

The NPA model assumes spherical symmetry when dealing with fluid phases, and calculates the KS states of a nucleus of charge Z immersed in an electron gas of input density $\bar{n}$. The ion distribution $\rho(r)$ is approximated by a neutralizing uniform positive background containing a cavity of radius r_{ws}, with the nucleus at the origin. The Wigner-Seitz (WS) radius r_{ws} is that of the ion-density $\bar{\rho}$, i.e., $r_{ws} = \{3/(4\pi\bar{\rho})\}^{1/3}$. The effect of the cavity is subtracted from the final result where by the density response of a uniform electron gas to the nucleus is obtained. The validity of this approach has been established in previous work, for the WDM systems investigated here and reviewed in Ref. [115]. The solution of the KS equation extends up to $R_c = 10r_{ws}$, defining a correlation sphere (CS) large enough for all electronic and ionic correlations with the central nucleus to have gone to zero. The WS cavity plays the role of a nominal $\rho(r)$ to create a pseudoatom which is a neutral scatterer and greatly facilitates the calculation. The KS equations produce two groups of energy states, viz, negative and positive with respect to the energy zero at $r \to \infty$ outside the CS. States in one group decay exponentially to zero as $r \to R_c$, and in fact become negligible already for $r \to r_{ws}$ in the case of low-Z elements. These states, fully contained within the WS sphere, are deemed bound states, and allow one to define a mean ionization per ion, $Z_b = Z - n_b$, where n_b is the total number of electrons in the bound states and Z is the nuclear charge:

$$Z_b = Z - n_b;\ n_b = \sum_{nl} 2(2l+1) \int d\vec{r} f_{nl} |\phi_{nl}(r)|^2. \tag{7.1}$$

Here $f_{nl} = 1/\{1 + \exp(x_{nl})\}$, $x_{nl} = \{\epsilon_{nl} - \mu_0\}/T$ is the Fermi factor for the KS state ϕ_{nl} with energy ϵ_{nl}. The non-interacting electron chemical potential μ_0 is used here. Furthermore, there are plane-wave-like phase-shifted KS states which extend through the whole

correlation sphere. These are continuum states and their electron population is the free-electron distribution $n_f(r)$. The nucleus Z, the bound electrons n_b, the cavity with a charge $Z_c = (4\pi\bar{n}/3)r_{ws}^3$ and the free electrons form a neutral object and hence it is a weak scatterer called the 'neutral pseudoatom' (NPA). The Friedel sum Z_F of the phase shifts of the continuum states and the cavity charge Z_c add up to zero when the KS-equations are solved self-consistently. Thus

$$Z_c = Z_F = \frac{2}{\pi T}\int_0^\infty k f_{kl} k\{1 - f_{kl}\}\sum_l (2l+1)\delta_l(k)dk. \tag{7.2}$$

Here f_{kl} is the Fermi occupation factor for the k,l-state with energy $\epsilon = k^2/2$. Full self-consistency requires that

$$Z_b = Z_c = Z_F,\ \ \bar{n} = \bar{Z}\bar{\rho}. \tag{7.3}$$

Hence, given an input mean free-electron density $\bar{n}$, the WS radius (equivalently $\bar{\rho}$) is iteratively adjusted till self-consistency is obtained, i.e., Eq. 7.3 is satisfied to a chosen precision. The mean ionization $\bar{\rho}$ is thus seen to be the Lagrange multiplier ensuring charge neutrality, as first discussed in Ref. [61]. The $\bar{\rho}$ resulting from the input $\bar{n}$ may not be the required physical ion density, and hence several values of $\bar{n}$ and the corresponding $\bar{\rho}$ are determined to obtain the actual $\bar{n}$ that corresponds to the required experimental ion density $\bar{\rho}$. This process produces a unique value of $\bar{Z}$, and the problem of having several different estimates of $\bar{Z}$, as found in IS-AA models [54, 52] does not arise here. The agreement among Z_F,Z_c, Z_b is essential to the convergence of the NPA-KS equations. It is sensitive to the exchange-correlation (XC)-functional $F_{xc}(T)$ and to the proper handling of self-interaction (SI) corrections, whenever $\bar{Z}$ is close to a half-integer. Using a valid $\bar{Z}$ is essential to obtaining good conductivities.

We emphasize that a key difference between IS models and the NPA is that the free electrons are not confined to the Wigner-Seitz sphere, but move in all of space as approximated by the correlation sphere. These differences are discussed in Sec. 7.5.3.

In this study we use the local-density approximation to the finite-T XC-functional as parametrized by Perrot and Dharma-wardana [84]. This simplest implementation (in LDA) is a useful reference step needed before more elaborate implementations (involving SI, non-locality, etc. in the XC-functionals) are used.

Since $\bar{Z}$ is the free-electron density per ion, it can develop discontinuities whenever the ionization state of the element under study changes due to, e.g., increase of T or compression. This behaviour is analogous to the formation or disappearance of band gaps in solids. In fact, if the NPA model is treated with periodic boundary conditions, as for a solid with one atom in the unit cell, then the discontinuity in Z appears as the problem of correctly

treating the formation of a gap in the density of states (DOS) at the Fermi energy. A proper evaluation of such features in the DOS and band gaps is difficult in DFT as this is a theory of the total energy as a functional of the one-body density, *not* a theory of individual energy levels. The one-electron states are given by the Dyson equation. Thus band-structure calculations inclusive of GW-corrections are used in solids to obtain realistic band gaps and excitation energies. In dealing with discontinuities in $\bar{Z}$, a similar procedure is needed [200], including the use of self-interaction (SI) corrections and XC functionals that include electron-ion correlation corrections $F_{ei}(n,\rho)$ [116, 112].

It should be mentioned that some authors have claimed that $\bar{Z}$ "does not correspond to any well-defined observable in the sense of quantum mechanics" [53],i.e, that there is no quantum operator corresponding to $\bar{Z}$. This view is incorrect as quantities like the temperature T, the chemical potential μ, and the mean ionization $\bar{Z}$ are quantities in quantum *statistical* physics. There may be no operator for them in simple $T = 0$ quantum theories. In most formulations of quantum statistical physics these appear as Lagrange multipliers related to the conservation of the energy, particle number and charge neutrality. They can also be incorporated as operators in more advanced field-theoretic formulations of statistical physics (e.g., as in "thermofield-dynamics" of Umezawa). Some of these broader issues are discussed in Chapter 8 of Ref. [201].

Finally, it is noted that the mean number of electrons per ion, viz., $\bar{Z}$ in, e.g., gas-discharge plasmas, is routinely measured using Langmuir probes, or derived from optical measurements of various properties including the conductivity and the XRTS profile [2] for WDM-plasmas. Hence $\bar{Z}$ is a well-established *measurable* property.

7.5.3. Some Differences between the NPA model and typical average-atom models.

To our knowledge, no conductivity calculations using the Purgatorio model for isobaric aluminum are available for comparison with experimental data. Such a comparison is problematic due to the lack of an unequivocal value for the mean ionization $\bar{Z}$ in IS-AA models [52]. We list several differences with the NPA which particularly affect conductivity calculations:

1. Most average-atom models are based on the IS model where the free-electron pileup around the nucleus is strictly confined to the Wigner-Seitz sphere:

$$\bar{Z} = 4\pi \int_0^{R_{ws}} \Delta n_f(r) r^2 dr; \text{ IS-AA model.} \tag{7.4}$$

This condition, Eq. 7.4, was used in Salpeter's early IS model, in the Inferno model of Lieberman, and in codes like Purgatorio [52] derived from it, to fix an electron chemical potential $\mu^0_{\rm ws}$. It is also used in Yuan *et al.* [193], Faussurier *et al.* [192], Starrett and Saumon [55], and in other AA codes discussed in Murillo *et al.* [54]. However, $\mu^0_{\rm ws}$ is not identical with the non-interacting μ_0 because it includes a confining potential applied to the free electron density $n_f(r)$ constraining the electrons to the IS. As it is applied via a boundary condition, it is a non-local potential. The KS XC potential is also a non-local potential and hence the use of Eq. 7.4 contaminates the XC potential. On the other hand, DFT is based on mapping the interacting electrons to a system of *non-interacting electrons* whose chemical potentially is rigorously μ_0, as used in the NPA model that we employ. In the NPA we use a CS with a large radius R_c.

$$\bar{Z} = \pi \int_0^{R_c} \Delta n_f(r) r^2 dr; \text{ NPA model.} \tag{7.5}$$

The upper limit of the integral is $R_c \approx 10 r_{ws}$ and hence deals with a sphere large enough for all correlations with the central ion to have died down at the surface of the sphere. This enables the use of the non-interacting chemical potential in the NPA, as needed in DFT, since all equations use the large-r limit beyond the CS as the reference state.

The constraint placed by Eq. 7.4 is clearly invalid at low temperatures where the de Broglie wavelength of the electrons, being proportional to $1/\sqrt{T}$, exceeds r_{ws} at sufficiently low T. Hence such AA-models become invalid at low temperatures and are not true DFT models. In contrast, the first successful applications of the NPA (in the 1970s) were to low-temperature solids.

2. The use of the constraint placed by Eq. 7.4 in AA models has far reaching consequences as it prevents the possibility of providing a unique definition of the mean ionization, as emphasized by Stern *et al.* [52] in regard to the Inferno code. In fact even at high temperatures, there are at least two definitions of $\bar{Z}$ that differ, and hence the estimates of the electrical conductivity are not unambiguous. This is not the case in the NPA. The problem of discontinuities in $\bar{Z}$ and the under-estimate of bandgaps by DFT theory were already discussed in the previous subsection.

3. The IS-AA models do not satisfy a Friedel sum rule for $\bar{Z}$, while the f-sumrule is also constrained by the condition imposed by Eq. 7.4.

4. As the electrons are confined to the WS sphere in IS-AA models, they cannot display pre-peaks due to transient covalent bonding as found in liquid carbon, hydrogen and other low-Z WDMs. This was confirmed by Starrett *et al.* [56] for carbon for their AA model. The bonding occurs by an enhanced electron density in the inter-ionic region between two WS

spheres, and this is not allowed in IS models. In contrast, the NPA model shows pre-peaks in $g_{ii}(r)$ corresponding to transient C-C bonding in liquid carbon, and produces a pair-potential with a minimum corresponding to the C-C covalent bond distance at sufficiently low T [113]. Similar pre-peaks are found via NPA calculations for warm-dense hydrogen and low-Z elements in the appropriate temperature and density regimes [202].

7.5.4. Pseudopotentials and pair-potentials from the NPA.

The KS calculation for the electron states for the NPA in a fluid involves solving a simple radial equation. The continuum states $\phi_{k,l}(r), \epsilon_k = k^2/2$, with occupation numbers f_{kl}, are evaluated to a sufficiently large energy cutoff and for an appropriate number of l-states (typically 9 to 39 were found sufficient for the calculations presented here). The very high-k contributions are included by a Thomas-Fermi correction. This leads to an evaluation of the free-electron density $n_f(r)$, and the free-electron density pileup $\Delta n'(r) = n_f(r) - \bar{n}$. A part of this pileup is due to the presence of the cavity potential. This contribution $m(r)$ is evaluated using its linear response to the electron gas of density $\bar{n}$ using the interacting electron response $\chi(q,T_e)$. The cavity corrected free-electron pileup $\Delta n_f(r) = \Delta n'(r) - m(r)$ is used in constructing the electron-ion pseudopotential as well as the ion-ion pair potential $V_{ii}(r)$ according to the following equations (in Hartree atomic units) given for Fourier-transformed quantities:

$$
\begin{aligned}
U_{ei}(k) &= \Delta n_f(k)/\chi(k,T_e), && (7.6)\\
\chi(k,T_e) &= \frac{\chi_0(k,T_e)}{1 - V_k(1-G_k)\chi_0(k,T_e)}, && (7.7)\\
G_k &= (1-\kappa_0/\kappa)(k/k_{\rm TF}); \quad V_k = 4\pi/k^2, && (7.8)\\
k_{\rm TF} &= \{4/(\pi\alpha r_s)\}^{1/2}; \quad \alpha = (4/9\pi)^{1/3}, && (7.9)\\
V_{ii}(k) &= Z^2 V_k + |U_{ei}(k)|^2 \chi_{ee}(k,T_e). && (7.10)
\end{aligned}
$$

Here χ_0 is the finite-T Lindhard function, V_k is the bare Coulomb potential, and G_k is a local-field correction (LFC). The finite-T compressibility sum rule for electrons is satisfied since κ_0 and κ are the non-interacting and interacting electron compressibilities respectively, with κ matched to the $F_{xc}(T)$ used in the KS calculation. In Eq. 7.9, $k_{\rm TF}$ appearing in the LFC is the Thomas-Fermi wavevector. We use a G_k evaluated at $k \to 0$ for all k instead of the more general k-dependent form (e.g., Eq. 50 in Ref. [84]) since the k-dispersion in G_k has negligible effect for the WDMs of this study. Steps towards a theory using self-interactions

corrections in the F_{xc}, a modified electron DOS, self-energy corrections etc., have also been given [200]. In this study we use the above equations, and only in the LDA.

7.5.5. Calculation of the ion-ion Structure factor.

The ion-ion structure factor $S(k)$ is also a first-principles quantity as it is calculated using the ion-ion pair potential, Eq. 7.10 given above. For simple fluids like aluminum we use the modified hyper-netted-chain (MHNC) equation.

$$g(r) = \exp\{-\beta V_{ii}(r) + h(r) - c(r) + B(r)\}, \tag{7.11}$$

$$h(r) = c(r) + \bar{\rho} \int d\vec{r}_1 h(\vec{r} - \vec{r}_1) c(\vec{r}_1), \tag{7.12}$$

$$h(r) = g(r) - 1. \tag{7.13}$$

Here $c(r)$ is the direct correlation function. Thermodynamic consistency (e.g., the virial pressure being equal to the thermodynamic pressure) is obtained by using the Lado-Foiles-Ashcroft (LFA) criterion (based on the Gibbs-Bogoliubov bound for the free energy) for determining $B(r)$ using the hard-sphere model bridge function [68]. That is, the hard-sphere packing fraction η is selected according to an energy minimization that satisfies the LFA criterion. The iterative solution of the MHNC equation, i.e., Eq. (7.11), and the Ornstein-Zernike (OZ) equation, Eq. (7.12), yield a $g_{ii}(r)$ for the ion subsystem. The LFA criterion and the associated hard-sphere approximation can be avoided if desired, by using MD with the pair potential to generate the $g(r)$. The hard-sphere packing fraction η calculated via the LFA criterion is the only parameter extraneous to the KS scheme used in our theory. In calculating the $S(k)$ of complex fluids like carbon, where the leading peak in $g(r)$ is *not* determined by packing effects but by transient C-C bonding, we use the simple HNC equation.

7.5.6. Calculation of the electrical conductivity.

The electrical conductivity is calculated from the numerically convenient form of the Ziman formula given in Ref. [64]. The Ziman formula is sometimes derived from the Boltzmann equation. However, the KG formula and also the Ziman formula can both be derived from the Fermi golden rule [203]. The Ziman formula uses the 'momentum-relaxation time' approximation, while the KG formula typically uses the same approximation when extracting the static conductivity using a Drude fit to the dynamic conductivity $\sigma(\omega)$. The Ziman formula used here is:

$$\sigma = 1/R \; R = (\hbar/e^2)(3\pi\bar{n}\bar{Z})^{-1} I \tag{7.14}$$

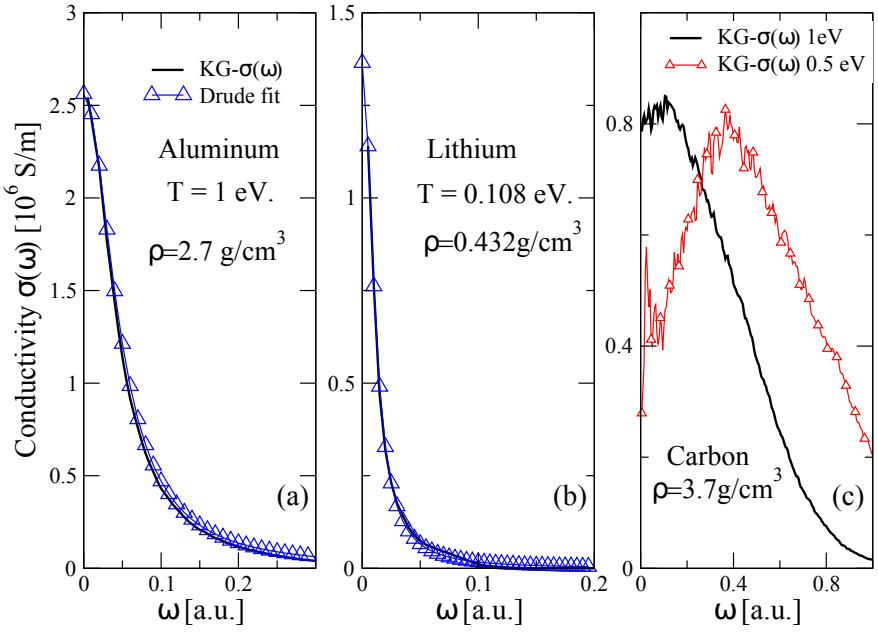

Figure 7.9. KG conductivity $\sigma(\omega)$ for Al, Li, and C. Note the slight non-Drude behaviour of Li $\sigma(\omega)$ near 0.08 a.u. in panel (b). The carbon $\sigma(\omega)$ is highly non Drude-like, with the peak moving to higher energy as T is lowered; no Drude form is shown for carbon.

$$I = \int_0^\infty \frac{q^3 \Sigma(q) dq}{1 + \exp\{\beta(\epsilon_q/4 - \mu)\}}, \tag{7.15}$$

$$\epsilon_q = (\hbar q^2/2m),\ \beta = 1/T, \tag{7.16}$$

$$\Sigma(a) = S(q)|U_{ei}(q)/\{2\pi\varepsilon(q)\}|^2, \tag{7.17}$$

$$1/\varepsilon(q\ \ ) = 1 + V_q \chi(q,T). \tag{7.18}$$

The "Born-approximation-like" form used here is valid to the same extent that the pseudopotential $U_{ei}(q)$ constructed from the (non-linear) KS $n_f(r)$ via linear response theory (Eq. 7.7) is valid. The $S(k)$ used are available even for small-k unlike in DFT+MD simulations where the smallest accessible k-value is limited by the finite size L_{bx} of the simulation cell.

7.5.7. The Kubo-Greenwood conductivity.

The KG dynamic conductivity $\sigma(\omega)$ is a popular approach to determining the static conductivity of WDM systems via DFT+MD [204]. In our simulations we have used N=108 atoms in the simulation cell, with a $2\times2\times2$ Monkhorst-pack k grid; the PBE XC functional was used. The energy cutoff was taken to be sufficiently high that the occupations in the highest KS states were virtually negligible. The quenched-crystal KS-eigenstates $\phi_\nu(r)$ and eigenvalues ϵ_ν, where ν is a band-index quantum number, are used in the Kubo-Greenwood

conductivity as provided in the standard ABINIT code. Usually six to ten such evaluations were obtained by evolving the quenched crystal by further MD simulations (using only the Γ point), and in each case the $\sigma(\omega)$ was obtained – see Fig. 7.9 for typical aluminum, lithium and carbon results for $\sigma(\omega)$.

The aluminum $\sigma(\omega)$ is well-fitted by the Drude form:

$$\sigma(\omega) = \sigma_0/(1 + (\omega\tau)^2), \sigma_0 = \bar{n}\tau. \tag{7.19}$$

However, there is no justification for using a Drude form for carbon. The peak position in $\sigma(\omega)$ roughly corresponds to the 'bonding $\rightarrow$ antibonding' transition in the fluid containing significant covalent bonding (see Fig. 4(b) of the main text) at 0.5 eV. This is seen from the strong peak in $g(r)$ near 3 a.u. (1.55 Å) corresponding to the C-C bond length. This suggests that the $N = 108$ simulation is quite inadequate for complex liquids like carbon, as bonding reduces the effective N of the simulation. In the case of carbon, the static limit of the KG $\sigma(\omega)$ was simply estimated from the trend in the $\omega \rightarrow 0$ region rather than using a Drude fit. Furthermore, the different quenched crystals (108 atoms in the simulation) gave significant statistical variations, as reflected in the error bars shown in Fig. 4(a) of the main text. At higher T, e.g., for $T = 1 - 2$ eV, the estimated conductivity behaves similar to that from the NPA, but somewhat less conductive. The KG formula does not include any self-energy corrections in the one-electron states and excitation energies, and less importantly, no ion-dynamical contributions either, as the ions are stationary (Born-Oppenheimer approximation). The form of $\sigma(\omega)$ including ion dynamics has been discussed by Dharma-wardana at the Cargèse NATO work shop in 1992 [205].

7.5.8. The conductivity of Li at T =4.5 eV and density 0.6 g/cm^3.

The conductivity of Li, at density $\rho = 0.6$ g/cm^3 at 4.5 eV estimated by Witte *et al.* [199], is roughly a factor of five less than that obtained from NPA+Ziman. While the NPA calculation may differ from another calculation by, at worst, a factor of 2, it is hard to find an explanation for this strong disaccord, given the good agreement in the XRTS calculation. One possibility is the use of a 64-atom cell in DFT+MD for Li at a chemical potential $\mu \sim 0$. DFT+MD and KG using $N \sim 100$ atoms in the simulation seems to significantly underestimate σ_0 for low-valence substances like Li, Na, especially as T is increased. Low-valence materials have a small $\mu = E_F$ and hence a modest increase in T can push μ to small values where small-k scattering is important, and finally to $\mu < 0$ values (classical regime).

At low T/E_F the major contributions to σ are provided by electron scattering between $-k_F$ and k_F, $k_F = \sqrt{2E_F}$, i.e., momentum changes of the order of $2k_F$. However, at finite T,

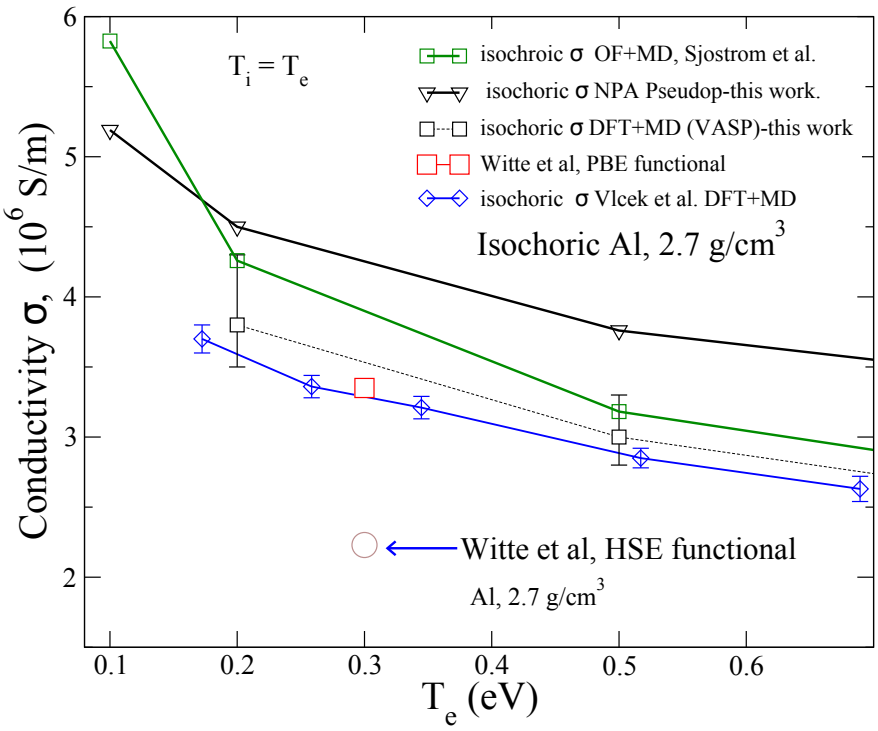

Figure 7.10. Isochoric conductivity of aluminum from near its melting point to about 0.7 eV, expanded from Fig. 1 of the main text, and now including the Witte *et al.* [194] calculation of the Al-conductivity at 0.3 eV and $\rho = 2.7$ g/cm^3. Our DFT+MD data and those of Vlček are shown.

μ replaces E_F, and as T increases $\mu \to 0$ and to negative values. The scattering momenta near $\mu \to +0$ are in the small-k region, These contribute significantly to σ at $T = 4.5$ eV for Li at 0.6 g/cm^3. In Li, if a 64-atom simulation is used, an appropriate length a of the cubic simulation cell would be $a = 20.26$ a.u. The smallest momentum accessible by such a simulation is π/a=0.16/(a.u.) and hence the corresponding Kubo-Greenwood formula will not sample the small $k < 0.16$ region. We see from Fig. 7.8 also that the DFT+MD simulations do not provide values for k smaller than ≈ 0.6/Å due to the finite size of the cell used in Ref. [194].

Hence such DFT+MD+KG calculations of σ are strongly weighted to the larger-k strong scattering regime and predict a low conductivity. The results of Pozzo *et al.*, where a 1000-atom simulation was needed for Na is a case in point. However, such large simulations are beyond the scope of many laboratories while NPA-type approaches usually provide results to within a factor of two in the worst case.

7.5.9. Isobaric and isochoric conductivity of aluminum in the liquid-metal region.

High-quality experimental data (errors of ± 6 %) are available for the isobaric conductivity $\sigma_{\rm ib}$ of liquid aluminum at low T [185, 186]. The relevant region, viz., (a) of Fig. 1 of the main text, is shown enlarged to display the experimental and calculated data in Fig. 7.2. The NPA calculation is in excellent agreement with the experiment of Gathers, to well within the error bars. On the other hand, the DFT+MD calculation captures about 75% of the experimental conductivity. A ∼100-atom simulation cannot capture the k-values smaller than $\pi/a \sim 0.12/$(a.u.) for Al at this density, and may contribute to some of the under-estimate.

Isochoric conductivities (with $\rho = 2.7$ g/cm^3) of aluminum obtained from the NPA and from DFT+MD by us and by Vlček *et al.* [190] are shown in Fig. 7.10, together with a single data point from Witte *et al.* [194] with the PBE functional, and with the HSE functional. The result obtained using the HSE XC-functional is a strong underestimate compared to other DFT+MD [197, 206], the orbital-free calculation and the NPA estimates.

In Ref. [194] Witte *et al.* strongly argue for the HSE functional even for aluminum, a 'simple' metal proven to work well with more standard approaches. The value of 2.23 $\times 10^6$ S/m quoted by them at 0.3 eV, 2.7 g/cm^3, is taken to agree with experiment, based on their interpretation of the experimental data of Gathers [185]. However, as discussed below, Gathers' datum at 0.3 eV (≃3500K) is for isobaric aluminum at $\rho = 1.875$ g/cm^3 and 0.3 GPa.

7.5.10. The experimental data of Gathers.

Gathers measures the resistivity of aluminum in an isobaric experiment, starting from the solid (ρ_0=2.7 g/cm^3, v_0=0.37 cm^3/g) and heating to the range 933K to 4000K at 0.3 GPa [185]. Gathers himself recommends the Gol'tsova-Wilson [207, 208] volume expansion data rather than those measured by him. In Table II of the 1983 publication of Gathers [185], the experimental resistivity ("raw data") calculated using the nominal enthalpy input to the sample is given in column 5. The apparatus and the sample undergo volume expansion; the resistivities for the input enthalpy corresponding to the volume expanded sample (using the Gol'tsova-Wilson data) are given in column 4 of the same table. Hence the "volume corrected" isobaric resistivity for aluminum in the range (T=993K, ρ=2.42g/cm^3) to (T=4000K, ρ=1.77g/cm^3) are the values found in column 4 while column 5 gives the "raw data". Column 4 resistivities agree with the isobaric resistivity values that may also be obtained from the fit formula given in the last row of Table 23 of the 1986 Gathers review[186].

Since Table II as given by Gathers is somewhat misleading, we have recalculated the resistivities R using the fit equations given by Gathers. Eq. (8) gives the (expansion-uncorrected) "raw data", labeled $R_{\rm G}$. The expansion correction essentially brings the input heat to the actual volume of the sample. Thus equation (9), where the enthalpy input is corrected for volume expansion agrees with Gathers' fit equation given subsequently in 1986 [186] and hence labeled R_{1986}. Gathers uses the enthalpy as the primary variable in equation (8) and (9), but also gives $R_{\rm G}$ directly as a function of v/v_0 in equation (10). Thus Eqs. (8) and (10) yield the same resistivity $R_{\rm G}$ at a given density and corresponding T, while Eq. (9) is the volume-corrected equation restated in the 1986 review.

According to Gathers, the experimental resistivities have an error of $\sim \pm 6\%$. The relevant equations from Gathers' 1983 work are given below:

$$\begin{aligned} H &= 0.0048910 + 0.0010704T \\ &\quad +2.3084 \cdot 10^{-8}T^2, \text{Gathers Eq.(6)}, \end{aligned} \tag{7.20}$$

$$\begin{aligned} v/v_0 &= 1.0205 + 8.3779 \cdot 10^{-2}H \\ &\quad +4.9050 \cdot 10^{-3}H^2, \text{Gathers Eq.(7)}, \end{aligned} \tag{7.21}$$

$$\begin{aligned} R_9 &= 0.1494 + 7.9448 \cdot 10^{-2}H \\ &\quad -1.3189 \cdot 10^{-3}H^2, \text{Gathers Eq.(9)}, \end{aligned} \tag{7.22}$$

$$\begin{aligned} 1.12 &\leq v/v_0 \leq 1.56; \quad \text{i.e.} \\ &\quad 2.411\,\text{g/cm}^3 \leq \text{density} \leq 1.731\,\text{g/cm}^3. \end{aligned} \tag{7.23}$$

The enthalpy H can be eliminated in Gathers' Eq. (9), i.e. (A.22), using the preceding equations. The result agrees with the fit equation given in the subsequent 1986 review article [186], Table 23 (last row). This is given as a fit for the isobaric resistivity (at 0.3 GPa) ($\mu\Omega$ m), viz.,

$$R(v) = -1.0742 + 4.1997 \times 10^3 \cdot v - 2.5124 \times 10^6 \cdot v^2. \tag{7.24}$$

Here v is the volume in m^3kg^{-1} with $4.1{\times}10^{-5} \leq v \leq 5.78{\times}^{-4}$. The resistivity calculated from this equation agrees with column 4 of Table II of Gathers [185].

The NPA calculation which takes the nuclear charge, temperature and density as the only inputs and uses the finite-T PDW XC-functional(LDA) [84] gives excellent agreement for $\sigma_{\rm ib}$ with the Gathers' data at all densities listed in Table 7. I, as seen in Fig. 7.2. At $T = 0.3$ eV, ρ =1.875 g/cm^3 $\sigma_{\rm ib} = 2.22 \times 10^6$ S/m, while the HSE functional used with MD+DFT+KG gives this conductivity only at 2.7 g/cm^3, as reported by Witte *et al.* [194].

Table 7. I. Gathers' data for Al recalculated from his 1983 fit equations (6)-(10) and also from his fit equation (reproduced as Eq. 7.24) given in the last row of Table 23 of the 1986 review [186]

T (K)	v/v_0 — Eq.(7)	ρ (g/cm^3)	$R_{\rm G}$ ($\mu\Omega$m) Eq.(8)	$R_{\rm Eq.(9)} = R_{1986}$ ($\mu\Omega$m) Eq.(9)	$\sigma_{\rm ib}$ 10^6 (S/m) $1/R_{\rm Eq.(9)}$
Gathers	Col.3	—	Col.5	Col.4	$1/R_{1986}$
933	1.12	2.42	0.261	0.233	4.30
1000	1.12	2.41	0.268	0.238	4.20
1500	1.18	2.29	0.331	0.281	3.56
2000	1.24	2.18	0.370	0.324	3.08
2500	1.30	2.08	0.476	0.367	2.73
3000	1.37	1.97	0.560	0.409	2.44
3500	1.44	1.87	0.651	0.451	2.22
4000	1.52	1.77	0.751	0.494	2.03

Our DFT+MD estimates of the isochoric conductivity using the PBE functional, the DFT+MD estimates of Vlček *et al.*, and the Witte *et al.* DFT+MD estimate [194] using the PBE functional for 2.7 g/cm^3 at 0.3 eV are in close agreement. They all fall below the NPA+Ziman estimate, and we attribute this partly to the inability of the DFT+MD+KG approach to access small-k scattering contributions unless the number of atoms N in the simulation is sufficiently large. Furthermore, as $T/E_F \to 0$, the estimate of the derivative of the Fermi function and also the matrix-element of the velocity operator probably require an increasingly more dense mesh of k-points.

Chapitre 8

CONCLUSION

> "The underlying physical laws necessary for the mathematical theory of a large part of physics and the whole of chemistry are thus completely known, and the difficulty is only that the exact application of these laws leads to equations much too complicated to be soluble. It therefore becomes desirable that approximate practical methods of applying quantum mechanics should be developed, which can lead to an explanation of the main features of complex atomic systems without too much computation. "
> — Paul Dirac, *Proceedings of the Royal Society of London, Containing Papers of a Mathematical and Physical Character*, **123**, 792 (1929)

Tous les systèmes atomiques, qu'ils soient dans une phase solide ou une phase plasma, sont totalement définis par une seule équation connue exactement ; un Hamiltonien dont la simplicité camoufle son immense complexité. Suivant les conseils de Dirac, les physiciens développèrent de puissants modèles, basés sur d'élégantes approximations, qui permirent une compréhension profonde de la matière qui nous entoure. Que ce soit l'étude de la matière condensée qui propulsa l'électronique moderne ou celle des plasmas dont l'utilisation industrielle est sans limites, l'étude des systèmes atomiques est la principale source des avancements technologiques des dernières décennies. Malgré tout, lorsque la matière est soumise à des conditions extrêmes de pression et de température, telles qu'observées au centre de planètes géantes où à l'intérieur de capsules utilisées pour la fusion à confinement inertiel, ces modèles standards deviennent inapplicables. À la frontière entre la phase solide et plasma, le régime de la matière dense et chaude offre donc un nouveau défi aux physiciens. La modélisation de ce régime complexe, en particulier les systèmes en quasi-équilibre où la température électronique diffère de celle ionique, est l'objectif principal de cette thèse. Puisqu'il était nécessaire de combiner des techniques théoriques provenant de la physique de la matière condensée et de la physique des fluides, une description détaillée de ces méthodes a été présentée dans le chapitre 2. Nous avons aussi introduit le modèle du pseudo-atome

neutre qui est l'outil principal utilisé dans cet ouvrage. D'une très grande efficacité numérique, ce modèle s'est avéré être aussi précis que les méthodes purement *ab initio* qui sont extrêmement couteuses computationnellement. L'intérêt grandissant pour la matière dense et chaude provient essentiellement de notre récente habilité à créer de type de systèmes expérimentalement en laboratoire. L'irradiation de cibles métalliques par des lasers à impulsions courtes permet, selon l'énergie des photons, d'obtenir deux systèmes distincts, soit la matière ultra-rapide et la matière compressée par choc.

Dans les chapitres 3 et 4, on s'est intéressé principalement à la description la matière ultra-rapide où la température électronique est largement supérieure à la température ionique qui reste sensiblement à la température ambiante. Dans le chapitre 3, nous avons tout d'abord illustré la validité des potentiels de paires construits au sein du modèle PAN en reproduisant les spectres de phonons expérimentaux ainsi que ceux obtenus par TPFD dans le cas de l'aluminium, le sodium et le potassium. En calculant les relations de dispersion des phonons pour les systèmes en quasi-équilibre, on a pu valider l'hypothèse du durcissement des phonons. Nous avons aussi montré que la modification du spectre dépendait de la structure cristalline du matériau étudié. Dans le Chapitre 4, on a démontré que le durcissement des phonons était aussi prédit par des simulations TPFD qui s'avèrent être en excellent accord avec les prédictions du modèle PAN. Les systèmes de MUR développent une large pression interne résultant de l'ablation de la surface de l'échantillon. En comparant le temps d'ablation de la surface avec les fréquences modifiées du cristal MUR, on a déterminé, qu'au-delà une certaine température électronique, le concept de phonons n'avait plus de signification physique. La nécessité d'utiliser un pseudo-potentiel électron-ion contenant exactement le nombre d'électrons libres dans le système s'est avérée cruciale pour une modélisation adéquate de la MUR au sein des codes de TFD. On a déterminé que le calcul de la pression était peu affecté par l'utilisation d'une fonctionnelle d'échange et corrélation dépendante de la température. La comparaison de la pression de la MUR avec celle d'un système à l'équilibre a clairement illustré à quel point ces deux types de système sont différents.

Dans le chapitre 5, on a utilisé le modèle PAN pour analyser quatre expériences de diffusion Thomson de rayons X sur de la matière compressée par choc dont deux sur l'aluminium et deux sur le béryllium. Les propriétés de ces systèmes sont obtenues par le lissage du spectre expérimental avec le spectre théorique qui est généralement donné par la décomposition de Chihara. Tandis que la densité et température électronique sont déterminée par le spectre inélastique, la température ionique entre en jeu uniquement dans la partie élastique. Le spectre PAN s'est avéré reproduire fidèlement le spectre de l'expérience I sur l'aluminium en prédisant un système à l'équilibre. Cependant, pour reproduire le spectre de l'expérience

II sur l'aluminium, il a été nécessaire d'utiliser une température ionique approximativement six fois inférieure à la température électronique. Cette prédiction fut soutenue par les prédictions d'un autre modèle d'atome moyen ainsi que par des simulations TFD+DM. Dans le cas du béryllium, aucune des deux expériences n'était suffisamment précise pour prédire adéquatement les propriétés du système ionique, mais suggérait tout de même que ces systèmes étaient aussi dans un état hors d'équilibre. Toutefois, la comparaison de facteurs de structure statique à deux températures du modèle PAN avec ceux de simulations TFD+DM illustra la validité des nos potentiels de paires ainsi que de l'approche MHNC pour le béryllium.

Dans le chapitre 6, on s'est intéressé au facteur de structure dynamique ion-ion de l'aluminium en quasi-équilibre en effectuant des simulations de DM avec nos potentiels de paires. Le calcul de la fonction de van Hove permit d'établir que les corrélations spatiales ion-ion s'atténuent bien plus rapidement que le temps de thermalisation électron-ion impliquant que les propriétés dynamiques du système en quasi-équilibre ont une signification physique. Le calcul de la relation de dispersion des modes acoustiques de vibrations du fluide permit de prédire que la vitesse du son augmentait considérablement avec la température électronique. La vitesse du son peut aussi être calculée par le facteur de structure statique et on a démontré que l'utilisation d'un terme de pont dans la procédure HNC était cruciale pour reproduire les résultats obtenus par DM. Puisque les équations d'états sont primordiales pour des simulations hydrodynamiques des fluides, on a démontré qu'il existe d'importantes différences au sein de l'énergie libre, l'énergie interne et la pression entre un système à l'équilibre et un système à deux températures. Puisque le modèle PAN permet un calcul extrêmement rapide de ces quantités, il serait idéal pour ce type de simulations où les équations d'états doivent être calculées pour chaque combinaison de températures.

L'une des propriétés les plus importantes pour le progrès les capsules nécessaire à la fusion est la conductivité électrique et thermique dont le calcul pour le régime de la matière dense et chaude a été discuté dans le chapitre 7. Les prédictions du modèle PAN couplé à la formule de Ziman ainsi que celles obtenues par TFD+DM couplé à la formule de Kubo-Greenwood furent comparées pour l'aluminium, le lithium et le carbone pour des conditions isobariques, isochoriques et dans le cas particulier de la matière ultra-rapide. De façon générale, on a observé que les calculs TFD+DM+KG ont tendance à prédire des conductivités inférieures aux valeurs expérimentales tandis que le modèle PAN+Ziman les surestime. L'important désaccord entre ces deux méthodes théoriques illustre la complexité de ce problème et l'importance d'avoir davantage de résultats expérimentaux.

Comme nous l'avons démontré au travers de plusieurs articles, l'un des avantages principaux du modèle PAN est sa polyvalence puisqu'il est possible de l'appliquer à une grande

variété de problèmes fondamentaux pour l'étude de la MDC. Malgré tout, le modèle possède plusieurs limitations qu'il est important de garder en tête lors de son utilisation. D'une part, la construction du PAN nécessite une densité d'électrons libres uniformes ce qui rend le traitement de surfaces plus difficile, mais pas impossible. En effet, les travaux de Lang et Kohn [209] ont permis d'adapter le modèle du pseudo-atome pour un gaz d'électrons non-homogène afin d'obtenir la densité électronique ainsi que l'énergie d'une surface. D'autre part, pour certaines conditions de densités et températures, la formation permanente de molécules peut survenir et rendre le modèle PAN inutilisable. Par contre, comme illustré par Dharma-wardana [113], lorsque l'état moléculaire est transitoire, c'est-à-dire lorsque les atomes s'associent et se dissocient suffisamment rapidement, le modèle PAN est toujours valide et permet de prédire ce type de comportement. En effet, Dharma-wardana observa, dans le carbone, l'apparition d'un nouveau maximum dans la fonction de distribution de paires positionné exactement à la distance du dimère carbone-carbone ce qui permet de prédire la formation de molécules dans le système. Une autre situation où le modèle n'est plus applicable survient lorsque les électrons de cœur des atomes s'étendent loin de leur noyau et participent ainsi à l'interaction inter-ionique telle que pour l'or ou le fer par exemple. La procédure effectuée pour construire le potentiel de paires du modèle devient impraticable. Malgré tout, l'application du modèle PAN est parfaitement adaptée à l'étude des métaux simples dont les propriétés sont cruciales pour la compréhension fondamentale de la MDC, mais aussi pour de futures applications technologiques.

La simplicité, la précision ainsi que la polyvalence du modèle PAN en font un outil d'une très grande puissance pour l'étude de plusieurs systèmes physiques qu'ils soient dans la phase solide ou plasma. L'utilisation de potentiels de paires, sans paramètre libre, a permis de débuter l'étude des propriétés dynamiques de la MDC avec une précision équivalente aux méthodes totalement *ab initio* tout en nécessitant une fraction des ressources computationnelles. Tandis que nous avons étudié l'aluminium à la densité ambiante, il serait intéressant d'étendre la procédure pour des systèmes compressés par choc où la densité et la température peuvent prendre des valeurs extrêmes. De plus, l'obtention des propriétés dynamiques pour d'autres matériaux essentiels à la fusion par confinement inertiel, tel que le béryllium et l'hydrogène, serait très intéressant. De plus, tandis que nous avons uniquement étudié des systèmes contenant un seul type d'ion, il y a un grand intérêt pour les mixtures, tel que le mixte carbone-hydrogène [178], où le modèle PAN est facilement adaptable. En effet, dans notre étude, nous avons utilisé une charge ionique moyenne $\bar{Z}$ qui pouvait prendre des valeurs fractionnaires, mais une description plus élaborée est disponible au sein du modèle PAN tel que décrit par Perrot et Dharma-wardana [210]. Pour traiter une mixture de différents ions

d'un même atome, il est possible de construire un PAN pour chaque ion de charge Z_i et de déterminer la concentration x_i de ceux-ci en minimisant l'énergie libre du système en fonction de x_i. Il est possible d'appliquer cette procédure pour de différents atomes ce qui permet d'envisager le modèle PAN comme un très bon outil pour le traitement des mixtures. Une autre application possible du modèle PAN est la description de l'ablation de surface métallique par un laser. En effet, dans ce type d'étude, le système ionique, initialement à la température ambiante et dont l'interaction inter-ionique est généralement décrit par des potentiels empiriques, est couplé à un système électronique fictif dont la température est grandement augmentée par l'absorption du laser. En utilisant un modèle à deux-températures, tel que décrit dans la section 1.2.2, le système ionique se réchauffe pour finalement provoquer l'ablation de la surface par le mouvement thermique des ions. Cependant, nous avons démontré à maintes reprises que la température électronique affecte directement l'interaction inter-ionique. En effet, le potentiel de paires possédant plusieurs minimums responsables de la structure cristalline à $T_e = T_i = T_r$ devient purement répulsif lorsque $T_e > T_i$. Cette modification de l'interaction inter-ionique modifiera clairement la dynamique des ions de surface et le phénomène d'ablation risque d'en être grandement modifié. L'utilisation du modèle PAN serait alors très intéressant dans le cadre de l'ablation laser et serait un bon projet futur.

Finalement, cette thèse permit de mettre en évidence l'efficacité du modèle PAN pour la description de la matière dense et chaude. Tandis qu'on a utilisé les potentiels de paires du modèle pour décrire adéquatement la partie élastique du spectre de diffusion de rayons X, il serait idéal d'effectuer le calcul du spectre total au sein même du modèle PAN. En effet, puisque toutes les quantités nécessaires aux calculs sont déjà disponibles dans le modèle, cela permettrait une détermination cohérente de la densité et de la température du système ionique et électronique. De plus, comme mentionné dans l'introduction, la théorie de la fonctionnelle de la densité totale envisage une description auto cohérente de la densité électronique et ionique autour d'un ion. Puisque le modèle PAN s'avère être la première étape de cette approche, la continuation de cette procédure serait idéale pour l'obtention d'une description complète de la matière dense et chaude dont la compréhension est cruciale à la fusion nucléaire contrôlée.

Annexe A

RÈGLE DE SOMME DE LA COMPRESSIBILITÉ

Le point de départ pour démontrer la *règle de somme de la compressibilité* [66]

$$S(0) = \rho k_B T \kappa, \tag{A.1}$$

est la fonction de partition dans l'ensemble *grand canonique*

$$\Theta = \sum_{N=0}^{\infty} \frac{h^{-3N}}{N} \exp(N\beta\mu) \iint \exp(-\beta H(\mathbf{r}^N,\, \mathbf{p}^N))\; d\mathbf{r}^N d\mathbf{p}^N \tag{A.2}$$

$$\equiv \sum_{N=0}^{\infty} \exp(N\beta\mu) Q_N(V,T) \tag{A.3}$$

où h est la constante de Planck, N est le nombre de particules dans le système, $\beta = (k_B T)^{-1}$ est l'inverse de la température, μ est le potentiel chimique, H est l'hamiltonien du système, $\mathbf{r}^N \equiv \{\mathbf{r}^1,\mathbf{r}^2 \cdots \mathbf{r}^N\}$ est l'ensemble des positions des N particules et $\mathbf{p}^N \equiv \{\mathbf{p}^1,\mathbf{p}^2 \cdots \mathbf{p}^N\}$ est l'ensemble des impulsions des N particules. La probabilité $P(N)$ que le système possède N particules, peu importe leurs positions et impulsions, prend alors la forme

$$P(N) = \frac{1}{\Theta} \exp(N\beta\mu) Q_N(V,T), \tag{A.4}$$

ce qui permet de calculer la nombre moyen de particules dans le système

$$\langle N \rangle = \sum_{N=0}^{\infty} N P(N) = \frac{1}{\Theta} \frac{\partial \Theta}{\partial(\beta\mu)} = \frac{\partial \ln \Theta}{\partial(\beta\mu)}. \tag{A.5}$$

En dérivant l'Eq.(A.5) par rapport à $\beta\mu$, il est possible d'obtenir la fluctuation du nombre de particules par rapport à la moyenne

$$\boxed{\frac{\langle N^2 \rangle - \langle N \rangle^2}{\langle N \rangle} = \frac{1}{\langle N \rangle} \frac{\partial \langle N \rangle}{\partial(\beta\mu)},} \tag{A.6}$$

qui est le premier résultat nécessaire à la démonstration.

Un changement infinitésimal du grand potentiel $\Omega = -PV$ prend la forme

$$d\Omega = -P\; dV - V\; dP = -P\; dV - S\; dT - N\; d\mu, \tag{A.7}$$

qui, pour un changement infinitésimal à température constant, permet d'obtenir la relation $V\ dP = N\ d\mu$. Lorsque le changement est effectué à volume constant, les termes dP et $d\mu$ sont proportionnelles à dN tels que

$$dP = \left(\frac{\partial P}{\partial N}\right)_{V,T} dN, \qquad d\mu = \left(\frac{\partial \mu}{\partial N}\right)_{V,T} dN. \tag{A.8}$$

En utilisant l'Eq.(A.8) dans l'Eq.(A.8), on obtient

$$N\left(\frac{\partial \mu}{\partial N}\right)_{V,T} = V\left(\frac{\partial P}{\partial N}\right)_{V,T} = \left(\frac{\partial P}{\partial \rho}\right)_{N,T} = \frac{1}{\rho\kappa}. \tag{A.9}$$

Dans la limite thermodynamique $N \to \langle N\rangle$ et en utilisant les résultats de l'Eq.(A.9) et de l'Eq.(Eq.Resultat1), on obtient alors le deuxième résultant important pour la démonstration

$$\boxed{\frac{\langle N^2\rangle - \langle N\rangle^2}{\langle N\rangle} = \rho k_B T \kappa.} \tag{A.10}$$

Pour la suite, il est nécessaire de définir la n-densité dans l'ensemble *canonique*

$$\rho_N^{(n)}(\mathbf{r}^n) = \frac{1}{Q_N(V,T)}\frac{N!}{(N-n)!)}\iint \exp(-\beta H(\mathbf{r}^N,\, \mathbf{p}^N))\ d\mathbf{r}^{N-n}\ \mathbf{p}^N, \tag{A.11}$$

qui permet de définir la n-densité dans l'ensemble *grand canonique*

$$\rho^{(n)}(\mathbf{r}^n) = \sum_{N\geqslant n}^{\infty} P(N)\rho_N^{(n)}(\mathbf{r}^n). \tag{A.12}$$

En intégrant l'Eq.(A.12) sur toutes les positions $\mathbf{r}^1 \cdots \mathbf{r}^n$, on obtient la normalisation

$$\int \rho^{(n)}(\mathbf{r}^n) d\mathbf{r}^n = \left\langle \frac{N!}{(N-n)!)} \right\rangle, \tag{A.13}$$

où en particulier

$$\int \rho^{(1)}(\mathbf{r}^1) d\mathbf{r}^1 = \langle N\rangle \qquad \text{et} \qquad \iint \rho^{(1)}(\mathbf{r}^1,\mathbf{r}^2) d\mathbf{r}^1 d\mathbf{r}^2 = \langle N^2\rangle - \langle N\rangle. \tag{A.14}$$

Cela permet d'écrire la relation

$$\frac{1}{\langle N\rangle}\iint [\rho^{(1)}(\mathbf{r}^1,\mathbf{r}^2) - \rho^{(1)}(\mathbf{r}^1)\rho^{(1)}(\mathbf{r}^2)] d\mathbf{r}^1 d\mathbf{r}^2 = \frac{\langle N^2\rangle - \langle N\rangle - \langle N\rangle^2}{\langle N\rangle}. \tag{A.15}$$

En utilisant la définition de la n-fonction de distribution

$$g^{(n)}(\mathbf{r}^n) = \frac{\rho^{(n)}(\mathbf{r}^n)}{\prod_{i=1}^n \rho^{(1)}(\mathbf{r}^i)} \tag{A.16}$$

avec l'Eq.(A.15), on obtient alors le résultat

$$1 + \iint [g^{(2)}(\mathbf{r}^1,\mathbf{r}^2) - 1] d\mathbf{r}^1 d\mathbf{r}^2 = \frac{\langle N^2 \rangle - \langle N \rangle^2}{\langle N \rangle} = \rho k_B T \kappa. \tag{A.17}$$

Finalement, pour un hamiltonien $H(\mathbf{r}^N, \mathbf{p}^N)$ dont le terme d'interaction dépend uniquement de la distance entre les particules $V(\mathbf{r}^1,\mathbf{r}^2) \to V(|\mathbf{r}^1 - \mathbf{r}^2|)$, la 2-fonction de distribution prend la forme de la fonction de distribution de paires $g^{(2)}(\mathbf{r}^1,\mathbf{r}^2) \to g(\mathbf{r})$ définie à l'Eq.(2.14. On obtient finalement la *règle de somme de la compressibilité*

$$\boxed{1 + \int [g(\mathbf{r}) - 1] d\mathbf{r} = S(\mathbf{k} = 0) = \rho k_B T \kappa.} \tag{A.18}$$

Annexe B

SOLUTION NUMÉRIQUE DE L'ÉQUATION D'ORNSTEIN-ZERNIKE

L'objectif de cette annexe est de décrire la procédure numérique permettant d'obtenir la fonction de corrélation totale $h(r)$ et la fonction de corrélation directe $c(r)$ pour un potentiel de paires $V(r)$ à partir de la relation de OZ

$$h(k) = c(k) + \rho c(k)h(k) \tag{B.1}$$

et de la relation de fermeture

$$h(r) = \exp[-\beta V(r) + h(r) - c(r) + B(r)] + 1. \tag{B.2}$$

Lors de la procédure, il sera nécessaire de passer fréquemment de l'espace réel $h(r)$ à l'espace de Fourier $h(k)$. Il est à noter que puisqu'on étudie uniquement des systèmes à symétrie radiale, les transformées de Fourier se simplifient sous la forme d'une transformation de Fourier-Bessel

$$f(k) = 4\pi \int_0^\infty f(r)\frac{\sin(kr)}{kr}r^2\ dr \qquad \text{et} \qquad f(r) = \frac{1}{2\pi^2}\int_0^\infty f(k)\frac{\sin(kr)}{kr}k^2\ dk. \tag{B.3}$$

En définissant la fonction $N \equiv h - c$, il est possible de réécrire l'Eq.(A.1) et l'Eq.(A.2) sous les formes suivantes

$$h(k) = \exp[-\beta V(r) + N(r) + B(r)] + 1 \tag{B.4}$$

et

$$N(k) = \frac{\rho h^2(k)}{1 + \rho h(k)}. \tag{B.5}$$

La procédure consiste alors à choisir des valeurs d'essais pour $N^{(0)}(r)$ et $B^{(0)}(r)$(par exemple $N^{(0)}(r) = B^{(0)} = 0$) et de les introduire dans la relation de fermeture de l'Eq.(A.4) pour obtenir $h^{(0)}(r)$. En effectuant la transformée de Fourier de $h^{(0)}(r)$ à l'aide de l'Eq.(A.3), il est possible d'introduire la fonction $h^{(0)}(k)$ dans la relation de OZ de l'Eq.(A.5) pour obtenir $N^{(1)}(k)$. En effectuant la transformée de Fourier inverse, on obtient finalement la première itération de $N^{(1)}(r)$. En introduisant $h^{(0)}(r)$ dans l'Eq.(2.29), on obtient alors la première itération du terme de pont $B^{(1)(r)}$. Les fonctions $N^{(1)}(r)$ et $B^{(1)(r)}$ sont alors utilisées pour recommencer le processus itératif jusqu'à l'obtention de la convergence désirée.

Annexe C

MÉTHODE "CLASSICAL HYPER-NETTED-CHAIN"

L'énergie d'échange et corrélation par électron pour un système paramagnétique de densité n peut s'écrire sous la forme

$$f_{\rm xc} = \frac{n}{2}\int_0^1 \frac{d\lambda}{2\lambda}\int d\mathbf{r}\ \frac{\lambda}{r}\left[h_{11}(r,\lambda)+h_{12}(r,\lambda)\right] \tag{C.1}$$

où l'interaction de Coulomb $1/r$ est modifiée par un paramètre de couplage λ/r et $h_{ij}(r) = g_{ij}(r) - 1$ est la fonction de corrélation totale pour les spins i et j. L'énergie d'échange et corrélation du système d'électron en interaction peut alors être calculée à condition de connaître les fonctions $g_{ij}(r)$ en fonction de la température.

La méthode consiste à effectuer une application du fluide quantique à la température T vers un fluide de Coulomb classique à la température $T_{\rm CF} = \sqrt{T^2+T_q^2}$ où T_q est un paramètre s'assurant que le fluide classique possède la même énergie de corrélation que le fluide quantique. Cela permet alors d'utiliser la relation OZ et l'approximation HNC, présentées dans la section 2.1.2, afin d'obtenir les fonctions de distributions de paires. Pour tenir compte du principe d'exclusion de Pauli dans notre fluide classique, on utilise un potentiel de paires effectif tel que

$$\phi_{ij}(r) = \mathcal{P}(r)\delta_{ij} + V_{\rm Coul}(r), \tag{C.2}$$

où $\mathcal{P}(r)$ est le "potentiel de Pauli" introduit, notablement, par Lado [211] et où $V_{\rm Coul}(r)$ est le potentiel de Coulomb. Puisque l'exclusion de Pauli est présente même lorsque les électrons n'interagissent pas, il est possible d'obtenir le potentiel $\mathcal{P}(r)$ en inversant l'équation HNC appliquée à la fonction de distribution de paires d'électrons de même spin sans interaction. Celle-ci est connue exactement et prend la forme

$$\beta_{\rm cf}\mathcal{P}(r) = -\ln[g_{ii}^0(r)] + h_{ii}^0(r) - c_{ii}^0(r). \tag{C.3}$$

À la température T, un électron peut uniquement être localisé dans l'espace à sa longueur d'onde thermique près et il est nécessaire de modifier le potentiel de Coulomb pour tenir

compte de cet effet quantique. Suivant les travaux de Minoo, Gombert et Deutsch [212], la méthode utilise un potentiel de Coulomb modifié tel que

$$V_{\mathrm{Coul}}(r) = \frac{1}{r}\left(1 - e^{-r/\lambda_T}\right) \tag{C.4}$$

où la longueur de diffraction est donnée par $\lambda_T = (\pi m^* T)^{-1/2}$ avec m^* la masse réduite de l'électron. En utilisant le potentiel de l'Eq.(C.2), il est alors possible de résoudre les équations couplées HNC et OZ pour le fluide en interaction permettant d'obtenir l'énergie d'échange et corrélation en fonction de la température. La paramétrisation de la fonctionnelle $f_{\mathrm{xc}}(r_s,T)$ en fonction du rayon de Wigner-Seits r_s est présentée dans la Ref.[84] et prend la forme

$$f_{\mathrm{xc}}(n,T) = \frac{\epsilon_{\mathrm{xc}}(n,0) - P_1(n,T)}{P_2(n,T)}, \tag{C.5}$$

où

$$P_1 = (A_2u_1 + A_3u_2)T^2 + A_2u_2T^{5/2} \qquad \text{et} \qquad P_2 = 1 + A_1T^2 + A_3T^{5/2} + A_2T^3 \tag{C.6}$$

avec

$$A_k(r_s) = \exp\left[\frac{y_k(r_s) + \beta_k(r_s)z_k(r_s)}{1 + \beta_k(r_s)}\right], \tag{C.7}$$

$$y_k(r_s) = v_k \ln(r_s) + \frac{a_{1,k} + b_{1,k}r_s + c_{1,k}r_s^2}{1 + 0.2r_s^2}, \tag{C.8}$$

$$z_k(r_s) = r_s\frac{a_{2,k} + b_{2,k}r_s}{1 + c_{2,k}r_s^2} \qquad \beta_k(r_s) = \exp[(r_s - r_k)/0.2]. \tag{C.9}$$

Les différents coefficients de cette paramétrisation sont présenté à la table C. I.

Tableau C. I. Coefficients de la paramétrisation de $f_{\mathrm{xc}}(r_s,T)$ de l'Eq.(B.5) pour le gaz homogène d'électrons à température finie obtenue par la méthode CHNC

k	$a_{1,k}$	$b_{1,k}$	$c_{1,k}$	$a_{2,k}$	$b_{2,k}$	$c_{2,k}$	v_k	r_k
1	5.6304	-2.2308	1.7624	2.6083	1.2782	0.16625	1.5	4.4467
2	5.2901	-2.0512	1.6185	-15.076	24.929	2.0261	3.0	4.5581
3	3.6854	-1.5385	1.2629	2.4071	0.78293	0.0959	3.0	4.3909

Annexe D

ALGORITHME DE VERLET-NOSÉ-HOOVER

Lors de simulations de DM, l'algorithme de Verlet permet d'effectuer l'intégration des équations du mouvement d'un pas de temps Δt de chaque ion en effectuant les étapes suivantes

$$\mathbf{r}_i(t+\Delta t) = \mathbf{r}_i(t) + \mathbf{v}_i(t)\Delta t + \frac{\mathbf{F}_i(t)}{2m}\Delta t^2 \tag{D.1}$$

$$\mathbf{v}_i(t+\Delta t/2) = \mathbf{v}_i(t) + \frac{\mathbf{F}_i(t)}{m}\frac{\Delta t}{2} \tag{D.2}$$

$$\mathbf{F}_i(t+\Delta t) = \mathbf{F}_i(\mathbf{r}_i(t+\Delta t)) \tag{D.3}$$

$$\mathbf{v}_i(t+\Delta t) = \mathbf{v}_i(t+\Delta t/2) + \frac{\mathbf{F}_i(t+\Delta t)}{m}\frac{\Delta t}{2}. \tag{D.4}$$

Malgré l'efficacité de cette algorithme, il n'est pas suffisant pour simuler un système en gardant une température désirée. L'introduction du thermostats de Nosé-Hoover [72, 73] permet de simuler un système avec le nombre de particule N, le volume V et la température T conservés. L'utilisation d'un terme de friction modifie les étapes de l'algorithme de Verlet telles que

$$\mathbf{r}_i(t+\Delta t) = \mathbf{r}_i(t) + \mathbf{v}_i(t)\Delta t + \left(\frac{\mathbf{F}_i(t)}{m} - \xi(t)\mathbf{v}_i(t)\right)\frac{\Delta t^2}{2} \tag{D.5}$$

$$\mathbf{v}_i(t+\Delta t/2) = \mathbf{v}_i(t) + \left(\frac{\mathbf{F}_i(t)}{m} - \xi(t)\mathbf{v}_i(t)\right)\frac{\Delta t}{2} \tag{D.6}$$

$$\mathbf{F}_i(t+\Delta t) = \mathbf{F}_i(\mathbf{r}_i(t+\Delta t)) \tag{D.7}$$

$$\xi(t+\Delta t/2) = \xi(t) + \left(\sum_{i=1}^{N}\frac{m\mathbf{v}_i(t)^2}{2} - \frac{3N+1}{2}k_bT\right)\frac{\Delta t}{2Q} \tag{D.8}$$

$$\xi(t+\Delta t) = \xi(t+\Delta t/2) + \left(\sum_{i=1}^{N}\frac{m\mathbf{v}_i(t+\Delta t/2)^2}{2} - \frac{3N+1}{2}k_bT\right)\frac{\Delta t}{2Q} \tag{D.9}$$

$$\mathbf{v}_i(t+\Delta t) = \left(\mathbf{v}_i(t+\Delta t/2) + \frac{\mathbf{F}_i(t+\Delta t)}{m}\frac{\Delta t}{2}\right)\left(1+\xi(t+\Delta t)\frac{\Delta t}{2}\right)^{-1}. \tag{D.10}$$

Bibliographie

[1] F. Graziani, M. P. Desjarlais, R. Redmer, and S. D. B. Trickey. *Frontiers and Challenges in Warm Dense Matter*. Springer, Berlin , Germany, 2014.

[2] S. H. Glenzer and R. Redmer. X-ray thomson scattering in high energy density plasmas. *Rev. Mod. Phys.*, 81(1625), 2009.

[3] M Baus and J.-P. Hansen. *Statistical Mechanics of Simple Coulomb Systems*.

[4] J. C. Slater and G. F. Koster. Simplified lcao method for the periodic potential problem. *Physical Review*, 94(4), 1954.

[5] J. C. Slater. Damped electron waves in crystals. *Physical Review*, 51(840), 1937.

[6] J. A. Bittencourt. *Fundamentals of Plasma Physics*.

[7] M Baus and J.-P. Hansen. Statistical mechanics of simple coulomb systems. *Physics Reports*, 59(1), 1990.

[8] N. Singh. Two-temperature model of nonequilibrium electron relaxation : a review. *Int. J. Mod. Phys. B*, 24(1141), 2010.

[9] J. K. Chen, D. Y. Tzou, and J. E. Beraun. A semiclassical two-temperature model for ultrafast laser heating. *Int. J. Heat Mass Tram.*, 49(1), 2006.

[10] B. Chimier, V. Tikhonchuk, and L. Hallo. Heating model for metals irradiated by a subpicosecond laser pulse. *Phys. Rev. B*, 75(195124), 2007.

[11] A. Kozyreva, M. Basko, F. B. Rosmej, T. Schlegel, A. Tauschwitz, and D. H. H. Hoffmann. Dynamic confinement of targets heated quasi-isochorically with heavy ion beams. *Phys. Rev. E*, 68(056406), 2003.

[12] Y. Ping, A.A. Correa, T. Ogitsu, E. Draeger, E. Schwegler, T. Aob, K. Widmanna, D.F. Price, E. Lee, H. Tamb, P.T. Springer, D. Hansonb, I. Koslowb, D. Prendergast, G. Collins, and A. Ng. Warm dense matter created by isochoric laser heating. *High Energy Density Physics*, 6, 2010.

[13] J. Hohlfeld, S.-S. Wllershoff, J Güdde, U. Conrad, V. Jähnke, and E. Matthias. Electron and lattice dynamics following optical excitation of metals. *Chemical Physics*, 251 :237–258, 2000.

[14] T. R. Bochly, R. S. Craxton, T. H. Hinterman, J. H. Kelly, T. J. Kessler, S. A. Kumpan, S. A. Letzring, R. L. Mccrory, S. F. B. Morse, and W. Seka *et al. Rev. Dci. Intrum.*, 66(508), 1995.

[15] B. Nagler, B. Arnold, G. Bouchard, R. F. Boyce, R. M. Boyce, A. Callen, M. Campell, and R. Curiel *et al.* The matter in extreme conditions instrument at the linac coherent light source. *J. Synchrotron Rad.*, 22 :520–525, 2015.

[16] E García Saiz *et al.* Probing warm dense lithium by inelastic x-ray scattering. *Nature*, 4 :940–944, 2008.

[17] H. J. Lee *et al* . X-ray thomson-scattering measurements of density and temperature in shock-compressed beryllium. *Phys. Rev. Lett.*, 102(115001), 2009.

[18] R. R. Fäustlin, Th. Bornath, T. Döppner, D S. Düsterer, E. Förster, C. Fortmann, S. H. Glenzer, S. Göde, G. Gregori, R. Irsig, T. Laarmann, H. J. Lee, B. Li, K.-H. Meiwes-Broer, J. Mithen, B. Nagler, A. Przystawik, H. Redlin, R. Redmer, H. Reinholz, G. Röpke, F. Tavella, R. Thiele, J. Tiggesbumker, S. Toleikis, I. Uschmann, S. M. Vinko, T. Whitcher, U. Zastrau, B. Ziaja, and B. Tschentscher. Observation of ultrafast nonequilibrium collective dynamics in warm dense hydrogen. *Phys. Rev. Lett.*, 104(125002), 2010.

[19] S. H. Glenzer *et al.* Observations of plasmons in warm dense matter. *Phys. Rev. Lett.*, 98(065002), 2007.

[20] J. Sheffield. *Plasma scattering of electromagnetic radiation.*

[21] J. Chihara. Difference in x-ray scattering between metallic and non-metallic liquids due to conduction electrons. *J. Phys. F : Met. Phys.*, 17 :295–304, 1987.

[22] H. B. Callen and Welton T. A. Irreversibility and generalized noise. *Physical Review*, 83(1), 1951.

[23] K.-U. Plagemann, P. Sperling, R. Thiele, M. P. Desjarlais, C. Fortmann, T. Döppner, H. J. Lee, S. H. Glenzer, and R. Redmer. Dynamic structure facor ine warm dense beryllium. *New Journal of Physics*, 14(055020), 2012.

[24] A. N. Souza, D. J. Perkins, C. E. Starrett, D. Saumon, and S. B. Hansen. Predictions of x-ray scattering spectra for warm dense matter. *Phys. Rev. E*, 89(023108), 2014.

[25] M. W. C. Dharma-wardana and F. Perrot. Energy relaxation and the quasiequation of state of dense two-temperature nonequilibrium plasma. *Phys. Rev. E*, 58(3), 1998.

[26] P. Sperling *et al.* Free-electron x-ray laser measurements of collisional-damped plasmons in isochorically heated warm dense matter. *Phys. Rev. Lett.*, 115(115001), 2015.

[27] R. K. Williams, G. L. Coleman, and D. W. Yarbrough. Oak ridge national laboratory technical report,. *ORNL/TM-*, 10622, 1988.

[28] J. M. Ziman. A theory of the electrical properties of liquid metals i : The monovalent metals. *Philosophical Magazine*, 6(68), 1961.

[29] V. Recoules, J. Clérouin, G. Zérah, P.M. Anglade, and S. Mazevet. Effect of intense laser irradiation on the lattice stability of semiconductors and metals. *Phys. Rev. Lett.*, 96(055503), 2006.

[30] R. Ernstorfer, M. Harb, C. T. Hebeisen, G. Sciaini, T. Dartigalongue, and R. T. D. Miller. The formation of warm dense matter : experimental evidence for electronic bond hardening in gold. *Science*, 323(1033), 2009.

[31] R. Stedman and G. Nilsson. Dispersion relations for phonons in aluminum at 80 and 300°k. *Phys. Rev.*, 145(492), 1966.

[32] A. D. B. Woods, B. N. Brockhouse, R. H. March, A. T. Steward, and R. Bowers. Crystal dynamics of sodium at 90°k. *Phys. Rev.*, 128(1112), 1962.

[33] R. A. Cowler, A. D. B. Woods, and G. Dolling. Crystal dynamics of potassium. i. pseudopotential analysis of phonon dispersion curves at 9°k. *Phys. Rev.*, 150(487), 1966.

[34] P. Hohenberg and W. Kohn. Inhomogeneous electron gas. *Phys. Rev.*, 136(B864), 1964.

[35] W. Kohn and L. J. Sham. Self-consistent equations including exchange and correlation effects. *Phys. Rev.*, 140(A1133), 1965.

[36] E. Fermi, J. Pasta, and S. Ulam. Los alamos report la-1940. 1955.

[37] B. J. Alder and T. E. Wainwright. Studies in molecular dynamics. i. general method. *J. Chem. Phys.*, 31(459), 1959.

[38] X. Gonze *et al.* Abinit : First-principles approach to material and nanosystem properties. *Comp. Phys. Com.*, 180 :2582–2615, 2009.

[39] X. Gonze. First-principles responses of solids to atomic displacements and homogeneous electric fields : Implementation of a conjugate-gradient algorithm. *Phys. Rev. B*, 55(10337), 1997.

[40] G. Kresse and J. Furthmuller. Efficient iterative schemes for ab initio total-energy calculations using a plane-wave basis set. *Phys. Rev. B*, 54(11169), 1996.

[41] PAGES = 285 H. Hellmann publisher=Leipzig : Franz Deuticke, YEAR = 1937. *Einführung in die Quantenchemie.*

[42] R. P. Feynman. Forces in molecules. *Physical Review*, 56(340), 1939.

[43]

[44] M. E. Tuckerman. *Ab initio* molecular dynamics : basic concepts, current trends, and novel applications. *Journal of Physics : Condensed Matter*, 14(50), 2002.

[45] N. W. Ashcroft and N. D. Mermin. *Solid State Physics.* Sanders College, Philadelpia, USA, 1976.

[46] T. G. White, S. Richardson, B. J. B. Crowley, L. K. Pattison, J. W. O. Harris, and G. Gregori. Orbital-free density functional theory simulations of the dynamic structure factor of warm dense aluminum. *Phys. Rev. Lett.*, 111(175002), 2013.

[47] K. Wünsch, J. Vorberger, and D. O. Gericke. Ion structure in warm dense matter : Benchmarking solutions of hypernetted-chain equations by first-principle simulations. *Phys. Rev. E*, 79(010201), 2009.

[48] L. B. Fletcher *et al.* Ultrabright x-ray laser scattering for dynamic warm dense matter physics. *Nature Photonics*, 9(274), 2015.

[49] T. Ma *et al.* X-ray scattering measurements of strong ion-ion correlations in shock-compressed aluminum. *Phys. Rev. Lett*, 110(065001), 2013.

[50] R. Piron and T. Blenski. Variational-average-atom-in-quantum-plasmas (vaaqp) code and virial theorem : Equation-of-state and shock-hugoniot calculations for warm dense al, fe, cu, and pb. *Phys. Rev. E*, 83(026403), 2011.

[51] V Wilson, B.and Sonnad, P. Sterne, and W. Isaacs. Purgatorio — a new implementation of the inferno algorithm. *JQSRT*, 99 :658–679, 2006.

[52] P. A. Sterne, S.B. Hansen, B.G. Wilson, and W.A. Isaacs. Equation of state, occupation probabilities and conductivities in the average atom purgatorio code. *High Energy Density Physics*, 3(278), 2007.

[53] R. Piron and T. Blenski. Variational-average-atom-in-quantum-plasmas (vaaqp) code and virial theorem : Equation-of-state and shock-hugoniot calculations for warm dense al, fe, cu, and pb. *Phys. Rev. E*, 83(026403), 2011.

[54] M. S. Murillo, J. Weisheit, S. B. Hansen, and M. W. C. Dharma-wardana. Partial ionization in dense plasmas : Comparisons among average-atom density functional models. *Phys. Rev. E*, 87(063113), 2013.

[55] C. E. Starrett and D. Saumon. Electronic and ionic structures of warm and hot dense matter. *Phys. Rev. E*, 87(013104), 2013.

[56] C. E. Starrett, D. Saumon, J. Daligault, and S. Hamel. Integral equation model for warm and hot dense mixtures. *Phys. Rev. E*, 90(033110), 2014.

[57] C. E. Starrett and D. Saumon. Models of the elastic x-ray scattering feature for warm dense aluminum. *Phys. Rev. E*, 92(033101), 2015.

[58] Y. Hou, R. Bredow, J. Yuan, and R Redmer. Average-atom model combined with the hypernetted chain approximation applied to warm dense matter. *Physical Review E*, 91(033114), 2015.

[59] W. R. Johnson, J. Nilsen, and K. T. Cheng. Average-atom model for x-ray scattering from warm dense matter. *Presentation at Workshop IV : Computational Challenges in Warm Dense Matter at IPAM (UCLA)*, 2012.

[60] R. P. Feynman, M. Metropolis, and E Teller. Equations of state of elements based on the generalized fermi-thomas theory. *Physical Review*, 75(1561), 1949.

[61] M. W. C. Dharma-wardana and F. Perrot. Density-functional theory of hydrogen plasmas. *Phys. Rev. A*, 26(4), 1982.

[62] F. Perrot. Dense simple plasmas as high-temperature liquid simple metals. *Phys. Rev. A*, 42(8), 1990.

[63] F Perrot. Ion-ion interaction and equation of state of a dense plasma : Application to beryllium. *Phys. Rev. E*, 47(570), 1993.

[64] F. Perrot and M. W. C. Dharma-wardana. Equation of state and transport properties of an interacting multispecies plasma : Application to a multiply ionized al plasma. *Phys. Rev E*, 52(5352), 1995.

[65] N. W. Ashcroft and N. D. Mermin. *Solid State Physics*. Sanders College, Philadelpia, USA, 1976.

[66] J.-P. Hansen and I. R. McDonald. *Theory of simple liquids*. Academic Press, San Diego, 1990.

[67] S. Ornstein, L and F. Zernike. Accidental deviations of density and opalescence at the critical point of a single substance. *Huygens Institute - Royal Netherlands Academy of Arts and Sciences Proceedings*, 17 :793–806, 1914.

[68] F. Lado, S. M. Foiles, and N. W. Ashcroft. Solutions of the reference-hypernetted-chain equation with minimized free energy. *Phys. Rev. A*, 28(2374), 1983.

[69] L Verlet and J-J Weis. Equilibrium theory of simple liquids. *Phys. Rev. A*, 5(939), 1972.

[70] D Henderson and E. W. Grundke. Direct correlation function : Hard sphere fluid. *J. Chem. Phys.*, 63(601), 1975.

[71] L. Verlet. Computer "experiments" on classical fluids. i. thermodynamical properties of lennard-jones molecules. *Phys. Rev.*, 159 :98–103, 1967.

[72] S. Nose. A unified formulation of the constant temperature molecular-dynamics methods. *Journal of Chemical Physics*, 81 :511–519, 1984.

[73] W. G. Hoover. Canonical dynamics equilibrium phase-space distributions. *Phys. Rev. A*, (31), 1985.

[74] E. Engel and R. M. Dreizler. *Density Functional Theory : An Advanced Course*. Springer-Verlag Berlin Heidelberg, 2011.

[75] E. S. Kryachko and E. V. Ludea. Formulation of n- and v-representable density-functional theory. i. ground states. *Phys. Rev. A*, 43(2179), 1991.

[76] K. Capelle. A bird's-eye view of density-functional theory. *arXiv :cond-mat/0211443v5 [cond-mat.mtrl-sci]*.

[77] N. David Mermin. Thermal properties of the inhomogeneous electron gas n. david mermin. *Phys. Rev.*, 137(1), 1965.

[78] D. M. Ceperley and B. J. Alderd. Ground state of the electron gas by a stochastic method. *Phys. Rev. Lett.*, 45(7), 1980.

[79] J. P. Perdew, K. Burke, and M. Ernzerhof. Generalized gradient approximation made simple. *Phys. Rev. Lett.*, 77(3865), 1996.

[80] F. Perrot and M. W. C. Dharma-wardana. Exchange and correlation potentials for electron-ion systems at finite temperatures. *Phys. Rev. A*, 30(2619), 1984.

[81] D. G. Kanhere, P. V. Panat, A. K. Rajagopal, and J. Callaway. *Phys. Rev. A*, 33(490), 1986.

[82] H. Iyeetomi and S. Ichimaru. Free energies of electron-screened ion plasmas in the hypernetted-chain approximation. *Phys. Rev. A*, 34(433), 1986.

[83] M W C Dharma-wardana. Density-functional theory, finite-temperature classical maps, and their implications for foundational studies of quantum systems. *Journal of Physics : Conference Series*, (1).

[84] F. Perrot and M. W. C. Dharma-wardana. Spin-polarized electron liquid at arbitrary temperatures : Exchange-correlation energies, electron-distribution functions, and the static response functions. *Phys. Rev. B*, 62(16536), 2000.

[85] P. Pulay. Ab initio calculation of force constants and equilibrium geometries in polyatomic molecules. *Molecular Physics*, 17(2) :197–204, 1969.

[86] P Bendt and A. Zunger. Simultaneous relaxation of nuclear geometries and electric charge densities in electronic structure theories. *Phys. Rev. Lett.*, 50(21), 1983.

[87] J. M. Ziman. Some non-structural aspects of the theory of metals. *Proc. R. Soc. London*, 91(701), 1967.

[88] L. Dagens. A selfconsistent calculation of the rigid neutral atom density according to the auxiliary neutral atom model. *J. Phys. C*, 5(2333), 1972.

[89] L. Dagens. Densité de valence et énergie de liaison d'un métal simple par la méthode de l'atome neutre : le potentiel ionique hartree-fock. *J. Phys. (Paris)*, 36(521), 1975.

[90] L. Dagens. Application de la méthode de l'atome neutre auxiliaire au calcul de l'énergie des métaux simples. *J. Phys. (Paris)*, 34(8), 1973.

[91] V. Heine and J. E. Shiveley. A 'minimum perturbation' pseudopotential in terms of phase shifts. *J. Phys. C*, 4(13), 1972.

[92] P. Lorazo, L. J. Lewis, and M. Meunier. Short-pulse laser ablation of solids : From phase explosion to fragmentation. *Phys. Rev. Lett.*, 22(225502), 2003.

[93] G. Dimonte and J. Daligault. Molecular-dynamics simulations of electron-ion temperature relaxation in a classical coulomb plasma. *Phys. Rev. Lett.*, 101(135001), 2008.

[94] P. Lorazo, L.J. Lewis, and M. Meunier. Thermodynamic pathways to melting, ablation, and solidification in absorbing solids under pulsed laser irradiation. *Phys. Rev. B*, 73(134108), 2006.

[95] K. P. Driver and B. Militzer. All-electron path integral monte carlo simulations of warm dense matter : Application to water and carbon plasmas. *Phys. Rev. Lett.*, 108(115502), 2012.

[96] Z. Chen, B. Holst, S. E. Kirkwood, V. Sametoglu, M. Reid, Y. Y. Tsui, V. Recoules, and A. Ng. Evolution of ac conductivity in nonequilibrium warm dense gold. *Phys. Rev. Lett.*, 110(135001), 2013.

[97] P. Audebert, R. Shepherd, K. Fournier, O. Peyrusse, D. Price, R. Lee, P. Springer, J.-C. Gauthier, and L. Klein. Heating of thin foils with a relativistic-intensity short-pulse laser. *Phys. Rev. Lett.*, 89(264001), 2002.

[98] A. Mančić, A. Lévy, M. Harmand, M. Nakatsutsumi, P. Antici, P. Audebert, P. Combis, S. Fourmaux, S. Mazevet, O. Peyrusse, V. Recoules, P. Renaudin, J. Robiche, F. Dorchies, and J. Fuchs. Picosecond short-range disordering in isochorically heated aluminum at solid density. *Phys. Rev. Lett.*, 104(035002), 2010.

[99] H. M. Milchberg, R. R. Freeman, S. C. Davey, and R. M. More. Resistivity of a simple metal from room temperature to 10^6 k. *Phys. Rev. Lett.*, 61(2364), 1988.

[100] J. Plimpton. Fast parallel algorithms for short-range molecular dynamics. *J. Comp. Phys.*, 117(1), 1995.

[101] Y. Mishin, D. Farkas, M. J. Mehl, and Papaconstantopoulos D. A. Interatomic potentials for monoatomic metals from experimental data and ab initio calculations. *Phys. Rev. B*, 59(3393), 1999.

[102] V. V. Karasiev, T. Sjostrom, and S. B. Trickey. Comparison of density functional approximations and the finite-temperature hartree-fock approximation in warm dense lithium. *Phys. Rev. E*, 86(056704), 2012.

[103] M. W. C. Dharma-wardana and F. Perrot. Simple classical mapping of the spin-polarized quantum electron gas : Distribution functions and local-field corrections. *Phys. Rev. Lett.*, 84(959), 2000.

[104] E. W. Brown, J. L. DuBois, M. Holzmann, and D. M. Ceperley. Exchange-correlation energy for the three-dimensional homogeneous electron gas at arbitrary temperature. *Phys. Rev. B*, 88(081102), 2013.

[105] M. W. C. Dharma-wardana. Electron-ion and ion-ion potentials for modeling warm dense matter : Applications to laser-heated or shock-compressed al and si. *Phys. Rev. E*, 86(036407), 2012.

[106] R. W. Shaw, W. A. Jr Harrison, and W. A. Harrison. Reformulation of the screened heine-abarenkov model potential. *Phys. Rev.*, 163(604), 1967.

[107] M. S. Duesbery and R. Taylor. The effective interionic potential in simple metals. *Phys. Lett. A*, 30(497), 1969.

[108] X. Gonze and C. Lee. Dynamical matrices, born effective charges, dielectric permittivity tensors, and interatomic force constants from density-functional perturbation theory. *Phys. Rev. B*, 55(10355), 1997.

[109] L. Harbour, M. W. C. Dharma-wardana, D. D. Klug, and L. J. Lewis. Pair potentials for warm dense matter and their application to x-ray thomson scattering in aluminum and beryllium. *Phys. Rev. E*, 94(053211), 2016.

[110] N. Medvedev, U. Zastrau, E. Forster, D. O. Gericke, and B. Rethfeld. Short-time electron dynamics in aluminum excited by femtosecond extreme ultraviolet radiation. *Phys. Rev. Lett.*, 107(165003), 2011.

[111] M. W. C. Dharma-wardana and M. S. Murrilo. Pair-distribution functions of two-temperature two-mass systems : Comparison of molecular dynamics, classical-map hypernetted chain, quantum monte carlo, and kohn-sham calculations for dense hydrogen. *Phys. Rev. E*, 77(026401), 2008.

[112] F. Perrot, Y. Furutani, and M. W. C. Dharma-wardana. Electron-ion correlation potentials in the density-functional theory of h and he plasmas. *Phys. Rev. A*, 41(1096), 1990.

[113] M. W. C. Dharma-wardana. Theory of complex fluids in the warm-dense-matter regime, and application to an unusual phase-transitions in liquid carbon. *Contr. Plasma Phys.*, 58(2), 2018.

[114] V. V. Karasiev, T. Sjostrom, J. Dufty, and S. B. Trickey. The importance of finite-temperature exchange-correlation for warm dense matter calculations. *Phys. Rev. Lett.*, 112(076403), 2014.

[115] M. W. C. Dharma-wardana. Strongly-coupled coulomb systems using finite-t density functional theory : A review of studies on strongly-coupled coulomb systems since the rise of dft and sccs-1977. *Contr. Plasma Phys.*, 55(97), 2015.

[116] E. K. U. Gross and R. M. Dreizler. Density functional theory. *NATO ASI series*, 337(625).

[117] I. Tamblym, J.-Y. Raty, and S. A. Bonev. Tetrahedral clustering in molten lithium under pressure. *Phys. Rev. Lett.*, 101(075703), 2008.

[118] R. W. Shaw and W. A. Harrison. Reformulation of the screened heine-abarenkov model potential. *Phys. Rev.*, 163, 1967.

[119] H. Wagenknecht, W. Ebeling, and Förster.

[120] A. J. Archer, P. Hopkins, and R. Evans. Screening in yukawa fluid mixtures. *Phys. Rev. E*, 74(010402(R)), 2006.

[121] R. G. Gordon and Y. S. Kim. Theory for the forces between closed shell atoms and molecules. *J. Chem. Phys.*, 56(3122), 1972.

[122] G. Faussurier, C. Blancard, and P. Cossé. Coupling of an average-atom model with a collisional-radiative equilibrium model. *Physics of Plasmas*, 21(112707), 2014.

[123] L. Harbour, M. W. C. Dharma-wardana, D. D. Klug, and L. J. Lewis. Two-temperature pair potentials and phonon spectra for simple metals in the warm dense matter regime. *Contr. Plasma Phys.*, 55(144), 2015.

[124] T. Blenski, R. Piron, C. Caizergues, and B. Cichocki. Models of atoms in plasmas based on common formalism for bound and free electrons. *High Energy Density Physics*, 9 :687–695, 2013.

[125] P. B. Johnson and R. W. Christy. Optical constants of the noble metals. *Phys. Rev. B*, 6(4370), 1972.

[126] L. Dagens, M. Rasolt, and R. Taylor. Charge densities and interionic potentials in simple metals : Nonlinear effects. ii. *Phys. Rev. B*, 11(8), 1975.

[127] H. C. Chen and S. K. Lai. Structure and thermodynamics of liquid alkali metals in variational modified hypernetted-chain theory. *Phys. Rev. A*, 45(3831), 1992.

[128] A. Kietzmann, R. Redmer, M. P. Desjarlais, and T. R. Mattson. Complex behavior of fluid lithium under extreme conditions. *Phys. Rev. Lett.*, 101(070401), 2008.

[129] V. V. Karasiev, T. Sjostrom, and S.B. Trickey. Finite-temperature orbital-free dft molecular dynamics : Coupling profess and quantum espresso. *Computer Physics Communications*, 185(3240), 2014.

[130] F. R. *et al.* Graziani. *Lawrence Livermore National Laboratory report, USA, LLNL-JRNL-469771*, 2011.

[131] P. Lorazo, Lewis L. J., and M. Meunier. Thermodynamic pathways to melting, ablation, and solidification in absorbing solids under pulsed laser irradiation. *Phys. Rev. B*, 73(225502), 2003.

[132] D. Perez and L. J. Lewis. Molecular-dynamics study of ablation of solids under femtosecond laser pulses. *Phys. Rev. B*, 67(184102), 2003.

[133] M. W. C. Dharma-wardana. Rapid communication results on the energy-relaxation rates of dense two-temperature aluminum, carbon, and silicon plasmas close to liquid-metal conditions. *Phys. Rev. E*, 64(035432(R)), 2001.

[134] S. I. Anisimov, B. L. Kapeliovich, and T. L. Perelman. Electron emission from metal surfaces exposed to ultrashort laser pulses. *Sov. Phys.*, 39(375), 1974.

[135] J. Vorberger and D. O. Gericke. Ab initio approach to model x-ray diffraction in warm dense matter. *Phys. Rev. E*, 91(033112), 2015.

[136] N. W. Ashcroft. The fermi surface of aluminium. *Philos. Mag.*, 8(2055), 1963.

[137] N. W. Ashcroft. *Phys. Lett.*, 23(48), 1966.

[138] G. Gregori, S. H. Glenzer, and O. L. Landen. Generalized x-ray scattering cross section from nonequilibrium plasmas. *Phys. Rev. E*, 74(026402), 2006.

[139] J. Ye, B. Zhao, and J. Zheng. Extraction of effective ion pair interactions in warm dense beryllium and helium plasmas within integral equation theory. *Phys. Plasma*, 4(032701), 2011.

[140] E. K. U. Gross and R. M. Dreizler. Density functional theory. *NATO ASI series, Plenum Press, New York*, 387(625), 1993.

[141] A. Cangi and A. Pribram-Jones. *Phys. Rev. B*, 92(161113(R)), 2015.

[142] D. A. Chapman *et al.* Observation of finite-wavelength screening in high-energy-density matter. *Nature Communications*, 6(6839), 2015.

[143] H. C. Chen and S. K. Lai. Structure and thermodynamics of liquid alkali metals in variational modified hypernetted-chain theory. *Phys. Rev. A*, 45(3831), 1991.

[144] We have contacted the authors of ref. [48] regarding this. if $\sigma = 9.4$, then the classical coupling constant at $r_{\rm ws} = 1$ a.u. would be over 7800 at all temperatures as this term is independent of t. the hnc does not converge for $\sigma \sim 9$, although it may be treated using md.

[145] H. R. Rüter and R. Redmer. Ab initio simulations for the ion-ion structure factor of warm dense aluminum. *Phys. Rev. Lett.*, 112(145007), 2014.

[146] J. Clérouin, G. Robert, P. Arnault, C. Tricknor, J. D. Kress, and L. A. Colins. Evidence for out-of-equilibrium states in warm dense matter probed by x-ray thomson scattering. *Phys. Rev. E*, 91(011101(R)), 2015.

[147] D. A. Chapman and D. O. Gericke. Analysis of thomson scattering from nonequilibrium plasmas. *Phys. Rev. Lett.*, 107(165004), 2011.

[148] G. Hazak, Z. Zinamon, Y. Rosenfeld, and M. W. C. Dharma-wardana. Temperature relaxation in two-temperature states of dense electron-ion systems. *Phys. Rev. E*, 64(035432(R)), 2001.

[149] N. H. March. Structure and forces in liquid metals and alloys. *Canadian Journal of Physics*, 65 :219–240, 1987.

[150] M. W. C. Dharma-wardana and G. C. Aers. Determination of the pair potential and the ion-electron pseudopotential for aluminum from experimental structure-factor data for liquid aluminum. *Phys. Rev. B*, 28(1701), 1983.

[151] M. W. C. Dharma-wardana and G. C. Aers. Comment on "pair interaction from structural data of dense classical liquids". *Phys. Rev. Lett.*, 56(121), 1986.

[152] Y. Rosenfeld and G. Kahl. The inverse problem for simple classical liquids : a density functional approach. *Journal of Physics : Condensed Matter*, 9(L89), 1997.

[153] T Bonarth, R. Bredow, and R. Redmer. Private communication,.

[154] T. Sjostrom and J. Daligault. Ionic and electronic transport properties in dense plasmas by orbital-free density functional theory. *Phys. Rev E*, 92(063304), 2015.

[155] M. W. C. Dharma-wardana. Dynamic conductivity and plasmon profile of aluminum in the ultra-fast-matter regime. *Phys. Rev. E*, 93(063205), 2016.

[156] J. F. Benage, W. R. Shanahan, and M. S. Murillo. Electrical resistivity measurements of hot dense aluminum. *Phys. Rev. Lett.*, 83(2953), 1999.

[157] D. Li, H. Liu, S. Zeng, C. Wang, Z. Wu, P. Zhang, and J. Yan. Quantum molecular dynamics study of expanded beryllium : Evolution from warm dense matter to atomic fluid. *Nature Communications, Scientific reports*, 4(5898), 2014.

[158] K. Plagemann, H. R. Rüter, T. Bornath, M. Shihab, M. P. Desjarlais, C. Fortmann, S. H. Glenzer, and R. Redmer. Ab initio calculation of the ion feature in x-ray thomson scattering. *Phys. Rev. E*, 92(013103), 2015.

[159] N.D. Mermin. Lindhard dielectric function in the relaxation-time approximation. *Phys. Rev. B*, 1(2362), 1970.

[160] A. D. Baczewski, L. Shulenburger, M. P. Desjarlais, S.B. Hansen, and R.J. Magyar. X-ray thomson scattering in warm dense matter without the chihara decomposition. *Phys. Rev. Lett.*, 116(115004), 2016.

[161] T. Guillot. Interiors of giant planets inside and outside the solar system. *Science*, 286(72), 1999.

[162] S Atzeni and J. Meyer-Ter-Vehn. *The Physics of Inertial Fusion*, 2004.

[163] A. D. Baczewski, L. Shulenburger, M. P. Desjarlais, S. B. Hansen, and R. J. Magyar. X-ray Thomson scattering in warm dense matter without the Chihara decomposition. *Phys. Rev. Lett.*, 116 :115004, 2016.

[164] L. Harbour, M. W. C. Dharma-wardana, D. D. Klug, and L. J. Lewis. Equation of state, phonons, and lattice stability of ultrafast warm dense matter. *Phys. Rev. E*, 95(043201), 2017.

[165] Y. Hou, Y. Fu, R. Bredow, D. Kang, and R. Redmer. Average-atom model for two-temperature states and ionic transport properties of aluminum in the warm dense matter regime. *High Energy Density Phys.*, 22 :21–26, 2017.

[166] F Nardin, Jacucci G., and M. W. C. Dharma-wardana. Dynamic ion-ion structure factor of strongly coupled hydrogen plasmas at arbitrary degeneracies. *Phys. Rev. A*, 37(1025), 1988.

[167] M. W. C. Dharma-wardana, D. D. Klug, L. Harbour, and L. J. Lewis. Isochoric, isobaric, and ultrafast conductivities of aluminum, lithium, and carbon in the warm dense matter regime. *Phys. Rev. E*, 96 :053206, 2017.

[168] M. W. C. Dharma-wardana. Current issues in finite-t density-functional theory and warm-correlated matter. 50^{th} anniversary of kohn-sham theory : Proceedings of the conference in density functional theory, debrecen, hungary. *Computation*, 2(16), 2016.

[169] A. E. Depristo. *Recent Advances in Density Functional Methods I : Evaluation and Application of Corrected Effective Medium Methods*, pages 193–218. World Scientific, Singapore, 2011.

[170] D. Kraus, J Vorberger, D. O. Gericke, V. Bagnoud, A. Blazevic, W. Cayzac, A. Frank, G. Gregori, A. Ortner, A. Otten, F. Roth, G. Schaumann, D. Schumacher, K. Siegenthaler, F. Wagner, K. Wunsch, and M. Roth. Probing the complex ion structure in liquid carbon at 100 gpa. *Phys. Rev. Let.*, 111(255501), 2013.

[171] J. F. Benage, W. R. Shanahan, and M. S. Murillo. Electrical resistivity measurements of hot dense aluminum. *Phys. Rev. Lett.*, 83 :2953–2956, 1999.

[172] M. W. C. Dharma-wardana. Static and dynamic conductivity of warm dense matter within a density-functional approach : Application to aluminum and gold. *Phys. Rev. E*, 73 :036401, 2006.

[173] M. W. C. Dharma-wardana and F. Perrot. Density-functional study of C, Si, and Ge metallic liquids. *Phys. Rev. Lett.*, 65 :76–79, 1990.

[174] Y. Waseda. *The structure of non-crystalline materials : Liquids and amorphous solids*. McGraw-Hill, New York, 1980.

[175] L. M. Ghiringhelli, J. H. Los, A. Fasolino, and E. J. Meijer. Improved long-range reactive bond-order potential for carbon. II. Molecular simulation of liquid carbon. *Phys. Rev. B*, 72 :214103, 2005.

[176] S. Khakshouri, D. Alfè, and D. M. Duffy. Development of an electron-temperature-dependent interatomic potential for molecular dynamics simulation of tungsten under electronic excitation. *Phys. Rev. B*, 78 :224304, 2008.

[177] V. Recoules, J. Bouchet, M. Torrent, and S. Mazevet. Studies of dynamically compressed matter with X-rays. *Rapport, CEA, Arpajon, France*, 2015.

[178] N. M. Gill, R. A. Heinonen, C. E. Starrett, and D Saumon. Ion-ion dynamic structur factor of warm dense mixtures. *Phys. Rev. E*, 91(063109), 2015.

[179] T. Sjostrom, S. Crockett, and S. Rudin. Multiphase aluminum equations of state via density functional theory. *Phys. Rev. B*, 94 :036407, 2016.

[180] A Ng. Outstanding questions in electron-ion energy relaxation, lattice stability, and dielectric function of warm dense matter. *Int. J. Quant. Chem.*, 112(150), 2012.

[181] M. W. C. Dharma-wardana. Coupled-mode hot electron relaxation and the hot-phonon effect in polar semiconductors. *Solid. S. Com.*, 86(83), 1993.

[182] S. Vaziri, G. Lupina, C. Henkel, A. D. Smith, M. Östling, J. Dabrowski, G. Lippert, W. Mehr, and M. C. Lemme. A graphene-based hot electron transistor. *Nano Lett.*, 13 :1435–1439, 2013.

[183] M Pozzo, M. P. Desjarlais, and D. Alfè. Electrical and thermal conductivity of liquid sodium from first-principles calculations. *Phys. Rev. B*, 84(054203), 2011.

[184] S. Sinha, P. L. Srivastava, and R. N. Singh. Temperature-dependent structure and electrical transport in liquid metals. *J. Phys. Condens. Matter*, 1(1695), 1989.

[185] G. R. Gathers. Thermophysical properties of liquid copper and aluminum. *Int. J. Thermophys.*, 4(209), 1983.

[186] G. R. Gathers. Dynamic methods for investigating thermophysical properties of matter at very high temperatures and pressures. *Reports on Progress in Physics*, 49(341), 1985.

[187] H. D. Whitley, D. M. Sanchez, S. Hamel, A. A. Correa, and L. X. Benedict. Molecular dynamics simulations of warm dense carbon. *Contrib. Plasma Phys.*, 55(390), 2015.

[188] H. Reinholz, R. Redmer, G. Röpke, and A. Wierling. Long-wavelength limit of the dynamical local-field factor and dynamical conductivity of a two-component plasma. *Phys. Rev. E*, 62(5648), 2000.

[189] R. Leavens, A. H. MacDonald, R. Taylor, A. Ferraz, and N. H. March. Finite mean-free-paths and the electrical resistivity of liquid simple metals. *Phys. Chem. Liq.*, 11(115), 1981.

[190] V. Vlček, N. de Koker, and G. Steinle-Neumann. Electrical and thermal conductivity of al liquid at high pressures and temperatures from *ab initio* computations. *Phys. Rev. B*, 85(184301), 2012.

[191] F Perrot and M. W. C. Dharma-wardana. Theoretical issues in the calculation of the electrical resistivity of plasmas. *Int. J of Thermophys*, 20(1299), 1999.

[192] G Faussurier and C Blancard. Resistivity saturation in warm dense matter. *Phys. Rev. E*, 91(013105), 2015.

[193] J. K. Yuan, Y. S. Sun, and S. T. Zheng. Differential cross sections for the elastic scattering of electrons in hot plasmas. *J. Phys. B : At. Mol. Opt. Phys.*, 28(457), 1994.

[194] B. B. L. Witte, L. B. Fletcher, E. Galtier, E. Gamboa, H. J. Lee, U. Zastrau, R. Redmer, S. H. Glenzer, and P. Sperling. Warm dense matter demonstrating non-drude conductivity from observations of nonlinear plasmon damping. *Phys. Rev. Lett.*, 118(225001), 2017.

[195] J. Heyd, G. E. Scuseria, and M. Enzerhof. Hybrid functionals based on a screened coulomb potential. *J. Chem. Phys.*, 118(219906), 2003.

[196] R. Redmer, S. Glenzer, B. Witte, P. Sperling, G. Röpke, and H. Reinholz. Private communication. 2017.

[197] M. P. Desjarlais, J. D. Kress, and L. A. Collins. Electrical conductivity for warm, dense aluminum plasmas and liquids. *Phys. Rev. E*, 66(025401(R)), 2002.

[198] D Alf'e. Private communication. 2017.

[199] B. B. L. Witte, M. Shihab, S. H. Glenzer, and R. Redmer. Ab initio simulations of the dynamic ion structure factor of warm dense lithium. *Phys. Rev. B*, 95(144105), 2017.

[200] F Perrot and M. W. C. Dharma-wardana. Hydrogen plasmas beyond density-functional theory : Dynamic correlations and the onset of localization. *Phys. Rev. A*, 29(1378), 1984.

[201] M. W. C. Dharma-wardana. *A physicist's view of matter and mind*. World Scientific, New Jersey, 2013.

[202] M. W. C. Dharma-wardana. A calculation of the deuterium hugoniot using the classical-map hypernetted-chain (chnc) approach. *arXiv*, 2017.

[203] M. W. C. Dharma-wardana. Static and dynamic conductivity of warm dense matter within a density-functional approach : Application to aluminum and gold. *Phys. Rev. E*, 73(036401), 2006.

[204] V. Recoules, P. Renaudin, J. Clérouin, P. Noiret, and G. Zérah. Electrical conductivity of hot expanded aluminum : Experimental measurements and ab initio calculations. *Phys. Rev. E*, 86, 2002.

[205] M. W. C. Dharma-wardana. *Laser Interactions with Atoms, Solids, and Plasmas*. Plenum, New York, USA, 1994.

[206] V. Recoules and J. P. Crocombette. Ab initio determination of electrical and thermal conductivity of liquid aluminum. *Phys. Rev. B*, 72(104202), 2005.

[207] E. J. Gol'tsova. *High Temp. (USSR)*, 3(438), 1965.

[208] R. P. Wilson Jr. *High Temp. Sci.*, 1(367), 1969.

[209] N. D. Lang and W. Kohn. Theory of metal surfaces : Charge density and surface energy. *Phys. Rev. B*, 1(4555), 1970.

[210] F. Perrot and M. W. C. Dharma-wardana. Equation of state and transport properties of an interacting multispecies plasma : Application to a multiply ionized al plasma. *Phys. Rev. E*, 52(2920), 1995.

[211] F. Lado. Effective potential description of the quantum ideal gases. *Journal of Chemistry and Physics*, 47(5869), 1967.

[212] H. Minoo, M. Gombert, and C. Deutsh. Temperature-dependent coulomb interactions in hydrogenic systems. *Physical Review A*, 23(924), 1981.